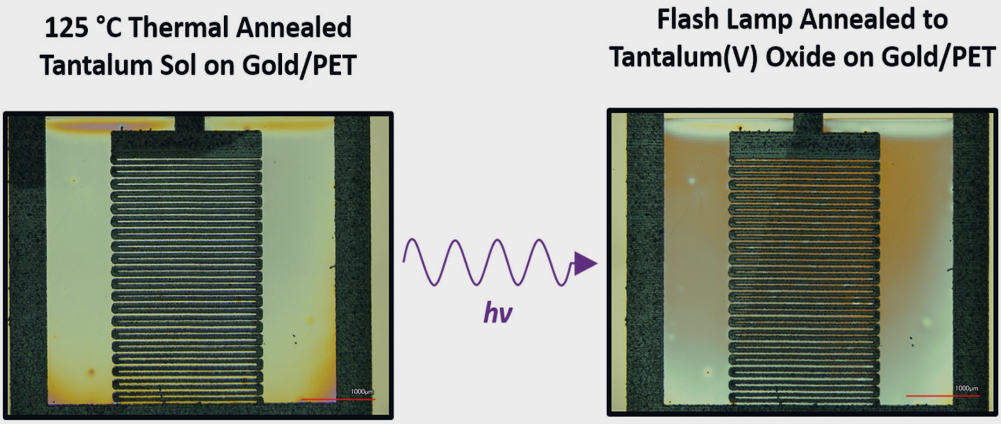

Sol-Gel-Synthese, Tintenstrahldruck und Blitzlampentemperung von Tantaloxid-Dünnschichten zur pH-Messung

Christopher Dyer Beale

Information
Band / Volume 87
ISBN 978-3-95806-656-4

Mitglied der Helmholtz-Gemeinschaft

JÜLICH
Forschungszentrum

Schriften des Forschungszentrums Jülich
Reihe Information / Information Band / Volume 87

Forschungszentrum Jülich GmbH
Institut für Biologische Informationsprozesse (IBI)
Bioelektronik (IBI-3)

Sol-Gel-Synthese, Tintenstrahldruck und Blitzlampentemperung von Tantaloxid-Dünnschichten zur pH-Messung

Christopher Dyer Beale

Schriften des Forschungszentrums Jülich
Reihe Information / Information
Band / Volume 87

ISSN 1866-1777
ISBN 978-3-95806-656-4

Bibliografische Information der Deutschen Nationalbibliothek.
Die Deutsche Nationalbibliothek verzeichnet diese Publikation in der
Deutschen Nationalbibliografie; detaillierte Bibliografische Daten
sind im Internet über http://dnb.d-nb.de abrufbar.

Herausgeber und Vertrieb: Forschungszentrum Jülich GmbH
Zentralbibliothek, Verlag
52425 Jülich
Tel.: +49 2461 61-5368
Fax: +49 2461 61-6103
zb-publikation@fz-juelich.de
www.fz-juelich.de/zb

Umschlaggestaltung: Grafische Medien, Forschungszentrum Jülich GmbH

Druck: Grafische Medien, Forschungszentrum Jülich GmbH

Schriften des Forschungszentrums Jülich
Reihe Information / Information, Band / Volume 87

D 82 (Diss. RWTH Aachen University, 2022)

ISSN 1866-1777
ISBN 978-3-95806-656-4

PUBLIKATIONSLISTE

Beale, C., Altana, A., Hamacher, S., Yakushenko, A., Mayer, D., Wolfrum, B., & Offenhäusser, A. (2022). Inkjet printed Ta2O5 on a flexible substrate for capacitive pH sensing at high ionic strength. *Sensors and Actuators B: Chemical*, *369*, 132250. https://doi.org/10.1016/j.snb.2022.132250

Beale, C., Hamacher, S., Mayer, D., & Offenhäusser, A. (2021). Verfahren zur Herstellung einer Metallglykolat-ß-diketonatlösung oder einer Metallglykolat-ß-diketoesterlösung, Metallglykolat-ß-diketonatlösung oder Metallglykolat-ß-diketoesterlösung und deren Verwendung (Patent Application No. DE102019006976A1). German Patent and Trademark Office.

Beale, C., Hamacher, S., Yakushenko, A., Bensaid, O., Willbold, S., Beltramo, G., Möller, S., Hartmann, H., Neumann, E., Mussler, G., Shkurmanov, A., Mayer, D., Wolfrum, B., & Offenhäusser, A. (2020). Correction: Tantalum(v) 1,3-propanediolate β-diketonate solution as a precursor to sol–gel derived, metal oxide thin films. *RSC Advances*, *10*(53), 32102–32102. https://doi.org/10.1039/D0RA90092C

Beale, C., Hamacher, S., Yakushenko, A., Bensaid, O., Willbold, S., Beltramo, G., Möller, S., Hartmann, H., Neumann, E., Mussler, G., Shkurmanov, A., Mayer, D., Wolfrum, B., & Offenhäusser, A. (2020). Tantalum(v) 1,3-propanediolate β-diketonate solution as a precursor to sol–gel derived, metal oxide thin films. *RSC Advances*, *10*(23), 13737–13748. https://doi.org/10.1039/D0RA02558E

Beale, C., Hamacher, S., Bensaid, O., Yakushenko, A., Mayer, D., Wolfrum, B., & Offenhäusser, A. (2019). Characterization of Flash Lamp Cured, Sol-Gel Derived Tantalum Oxide Films. *MRS Fall Meeting & Exhibit*.

ZUSAMMENFASSUNG

Die Messung des pH-Wertes und der Temperatur spielt in vielen Anwendungen eine wichtige Rolle. Dazu gehören z.B. die Lebensmittelanalyse, Umweltüberwachung, chemische Herstellungsverfahren und die Medizin. Die Integration von pH- und Temperatursensoren in Verpackungen und elektronischen Bauelementen wird weiter an Bedeutung gewinnen, weil sich die Welt in Richtung Industrie 4.0 und Internet der Dinge bewegt und immer mehr Branchen datenbasiert sein werden. Die Herstellung von Sensoren auf flexiblen Substraten kann neue Anwendungen ermöglichen. Darüber kann die Herstellung und Betrieb eines pH-Sensors ohne Referenzelektrode viele Vorteile bieten, wie z.B. der einfachere Frabrikationsprozess und die Langzeitstabilität des Sensors.

Um diesem Ziel einen Schritt näher zu kommen, wurde in dieser Arbeit die additive Herstellung von Tantaloxidschichten für die pH-Messung untersucht. Insbesondere wurden das Sol-Gel-Verfahren und die Blitzlampentemperung verwendet, um diese Schichten auf Gold-metallisierten Polyethylenterephthalat-Folien (PET-Folien) abzuscheiden. Nach der Abscheidung der Sensorschichten auf die Folie wurden sowohl ein Feldeffekttransistor mit erweitertem Gate (eng: extended-gate field-effect transistor – EGFET), als auch eine impedimetrische Konfiguration verwendet, um die Tantaloxidschichten auf pH-Sensitivität zu testen. Zusätzlich wurde ein negativer Temperaturkoeffizient (eng: negative temperature coefficient – NTC) in Sol-Gel abgeleiteten Rutheniumoxid-Tantaloxid-Schichten zur Verwendung als Temperatursensor untersucht. Diese Rutheniumoxid-Tantaloxid-Schichten wurden ohne Photohärtung auf einem Borosilikatwafer thermisch getempert.

Bei der Herstellung der Tantal-Sol-Gel-Lösung für eine eventuelle Schichtabscheidung durch Photohärtung wurde ein optimiertes Syntheseverfahren für die β-Diketonat- und β-Ketoester-Komplexbildung mit Tantal in 1,3-Propandiol durchgeführt und für die Photosensitivität im Nah-UV-Bereich charakterisiert. Suboptimale Syntheseverfahren funktionieren (immer) noch für die elektrische Bauelementenherstellung und wurden bei der Herstellung der pH-Sensoren verwendet. Diese Lösungen sind in der Atmosphäre stabil, was für den Tintenstrahldruck der Lösungen sowohl in einem Labor als auch in einer industriellen Umgebung wichtig ist.

Anschließend wurden die Lösungen im Tintenstrahldruckverfahren in Schichten aufgetragen, gefolgt von einer Kombination aus einem thermischen und einem Blitzlicht Tempern der Schichten. Die aus diesen Lösungen hergestellte Tantaloxidschichten wurden mit Hilfe verschiedene Materialcharakterisierungstechniken untersucht. Das Material wurde in einer EGFET-Konfiguration sauren und basischen Lösungen ausgesetzt und dabei wurde gezeigt, dass die Schicht Lösungen im Bereich zwischen pH 2 und pH 12 standhält.

Diese photogehärteten Tantaloxidschichten wurden anschließend in einer impedimetrischen Konfiguration mit interdigitierenden Elektroden (oder Interdigitalstruktur) (eng: interdigitated electrodes – IDEs), ohne Referenzelektrode, auf pH-Sensitivität getestet. In Lösungen mit hoher Ionenstärke wurde eine pH-abhängige Doppelschichtkapazität gemessen. Die Daten wurden mit einem Ersatzschaltbild modelliert, das aus einer Doppelschichtkapazität parallel zu einer interferierenden spezifischen Ionenadsorptionskapazität bestand.

Schließlich wurde der negative Temperaturkoeffizient von Sol-Gel abgeleiteten Rutheniumoxid-Tantaloxid-Schichten charakterisiert. Eine erste Probe wurde von 20°C bis 100°C und dann bis zu kryogenen Temperaturen getestet. Anschließend wurde eine zweite Probe mit einem verbesserten Herstellungsverfahren untersucht und von -20°C bis 60°C getestet. In beiden Fällen wurde ein reproduzierbarer NTC beobachtet. Basierend auf den vielversprechenden Ergebnissen, könnte das Rutheniumoxid-Tantaloxid-Material die Möglichkeit bieten, in einem einzigen Bauelement einen Temperatursensor sowie einen pH-Sensor zu kombinieren.

Sol-Gel Synthesis, Inkjet Printing, and Flash Lamp Annealing of Tantalum Oxide Thin Films for pH Sensing

Dissertation submitted to the Faculty of Mathematics, Computer Science,
and Natural Sciences at the RWTH Aachen University for the academic degree of
Doctor of Natural Sciences

by

Beale, Christopher Dyer
from
Phoenix, Arizona, United States of America

Examiners: Univ.-Prof. Dr. rer. nat. Andreas Offenhäusser
Univ.-Prof. Dr. rer. nat. Ulrich Simon
Univ.-Prof. Dr. rer. nat. Sven Ingebrandt

Day of oral examination: March 3, 2022

ABSTRACT

The measurement of pH and temperature plays an important role in many applications, including food analysis, environmental monitoring, chemical manufacturing, and medicine. Integration of pH and temperature sensors into packaging and electronic devices will continue to grow in importance as the world moves further towards Industry 4.0 and the Internet of Things, particularly as more industries become data-driven. New applications would also become possible by fabricating sensors on flexible substrates. Furthermore, building and operating a pH sensor without a reference electrode would provide many advantages, such as simpler manufacturing processes and long-term stability of the sensor.

In a step towards achieving this goal, additive manufacturing of tantalum oxide films for pH sensing was explored in this work. Specifically, the sol-gel process and flash lamp annealing were used to deposit these films on gold metallized polyethylene terephthalate (PET) foils. After deposition of the sensing layers on the foil, both an extended-gate field-effect transistor (EGFET) and an impedimetric configuration were used to test the tantalum oxide layers for pH sensing. Additionally, a discovered negative temperature coefficient (NTC) in sol-gel derived ruthenium-tantalum oxide layers was examined for use as a temperature sensor, where the layers were thermally annealed with no photocuring on borosilicate wafer.

In preparing the tantalum sol-gel solution for eventual layer deposition via photocuring, an optimized synthesis procedure for β-diketonate and β-ketoester complex formation with tantalum in 1,3-propanediol was conducted and the thin films characterized for photosensitivity in the near-UV range. Suboptimal synthesis procedures still work for device fabrication and were used in the production of the pH sensors. These solutions are stable in atmosphere, which is important for inkjet printing the solutions both in a laboratory and in an industrial environment.

Inkjet printing of the solutions to form layers was then performed, followed by thermal annealing and flash lamp treatment of the layers. Photocured tantalum oxide layers derived from these solutions were characterized via various material characterization techniques. Exposure of the material to acidic and basic solutions in an EGFET configuration for pH sensing was also performed, and the layer was shown to withstand solutions in the range between pH 2 and pH 12.

A photocured tantalum oxide layer was then tested for pH sensing in an impedimetric configuration on interdigitated electrodes (IDEs) without a reference electrode. A pH dependent double layer capacitance was found in solutions of high ionic strength. The data was fitted with an equivalent circuit consisting of a double layer capacitance in parallel with an interfering ion specific adsorption capacitance.

Finally, the NTC of sol-gel derived ruthenium-tantalum oxide layers was characterized. A first material was tested from 20°C to 100°C, and then down to cryogenic temperatures. This was followed by investigating a second material, with an improved preparation procedure from the first material, and tested from -20°C to 60°C. In both cases, a reproducible NTC was observed which could potentially be combined as a temperature sensor with the fabricated pH sensor in a single device.

ACKNOWLEDGEMENTS

First and foremost, I would like to thank Alexey Yakushenko for being kind enough to ask me to join him in Jülich to work on inkjet printed sensors, and thereby Andreas Offenhäusser for allowing me to pursue a doctoral degree in chemistry at RWTH Aachen University and the Bioelectronics Institute at Forshungszentrum Jülich. Alexey's willingness to bet on me as the one to carry and develop his idea for a printed and flexible Ta_2O_5 pH sensor, while allowing me certain freedoms in my work with tantalum sol-gel chemistry, has resulted in this thesis which I hope inspires future research in sol-gel chemistry, photonic curing of metal oxides, and pH sensing.

In starting my investigations, Jekaterina Viktorova introduced me to inkjet printing of sol-gel based oxides, and she provided invaluable advice in creating a suitable ink; this yielded a foundation for further experiments and thus led to the results reported in this thesis. For additional aid, Stefanie Hamacher was always there to inform me of proper synthesis techniques in chemistry, which during my undergraduate years in engineering were never taught to me. Stefanie was also there to support me in navigating the research institute and to help me maintain a positive outlook. As far as device physics and fabrication goes, Jan Schnitker, Antonio Altana, Aleksandr Yakovlev, and Mathis Ernst pointed me in the right direction and showed me the relevant literature. Furthermore, Mathis helped me navigate speed bumps, whether scientific or otherwise, and thus kept me on track to completing this work. The master's students which worked with me, Christian Mevissen and Oumaima Bensaid, were both valuable aides in contributing to this thesis, and therefore deserve my gratitude in helping me complete my research.

For supervision in the institute, Dirk Mayer provided me with guidance in the lab and at frequent meetings, where he was never shy to provide strong but constructive critiques to my experiments. Bernhard Wolfrum, making the long trek from Munich to Jülich every month, was always willing to get into the weeds with me in characterizing the fabricated pH sensors, and was never afraid to point out the flaws in my analysis, thus making me a better scientist. In permitting me to work at this institute, Andreas Offenhäusser exposed me to aspects of impedance spectroscopy (specifically admittance and complex capacitance) which are covered to a lesser extent in the literature, while providing me with continued support and never doubting my work.

Additionally, I am forever grateful to Kathleen Nolta at the University of Michigan, who succeeded in making organic chemistry engaging and thus causing it to be my favorite subject during my undergraduate years, thereby influencing this work in a productive and positive manner. Furthermore, the Materials Science and Engineering department at the University of Michigan exposed me to the many material characterization techniques discussed in this work, which I much appreciate.

Finally, I would like to thank my parents, William Beale and Frances Munkenbeck, for the continued support throughout my university studies in Michigan and Germany, without which would not allow for this work to be possible. My older brother, Alexander, and my twin brother, Matthew, have also provided immeasurable support throughout the years since growing up in Seattle and Oregon, therefore deserving my appreciation.

FURTHER ACKNOWLEDGEMENTS

Much of the spectroscopy and some of the measurement results would not be possible without the help from others. Antonio Altana performed laser ablation of the gold foils to create the interdigitated electrodes. Sabine Willbold measured the nuclear magnetic resonance (NMR) spectra of the solutions, and aided in the analysis while suggesting other 2D NMR techniques. Guillermo Beltramo measured the Raman spectra of the deposited layers and analyzed the results, and suggested a-SiO_2 as the substrate to use for the measurement. Sören Möller performed Rutherford backscattering spectrometry (RBS) and nuclear reaction analysis (NRA) of the deposited layers, while suggesting c-Si as a substrate and carrying out the analysis. Heinrich Hartmann performed X-ray photoelectron spectroscopy (XPS) on all samples and performed the analysis. Elmar Neumann conducted scanning electron microscopy (SEM), energy-dispersive X-ray spectroscopy (EDX) of a RuTaOx material, and performed the focused ion beam (FIB) cut of a deposited Ta_2O_5 layer. Gregor Mussler and Alexander Shkurmanov used X-ray diffraction to see if the layers are crystalline or amorphous. Roger Wördenweber used a cryostat to measure the electrical resistance of the RuTaOx layers below 300 Kelvin. Norbert Wolters put together the hardware and programmed the automated temperature setup for the RuTaOx layers.

In preparing the patent application, Bernhard Mogge gave advice and structure to my ideas in the German language. Marko Banzet and Michael Prömpers provided the necessary materials from the clean room at the Helmholtz Nano Facility. Invaluable help with laboratory supplies and equipment came from Bettina Breuer, Elke Brauweiler-Reuters, Youlia Mourzina, and Vanessa Maybeck.

Finally, the following past doctoral dissertations served as guides and greatly influenced this work, and the authors thus deserve my thanks:

New Metal Alkoxides by Alice Whitley, 1954
Birkbeck College
University of London, United Kingdom

Sol-Gel Derived Tantalum Oxide Thin Films by Lee Arnold Silverman, 1987
Department of Materials Science and Engineering
Massachusetts Institute of Technology, United States of America

Thin and Ultrathin Films of Strontium Bismuth Tantalate Obtained from Tantalum Glycolate Derivatives for Use in Non-volatile Ferroelectric Memory by Ana González García, 2002
Title translated from Spanish: *Láminas delgadas y ultradelgadas de tantalato de estroncio y bismuto obtenidas a partir de derivados de glicolato de tántalo para su uso en memorias ferroeléctricas no volátiles*
Department of Inorganic Chemistry, Faculty of Sciences
Autonomous University of Madrid, Spain

I am also grateful for funding received from "Europäischer Fonds für regionale Entwicklung," for the project "EFRE-0800361 Packsense."

TABLE OF CONTENTS

CHAPTER

APPENDIX

LIST OF TABLES

LIST OF FIGURES

LIST OF ABBREVIATIONS

AC - Alternating Current

ALD - Atomic Layer Deposition

CSD - Chemical Solution Deposition

DC - Direct Current

DEGEE - Diethylene Glycol Monoethyl Ether

DNA - Deoxyribonucleic Acid

DRC - Democratic Republic of the Congo

EDX - Energy-Dispersive X-ray Spectroscopy

EGFET - Extended-Gate Field-Effect Transistor

ESR - Equivalent Series Resistance

FIB - Focused Ion Beam

HMBC - Heteronuclear Multiple Bond Correlation

IDEs - Interdigitated Electrodes

IR - Infrared

ISFET - Ion-Sensitive Field-Effect Transistor

IUPAC - International Union of Pure and Applied Chemistry

LAPS - Light-Addressable Potentiometric Sensor

MOCVD - Metal Organic Chemical Vapor Deposition

NMR - Nuclear Magnetic Resonance

NRA - Nuclear Reaction Analysis

NTC - Negative Temperature Coefficient

PCB - Printed Circuit Board

PCSD - Photochemical Solution Deposition

PET - Polyethylene Terephthalate

PTFE - Polytetrafluoroethylene

RBS - Rutherford Backscattering Spectrometry

SEM - Scanning Electron Microscopy

SPR - Surface Plasmon Resonance

TOCSY - Total Correlation Spectroscopy

UV - Ultraviolet

XPS - X-ray Photoelectron Spectroscopy

XRD - X-ray Diffraction

LIST OF PHYSICAL CONSTANTS

All values were obtained from the National Institute of Standards and Technology, United States Department of Commerce.[1]

b	$2.897\ 771\ 955 \times 10^{-3}$ m K	Wien's Constant
c	299 792 458 m s^{-1}	Speed of Light in Vacuum
e	$1.602\ 176\ 634 \times 10^{-19}$ C	Elementary Charge
ϵ_0	$8.854\ 187\ 8128 \times 10^{-12}$ F m^{-1}	Permittivity of Vacuum
F	96 485.332 12 C mol^{-1}	Faraday's Constant
h	$6.626\ 070\ 15 \times 10^{-34}$ J s	Planck's Constant
k	$1.380\ 649 \times 10^{-23}$ J K^{-1}	Boltzmann's Constant
R	8.314 462 618 J mol^{-1} K^{-1}	Molar Gas Constant
σ	$5.670\ 374\ 419 \times 10^{-8}$ W m^{-2} K^{-4}	Stefan-Boltzmann's Constant

Chapter One

Introduction

Receiving his Diploma in Engineering from the Technical University of Vienna in 1930, Paul Eisler was ready for a career in the production of electronics.[2] However, as at the time the electrical engineering jobs were reserved for members of the antisemitic German-Nationalist student organizations, and as Eisler was Jewish, he was forced to find work elsewhere. Eisler eventually co-founded the weekly radio journal *Rundfunk* in Vienna, where he worked as technical editor and gained experience in printing technology. The radio journal was later taken up by the publishing house *Vorwärts*, where he continued to develop his printing expertise.

However, the Austrian fascist putsch in February of 1934 led to the end of the publishing house, as it had a social-democratic bent. Fearing for his future in Austria, Eisler used two patent applications to get an invitation from a British-based firm, and was able to emigrate to London in 1936. By selling his patent rights once there, but unable to take up work, Eisler continued his inventive pursuits in an effort to support himself. With limited means, he decided to combine his engineering experience in electrical circuitry with the knowledge he gained from printing.

While gaining further printing experience at the British Museum, Eisler was captivated by the idea of the mass production of electrical circuits via printing, and at the time he observed that the radio receiver market would be the most promising. After developing a working radio prototype with a printed circuit, Eisler was able to secure an interview at the firm Plessey. Following a successful demonstration, his invention was nonetheless turned down as such a manufacturing method would replace the labor force of girls, and that “girls are cheaper and more flexible.”

Through personal struggle and family tragedy due to the course of events in his home country, Eisler held on to his idea of printed electronics until the Second World War. After forced internment due to his nationality, Eisler believed the best way for him to support the war effort was to continue developing his idea of printed electronics, and took an offer from a lithographic and music printing firm, Henderson & Spalding, where the firm hoped that printed electronics would garner them wartime funding. At this firm, Eisler developed his idea of printing on and subsequently etching metal-insulator foils, which in his case was copper foil bound to varnished paper.

Eisler applied for a British patent in February 1943,[3] and began presenting his ideas to the British and American militaries for possible military applications. During such presentations, Eisler and his assistant would print on the foils, etch them with ferric chloride, clean them, and pass them around the room. Ultimately, the British were uninterested, but the Americans borrowed the idea and printed electrical circuits for proximity fuses in anti-aircraft munitions;[4,5] these fuses work by emitting a radio signal after firing, and if this signal is reflected by a metal object and then detected, the fuse detonates the projectile.

However, instead of selectively etching the circuitry on copper foils via subtractive processing, the Americans printed silver paint on steatite (a ceramic insulator) via additive processing, which allowed for cheap and reliable production of electronic circuitry for the proximity fuses.[2,5] When combined with the emerging technology of radar, projectiles armed with these fuses destroyed roughly 4000 *Vergeltungswaffe 1* (V-1) rockets aimed at London. Furthermore, during the defense of Antwerp, 97% of the hits against V-1s aimed at Allied forces were armed with the proximity fuse. The Americans were so confident in such anti-aircraft munitions that they readied their Pacific fleet with them in a potential invasion of

Japan. However, the United States turned to nuclear weapons in ending the conflict, and after the war the printed fuse technology was released. Printed electronics then expanded to other military applications, and as with nuclear technology, to applications in the civilian sector.

Through all of his hardships and meager compensation for his forward-thinking ideas, Paul Eisler's stubborn belief in printed electronics proved correct: printed circuit boards (PCBs) and subtractive processing, along with some additive processes, are now ubiquitous in electronics. Nonetheless, the move to additive printing of all components for "Industry 4.0," especially for flexible devices and the "Internet of Things," is currently on the frontier in industry.[6] Within the modern field of printed and organic electronics, additive processing is desired for resource preservation, and researchers are also seeking to optimize fabrication processes for other goals, such as cost reduction, printing on-demand for changing designs and applications, scalable production, power efficiency, flexibility, and the fabrication of reliable devices able to withstand the environment which they are exposed to. An optimistic projection for this sector is for the market to grow from \$41.2 billion in 2020 to \$74 billion by 2030, where in 2019 the market for printed and flexible sensors (\$3.9 billion) exceeded that for conductive inks (\$2.3 billion).[7]

Considering the relatively large market for printed sensors, further research in this direction is warranted for advancing printed electronics. Thus, just as the durability of printed electronics was tested in anti-aircraft munitions, the aim of this thesis is to test the robustness and reliability of additively printed, low-temperature cured electrochemical sensors in aqueous solution, which is one of the more unfavorable environments for electronics. This will be accomplished by inkjet printing and testing a tantalum oxide pH sensing layer, where pH is one of the simplest yet most important parameters in the central science of chemistry.[8]

In order to achieve these goals, this thesis will begin by optimizing the synthesis of a tantalum sol-gel precursor solution in Chapter 3, which is both air-stable and photocurable. Such a precursor solution, which could be used in both subtractive and additive processing, has the potential to affect the capacitor industry and other industries where tantalum oxide is vital. However, later experiments will show that even with suboptimal synthesis parameters, the solutions can still be used to photocure tantalum oxide films on metallized polyethylene terephthalate (PET) substrates, which can be used in pH sensing.

After the tantalum solution synthesis is described, sensor fabrication in Chapter 4 will show how the optimal xenon flash lamp parameters were obtained for photocuring tantalum oxide on gold/titanium/PET foil, how these layers are chemically resistant in acidic and basic environments, and finally how the solutions from the optimized synthesis form tantalum oxide films which are likely amorphous; photocuring of the optimally synthesized solutions will be investigated with a variety of material characterization techniques. Films fabricated from solutions using suboptimal synthesis procedures will also be shown to be photocurable, as well as to be pH sensitive in an extended-gate field-effect transistor (EGFET) configuration from pH 2 to pH 12. Furthermore, as the fabrication procedure utilizes the parallel capacitance of the material on interdigitated electrodes (IDEs) as a function of flash lamp shots, which to the knowledge of the author has not been reported elsewhere, these results are important for photocuring metal oxide materials which are used in many industries.

Then in Chapter 5, a tantalum oxide layer on IDEs will be investigated as a capacitive pH sensor, where immittance spectroscopy will be used to see if the results are supported by the theory for a metal oxide insulator in solution. Four different buffer solutions, all with the same sensor, will be used where the first buffer has the least amount of interfering ions as possible, the second buffer has potassium chloride added (0.5 M KCl), the third buffer has sodium chloride added (0.5 M NaCl, a salinity similar to the ocean[9,10] and to "high sodium kimchi," a Korean food staple),[11] and the fourth buffer has lithium chloride added (0.5 M LiCl). The results will show that in the solution with no added chloride salt, a pH sensitivity can only be seen in the series capacitance around 50 kHz. On the other hand, the solutions with added alkali chloride salt will show a pH dependent double layer capacitance. This double layer capacitance is in parallel to an interfering ion specific adsorption capacitance, the latter of which is not affected as much by the pH. Rather, the specific adsorption capacitance appears to be influenced by interfering ion size without a hydration shell. Moreover, the larger Stern distance for lithium cations in solution at the insulator-electrolyte interface reduces the double layer capacitance with respect to sodium cations in solution, which is as expected for the larger hydration shell surrounding lithium cations and for the Gouy-Chapman-Stern model.[12] The larger polarity and volume for hydrated lithium cations, resulting in dielectric decrement and a reduced surface charge density, may also contribute to a reduced Stern capacitance when compared to sodium and potassium cations.[13] Additionally, the Appendix shows immittance spectra for sensors in 0.28 M NaCl buffers (a salinity similar to "low sodium kimchi"),[11] which also exhibit a pH dependent series capacitance.

In Chapter 6, an observed thermistor effect, discovered when attempting to fabricate ruthenium-tantalum oxide pH sensors, will be presented in two experiments. The first experiment resulted in a precipitate-free precursor solution, which came from a highly filtered solution originally containing precipitate. The filtered solution was thermally annealed to unexpectedly form a material with a negative temperature coefficient (NTC). The second experiment then successfully reverse engineers the first experiment, and the potential synthesis mechanism and the temperature sensitivity of the thermally annealed layers will be subsequently discussed.

As this thesis covers multiple topics, which are sometimes unrelated, the chapters are written so that they can be read independently of each other. The background information in Chapter 2 attempts to unify these topics as best as possible, while discussing prior research, material sourcing, and applications. In investigating the additive manufacturing of tantalum oxide and its tested application as a pH sensor (and when mixed with ruthenium, as a temperature sensor), the reported results in this work can hopefully drive major changes in the manufacturing of electronics. This is particularly important since the world is dealing with an energy and resource crisis, which could potentially be alleviated by the additive manufacturing of metal oxide materials using low-temperature annealing.

Chapter Two

Background

This chapter will cover the initial observational and theoretical background for the discussed topics, beginning with the definition of pH. This will be followed by a short discussion on conductive and insulating metal oxides, and how they have been used in pH sensing in the past. Once tantalum oxide is established as the best material for the application, a short discussion on its sourcing and applications will be presented. The purpose of this discussion is to show how the tantalum sol-gel solutions described in this thesis can be used in multiple applications to make a material which is in relatively high demand. Finally, a case will be made for the tested deposition technique, drop-on-demand inkjet printing, and how this technique serves as a foundation for researching other techniques, such as gravure printing for roll-to-roll processing.

2.1 Definition and Measurement of pH

The concept of pH dates back to 1889, when Nernst theorized that an electrode potential can be correlated to ion concentration.[8] Arrhenius, a contemporary of Nernst, had recently proposed the definition of an acid as a proton donor, and the combination of the two theories led to the idea of determining the H^+ (or H_3O^+) concentration in solution. Then in 1909, Sørensen[14,15] proposed an initial definition of the effective concentration of the hydrogen ion,

c_H, since the concentration of the H$^+$ ion is generally very low in solution:

$$c_\mathrm{H} = 10^{-p} = \frac{1}{10^p} \tag{2.1}$$

As Sørensen originally published in German and French, p was referred to as *Potenz* and *puissance*, respectively, and to *power* in English. This led to his definition of the hydrogen ion exponent, p_H, where likely due to convenience in typesetting turned into pH over time. However, his initial definition is not the pH value commonly accepted today, and this initial definition will be redefined as pc_H:

$$\mathrm{p}c_\mathrm{H} = -\log_{10} c_\mathrm{H} \tag{2.2}$$

Sørensen used the following electrochemical cell to measure pc_H (a " ; " represents a metal-electrolyte boundary, a " , " indicates multiple solutes in solution, and a " | " represents a liquid-liquid boundary):

$$\text{Pt ; H}_2\text{ , Solution X | Salt Bridge | 0.1 M Calomel Electrode} \tag{2.3}$$

In returning to Arrhenius and Nernst, the difference in e.m.f., $E_1 - E_2$, in Cell 2.3, was described with the hydrogen ion concentration of solution 1, $(c_\mathrm{H})_1$, and the hydrogen ion concentration of solution 2, $(c_\mathrm{H})_2$:

$$E_1 - E_2 = \frac{RT}{F} \ln\left[\frac{(c_\mathrm{H})_2}{(c_\mathrm{H})_1}\right] \tag{2.4}$$

Here, R is the molar gas constant, T is the temperature, and F is Faraday's constant. Then if $(c_\mathrm{H})_2$ is arbitrarily fixed at 1, E_2 would be fixed at a given temperature, where E_2 can be redefined as a standard potential, $E^{\circ\prime}$, when combining Equations 2.2 and 2.4:

$$E_1 = E^{\circ\prime} + \frac{RT}{F} \ln\left[\frac{1}{(c_\mathrm{H})_1}\right] = E^{\circ\prime} + \frac{RT \ln 10}{F} \mathrm{p}c_\mathrm{H} \tag{2.5}$$

The H$^+$ ion concentration, $(c_\mathrm{H})_1$, was further equated to the product of the acid concentration, c_1, and the degree of dissociation of the acid, α_1, determined classically by measuring electrolytic conductance:

$$(c_\mathrm{H})_1 = \alpha_1 c_1 \tag{2.6}$$

However, this definition has two main flaws: first, Equation 2.4 is only valid in ideal solutions and when the residual junction potential is zero; second, solutions containing a strong monobasic acid are known to have an acid concentration of c_1, therefore contradicting Equation 2.6.

Eventually, the e.m.f. in galvanic cells was found to be driven by ion activity rather than ion concentration, and a new definition was proposed by Sørensen and Linderstrøm-Lang in 1924. This would become the IUPAC definition of pH, or originally pa_H, and is based on the thermodynamic activity of the H^+ ion, a_H (and thereby the activity coefficient, y_H):[15,16]

$$\mathrm{pH} = \mathrm{p}a_\mathrm{H} = -\log_{10} a_\mathrm{H} = -\log_{10} y_\mathrm{H} c_\mathrm{H} \tag{2.7}$$

As the activity of the H^+ ion is immeasurable and varies among measuring cells, a convention is required which can be applied in most circumstances.

For example the Harned cell, which uses a hydrogen gas electrode versus a silver chloride electrode, is a primary standard which has good reproducibility and low uncertainty.[16] Cells which may be more convenient to use, such as the glass electrode, tend to have lower reproducibility and higher uncertainty and are deemed secondary standards. However, if a secondary standard is traceable to a primary standard (i.e., a secondary standard can be compared to a primary standard with stated uncertainties), then the use of a secondary standard is justified in place of a primary standard.

Accordingly, the pH of the standard S, pH(S), can be used to determine the pH of a solution X, pH(X), via the following relation:[15,17,18]

$$\mathrm{pH(X)} = \mathrm{pH(S)} + \frac{(E_\mathrm{X} - E_\mathrm{S})F}{RT \ln 10} \tag{2.8}$$

This relies on knowing the difference in e.m.f. between the standard, E_S, and the solution in question, E_X. In the case of a common glass electrode, this is typically between a Ag/AgCl electrode in KCl and a H^+ sensitive glass membrane in contact with the solution to be measured.[16]

2.2 Metal Oxide pH Sensors

Since glass electrodes are often large and relatively fragile, other constructions are often required when the sensor needs to be miniaturized. Thin metal oxide layers, for example, have been implemented in the past due to their durable construction,[8,19,20] and many of these layers can be deposited in standard clean room settings.[21]

2.2.1 Potentiometric Metal Oxide Sensors

In the potentiometric method, the potential difference of a stable reference electrode versus a pH-sensitive layer is measured.[8] Various oxides have been compared for the potentiometric configuration,[22] where iridium oxide is often preferred as the most reliable.[23] One of the pioneering uses for an iridium oxide pH sensor was reported for a pH-triggered pacemaker in 1978, with a quoted description below:[24]

> Our intention was to develop a pacemaker which could vary its stimulation rate, and thus the patient's cardiac output, in response to variations of the metabolic rate... Evaluation of the performance of the pH-triggered pacemaker one year after implantation in man encourages us to develop further and improve such a prosthetic device. The pH-triggered pacemaker reacted as expected with an increased firing rate to all situations in which an enhanced catecholamine release with resultant sudden blood pH variation toward acidity was stimulated. Physical exercise, cold, ischemia and emotional stress produced predictable results.

However, iridium is rather expensive,[23] and efforts to replace iridium oxide with ruthenium oxide, the latter being cheaper but less reliable, have also been performed as both metals undergo the same pH dependent $\mathrm{M(III)} \longleftrightarrow \mathrm{M(IV)}$ oxidation state change in aqueous solution. Nonetheless, the principle will only be explained for iridium oxide below in order to be concise, where an exhaustive and recent list of publications by Lonsdale,[25–30] who wrote his doctoral thesis on the topic,[23] describes the ruthenium oxide mechanism in detail.

Depending on the deposition technique, iridium oxide can exist as either anhydrous or hydrous. Anhydrous iridium oxide undergoes the following redox reaction in aqueous solution:[31]

$$2\,\mathrm{IrO_2} + 2\,\mathrm{H^+} + 2\,\mathrm{e^-} \rightleftharpoons \mathrm{Ir_2O_3} + \mathrm{H_2O} \tag{2.9}$$

When the oxide is partially hydrated, this reaction (simplified)[23] changes to:[31]

$$\mathrm{IrO_2} + 2\,\mathrm{H^+} + 2\,\mathrm{e^-} \rightleftharpoons \mathrm{IrO(H_2O)} \tag{2.10}$$

In both cases, the number of protons and electrons exchanged remains the same, with the Nernstian relation:[23,31,32]

$$E = E^\circ - \frac{RT}{2F} \ln \left[\frac{a_{(\mathrm{Ir^{III}})}}{a_{(\mathrm{Ir^{IV}})} a^2_{(\mathrm{H^+})}} \right] \tag{2.11}$$

In this case, E° is the standard redox potential and a_i is the thermodynamic activity for the respective species. Assuming the iridium oxide electrode activity remains constant at 23°C, the equation can be simplified to:

$$E = E^\circ + \frac{2RT}{2F} \ln \left[a_{(\mathrm{H^+})} \right] = E^\circ - 0.059\mathrm{pH} \tag{2.12}$$

Thus, in the ideal case the iridium oxide electrode yields a -59 mV pH^{-1} Nernstian response at room temperature. However, due to amphoteric effects, iridium oxide can become "super"-Nernstian when hydrated, being 1 to 1.5 times the typical Nernstian response. These amphoteric sites, where adsorption or desorption of protons can occur without electron transfer, come from an "oxide" which is described as a "hydrated oxyhydroxide in a cross-linked, open-polymeric chain," and results in the pH sensitive reaction below:[23,31]

$$2\,\mathrm{IrO_2(OH)_{(2-x)}(H_2O)_{(2+x)}^{(2-x)-}} + (3\,-\,2\,\mathrm{x})\mathrm{H^+} + 2\,\mathrm{e^-} \rightleftharpoons \mathrm{Ir_2O_3(OH)_3(H_2O)_3^{3-}} + 3\,\mathrm{H_2O} \tag{2.13}$$

The value of x is between 0 and 0.5, corresponding to the degree of dissociation of hydroxyl groups. This value depends on the oxidation state of the electrode, where fully reduced electrodes yield a Nernstian slope ($x = 0.5$) and a fully oxidized electrode has a slope close to 89 mV pH^{-1} at room temperature ($x = 0$). This Nernstian relation is as follows:[23,31,32]

$$E = E^{\circ} - \frac{RT}{2F} \ln \left[\frac{a_{(\mathrm{Ir^{III}})}}{a_{(\mathrm{Ir^{IV}})} a_{(\mathrm{H^+})}^{3-2x}} \right] \tag{2.14}$$

Again after simplifying, this becomes:

$$E = E^{\circ} + \frac{(3-2x)RT}{2F} \ln \left[a_{(\mathrm{H^+})} \right] = E^{\circ} - 0.059(1.5 - x)\mathrm{pH} \tag{2.15}$$

Unfortunately in ambient oxygen saturated solutions, reduced electrodes are not stable as the oxidation state will slowly change from Ir(III) to Ir(IV).[33] Once oxidized, the electrode pH sensitivity is stable, which nonetheless prolongs electrode fabrication time. In addition, the hydration of anhydrous iridium oxide is slow and can take months.[34] Thus, electrode conditioning procedures are often required, either through weeks of buffer exposure[31] or by placing the electrode in boiling, deionized water for 30 minutes.[29,34]

Additionally, both iridium oxide and ruthenium oxide, due to their pH sensitive oxidation state change, are sensistive to reducing agents such as ascorbic acid,[22,29,31] and these agents can permanently change the E° value of the electrode and thereby require a recalibration.[35] The deposition of a Nafion layer over the electrode can mitigate these effects, but the layer also prolongs the response time of the sensor.[29,36] Furthermore, in protecting such layers against dissolved oxygen for better stability, it may be necessary to deposit a Ta_2O_5 layer on the iridium oxide or ruthenium oxide electrode, whereby the Ta_2O_5 layer prevents the transfer of electrons from oxygen while maintaining pH sensitivity for the sensor; this keeps the M(III)/M(IV) ratio constant and yields a stable electrode potential.[29,37] Lauks, a coauthor on the paper where conditioning iridium oxide in water at high temperatures was suggested, obtained a patent claiming that an IrTaOx material, with a Ir/Ta molar ratio of 0.09, yields a pH sensitive electrode having both a fast potentiometric response time and normal function in the presence of reducing agents.[38]

Considering these factors, additive processing of an iridium oxide or a ruthenium oxide pH electrode would not be straightforward. The electrode conditioning steps, along with the additional layers required for proper function, would prolong and complicate the manufacturing process. The use of an insulating metal oxide, which in a potentiometric configuration is non-ideal (due to its low conductivity), would nonetheless be superior in other ways. For instance, insulative metal oxides are insensitive to reducing agents as they rely on amphoteric sites (no electron transfer) for pH sensitivity.[38] Therefore, instead of building a potentiometric iridium oxide sensor with both a Ta_2O_5 layer and a separate Nafion layer, it may be better to use the Ta_2O_5 layer alone in a measurement method that works for insulating oxides.

2.2.2 ISFET Metal Oxide Sensors

In 1970, Bergveld[39,40] reported a possible improvement in measuring neural activity, where typically measurement of the desired signal with an electrode includes the surrounding "biological noise." The idea was that instead of monitoring the potential, the measuring apparatus should be constructed so as to monitor the surface charge density at the electrode-solution interface. By monitoring the local charge density and correlating that to neural activity, the noise from surrounding cells would be reduced. As an example, Bergveld used an SiO_2 layer as a transistor gate which would also interact with NaCl in solution. As the NaCl solution concentration changes, the gate potential would also change and thereby regulate the source-drain current, I_{DS}.

This transistor configuration was termed an ion-sensitive field-effect transistor (ISFET), where the ion sensitivity of the gate oxide can also be used in pH sensing.[41] However, the mathematical relation between I_{DS} and pH, where pH influences the ISFET's threshold voltage, V_T, depends on whether the ISFET is operating in the unsaturated (linear) or saturated region. In the unsaturated region, I_{DS} and V_T are directly proportional:[41–43]

$$I_{DS} = \frac{\mu C_{ox} W}{L} \left([V_{GS} - V_T] V_{DS} - \frac{1}{2} V_{DS}^2 \right) \tag{2.16}$$

Whereas in the saturated region, I_{DS} is proportional to the square of V_T:[42,43]

$$I_{DS} = \frac{\mu C_{ox} W}{2L} \left(V_{GS} - V_T \right)^2 \tag{2.17}$$

In both cases, μ is the average channel electron mobility, C_{ox} is the gate oxide capacitance, W is the gate width, L is the gate length, V_{DS} is the source-drain potential, and V_{GS} is the source-gate potential. Along with the effects of solution pH, V_T has multiple contributions:[41]

$$V_T = E_{ref} - \psi_0 + \chi^{sol} - \frac{\Phi_{Si}}{e} - \frac{Q_{ox} + Q_{ss}}{C_{ox}} - \frac{Q_B}{C_{ox}} + 2\phi_f \tag{2.18}$$

Among the transistor parameters, Φ_{Si} is the silicon electron work function, e is the elementary charge, Q_{ox} are charges in the gate oxide, Q_{ss} are charges in the surface and interface states, Q_B is the depletion charge, and ϕ_f is the potential difference between the Fermi levels in doped and intrinsic silicon. For the solution parameters, E_{ref} is the reference potential, χ^{sol} is the surface dipole potential of the solution, and ψ_0 is the electrostatic potential of the oxide layer in solution. The transistor parameters and E_{ref} should remain constant, while χ^{sol} is independent of pH. Thus, changes in I_{DS} can be associated with changes in ψ_0, and therefore according to the site-binding model, pH. This model, as proposed by Yates, Levine, and Healy,[44] describes the proton binding sites on oxides in solution, without electron transfer and Faradaic current, where H_B^+ are protons in the bulk solution:

$$\mathrm{AOH} \rightleftharpoons \mathrm{AO^-} + \mathrm{H_B^+} \text{ and } \mathrm{AOH_2^+} \rightleftharpoons \mathrm{AOH} + \mathrm{H_B^+} \tag{2.19}$$

Bousse, de Rooij, and Bergveld[21] later applied the model to the ISFET, although this model suffers from being difficult to interpret, not applicable to the entire pH range, and ignores the contribution of ionic strength. Thus, the model was later improved by van Hal, Eijkel, and Bergveld,[41,45] which will be derived below so as to determine the best insulating oxide for pH sensing.

In defining the equilibrium conditions for Equation 2.19, H_S^+ are the protons at the oxide surface, v_i is the number of respective sites per unit area, a_i is the respective activity, and K_i is the respective dissociation constant:

$$K_a = \frac{\nu_{(AO^-)} a_{\left(H_S^+\right)}}{\nu_{(AOH)}} \text{ and } K_b = \frac{\nu_{(AOH)} a_{\left(H_S^+\right)}}{\nu_{\left(AOH_2^+\right)}} \tag{2.20}$$

This leads to the following Nernstian equation showing the relation of the bulk solution activity, $a_{(H_B^+)}$, to the surface activity, $a_{(H_S^+)}$, where k is the Boltzmann constant:

$$a_{(H_S^+)} = a_{(H_B^+)} \exp\left(\frac{-e\psi_0}{kT}\right) \tag{2.21}$$

Additionally, the surface charge density, σ_0, is defined as follows, with N_s being the number of sites per unit area, and Θ^+ and Θ^- being the fractions of sites with the charges of AOH_2^+ and AO^-, respectively:

$$\sigma_0 = e\left(\nu_{(AOH_2^+)} - \nu_{(AO^-)}\right) = eN_s\left(\Theta^+ - \Theta^-\right) \tag{2.22}$$

The fractions Θ^+ and Θ^- are determined from the equilibrium reactions in Equation 2.20, which when substituted into Equation 2.22 yields:

$$\sigma_0 = eN_s\left(\frac{a^2_{(H_S^+)} - K_aK_b}{K_aK_b + K_ba_{(H_S^+)} + a^2_{(H_S^+)}}\right) = -e\,[\mathrm{B}] \tag{2.23}$$

Here, [B] is the number of negatively charged groups minus the number of positively charged groups per unit area, and the pH at the point of zero charge, $\mathrm{pH_{pzc}}$, is when [B] equals zero. When taking the partial derivative of [B] with respect to $\mathrm{pH_S}$, one can arrive at the intrinsic buffer capacity of the metal oxide, β_{int}.

$$\frac{\delta\sigma_0}{\delta\mathrm{pH_S}} = -e\frac{\delta\,[\mathrm{B}]}{\delta\mathrm{pH_S}} = -eN_S\frac{K_ba^2_{(H_S^+)} + 4K_aK_ba_{(H_S^+)} + K_aK_b^2}{\left(K_aK_b + K_ba_{(H_S^+)} + a^2_{(H_S^+)}\right)^2}a_{(H_S^+)}\ln 10 = -e\beta_{int} \tag{2.24}$$

The charge that accrues on the metal oxide electrode is equal and opposite to the electrolyte charge, where the electrolyte charge forms at a distance x_2 from the surface. Within the Gouy-Chapman-Stern model, x_2 forms the boundary of the Stern layer, where the ion centers accumulate at this distance. The diffuse layer charge, σ_d, in the Gouy-Chapman-Stern model is defined as:

$$\sigma_d = -\left(8kT\epsilon\epsilon_0n^0\right)^{1/2}\sinh\left(\frac{ze\phi_2}{2kT}\right) = -C_i\psi_0 = -\sigma_0 \tag{2.25}$$

Here, ϵ_0 is the permittivity of vacuum, ϵ is the relative solution permittivity, ϕ_2 is the potential at x_2, n^0 is the number concentration of each ion in the bulk solution, z is the ion charge magnitude, and C_i is the integral capacitance per unit area. Following from this, the differential capacitance per unit area, C_{dif}, is the storage of charge in the electrolyte in response to a change in ψ_0:

$$\frac{\delta\sigma_d}{\delta\psi_0} = -\frac{\delta\sigma_0}{\delta\psi_0} = -\frac{\left(\frac{2\epsilon\epsilon_0 z^2 e^2 n^0}{kT}\right)^{1/2}\cosh\left(\frac{ze\phi_2}{2kT}\right)}{1+\left(\frac{x_2}{\epsilon\epsilon_0}\right)\left(\frac{2\epsilon\epsilon_0 z^2 e^2 n^0}{kT}\right)^{1/2}\cosh\left(\frac{ze\phi_2}{2kT}\right)} = -C_{dif} \tag{2.26}$$

Then, the combination of the diffuse layer side of the double layer in Equation 2.26 with the metal oxide electrode side in Equation 2.24 gives:

$$\frac{\delta\psi_0}{\delta \mathrm{pH_S}} = \frac{\delta\psi_0}{\delta\sigma_0}\frac{\delta\sigma_0}{\delta \mathrm{pH_S}} = \frac{-e\beta_{int}}{C_{dif}} \tag{2.27}$$

Then by substituting the Nernstian relation from Equation 2.21 into Equation 2.27 and with a subsequent rearrangement, pH changes in the bulk solution can be related to the electrostatic potential on the metal oxide electrode surface:

$$\frac{\delta\psi_0}{\delta \mathrm{pH_B}} = -\frac{kT\ln 10}{e}\alpha \tag{2.28}$$

In this case, α is a sensitivity parameter from 0 to 1, where when $\alpha = 1$ the slope is roughly -59 mV pH^{-1} at 23°C:

$$\alpha = \left(\frac{kTC_{dif}\ln 10}{e^2\beta_{int}} + 1\right)^{-1} \tag{2.29}$$

Thus, the larger the value of β_{int} for the particular metal oxide, the closer α is to 1 and the more Nernstian the pH response. Knowing from Equation 2.24 that β_{int} is directly proportional to N_s, the data from Table 2.1 can be used to determine which insulating metal oxide, among SiO_2, Al_2O_3, and Ta_2O_5, would give the largest value for β_{int}.

Table 2.1 Relevant constants for some metal oxide insulators.[41,45,46]

Metal Oxide	pK_a	pK_b	N_s (sites m^{-2})	pH$_{\mathrm{pzc}}$
SiO_2	6	-2	5×10^{18}	2
Al_2O_3	10	6	8×10^{18}	8
Ta_2O_5	4	2	10×10^{18}	3

Among the three metal oxides (and Si_3N_4),[46] Ta_2O_5 would thus give the best response, and is theoretically able to do so even as the ionic strength of the solution changes,[41,45] although there have been reported exceptions such as alkali interference.[47] In examining pH hysteresis measurements from pH 3 to pH 11 by Bousse et al.,[48] the increased interference in the basic region for Ta_2O_5 was suspected to be due to adsorbed alkali,[49,50] although superior hysteresis performance for Ta_2O_5 was found at acidic and basic pH (hysteresis ranked as follows: $Si_3N_4 > Al_2O_3 > Ta_2O_5$). In the absence of alkali, a recent study of amorphous Al_2O_3, Nb_2O_5, and Ta_2O_5 deposited via atomic layer deposition (ALD) showed that both group 5 oxides Nb_2O_5 and Ta_2O_5 are more resistant to corrosion than Al_2O_3 against NH_4OH.[51] Another advantage of Ta_2O_5, along with Nb_2O_5, is their ability to conduct protons in electrochromic window applications, although under high applied potentials.[52] Considering this ability to absorb protons for these oxides, as observed for Ta_2O_5 on ruthenium oxide[29] and iridium oxide[37] for pH sensing, Ta_2O_5 or Nb_2O_5 could potentially be used in an interdigitated electrode- (IDE-)based, reference electrode free sensor, where the capacitance across the Ta_2O_5/Nb_2O_5-electrolytic solution double layer,[53] and the "proton space charge" in the metal oxide layer,[54,55] changes with pH. Removing the reference electrode simplifies the device manufacturing, as one less material is needed to produce the sensor. Furthermore, a capacitive based sensor would remove the need to fabricate a transistor required in the ISFET configuration, further simplifying sensor construction.

Therefore, this thesis will investigate the additive manufacturing of Ta_2O_5 on IDEs for capacitive pH sensing, where Ta_2O_5 has been studied much more for pH sensing than Nb_2O_5. However, the results of this thesis may be relevant for the additive manufacturing of Nb_2O_5, which should be taken under consideration in future studies, especially as both are group 5 metals with similar atomic radii due to the lanthanide contraction (often giving them similar chemistry). Furthermore, the use of Ta_2O_5 and Nb_2O_5 extends far beyond pH sensing, and the ability to additively manufacture these oxides could influence many sectors. Thus, a short discussion on the sourcing and application of these oxides is warranted.

2.3 Sister Elements - Tantalum and Niobium

Tantalum and niobium (both lying in the mass number range A = 63 - 209) are suspected to have been formed via neutron absorption in pulsating red giant stars, and as niobium and tantalum have an odd atomic number, these elements have lower abundances in the universe, with tantalum being even more rare due to its higher mass.[56] As a consequence, niobium is more abundant on Earth and the Moon than tantalum, with a Nb/Ta ratio in the Earth-Moon system being lower than that of the solar system[57] and where tantalum is the rarest stable element in the solar system[58,59] - this has been further claimed as evidence of the impact hypothesis for the Moon's formation from Theia colliding with Earth[57] (although recent research has presented new questions regarding the impact hypothesis),[60,61] and the Nb/Ta ratio further helps to explain continent formation which is unique to Earth.[62]

About 4.5 billion years after Theia is thought to have impacted Earth, a mineral (columbite) from the American continent was examined by an Englishman named Charles Hatchett in 1801, which he stumbled across at the British Museum in London, originally being acquired from governor John Winthrop of Connecticut, United States. Obtained from the area of New London in Connecticut, Hatchett observed a new element in the mineral and named it columbium, after the Americas.[63–65] Then in early 1802, Anders Gustaf Ekeberg of Sweden examined minerals from Ytterby, Sweden (yttrotantalite) and Kimito, Finland (tantalite) where both appeared to contain a new element.[63,66,67] As the element was unable to react with any acid in Ekeberg's laboratory, he named the new element tantalum after Tantalus, who in Greek mythology was punished eternally by not being able to eat or drink.[63,67,68]

Later in 1809, William Hyde Wollaston of Britain examined columbite and tantalite minerals more closely, having already discovered palladium in 1802 and rhodium in 1804.[69] Wollaston was also the first to produce and market pure, malleable platinum ingots, while his partner, Smithson Tennant, discovered osmium and iridium from platinum ore. Despite his experience with platinum group metals, Wollaston's examination of the columbite and tantalite minerals mistakenly led to the determination that both columbium and tantalum were the same element, as quoted below:[63,70]

> Notwithstanding the quantity employed in my analyses was thus limited, I have, nevertheless, by proportionate economy of the materials, been enabled to render my experiments sufficiently numerous, and have found so many points of agreement in the modes by which each of these bodies can or cannot be dissolved or precipitated, as to prove very satisfactorily that these American and Swedish specimens in fact contain the same metal; and since the re-agents I have employed are in the hands of every chemist, the properties which I shall enumerate are such as will be most useful in the practical examination of any other minerals in which this metal may be found to occur.

However, upon further examination in 1844, Heinrich Rose suspected that two different elements occurred in a Bavarian tantalite sample.[63,68] Likely thinking that columbium and tantalum were mistaken for the same element (Rose mentions the naming of columbium in this study), Rose proceeded to name a new element and is quoted as follows:[68]

> Die Säure aus dem baierschen Tantalite... besteht aus zwei Säuren, von denen die eine sehr viele Aehnlichkeit mit der Tantalsäure aus dem finnländischen Tantalite hat, und von welcher ich in der nächsten Abhandlung umständlicher sprechen werde. Auch die andere Säure hat Aehnlichkeit mit der Tantalsäure, unterscheidet sich jedoch in mancher Hinsicht wesentlich von derselben. Sie ist das Oxyd eines Metalls, das sich von den bisherbekannten unterscheidet. Ich nenne dasselbe Niobium und sein Oxyd Niobsäure, von Niobe, der Tochter des Tantalus, um durch den Namen die Aehnlichkeit mit dem nach letzterem benannten Metalle und dessen Oxyde anzudeuten.

As both niobium and tantalum were found to be chemically similar, separation of the two proved to be difficult. Finally in 1866, Jean Charles Galissard de Marignac found that the two elements could be separated by using potassium fluoride salts of both niobium and tantalum, where K_2NbOF_7 was found to be more soluble than K_2TaF_7 in water.[63,71,72] The use of this process to separate the two elements led to the confirmation that columbium and niobium are the same element. This naming conflict lasted until 1949, where the American preferred tungsten (from wolfram) was made official in exchange for the European preferred niobium,[63,73] although it is claimed that columbium is still used by some to this day.[63]

In 1905, von Bolton and Feuerlein of Siemens & Halske AG reported the use of tantalum in a light bulb in Germany,[74] where tantalum would later be replaced by tungsten as a filament material.[75] By 1935, tantalum and niobium had many reported uses[76] - chief among them were the vacuum tube (the predecessor to the transistor), where tantalum proved superior in comparison to other metals and where niobium was also useful for this application. Tantalum's corrosion resistance seemed to be largely understood, where below 200°C the metal could only be attacked by hydrofluoric acid, concentrated sulfuric acid, strong alkalic solutions, and hydrogen gas. Due to a thin oxide film forming on the surface of the metal, tantalum was used in electrolytic rectifiers and capacitors. Tantalum's corrosion resistance allowed for it to be used in chemical apparatus, and its weldability in various machines. Tantalum and niobium carbides were also being used in cutting applications, due to the hardness of the ceramic material.

World War II later showcased tantalum as a biocompatible material, where in 1941 Lieutenant Commander O. Hugh Fulcher of the United States Navy performed the first cranioplasty on a wounded sailor using tantalum, which was performed in the United States Naval Hospital in Washington, DC. As the United States needed as many able bodied men as possible for the war effort, Fulcher claimed new implants were needed to keep "as many men at as many guns as many days as possible."[77,78]

The recommendation to use tantalum came from its malleability, as well as from tests beginning in 1940 where bits of tantalum were placed into Ringer's solution (an isotonic solution mimicking bodily fluids) at body temperature for 3 months.[77,79] After this period, no change in the weight or in the appearance of the solution and the metal were noticed. Animal studies then followed where plates and screws were placed into dogs and rabbits, where no negative immune reactions to the tantalum metal were observed. The success of tantalum implantation was attributed to a thin tantalum oxide layer which formed on the surface of the implant.[79]

Tantalum cranioplasty operations in cats confirmed these findings, while also noting that fixation to the bone was not required as a connective tissue capsule formed around the tantalum implant upon healing.[80] Based on these results, Fulcher proceeded with his operation and found post-operation, a month after the beginning of the United State's involvement in World War II, that his patient successfully recovered as quoted below:[78]

> The patient returned from his sick leave on Jan. 8, 1942, anxious to return to active duty. He was mentally alert, liked social life and was completely adjusted. On January 13 and 14 a thorough examination was made to determine his qualification for submarine duty, which included his ability to withstand an air pressure of 50 pounds to the square inch [3.4 atm]. He passed this test satisfactorily and on January 16 was returned to submarine duty on a North Atlantic patrol.

A year later in 1943, Spurling reported the repair of peripheral nerves with the same element, in this case using tantalum wire and foil to complete the task.[81] The idea is described in further detail by Weiss, where nerves are held into a sleeve by suction and are thereby encouraged to reunite; as tantalum foil is relatively malleable and biocompatible, the metal was used as a protective liner for the sleeve.[82] However, Norcross and Bakody found that unannealed tantalum foil may fragment in the body long term, and they recommended to use annealed foil as Weiss did.[83]

During the Korean War (1950-1953), the United States military began to realize the value of tantalum for defense purposes, which led to a national stockpile of niobium and tantalum ore - increasing the price worldwide until 1958, when the United States paused purchasing of the ore.[84] As tantalum was recognized as valuable for making capacitors, and since the Soviet Union was finding that their supplies were not sufficient, the Soviets pioneered niobium capacitor research since niobium was much easier for them to obtain.[85]

In the 1960s, niobium capacitors began to be mass produced in the Soviet Union, and tantalum was being utilized all over the world in consumer electronics, chemical production, aerospace, and machinery manufacturing.[85,86] Tantalum prices continued to cycle until the late 1970s, where prices for the metal spiked worldwide due to concerns about reserves (i.e., war in Mozambique and closing of a Canadian mine).[84,86] By 1983, the United States reported that 70% of consumed tantalum was used in electronic components, 15% in metalworking machinery, 8% in aerospace and transportation, 7% in chemical process equipment, and less than 1% in other uses (including medical implants).[84] Countries consuming the most tantalum until the end of the century were also forecast as being the United States, Japan, the Federal Republic of Germany, the Soviet Union, and other European countries - this is notable as China had yet to play a major role in the tantalum supply chain.[84]

After the Cold War ended, the United States began selling off its tantalum stock in 1993.[86] Then in the late 1990s, consumers were demanding more electronic products, and as a consequence some tantalum ore processors locked themselves into long-term contracts in order to meet this demand. Due to these contracts, other processors and electronic manufacturing companies found it harder to acquire the metal, and along with trader speculation this led to a large price spike at the end of the century. Notably, this resulted in Sony not being able to meet the demand for the PlayStation 2 at Christmas in 2000.

On the other side of the world, the Democratic Republic of the Congo (DRC) had internal conflicts beginning in the early 1990s, which were exacerbated by the Rwandan genocide through refugees flowing into the eastern Congo.[86] Eventually, this pitted the DRC against Uganda, Rwanda, and armed groups of the eastern Congo in the Second Congo War (1998-2003). Casualty numbers went into the millions, and armed groups were looking for ways to fund their campaigns. In 1998 and 1999, methods of exporting coltan (columbite [(Fe, Mn)Nb_2O_6] - tantalite [(Fe, Mn)Ta_2O_6])[87] out of the DRC were implemented, and the DRC and other armed groups were able to take advantage of the price spike in tantalum ore at the end of the decade.

Subsequently, coltan became notoriously associated with war and violence in the DRC, and local violence continues to this day.[86] However, coltan is only one of many resources that are used to fund conflicts in the DRC, and should not be considered as a direct cause of the violence. Additionally, not all of the artisanal mining operations are associated with armed groups, and they can provide the region with jobs when properly managed. Nonetheless, it is difficult to track the origin of "conflict free" coltan, although a German group has been developing a fingerprint method to track the origin of the mined ore.[86,88,89]

Despite these efforts, national governments and non-governmental organizations such as the United Nations are finding out how difficult it is to control and track where tantalum and niobium ore is coming from.[86] For example, in 2008 one source reported that Africa produced 37% of the world's tantalite ore,[90] whereas a more recent study (taking into account mined ore and products containing tantalum) found the figure to be almost 80%.[91] These discrepancies can largely be explained by the fact that organizations such as the United States Geological Survey and the Tantalum-Niobium International Study Center only report primary mine production and permitted artisanal, small scale mining - this leaves out illegally traded coltan from Africa, making up for the extra tantalum found in our products. As a direct result of much of African tantalum being unaccounted for, this lends to a resilient supply chain as when large producers in Brazil, Australia, or Canada decide to shut down, illegally mined tantalum in Africa can make up for the shortfall. Furthermore, 53% of African tantalum was sent to China in 2014, a manufacturing power,[91] demonstrating large changes in the supply chain since 1983.[84]

In the present day, tantalum and niobium play important roles in society, where their fields of use have largely not changed since the 1960s,[84,92] and both are known for having high corrosion resistant films.[51] Niobium is mostly used in ferrous metallurgy in order to improve the properties of steel,[92] and tantalum largely in the electronics industry. Tantalum is preferred for capacitors due to the small size, durability, and efficiency at which tantalum capacitors operate.[85,86,91,92] When costs need to be reduced, niobium capacitors can also be employed, although niobium capacitors have lower volumetric efficiencies, lower operating voltages, and larger leakage currents (the larger leakage current in niobium capacitors had a perplexing effect on Soviet researchers when they found that the leakage current increased with storage time, which was blamed on an "evil spirit." This spirit went away when the hermetic seal was opened to balance the moisture).[85] Thus, tantalum's reliablilty is why wet tantalum electrolytic capacitors are often chosen for aersopace and military applications, as well as for cardiac defibrillator devices.[85,93]

2.4 Biomedical Applications of Tantalum and Niobium

Aside from capacitors for biomedical applications, cold worked tantalum and niobium metal have been mechanically compared as orthopedic implant materials due to their corrosion resistance and biocompatibility (properties lended by their oxide surfaces), where tantalum showed a higher endurance limit than niobium in different environments.[94] Furthermore, porous tantalum implants are known to have enhanced osteointegration,[95–98] and cell promotion can be reduced by using argon plasma (thus increasing hydrophobicity) and making the material more suitable for angioplasty and vascular surgery.[99] Sol-gel produced TaOx nanoparticles, acting as bioreactors encapsulating a catalase, have even been studied for radiotherapy enhancement for tumors.[100] A more recent study showed that tantalum can be incorporated into soda lime borosilicate glasses in order to increase its hardness, while still showing cytocompatibility towards osteoblast cells.[101] Similarly, an investigation in 2020 used sol-gel-assisted micro-arc oxidation synthesis of tantalum and tantalum-strontium films on titanium for increased hydrophilicity and osteoblast attachment to the substrate.[102]

This biocompatibility has been further taken advantage of for both neural and cardiac electrodes.[103,104] Tantalum oxide neural electrodes operate through capacitive charge injection, which lends inherent disadvantages such as relying on ion diffusion.[103,105] Nonetheless, Medtronic finds uses for tantalum oxide in cardiac stimulation, which is due to tantalum's classification as a valve, or vacuum tube, metal (valve metals, which include titanium, tantalum, niobium, hafnium, zirconium, and tungsten, readily form thin oxide films on the surface of the metal),[106] meaning that tantalum oxide can pulse but not sense, and this can be integrated with metals such as platinum or iridium to reduce noise during physiological sensing.[104]

Surface plasmon resonance (SPR) biosensors have taken advantage of the high refractive index of both tantalum oxide and niobium oxide in order to improve sensor sensitivity and sensor stability.[107–109] Types of electrochemical biosensors employing tantalum oxide or niobium oxide include those for a variety of charged macromolecules (e.g., proteins and DNA),[110–115] bacteria,[116] cells and their behavior,[117] as well as pH and other ions.[111,118,119] Tantalum oxide and niobium oxide compete with other metal oxides as a pH sensing material,[8,22,41,45,119–121] where tantalum oxide pH sensors have been studied in applications such as tooth enamel erosion[122,123] and cleaning-in-place sensors for the food industry.[118] In particular for tantalum oxide, its cleanability,[118] high buffer capacity,[41,45,120] and insulative nature lend it many desired properties; as mentioned previously, Lauks of the I-Stat Corporation even claimed in 1991 that for potentiometric pH sensing, a sensing layer can be produced by codepositing a small amount of iridium oxide with tantalum oxide, whereby the high sensitivity of the former and the redox resistance of the latter combines to provide a superior metal oxide layer for potentiometric pH sensing in medical applications.[38] Niobium oxide[124] and tantalum oxide[125,126] have also been investigated as pH sensitive layers for light-addressable potentiometric sensors (LAPS),[127,128] allowing for 2D mapping of pH changes in applications such as cell metabolism.

2.5 Additive Processing of Sol-Gel Derived Metal Oxides

Considering the various applications of these metals, investigations into additive manufacturing of their oxides should take mass manufacturing into account. Being able to reliably produce many devices allows for a more significant impact in society, especially in the effort to save resources when avoiding subtractive processing.

One of the most cost effective ways of achieving mass manufacturing is roll-to-roll processing,[129] particularly when demand for the item in question is high.[130] Essentially, as the substrate enters the manufacturing line, several steps can be integrated, with the final product ready for packaging upon exiting the line. More specifically, a flexible substrate, initially stored in a roll, is unwound and modified by either additive (e.g., screen, inkjet, and gravure printing) or subtractive (e.g., photolithography and etching) manufacturing steps.[131,132] Such processing further permits additional steps such as thermal treatment and UV curing, where UV curing is often required on low melting point substrates.

Chemical solution deposition (CSD) and photochemical solution deposition (PCSD), both roll-to-roll friendly deposition techniques of oxides, are lower cost processing techniques than others such as atomic layer deposition (ALD), radio frequency sputtering, magnetron sputtering, ion beam sputtering, laser ablation, and metal organic chemical vapor deposition (MOCVD).[133] Furthermore, CSD and PCSD provide other advantages such as the modification of solution chemistry and stoichiometry for the required application, and incorporation into additive manufacturing processes, thereby reducing wasted materials.[134]

Highly scaled gravure printing, which utilizes silicon microfabrication techniques to create molds with dimensions between 1 µm to 10 µm, is a promising roll-to-roll manufacturing and CSD/PCSD technique which is able to increase throughput while reducing the feature size.[132] Other techniques, such as screen printing and inkjet printing, are able to achieve a similar throughput with larger minimum feature sizes, which range from 10 µm to 100 µm for inkjet printing, and are ~100 µm for screen printing.

As creating gravure plates is rather expensive, this work will optimize the created tantalum inks for drop-on-demand, piezoelectric inkjet printing, where future experiments could modify the ink for gravure printing. The drop-on-demand, piezoelectric inkjet technique is ideal for research applications, as patterns can be quickly made on a computer, which can be subsequently printed. In applying the signal to the print head for printing the ink, a positive voltage signal (being a trapezoid in its simplest form), or waveform, can be tailored for optimum droplet formation and deposition. Nonetheless, inkjet printing of sol-gel inks presents many obstacles, such as ink stabilization during printing, where Matavž and Malič[134] discuss drop-on-demand, piezoelectric inkjet printing of sol-gel solutions in more detail. Moreover, the deposition of tantalum oxide and niobium oxide via CSD or PCSD has run into obstacles in the past, and these challenges will be addressed in Chapter 3.

Chapter Three

Solution Synthesis

This chapter will begin with a short introduction to the sol-gel deposition of niobium oxide and tantalum oxide, followed by a series of experiments which lead to an optimized synthesis route to a near-UV curable tantalum solution. The final experiment will then show that the procedure can be shortened to make such solutions. However, some suboptimal syntheses will be described in Chapter 4 with the sensor fabrication, which were performed before the experiments shown here were conducted. Parts of this chapter have been published[135–137] and discussed in German patent application DE 10 2019 006 976.5 filed on October 8, 2019.[138]

3.1 Sol-Gel Deposition of Nb_2O_5 and Ta_2O_5

The sol-gel process, a subset of chemical solution deposition (CSD) and photochemical solution deposition (PCSD),[133] can be used to form oxide films and consists of forming a sol, a stable suspension of colloidal particles, followed by the formation of a gel, a three-dimensional solid network that may support a liquid phase.[139] As sol-gel science is a very broad topic, this section will focus on the alkoxide, diol, and β-diketonate/β-ketoester route to sol-gel derived tantalum oxide or niobium oxide films. One of the reasons for focusing on a halide-free route is to avoid halide impurities in the produced thin films.[140] Another reason to avoid metal halides is the possible production of acidic compounds, such as hydrochloric acid, which may be undesired.[141] However, metal alkoxide compounds were originally derived from metal chloride compounds, and therefore a brief history of the metal chloride to metal alkoxide transformation will be discussed below. This will be followed by sol-gel deposition of tantalum oxide and niobium oxide films.

From Halide to Organic Precursors - 1856-1970s

Unwittingly, the first tantalum alkoxide and sol-gel experiment was performed in 1856 by Heinrich Rose, where roughly a decade after the first formation of silica via the sol-gel route by Ebelmen,[142] and Rose's naming of niobium,[68] Rose described how he dissolved a tantalum chloride compound in alcohol and is quoted below:[143]

> Das Tantalchlorid löst sich im wasserfreien Alkohol auf. In der alkoholischen Lösung wird die Tantalsäure durch Schwefelsäure nicht gefällt, auch nicht wenn sie aufgekocht wird. Die Fällung geschieht erst dann, wenn nach einem Zusatz von Wasser durchs Erhitzen der größte Theil des Alkohols verflüchtigt worden ist.

Precipitate formation after the addition of water and alcohol's evaporation hinted as to why in 1923, Lindner and Feit struggled to isolate alkoxide-halide compounds of tantalum, as atmospheric moisture proved to be a major obstacle.[144] However, successful attempts were made by Funk and Niederländer in a series of experiments (1928-1934).[145–148] In one of their more relevant studies, mixed chloride-alkoxide compounds of niobium and tantalum were first prepared with either methanol or ethanol, where only three of the chloride ions could be substituted by an alkoxide ion (M = Nb, Ta; R = methyl, ethyl):[147]

$$\mathrm{MCl_5} + 3\,\mathrm{ROH} \longrightarrow \mathrm{M(OR)_3Cl_2} + 3\,\mathrm{HCl} \tag{3.1}$$

These compounds were later modified by Funk in 1934, where it was demonstrated that both acetylacetone and benzoylacetone could chelate to the metal center,[148] with a coordination number of six and a general formula of $M(OR)_2ACl_2$ (M = Nb, Ta; R = methyl, ethyl; A = acetylacetone, benzoylacetone). This is likely the first report of niobium or tantalum β-diketonate complex formation, and comes 5 years before the first sol-gel patent in 1939 from Jena Glassworks Schott & Associates in Germany for forming optical glass, where both tantalum and acetylacetone are mentioned as possible solution constituents.[149]

Then in 1954, Whitley, working with the metal alkoxide pioneer Bradley, describes in her doctoral thesis the isolation of several tantalum alkoxide compounds by driving the reaction forward with ammonia in a water free atmosphere, and the isolation was subsequently discovered to work for niobium (M = Nb, Ta; R = methyl, ethyl, n-propyl, n-butyl):[150–152]

$$\mathrm{MCl_5 + 5\,ROH + 5\,NH_3 \longrightarrow M(OR)_5 + 5\,NH_4Cl} \tag{3.2}$$

Such compounds were later found to be able to be produced electrochemically.[153] However, in order to conduct a proper synthesis, an inert atmosphere is necessary as alkoxide compounds of niobium and tantalum undergo hydrolysis in the presence of water to form an oxide,[150–152] and this may have been what Rose discovered in 1856;[143] for example, in the case of tantalum(V) ethoxide:[154,155]

$$\mathrm{Ta_2(OC_2H_5)_{10} + 5\,H_2O \longrightarrow Ta_2O_5 + 10\,C_2H_5OH} \tag{3.3}$$

In addition to synthesis, Whitley used ebullioscopy to determine that such penta-alkoxides are likely dimers at room temperature. This was also examined in later studies[156–159] and was eventually confirmed by nuclear magnetic resonance (NMR);[160] interestingly, similar alkoxide chemistry has been observed for uranium,[161–163] where the sol-gel process can be used to make nuclear fuel.[164]

Whitley further demonstrated the synthesis of an eight-coordinated tantalum(V) ethoxide benzoylacetonate compound, which would be the first reported alkoxide and β-diketonate compound of tantalum:[150,165]

$$\mathrm{Ta(OC_2H_5)_5 + 3\,C_{10}H_{10}O_2 \longrightarrow Ta(OC_2H_5)_2(C_{10}H_9O_2)_3 + 3\,C_2H_5OH} \tag{3.4}$$

Studies of such niobium and tantalum alkoxide chelate complexes were continued by Mehrotra and co-workers in the 1960s with acetylacetone, benzoylacetone, dibenzoylmethane, methyl acetoacetate, ethyl acetoacetate, and ethyl benzoylacetate.[165–170] Such complexing molecules are able to substitute up to three alkoxide ions (M = Nb, Ta, U; R = methyl, ethyl; AH = β-diketone or β-ketoester; A = chelated form; x = 1-3):[165]

$$\mathrm{M(OR)_5 + xAH \longrightarrow (RO)_{(5-x)}MA_x + xROH} \tag{3.5}$$

Around this time, Mehrotra and Kapoor also found that alkoxide groups could be replaced by glycols in tantalum and niobium compounds,[171,172] and other tantalum and niobium organometallic derivatives were also investigated.[173] Despite the variety of compounds that were studied, the goal of using such compounds in sol-gel deposition had yet to be recognized.

Sol-Gel Deposition - 1980s

In the early 1980s, Bulent Yoldas of Westinghouse Electric Corporation mentions the deposition of tantalum oxide films through the sol-gel route, whereby proper solution stability and subsequent oxide formation was controlled by adding tantalum(V) ethoxide, water, and an acid in certain ratios in an ethanol solution.[174,175] More detailed studies were subsequently carried about by two separate groups for tantalum oxide in the mid-1980s[154,155,176] and later for niobium oxide[177] which described the hydrolysis and condensation reactions of such compounds (M = Nb, Ta; R = alkyl):

Hydrolysis

$$\mathrm{H_2O + M(OR)_5 \longrightarrow HO{-}M(OR)_4 + ROH} \tag{3.6}$$

Condensation I - Yields Water

$$\mathrm{(RO)_4M{-}OH + HO{-}M(OR)_4 \longrightarrow (RO)_4M{-}O{-}M(OR)_4 + H_2O} \tag{3.7}$$

Condensation II - Yields Alcohol

$$\mathrm{(RO)_4M{-}OH + RO{-}M(RO)_4 \longrightarrow (RO)_4M{-}O{-}M(OR)_4 + ROH} \tag{3.8}$$

Further hydrolysis and condensation reactions eventually lead to the complete formation of tantalum oxide or niobium oxide films, often being M_2O_5. Other possibilities include an early attempt in 1984 at forming a solid solution of potassium, tantalum, and niobium for $K(Ta,Nb)O_3$ films, which consisted of mixing potassium ethoxide, tantalum(V) ethoxide, and niobium(V) ethoxide with subsequent heat treatment.[178]

In 1987, Silverman,[155] who wrote his doctoral thesis on sol-gel derived tantalum oxide thin films, reported mixing acetylacetone and tantalum(V) ethoxide in a 1:1 molar ratio in a solution of ethanol and water, where (depending on the amount of added water) the solution remained clear and precipitate free from 24 hours to more than a week in a closed container; this provided evidence for chelated β-diketones acting as stabilizers of metal alkoxides in the presence of water.[139]

At the end of the decade, Bradley, a colleague with whom Whitley obtained her doctorate for producing the first tantalum(V) alkoxide compounds, notes the use of metal alkoxide compounds in sol-gel deposition.[179]

Photochemical Solution Deposition - 1990s-Present

Early 1990s patent literature by Tanitsu and coworkers describes dissolving metal β-diketonate complexes in aprotic polar solvents for their eventual use in CSD[180] or PCSD,[181] where further solvent additions were also permitted. Tanitsu also mentions that photocuring is important in cases where the substrate can be adversely affected by excessive heat. Ohishi et al.[182] in 1992, and later Boyd et al.,[183] reported PCSD of tantalum oxide by exposing tantalum(V) ethoxide to far-UV irradiation.

One of the first reported academic studies of using β-diketones in photosensitive solutions was published in 1994 by Tohge et al.,[184] where the comparison between using titanium(IV) acetylacetonate and titanium(IV) benzoylacetonate complexes for PCSD was performed. In 1999, Suzuki et al. reported using metal benzoylacetonate complexes to fabricate $KTa_{0.5}Nb_{0.5}O_3$ films.[185] In 2003, Park et al.[186] (followed up by work from Lim et al.)[187] reported chelating various β-diketone and β-ketoester molecules to tantalum in 2-methoxyethanol for mixed oxides, where each tantalum β-diketonate or β-ketoester complex provides a different near-UV absorption peak. This allows the user to tailor the absorption to the light emitting device on hand for photocuring.

Later, the patent literature discusses photopatterning metal oxide films via drop-on-demand jetting in 2008[188] and nanoimprinting in 2011.[189] Then in 2012, Noma et al.[190] reported refluxing niobium(V) ethoxide with benzoylacetone in ethanol, resulting in a photocurable solution; this solution can be photopatterned by exposure to UV light, followed by leaching in methanol to remove the unexposed niobium solution. Segawa et al.[191] later examined the reaction mechanism of the photodecomposition of titanium(IV) dibenzoylmethane complexes during oxide deposition via PCSD. Nakajima et al.[192] and Bretos et al.[193] provide modern reviews on the subject of CSD and PCSD for the fabrication of metal oxide films, including the use of photosensitive compounds in low temperature crystallization.

Diol Route - 1990s-Present

In producing lead-titanate materials in 1995, Calzada et al.[194] reported substitution of isopropoxide groups in titanium(IV) diisopropoxide bis(acetylacetonate) with 1,3-propanediol in the presence of lead(II) acetate trihydrate. This was accomplished with an 8 hour reflux, with subsequent distillation and removal of isopropanol (Calzada et al. later discuss use of the precursor mixed with lead(II) acetate trihydrate for PCSD):[195]

$$\mathrm{Ti(OC_3H_7)_2(C_5H_7O_2)_2 + 2\,HOC_3H_6OH \longrightarrow Ti(OC_3H_6OH)_2(C_5H_7O_2)_2 + 2\,C_3H_7OH} \quad (3.9)$$

However, in preparing the precursor in the absence of lead(II) acetate trihydrate, Kemmitt and Daglish[196] reported in 1998 the decomposition of titanium(IV) and zirconium(IV) acetylacetonate complexes. This occurred via alcoholysis (the heavy diol reacting with chelated acetylacetone to create acetone and 3-hydroxypropyl acetate). Precipitate was found to form in solution over time, and was analyzed to be $M(IV)(OC_3H_6O)_2$ with M being zirconium or titanium, where both terminal oxygens on the diol are bound to the metal cation.

In 2002, Kao et al.[197] reported reflux of lithium acetylacetonate with 1,3-propanediol, followed by tantalum(V) isopropoxide addition and further reflux as a precursor to $LiTaO_3$ films. In the same year, González[198,199] submitted her Spanish doctoral thesis, describing a method to create a tantalum pentaglycolate precursor solution for strontium bismuth tantalate films, resulting in an ethanol free solution which could be stored for months; the work was later reported in 2005 with Calzada in an English publication.[200] The procedure involves the substitution of ethoxide groups in tantalum(V) ethoxide with 1,3-propanediol via reflux and distillation via heat:

$$\mathrm{Ta(OC_2H_5)_5 + 5\,HOC_3H_6OH \longrightarrow Ta(OC_3H_6OH)_5 + 5\,C_2H_5OH} \tag{3.10}$$

This work was based on experiments reported by Mehrotra and Kapoor in 1965, where substitution of ethoxide groups with glycols in tantalum and niobium compounds was performed.[171,172] Calzada et al.[201,202] also reported the use of 1,3-propanediol in niobium based solutions.

These investigations by Calzada's group were not purely out of academic curiosity, but rather an effort to replace 2-methoxyethanol with 1,3-propanediol as the solution solvent. 2-methoxyethanol is often used for stabilizing solutions, as the solvent creates a chelate complex as a way to hinder nucleophilic attack from water to the metal cation.[203] Despite its high use in CSD,[204] 2-methoxyethanol exposure has been observed to have toxic reproductive and developmental effects,[203] and the solvent can be easily inhaled due to its relatively high vapor pressure. Due to the solvent's toxicity, the use of 2-methoxyethanol has been restricted in some countries,[203] and therefore creates a major obstacle in manufacturing.

Thus, the goal of this work is to find the optimal procedure, via an Edisonian approach, for producing a tantalum(V) 1,3-propanediolate β-diketonate/β-ketoester solution. Such a low toxic, air stable solution would allow for photocuring in the near-UV range in ambient atmosphere, thereby reducing manufacturing costs. The results of Calzada's group, Kemmitt and Daglish, and the known use of metal acetylacetonate precursors in nanoparticle production[205–207] will be used to guide the investigation.

3.2 Introduction to Experiments

The goal of this section is to create a 2-methoxyethanol free, tantalum(V) β-diketonate/β-ketoester solution. This will be achieved by using 1,3-propanediol as the main solvent, as was done by Calzada and González[198–200] for solutions without a β-diketone where they removed ethanol via heat and distillation. The experiments will be derived, and later evolve, from what Whitley[150] performed with tantalum(V) ethoxide and benzoylacetone in her thesis. Additionally, photographs of the experiments are shown with time of day and dates in Jülich, Germany (military time with day.month.year, not the American format), as Silverman[155] pointed out in his thesis for tantalum sol-gel synthesis that the time of year in Cambridge, Massachusetts, likely because of humidity, can affect the final results.

Reagent Preparation

When working with moisture sensitive compounds, such as tantalum(V) ethoxide, the use of dry glassware and an inert atmosphere is often necessary for achieving the best results. For example, in order to dry a Schlenk flask for synthesis, the flask can be heated under vacuum, followed by filling the flask with argon; these steps can be performed when the flask is connected to a Schlenk line fitted with both vacuum and argon lines. The dry Schlenk flask can then be disconnected from the Schlenk line and transferred to an argon filled glovebox, where the reagents and magnetic stirring rod can be added to the flask in an inert atmosphere. The flask can then be removed from the glovebox and reconnected to the

Schlenk line, where synthesis can proceed. All glass joints used a polytetrafluoroethylene (PTFE) sleeve in order to avoid grease contamination. These preparation steps were used for all of the experiments described in this chapter.

Nuclear magnetic resonance (NMR) spectra, specifically ^{1}H and ^{13}C NMR, were performed for the reagents to aid in assigning peaks in the synthesis products. The peak assignments are labeled in the respective figures for tantalum(V) ethoxide (Alfa Aesar, 99+%, Figures 3.1 and 3.2), 1,3-propanediol (Sigma-Aldrich, for synthesis, Figures 3.3 and 3.4), acetylacetone (Alfa Aesar, 95%, Figures 3.5 and 3.6), and benzoylacetone (Sigma Aldrich, 99%, Figures 3.7 and 3.8). These reagents and their suppliers were used for all experiments unless otherwise noted. Additionally, total correlation spectroscopy (TOCSY) and heteronuclear multiple bond correlation (HMBC) were used for some of the products. All spectra were measured versus an external D_2O reference, except for benzoylacetone which was measured versus a $CDCl_3$ reference solvent, at 25°C by using a 600 MHz AVANCE NMR spectrometer (Bruker Corporation, USA). In making assignments for the enol tautomer of acetylacetone, $[H_3C(CO)CH(CO)CH_3]$ will represent either a H^+ bound molecule, being $[H_3C(COH)CH(CO)CH_3]$, or a Ta^{5+} bound complex, being $[H_3C(COTa)CH(CO)CH_3]$, as the NMR results are unable to resolve which is occurring for a particular peak (the same is true for the respective benzoylacetone-enol tautomer).

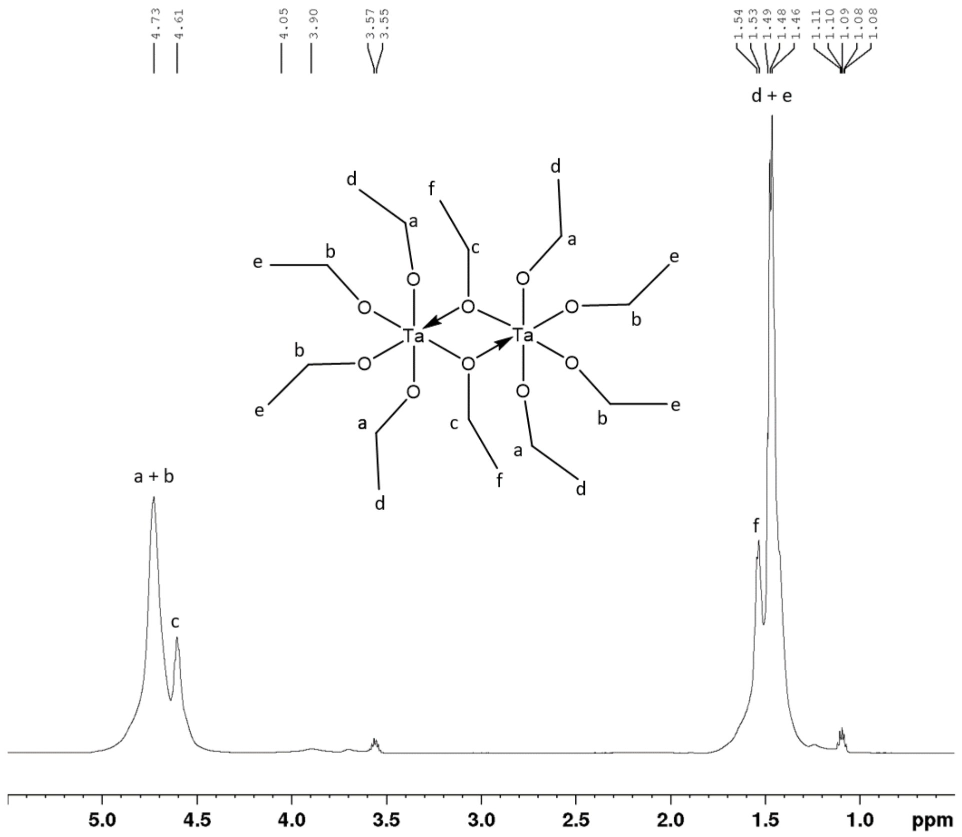

Figure 3.1 ^{1}H NMR [External D_2O]: Tantalum(V) Ethoxide [Alfa Aesar, 99+%] (© The Royal Society of Chemistry 2020).[136,137]

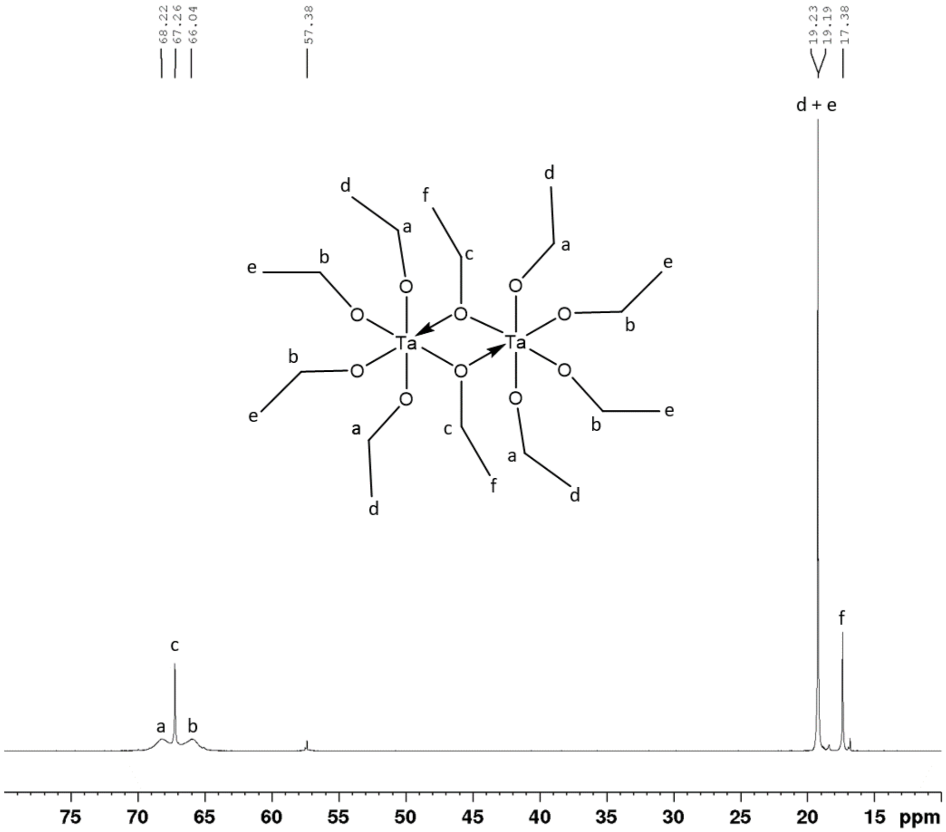

Figure 3.2 ^{13}C NMR [External D_2O]: Tantalum(V) Ethoxide [Alfa Aesar, 99+%] (© The Royal Society of Chemistry 2020).[136,137]

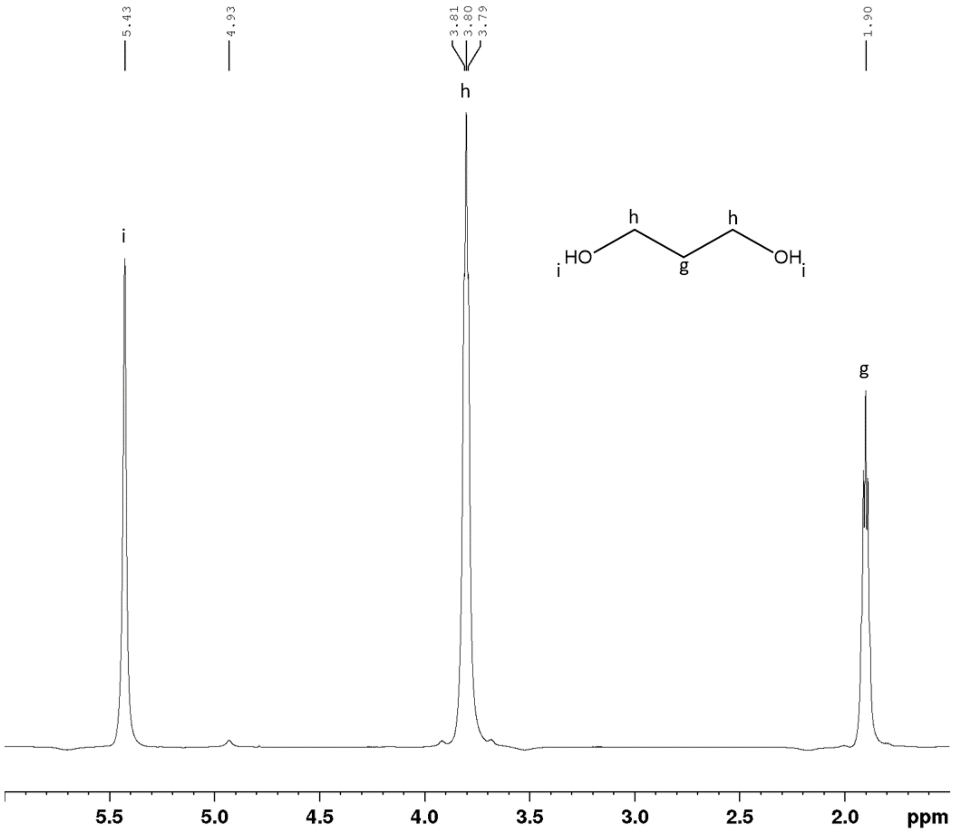

Figure 3.3 ^{1}H NMR [External D_2O]: 1,3-Propanediol [Sigma-Aldrich, for synthesis] (© The Royal Society of Chemistry 2020).[136,137]

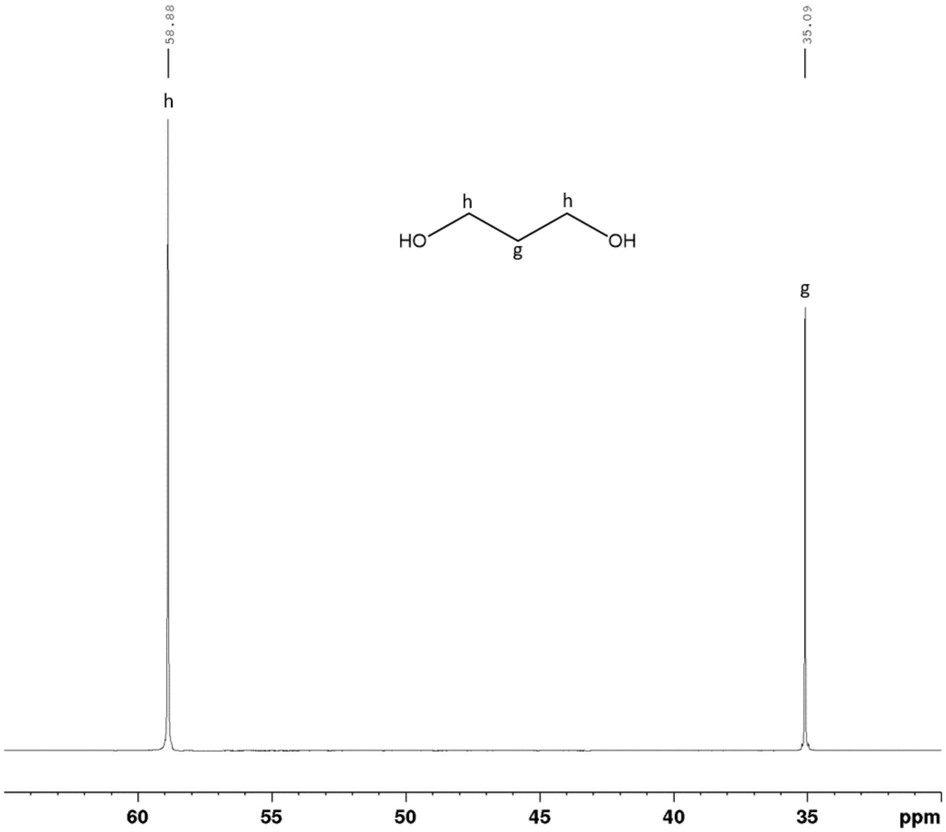

Figure 3.4 ^{13}C NMR [External D_2O]: 1,3-Propanediol [Sigma-Aldrich, for synthesis] (© The Royal Society of Chemistry 2020).[136,137]

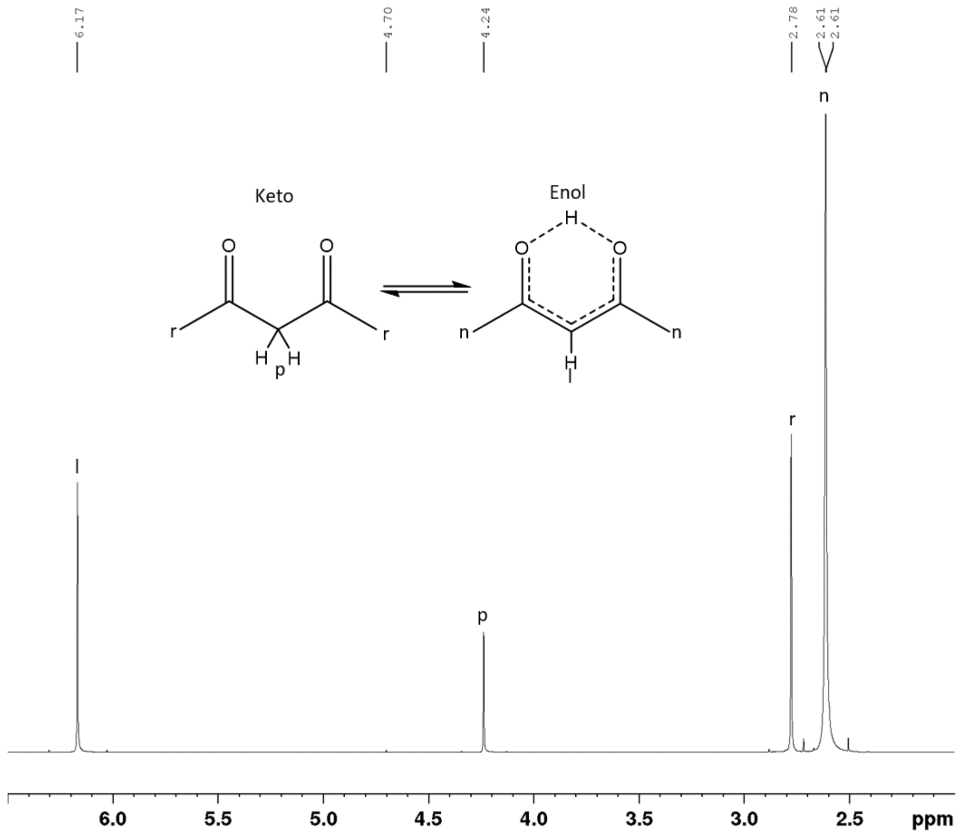

Figure 3.5 ^{1}H NMR [External D_2O]: Acetylacetone [Alfa Aesar, 95%] (© The Royal Society of Chemistry 2020).[136,137]

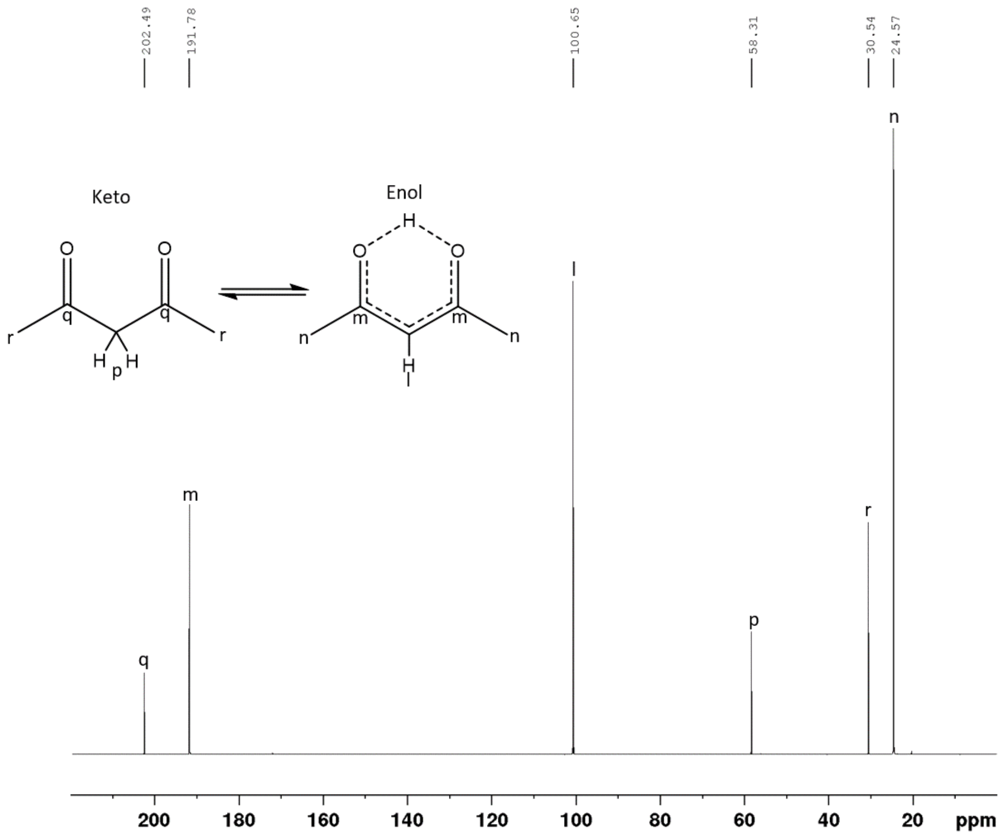

Figure 3.6 ^{13}C NMR [External D_2O]: Acetylacetone [Alfa Aesar, 95%] (© The Royal Society of Chemistry 2020).[136,137]

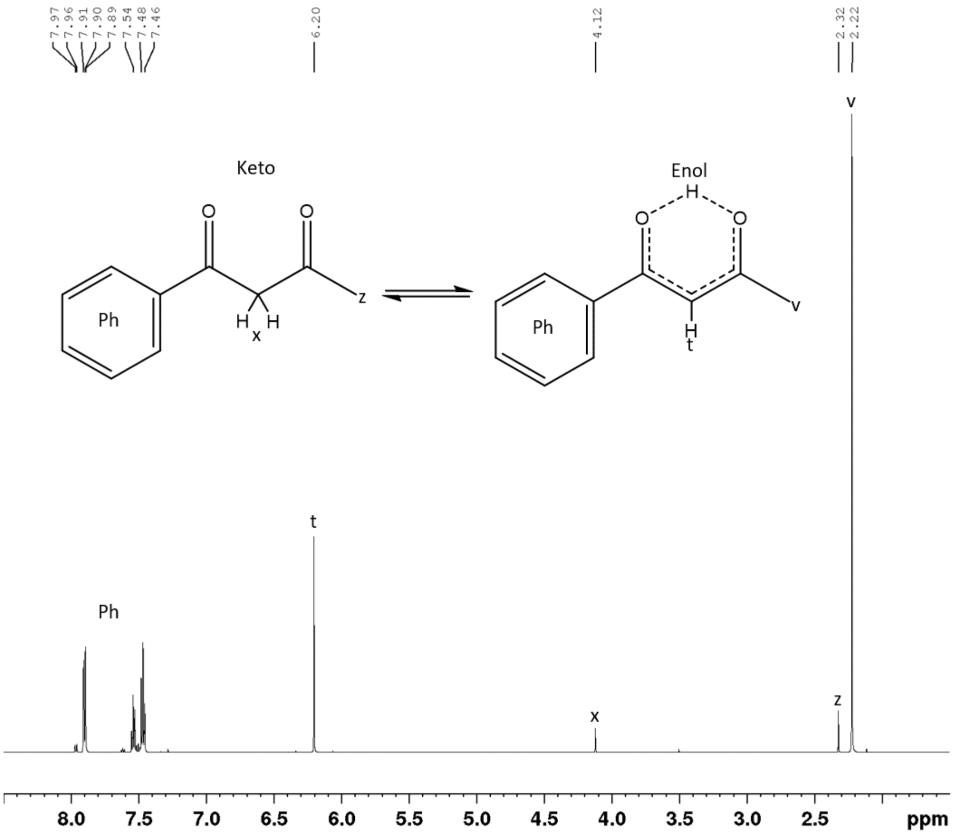

Figure 3.7 ^{1}H NMR [CDCl$_3$]: Benzoylacetone [Sigma Aldrich, 99%] (© The Royal Society of Chemistry 2020).[136,137]

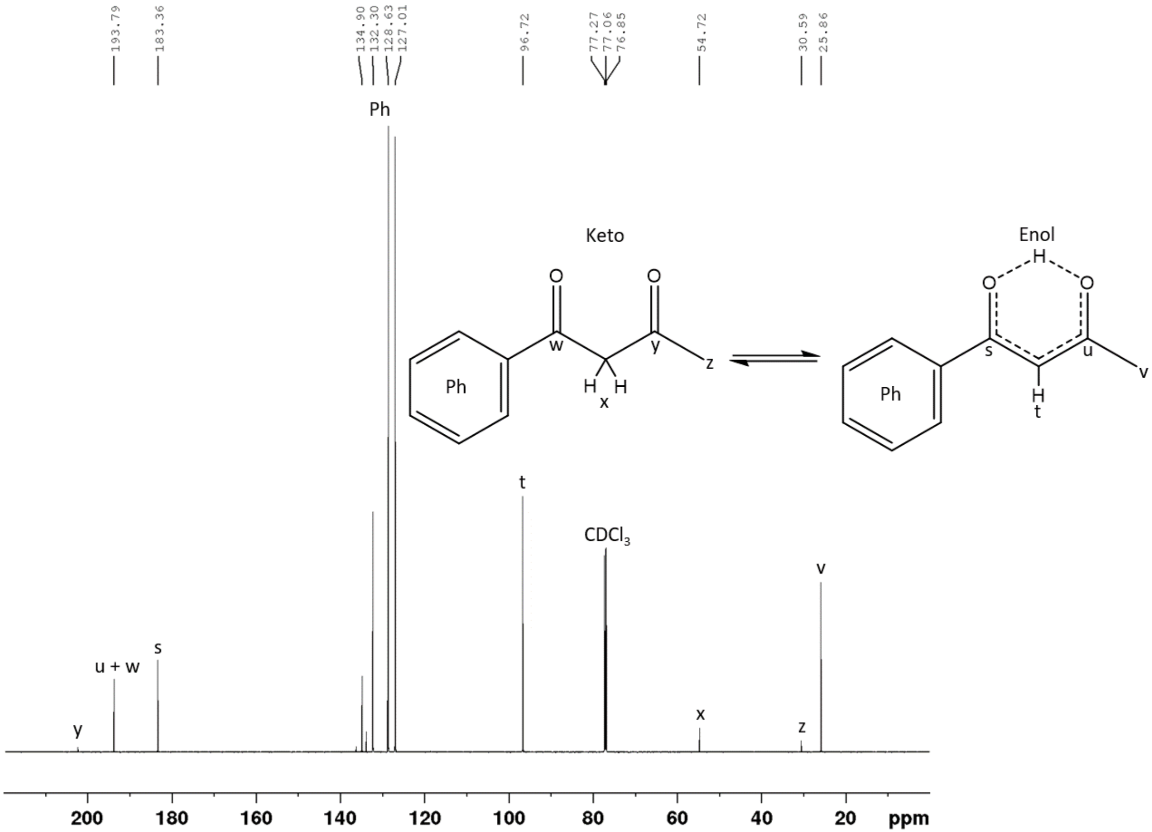

Figure 3.8 ^{13}C NMR [CDCl$_3$]: Benzoylacetone [Sigma Aldrich, 99%] (© The Royal Society of Chemistry 2020).[136,137]

3.3 Experiment 1 - Whitley Method with Acetylacetone

As Alice Whitley described in her doctoral thesis,[150] where tantalum(V) ethoxide and benzoylacetone were mixed under heat in benzene to achieve chelation, the first experiment will attempt the same with acetylacetone while replacing benzene with 1,3-propanediol. After assumed chelation of acetylacetone over 9 hours, distillation will begin so that ethanol will leave and be replaced by 1,3-propanediol under heat.

3.3.1 Synthesis

1,3-Propanediol (39.79 mmol, 3028 mg [Sigma-Aldrich, for synthesis]), acetylacetone (6.41 mmol, 642 mg [Alfa Aesar, 95%]), and tantalum(V) ethoxide (6.00 mmol, 2439 mg [Alfa Aesar, 99+%]) were mixed in a dried Schlenk flask under argon in a glovebox. The Schlenk flask with a magnetic stirring rod was removed from the glovebox and connected to a short-path distillation setup and a Schlenk line. The Schlenk flask with the reagents (reactor flask) was submerged in silicone oil, where the temperature of the silicone oil was maintained at 100°C. The reaction was conducted under argon and continuous stirring, and the vertical condenser (cold finger) was pointed towards the reactor flask for about 9 hours; this was done in order to facilitate the chelation of acetylacetone and to avoid its loss to the distillate flask. After 9 hours, the vertical condenser was rotated towards the distillate flask for ethanol removal. After 4 days, condensation on the vertical condenser appeared to cease, thus marking the end of the reaction.

As can be seen in Figure 3.9, the color of the solution in the reactor flask changes over 4 days from colorless and transparent, to a dark amber color. Furthermore, precipitate was not observable in the reactor flask. The distillate was colorless and transparent.

3.3.2 NMR Measurements

Distillate results shows the presence of ethanol; ^{1}H NMR (δ [ppm], Figure 3.10): δ 1.68 $[\mathrm{HOCH_2C}H_3]$, δ 4.11 $[\mathrm{HOC}H_2\mathrm{CH_3}]$, δ 5.45 $[H\mathrm{OCH_2CH_3}]$; ^{13}C NMR (δ [ppm], Figure 3.11): δ 15.8 $[\mathrm{HOCH_2}C\mathrm{H_3}]$, δ 55.1 $[\mathrm{HO}C\mathrm{H_2CH_3}]$. However, many other unassigned peaks are present in these spectra, showing either the presence of impurities or byproducts.

The ^{1}H NMR spectrum of the product (δ [ppm], Figure 3.12) shows the presence of the expected 1,3-propanediol peaks at δ 1.86 $[\mathrm{HOCH_2C}H_2\mathrm{CH_2OH}]$, δ 3.77 $[\mathrm{HOC}H_2\mathrm{CH_2C}H_2\mathrm{OH}]$, and δ 5.35 $[H\mathrm{OCH_2CH_2CH_2O}H]$. Two separate methine acetylacetone-enol peaks appear at δ 6.01, and δ 5.91 $[\mathrm{H_3C(CO)C}H\mathrm{(CO)CH_3}]$. The peaks from δ 2.40 to δ 2.10 overlap significantly. Further downfield, as the δ 4.26 triplet peak resonates at a higher frequency than the alcoholic methylene 1,3-propanediol peak at δ 3.77, in addition to the presence of the large methyl peak at δ 2.18, this likely indicates the presence of an unknown byproduct.

The ^{13}C NMR spectrum of the product (δ [ppm], Figure 3.13) shows the expected 1,3-propanediol peaks at δ 35.2 $[\mathrm{HOCH_2}C\mathrm{H_2CH_2OH}]$ and δ 59.0 $[\mathrm{HO}C\mathrm{H_2CH_2}C\mathrm{H_2OH}]$. Acetylacetone-enol peaks are present around δ 191.0 $[\mathrm{H_3C(}C\mathrm{O)CH(}C\mathrm{O)CH_3}]$, and around δ 98.0 $[\mathrm{H_3C(CO)}C\mathrm{H(CO)CH_3}]$. Methyl peaks in the δ 30.0 to δ 20.0 range are difficult to assign, with the δ 20.4 peak likely being associated with the unknown byproduct previously mentioned. The large peak at δ 171.6, not associated with any of the reagents, is located in the range typically found for ester carbonyl carbons.[208] As an ester was unexpected, this indicates the presence of a byproduct, where HMBC (measured 6 months later) in Figure 3.14 shows cross-peaks at ^{1}H δ 2.10 – ^{13}C δ 171.5 and ^{1}H δ 4.15 – ^{13}C δ 171.5. This suggests that acetylation of an alcohol group has occurred, resulting in either ethyl acetate or 3-hydroxypropyl acetate. However, the data is not clear enough to determine which molecule these peaks belong to, especially as ethanol was present from the beginning. In considering possible creation of acetone from alcoholysis, acetylacetone-keto $[\mathrm{H_3C(}C\mathrm{O)CH_2(}C\mathrm{O)CH_3}]$ or acetone[196,209] $[\mathrm{H_3C(}C\mathrm{O)CH_3}]$ carbonyl peaks are visible at δ 205.0 in Figure 3.11 for the distillate ^{13}C NMR and δ 207.6 in Figure 3.13 for the product ^{13}C NMR.

3.3.3 Discussion

As the distillate and product spectra both show the presence of unknown byproducts, the reaction method needs to be improved in order to increase the yield of the desired photosensitive complexes. Furthermore, the presence of byproducts in the distillate demonstrates that removal of ethanol via heat should be avoided in the presence of acetylacetone. However, this does not rule out whether this method will work for benzoylacetone, which will be attempted in Experiment 2.

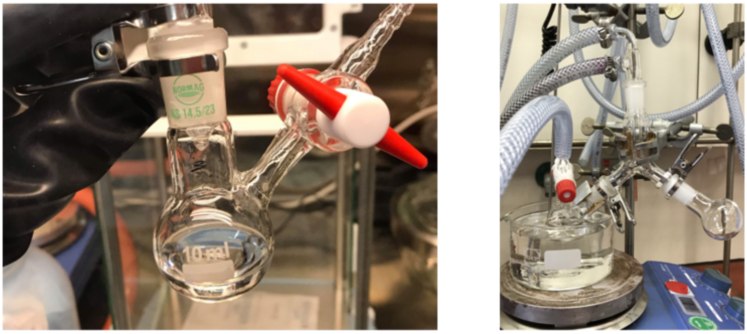

09:43 on 11.02.2019: Mixed reagents in glove box.

10:32 on 11.02.2019: Start under argon, finger towards reactor (left).

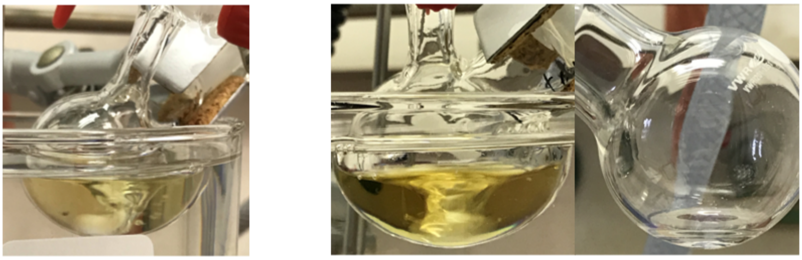

20:19 on 11.02.2019: Finger rotated.

10:51 on 12.02.2019: 1 day - reactor (left) and distillate (right).

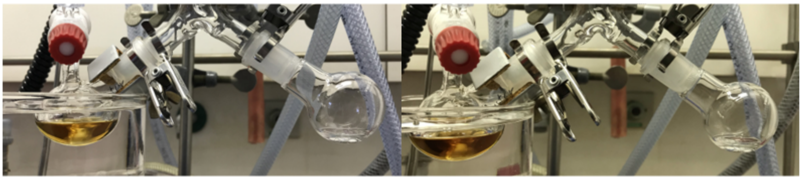

09:07 on 13.02.2019: 2 days.

07:33 on 14.02.2019: 3 days.

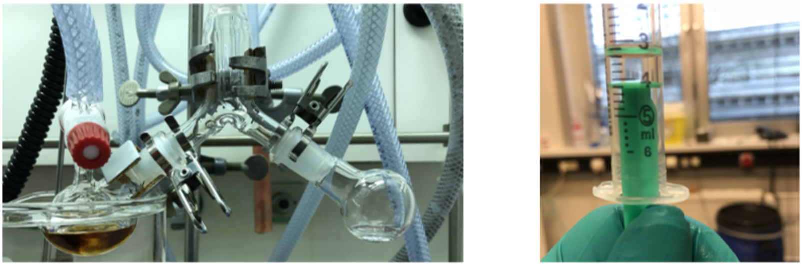

07:08 on 15.02.2019: 4 days – end.

Distillate <1 ml.

Figure 3.9 Photographic record of Experiment 1.

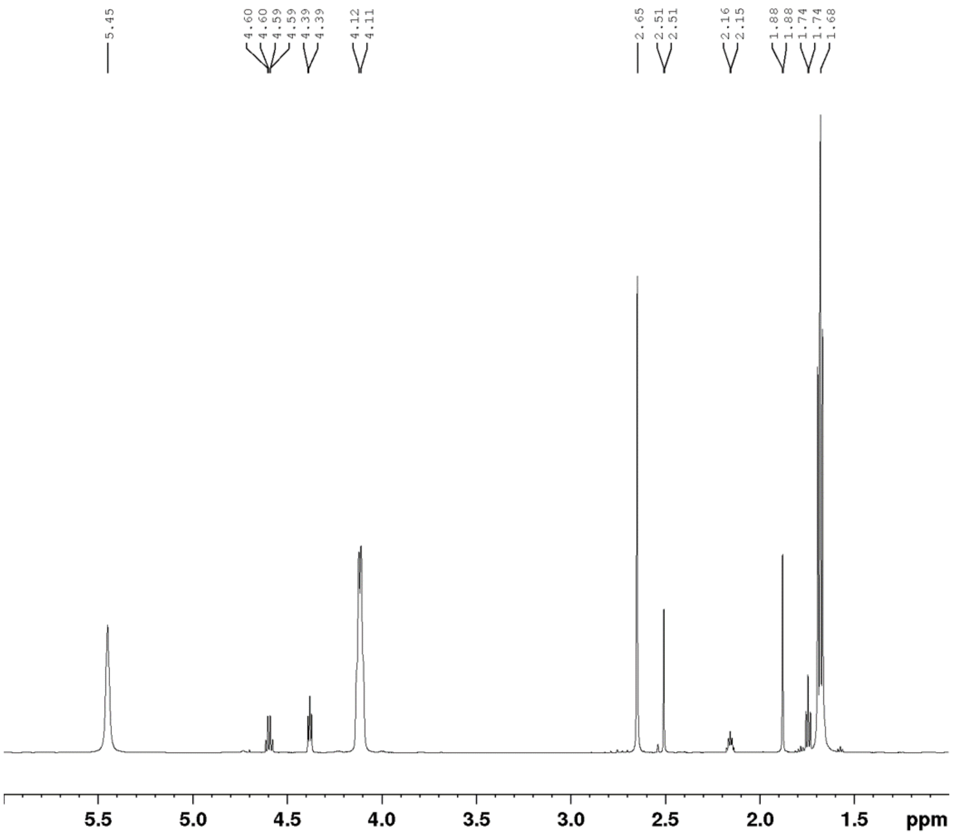

Figure 3.10 ^{1}H NMR [External D_2O]: Experiment 1 – Distillate.

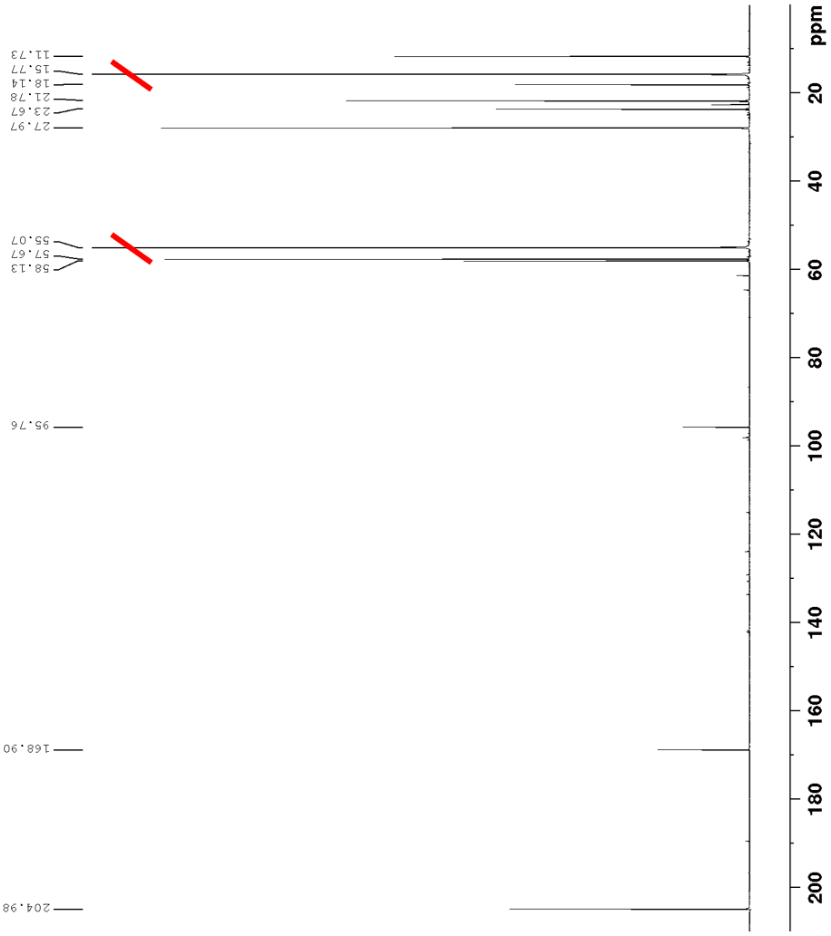

Figure 3.11 ^{13}C NMR [External D_2O]: Experiment 1 – Distillate.

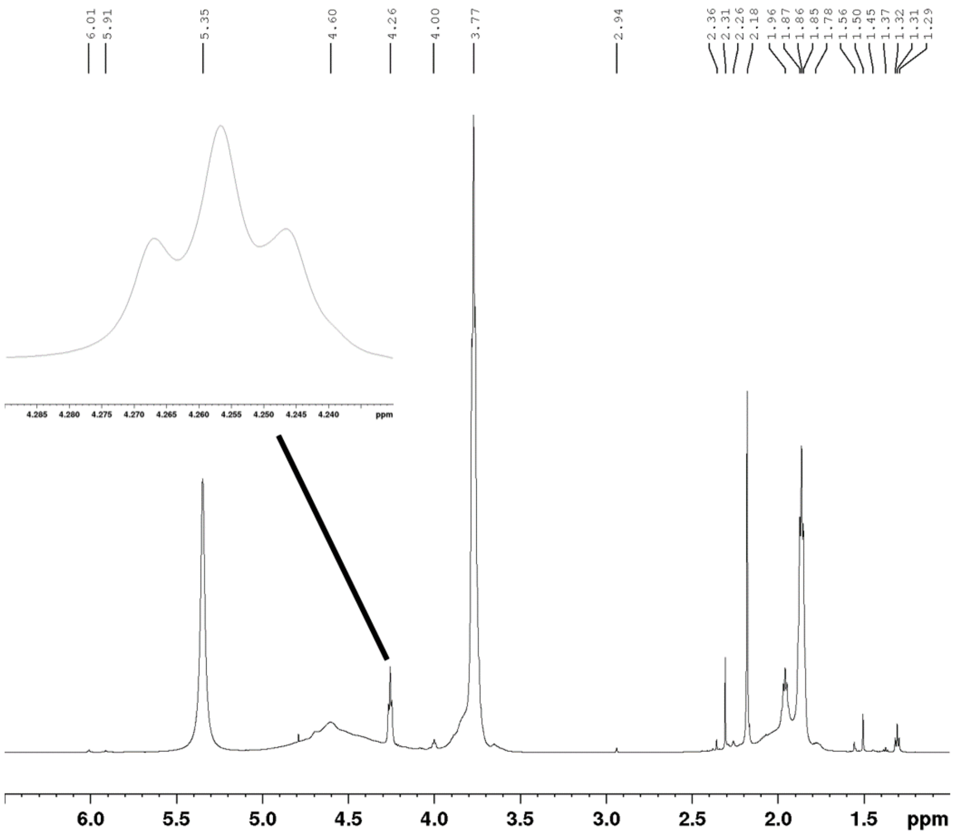

Figure 3.12 ^{1}H NMR [External D_2O]: Experiment 1 – Product.

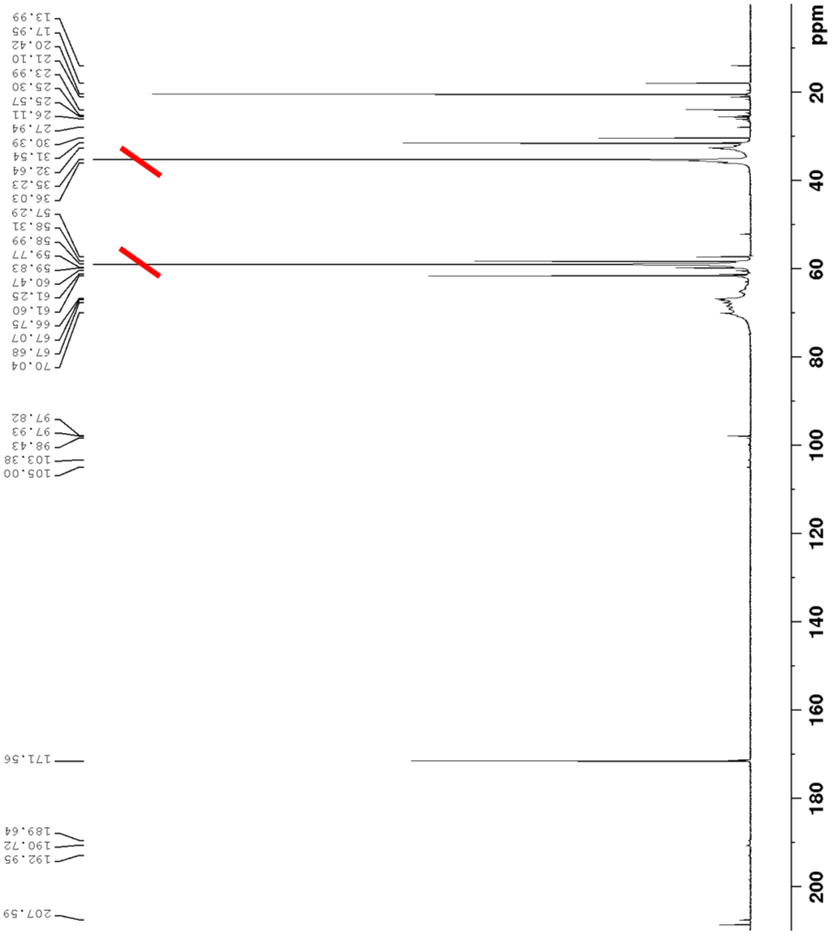

Figure 3.13 ^{13}C NMR [External D_2O]: Experiment 1 – Product.

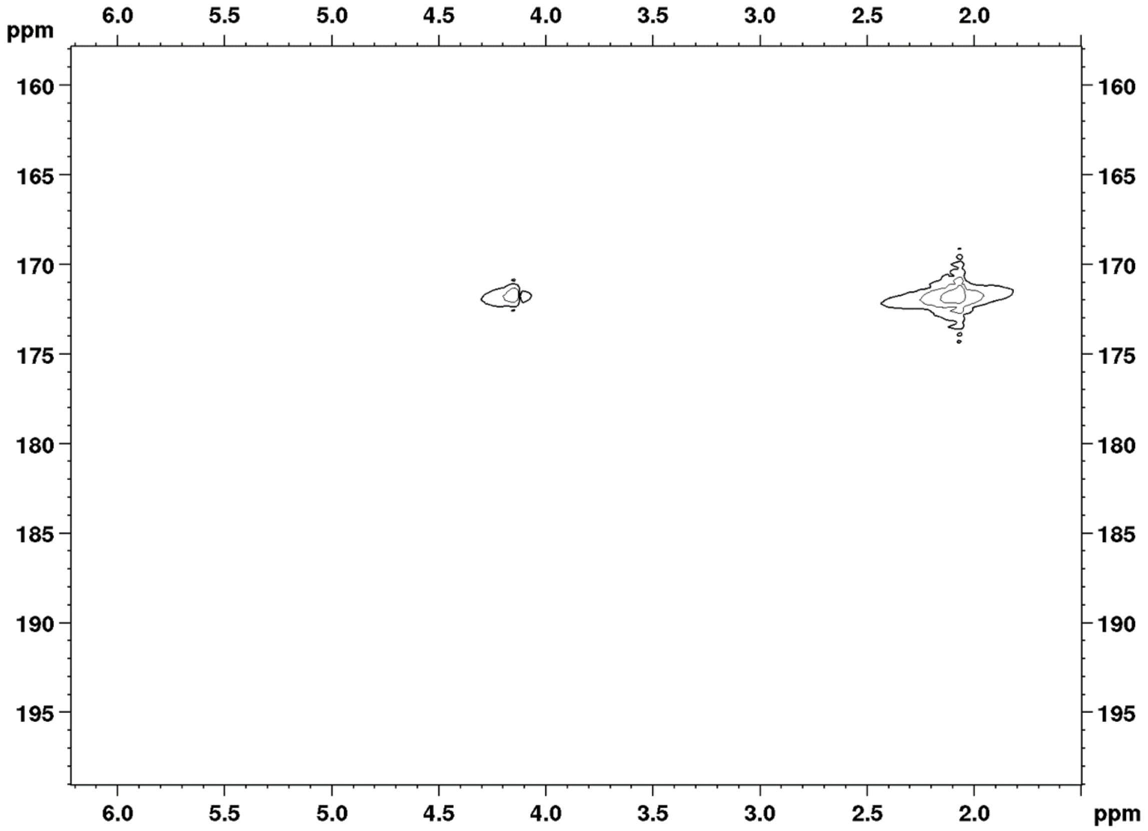

Figure 3.14 HMBC [External D_2O]: Experiment 1 – Product.

3.4 Experiment 2 - Whitley Method with Benzoylacetone

As Alice Whitley described in her doctoral thesis,[150] where tantalum(V) ethoxide and benzoylacetone were mixed under heat in benzene to achieve chelation, the second experiment will attempt the same with benzoylacetone while replacing benzene with 1,3-propanediol. After assumed chelation of benzoylacetone over 8 hours, distillation will begin so that ethanol will leave and be replaced by 1,3-propanediol under heat.

3.4.1 Synthesis

1,3-Propanediol (39.51 mmol, 3006 mg [Sigma-Aldrich, for synthesis]), benzoylacetone (6.21 mmol, 1007 mg [Sigma Aldrich, 99%]), and tantalum(V) ethoxide (6.01 mmol, 2442 mg [Alfa Aesar, 99+%]) were mixed in a dried Schlenk flask under argon in a glovebox. The Schlenk flask with a magnetic stirring rod was removed from the glovebox and connected to a short-path distillation setup and a Schlenk line. The Schlenk flask with the reagents (reactor flask) was submerged in silicone oil, where the temperature of the silicone oil was maintained at 100°C. The reaction was conducted under argon and continuous stirring, and the vertical condenser (cold finger) was pointed towards the reactor flask for about 8 hours; this was done in order to facilitate the chelation of benzoylacetone and to avoid its loss to the distillate flask. After 8 hours, the vertical condenser was rotated towards the distillate flask for ethanol removal. After 7 days, condensation on the vertical condenser appeared to cease, thus marking the end of the reaction.

As can be seen in Figure 3.15, the color of the solution in the reactor flask changes over 7 days from colorless and transparent, to a dark amber color. Furthermore, precipitate was not observable in the reactor flask. The distillate was colorless and transparent, but not enough distillate could be collected for NMR measurements.

3.4.2 NMR Measurements

The ^{1}H NMR spectrum of the product (δ [ppm], Figure 3.16) shows the presence of the expected 1,3-propanediol peaks at δ 1.73 [$HOCH_2CH_2CH_2OH$], δ 3.64 [$HOCH_2CH_2CH_2OH$], and δ 5.08 [$HOCH_2CH_2CH_2OH$]. The peaks around δ 2.00 overlap significantly and are difficult to assign. Further downfield, as the δ 4.09 peak resonates at a higher frequency than the alcoholic methylene 1,3-propanediol peak at δ 3.64, in addition to the presence of the large methyl peak at δ 1.94, this likely indicates the presence of an unknown byproduct (especially in the absence of observable benzoylacetone-enol methine peaks).

The ^{13}C NMR spectrum of the product (δ [ppm], Figure 3.17) shows the expected 1,3-propanediol peaks at δ 35.2 [$HOCH_2CH_2CH_2OH$] and δ 59.0 [$HOCH_2CH_2CH_2OH$]. Benzoylacetone-enol [$Ph(CO)CH(CO)CH_3$] or benzoylacetone-keto [$Ph(CO)CH_2(CO)CH_3$] peaks around δ 191.0, around δ 100.0 (enol) [$Ph(CO)CH(CO)CH_3$], peak(s) within the range δ 40.0 to δ 10.0 [$Ph(CO)CH_2(CO)CH_3$]/[$Ph(CO)CH(CO)CH_3$]/byproducts, and the multiple phenyl ring carbon peaks in the range δ 140.0 to δ 125.0 appear in the spectrum. The peak at δ 171.5, not associated with any of the reagents, is located in the range typically found for ester carbonyl carbons.[208] As an ester was unexpected, this indicates the presence of a byproduct, where HMBC (measured ∼6 months later) in Figure 3.18 shows relevant cross-peaks at ^{1}H δ 2.00 – ^{13}C δ 171.0 and ^{1}H δ 4.10 – ^{13}C δ 171.0; this suggests that acetylation of an alcohol group has occurred. Additionally, a benzoylacetone-keto [$Ph(CO)CH_2(CO)CH_3$] or acetone[196,209] [$H_3C(CO)CH_3$] carbonyl peak is visible at δ 198.9 in the ^{13}C NMR spectrum.

3.4.3 Discussion

As the product spectra show the presence of unknown byproducts, the reaction method needs to be improved in order to improve the yield of the desired photosensitive complexes. In order to determine whether the presence of ethanol leads to byproducts under heat, the next experiment will involve removing the ethanol from the solution before β-diketone addition.

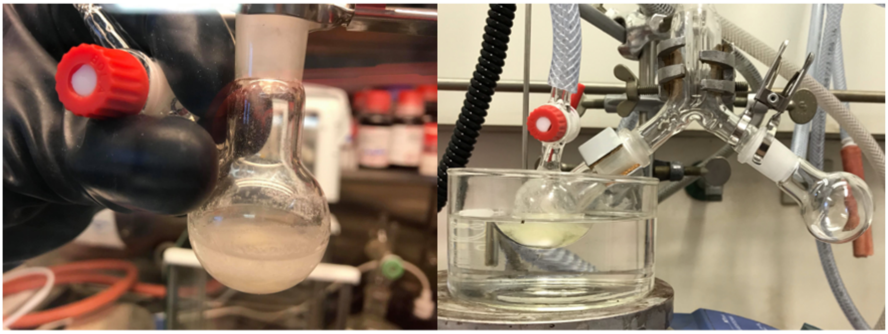

09:07 on 25.02.2019: Mixed reagents in glove box.

09:46 on 25.02.2019: Start under argon, finger towards reactor (left).

10:17 on 25.02.2019: 100°C reached.

19:10 on 25.02.2019: finger rotated.

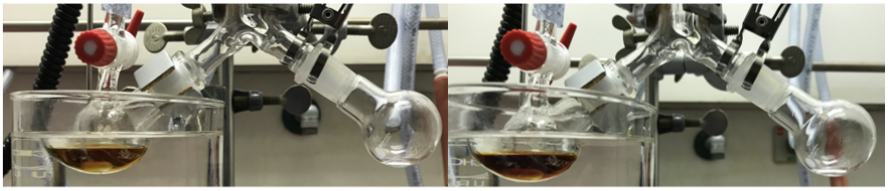

07:37 on 26.02.2019: 1 day checkpoint.

07:22 on 28.02.2019: 3 days checkpoint.

20:35 on 03.03.2019: 6 days checkpoint.

09:26 on 05.03.2019: 8 days – end.

Figure 3.15 Photographic record of Experiment 2. The white solid at the beginning is undissolved, solid benzoylacetone at room temperature, which disappears after heating the solution.

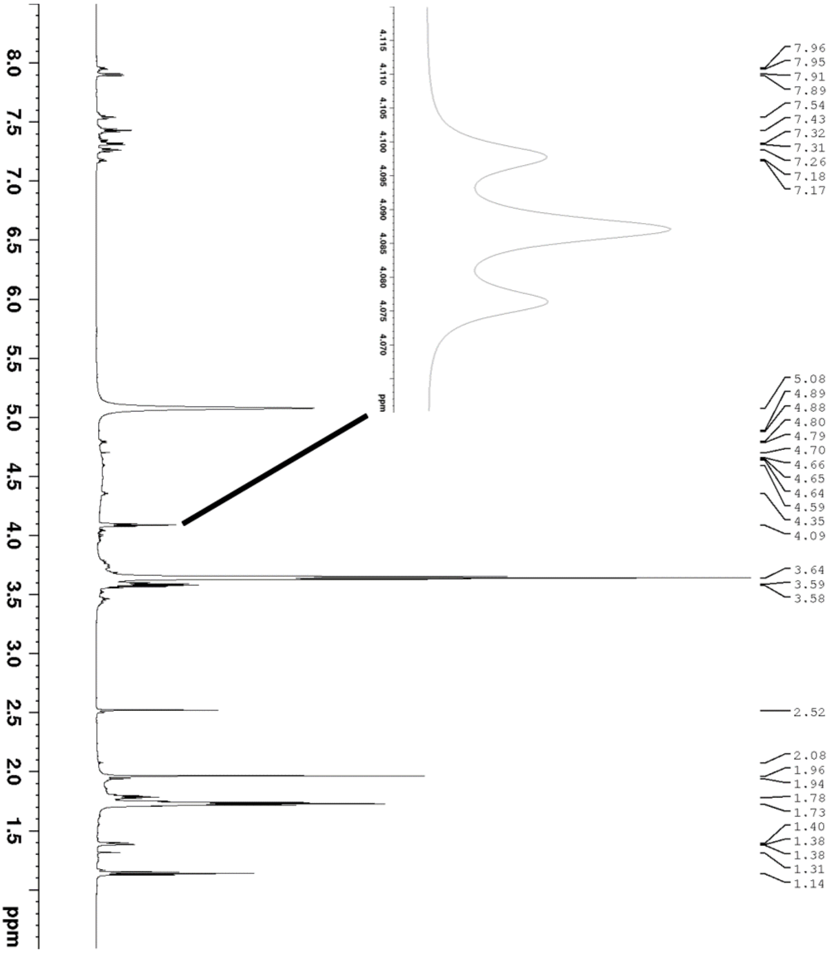

Figure 3.16 ^{1}H NMR [External D_2O]: Experiment 2 – Product.

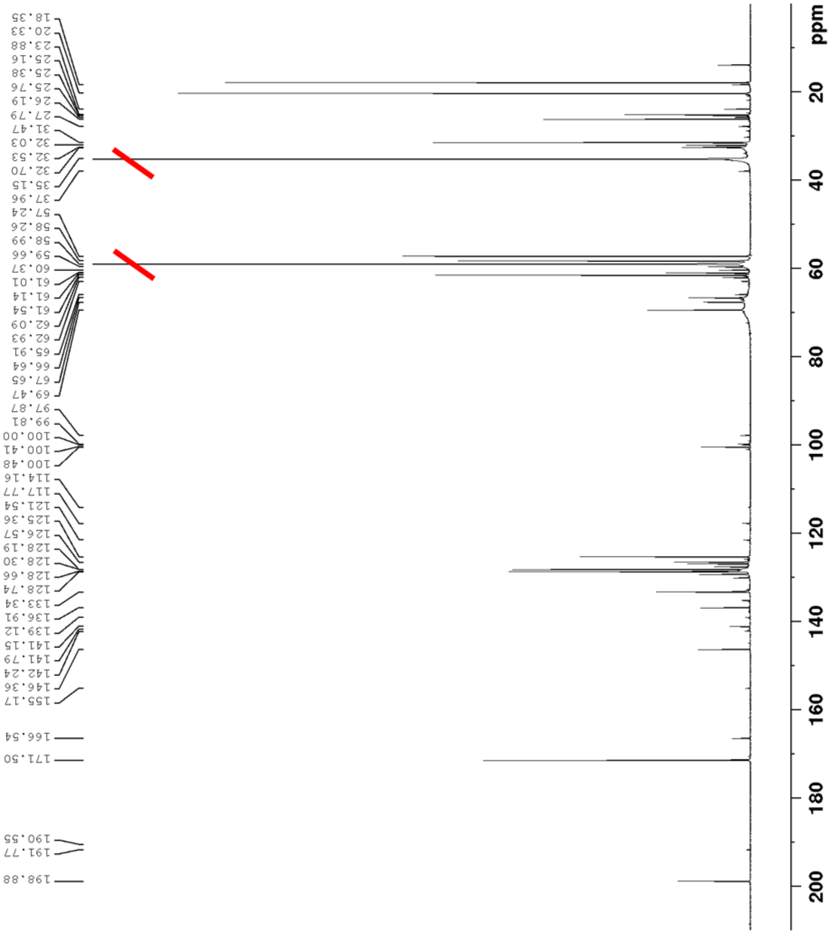

Figure 3.17 ^{13}C NMR [External D_2O]: Experiment 2 – Product.

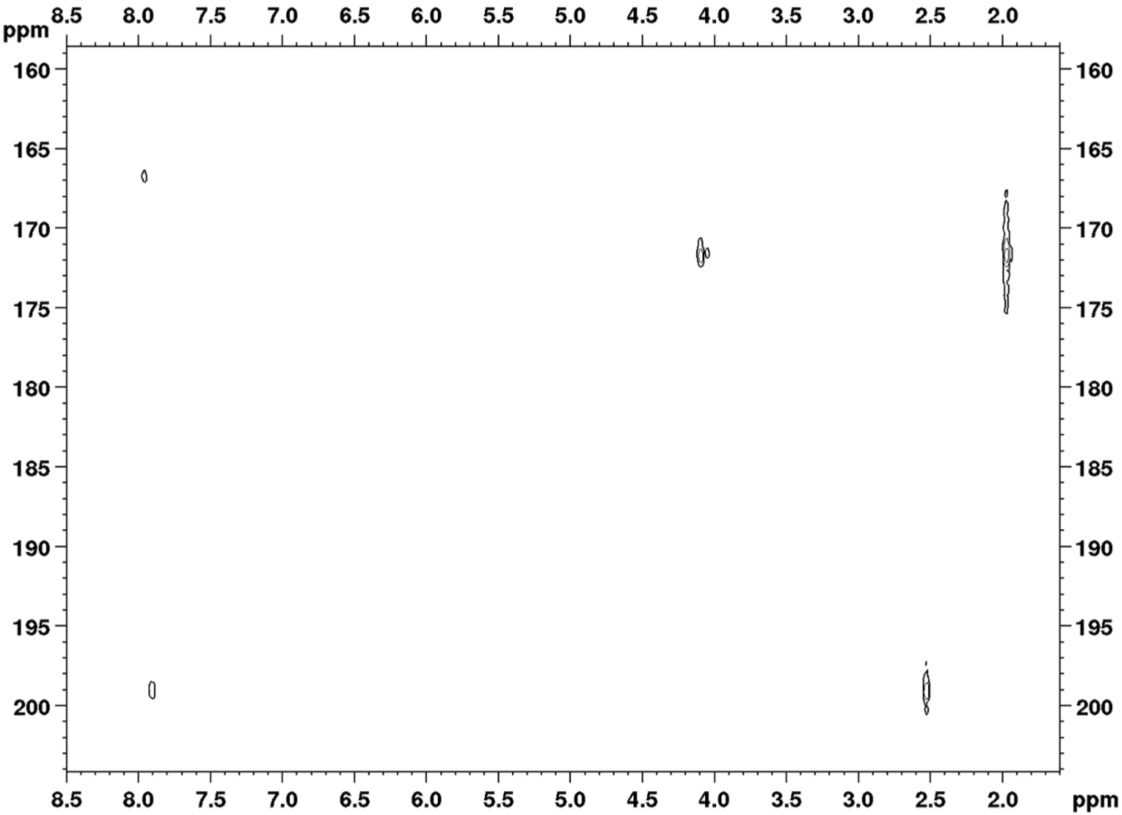

Figure 3.18 HMBC [External D_2O]: Experiment 2 – Product.

3.5 Experiment 3 - Calzada and González Method with Acetylacetone

In order to exclude ethanol as a reagent leading to side products, a modified procedure from Calzada and González[198,200] was used to create a tantalum(V) 1,3-propanediolate solution free of ethanol. Acetylacetone was then added to this solution under heat, in order to see if side products would still arise.

3.5.1 Synthesis

1,3-propanediol (42.37 mmol, 3224 mg [Sigma-Aldrich, for synthesis]) and tantalum(V) ethoxide (6.02 mmol, 2445 mg [Alfa Aesar, 99+%]) were mixed in a dried Schlenk flask under argon in a glovebox. The Schlenk flask with a magnetic stirring rod was removed from the glovebox and connected to a short-path distillation setup and a Schlenk line. The Schlenk flask with the reagents (reactor flask) was submerged in silicone oil, where the temperature of the silicone oil was maintained at 130°C under continuous stirring. With the vertical condenser (cold finger) pointed towards the distillation flask, the reaction was run under argon over 24 hours to collect the distillate for NMR. After 24 hours, the distillate was collected and the tantalum(V) 1,3-propanediolate solution remained under heat and mixing, with the reaction being exposed to atmosphere for 5 hours; this was done in order to reduce pressure over the solution and to ensure that as much ethanol was removed from the solution as possible. After 5 hours, some of the tantalum(V) 1,3-propanediolate solution (710 mg) was collected and stored in a syringe - unfortunately, as the solution was stored overnight before sample preparation, the syringe exploded upon adding the solution to the NMR tube (likely caused by the needle hole being filled with tantala glass or the high viscosity of the solution). This led to a loss of some of the solution, and thus giving suboptimal NMR spectra.

After the tantalum(V) 1,3-propanediolate NMR sample was removed, acetylacetone (5.05 mmol, 506 mg [Alfa Aesar, 95%]) was then added to the reaction flask, and the reaction flask was returned to argon (this time with the condenser pointed towards the reaction flask). The flask was maintained at 80°C in silicone oil with continuous mixing for 72 hours, with the intention of improving the chelation yield[190] and the solubility[210] with a longer running reaction.

The reaction steps are shown in Figure 3.19. During the 3 day reaction after acetylacetone addition, the solution changed from clear and transparent to having a yellow hue, with this color being much lighter than in Experiment 1.

3.5.2 NMR Measurements

In preparing the tantalum(V) 1,3-propanediolate product, distillate results show the presence of ethanol with few byproducts (unlike in Experiment 1); ^{1}H NMR (δ [ppm], Figure 3.20): δ 1.72 [$HOCH_2CH_3$], δ 4.15 [$HOCH_2CH_3$], δ 5.86 [$HOCH_2CH_3$]; ^{13}C NMR (δ [ppm], Figure 3.21): δ 15.8 [$HOCH_2CH_3$], δ 55.2 [$HOCH_2CH_3$]. Product results indicate the presence of 1,3-propanediol; ^{1}H NMR (δ [ppm], Figure 3.22): δ 1.77 [$HOCH_2CH_2CH_2OH$], δ 3.68 [$HOCH_2CH_2CH_2OH$], δ 5.41 [$HOCH_2CH_2CH_2OH$] (a relatively large D_2O peak at δ 4.54 is present due to the low sample volume); ^{13}C NMR (δ [ppm], Figure 3.23): δ 35.3 [$HOCH_2CH_2CH_2OH$], δ 59.0 [$HOCH_2CH_2CH_2OH$]. The results corroborate those obtained by Calzada and González.[198,200]

The ^{1}H NMR spectrum of the product with added acetylacetone (δ [ppm], Figures 3.24 and 3.25) shows the presence of the expected 1,3-propanediol peaks at δ 1.83 [$HOCH_2CH_2CH_2OH$], δ 3.74 [$HOCH_2CH_2CH_2OH$], and δ 5.18 [$HOCH_2CH_2CH_2OH$]. Two separate methine acetylacetone-enol peaks appear at δ 5.98 and δ 5.88 [$H_3C(CO)CH(CO)CH_3$]. An acetylacetone-keto methyl peak [$H_3C(CO)CH_2(CO)CH_3$] or acetone-methyl peak from alcoholysis[196,211] [$H_3C(CO)CH_3$] occurs at δ 2.28. An acetylacetone-enol methyl peak [$H_3C(CO)$-

$CH(CO)CH_3$] occurs at δ 2.23. The δ 4.23 peak occurs as a triplet and indicates coupling to two protons with the same coupling constant on neighboring carbon atom(s); the peak at δ 4.67 is difficult to assign with the available data. Due to the fact that the δ 4.23 peak resonates at a higher frequency than the alcoholic methylene 1,3-propanediol peak at δ 3.74, in addition to the large methyl peak at δ 2.15, this likely indicates the acetylation of 1,3-propanediol and the creation of 3-hydroxypropyl acetate.[208] The δ 2.15 peak would then correspond to the methyl attached to the ester carbonyl [$HOCH_2CH_2CH_2O(CO)C\mathit{H}_3$], and the peak at δ 4.23 would be the protons on the methylene carbon bound to the ester oxygen [$HOCH_2CH_2C\mathit{H}_2O(CO)CH_3$]. In support of this, the TOCSY spectrum in Figure 3.26 shows three distinct proton groups on three consecutive carbon atoms, and the ^{13}C NMR and HMBC spectra corroborate these findings, as well as the literature values for 3-hydroxypropyl acetate.[212]

The ^{13}C NMR spectrum of the product (δ [ppm], Figure 3.27) shows the expected 1,3-propanediol peaks at δ 35.3 [$HOCH_2\mathit{C}H_2CH_2OH$] and δ 59.0 [$HO\mathit{C}H_2CH_2\mathit{C}H_2OH$]. Enol peaks around δ 191.0 [$H_3C(\mathit{C}O)CH(\mathit{C}O)CH_3$], around δ 104.0 [$H_3C(CO)\mathit{C}H(CO)CH_3$], and around δ 26.2 [$H_3\mathit{C}(CO)CH(CO)\mathit{C}H_3$] appear in the spectrum. Either acetylacetone-keto, or acetone from alcoholysis[196,209] peaks are visible at δ 208.9 [$H_3C(\mathit{C}O)CH_2(\mathit{C}O)CH_3$] or [$H_3C(\mathit{C}O)CH_3$], and δ 30.5 [$H_3\mathit{C}(CO)CH_2(CO)\mathit{C}H_3$] or [$H_3\mathit{C}(CO)\mathit{C}H_3$]. The peak at δ 171.7 [$HOCH_2CH_2CH_2O(\mathit{C}O)CH_3$], not associated with any of the reagents, is located in the range typically found for ester carbonyl carbons[208] and would support the idea that 1,3-propanediol has been acetylated to create 3-hydroxypropyl acetate. This is supported by literature[212] and by the HMBC spectrum in Figure 3.28, which shows cross-peaks at ^{1}H δ 2.15 – ^{13}C δ 171.7 and ^{1}H δ 4.23 – ^{13}C δ 171.7. HMBC also shows no visible cross-peak at ^{1}H δ 4.67 – ^{13}C δ 171.7, possibly indicating that the compound with the ^{1}H δ 4.67 peak does not contain an acetylated alcohol.

3.5.3 Discussion

The NMR spectra in this experiment indicate that in the absence of ethanol, alcoholysis byproducts such as acetone and 3-hydroxypropyl acetate can be created with added acetylacetone under heat. Furthermore, the yellow color of the resulting solution in Figure 3.19 may be enhanced by light scattering from nanoparticle formation after alcoholysis.[205–207] However, confirmation from dynamic light scattering experiments would be needed to determine the presence of nanoparticles. Considering these factors, heating a β-diketone in the presence of 1,3-propanediol and a tantalum cation should be avoided when increased yield of photosensitive β-diketonate complexes is desired, as was reported for Zr(IV) and Ti(IV) acetylacetonate complexes.[196]

09:58 on 21.03.2019: Start under argon, finger towards distillation flask (right).

10:17 on 21.03.2019: 130°C reached.

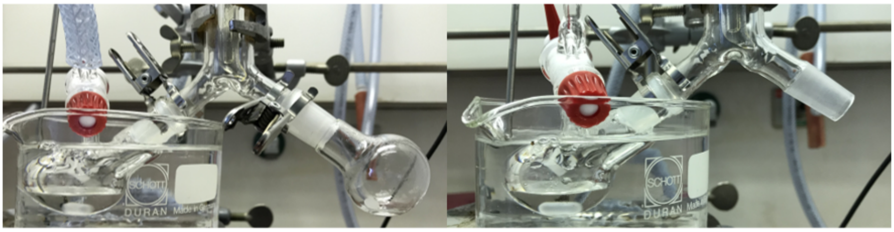

09:35 on 22.03.2019: 1 day checkpoint.

10:05 on 22.03.2019: exposed to atmosphere, distillate removed.

14:59 on 22.03.2019: acetylacetone added and returned to argon.

15:10 on 22.03.2019: 80°C reached, finger towards reactor (right).

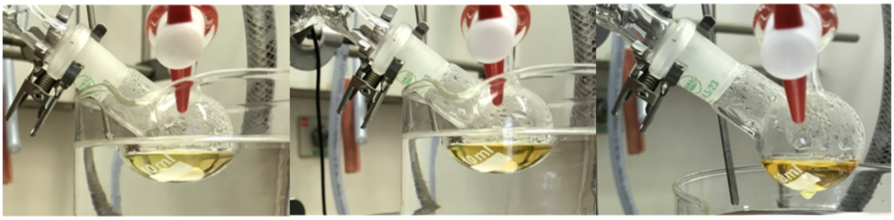

15:11 on 23.03.2019: 2 days checkpoint.

15:12 on 24.03.2019: 3 days checkpoint.

15:05 on 25.03.2019: 4 days end.

Figure 3.19 Photographic record of Experiment 3 (© The Royal Society of Chemistry 2020).[136,137]

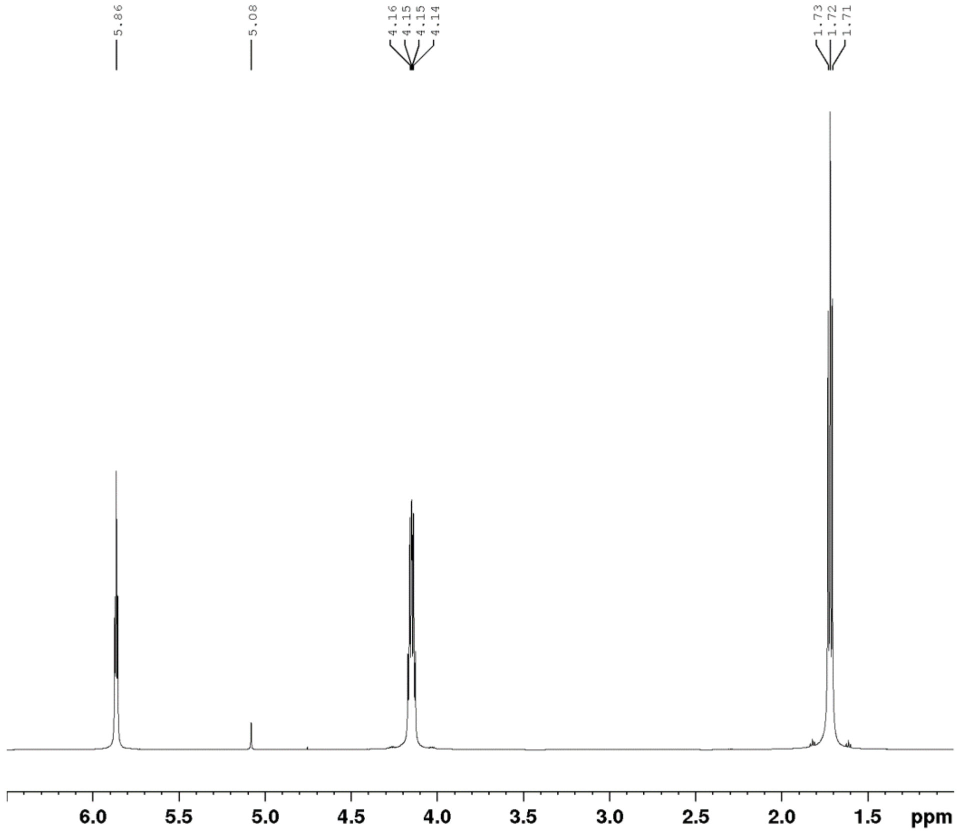

Figure 3.20 ^{1}H NMR [External D_2O]: Experiment 3 – Distillate (© The Royal Society of Chemistry 2020).[136,137]

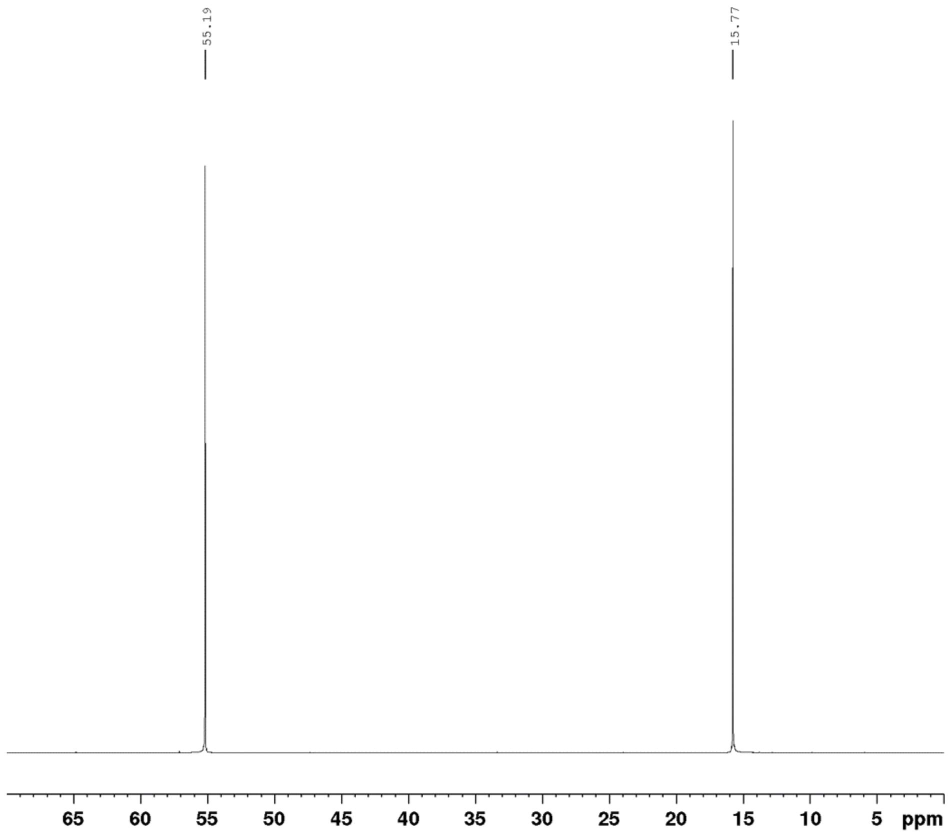

Figure 3.21 ^{13}C NMR [External D_2O]: Experiment 3 – Distillate (© The Royal Society of Chemistry 2020).[136,137]

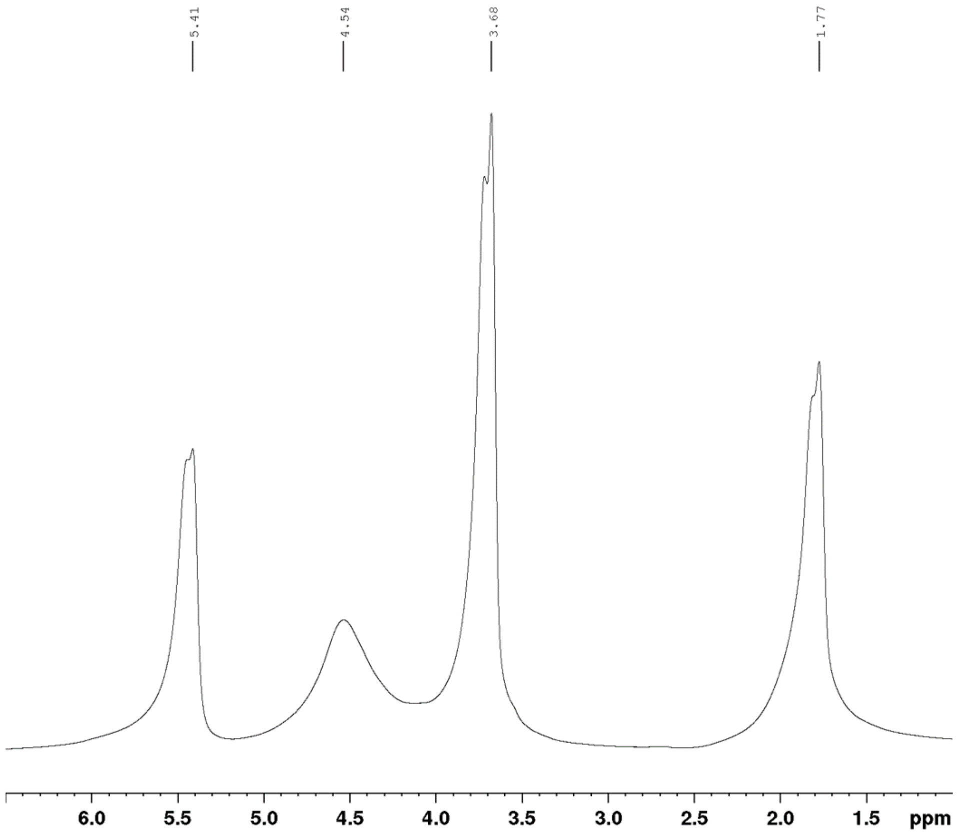

Figure 3.22 ^{1}H NMR [External D_2O]: Experiment 3 – Tantalum(V) 1,3-propanediolate (© The Royal Society of Chemistry 2020).[136,137]

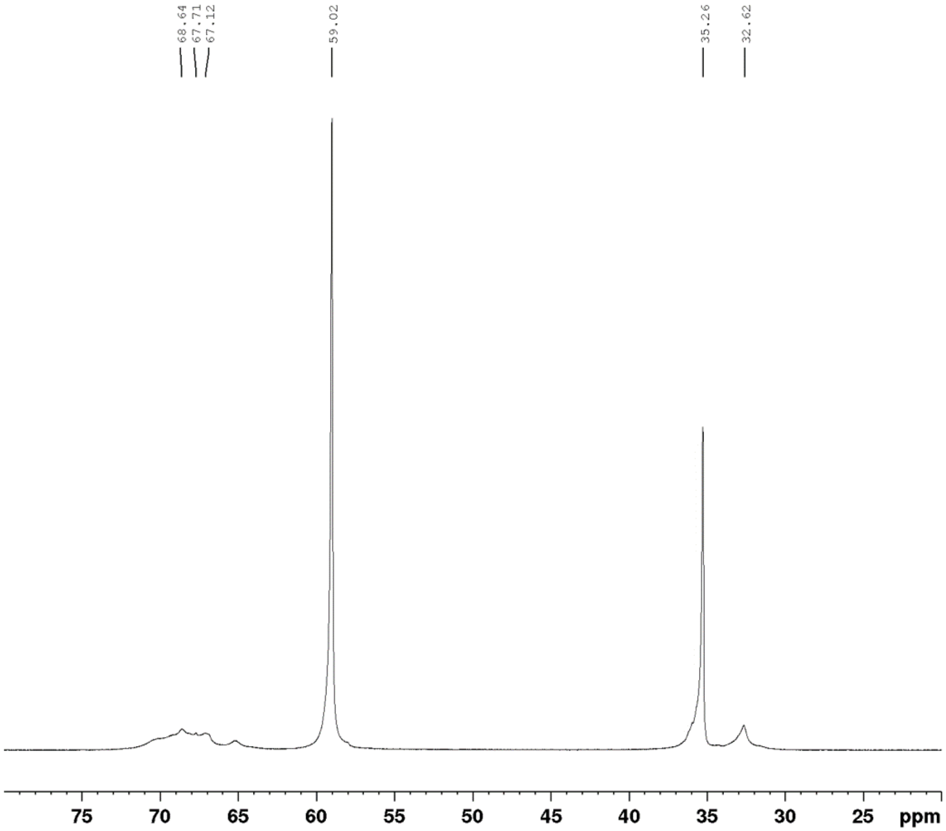

Figure 3.23 ^{13}C NMR [External D_2O]: Experiment 3 – Tantalum(V) 1,3-propanediolate (© The Royal Society of Chemistry 2020).[136,137]

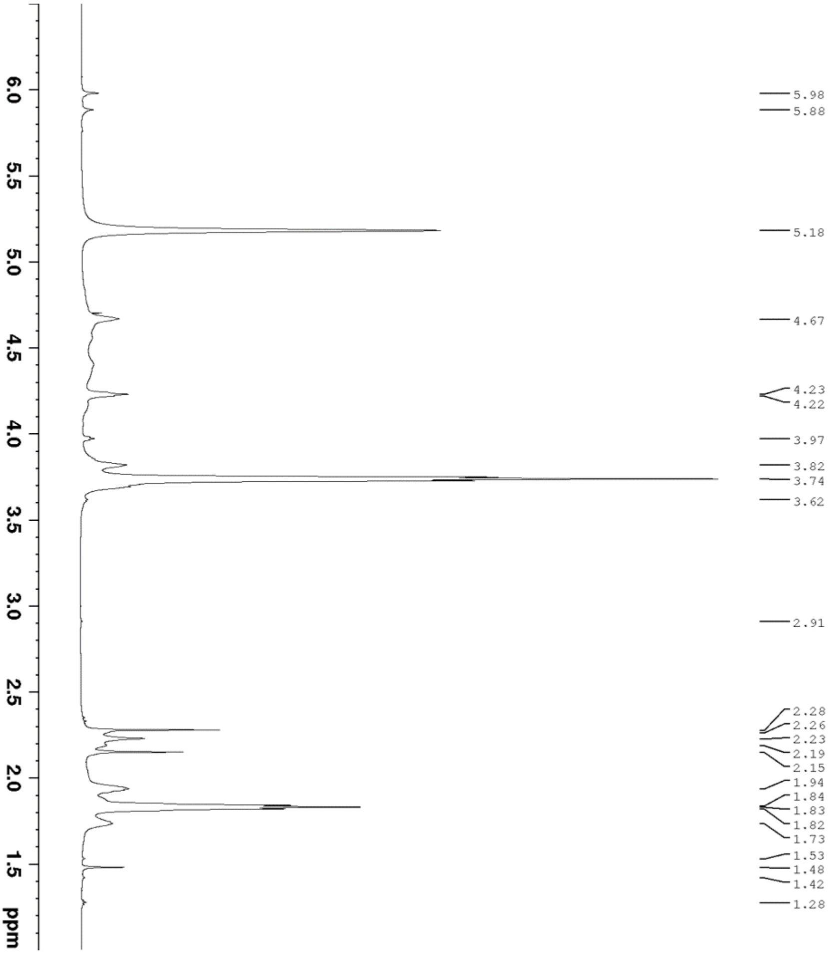

Figure 3.24 ^{1}H NMR [External D_2O]: Experiment 3 – Product (© The Royal Society of Chemistry 2020).[136,137]

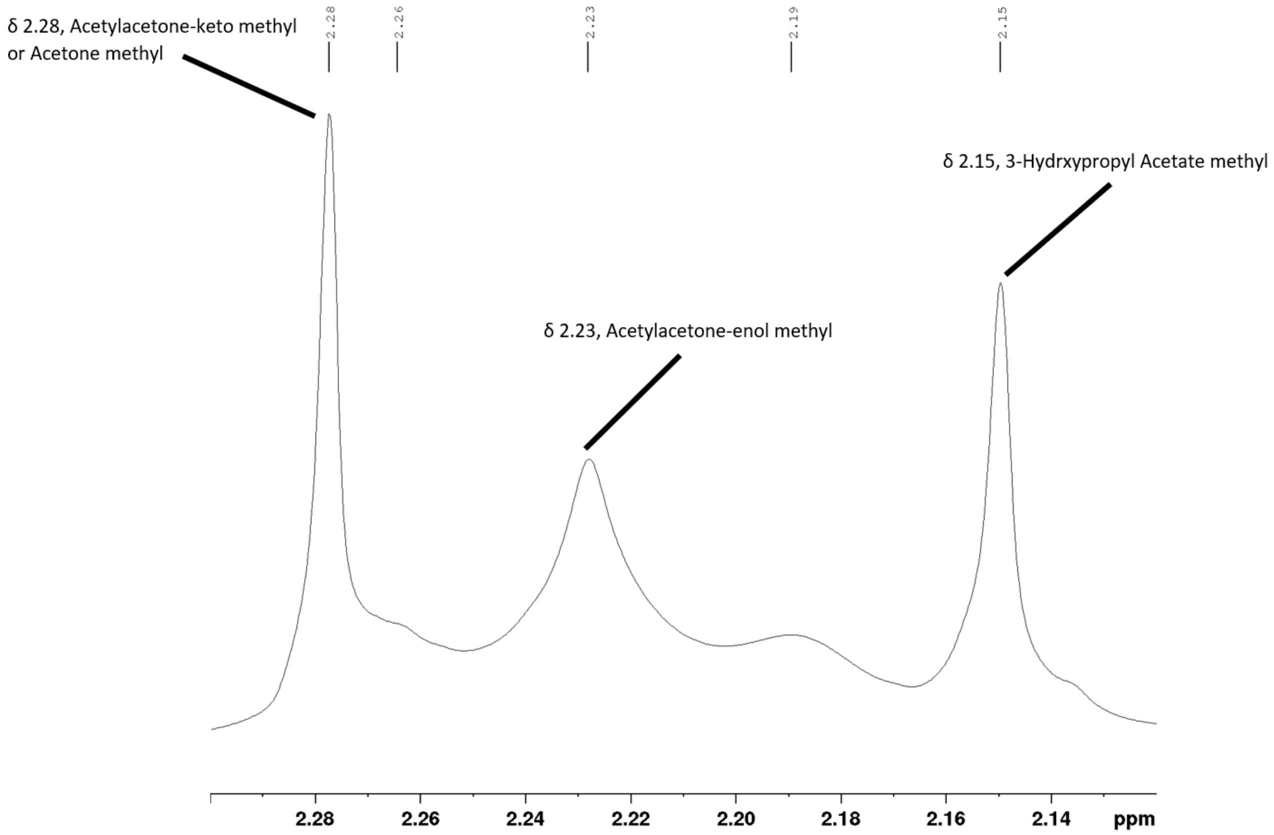

Figure 3.25 ^{1}H NMR [External D_2O]: Experiment 3 - Product (© The Royal Society of Chemistry 2020).[136,137]

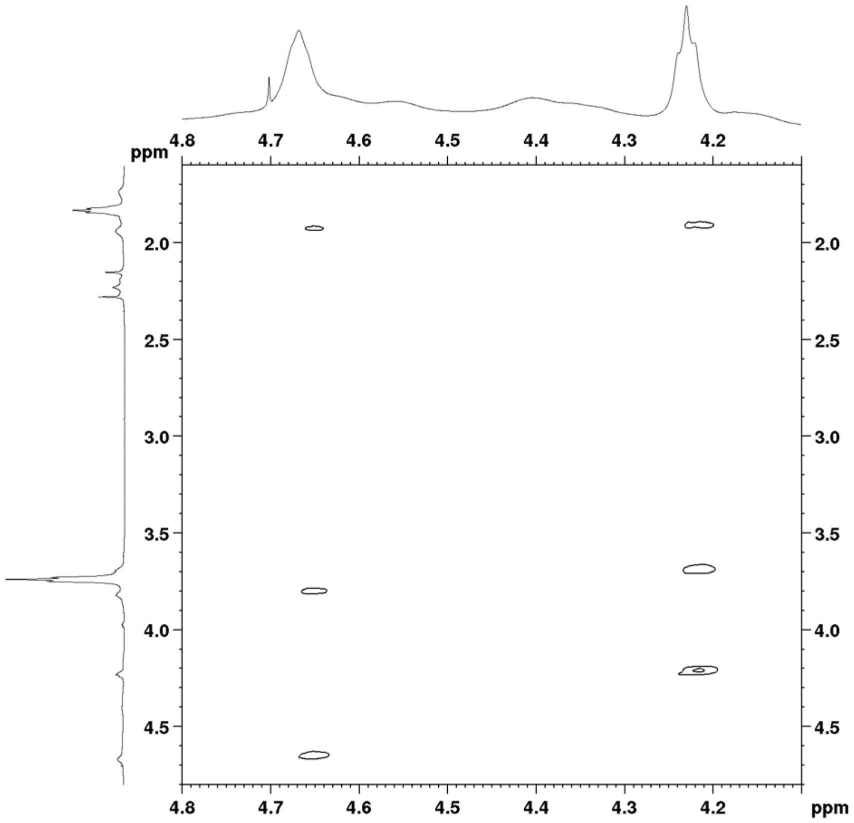

Figure 3.26 TOCSY [External D_2O]: Experiment 3 - Product (© The Royal Society of Chemistry 2020).[136,137]

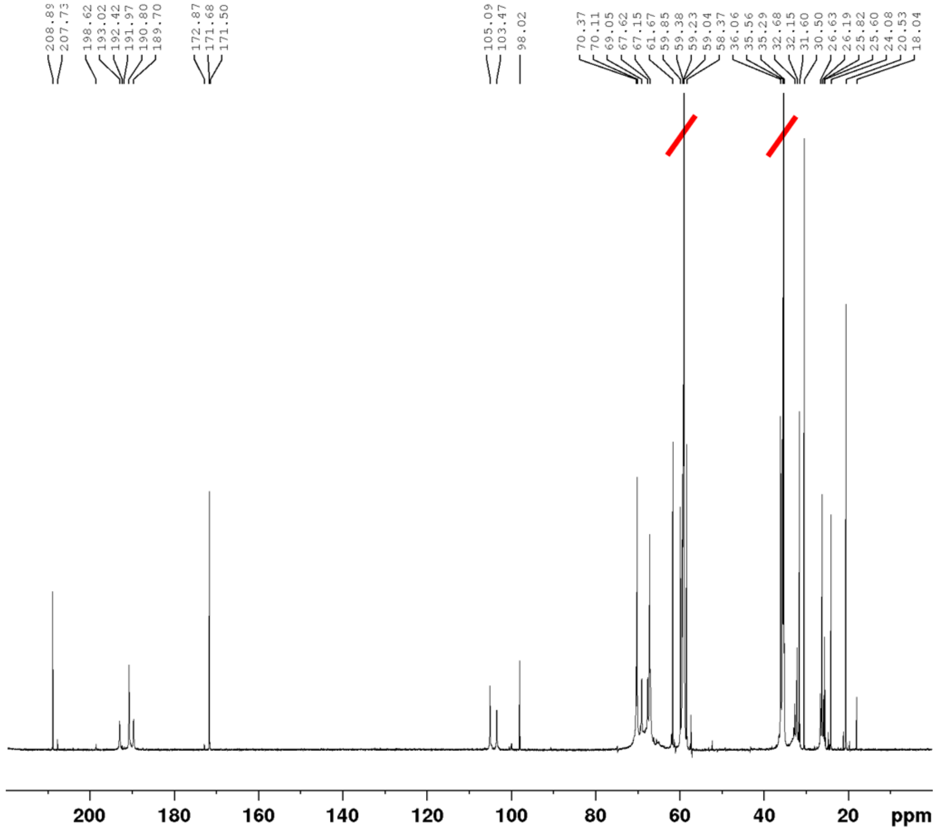

Figure 3.27 ^{13}C NMR [External D_2O]: Experiment 3 - Product (© The Royal Society of Chemistry 2020).[136,137]

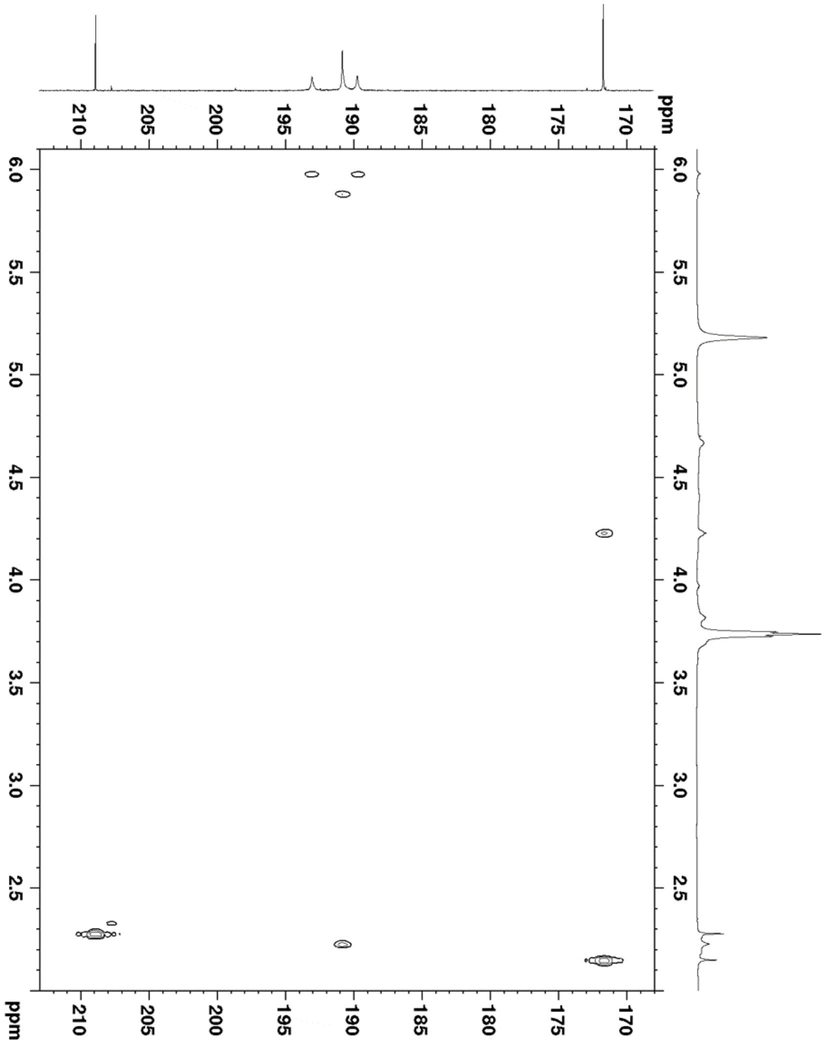

Figure 3.28 HMBC [External D_2O]: Experiment 3 - Product (© The Royal Society of Chemistry 2020).[136,137]

3.6 Experiment 4 - Proposed Method with Acetylacetone

In order to minimize alcoholysis of the tantalum(V) β-diketonate complex, this experiment will explore whether a reduction in both temperature and pressure can lead to ethanol removal and reduced alcoholysis. This entails first synthesizing (or obtaining) a tantalum(V) ethoxide β-diketonate complex, where in the case of using acetylacetone as the β-diketone in a 1:1 molar ratio with tantalum(V) ethoxide for synthesis, the reaction would proceed as shown under reflux at an elevated temperature:

$$\mathrm{Ta(OC_2H_5)_5 + C_5H_8O_2 \longrightarrow TaC_5H_7O_2(OC_2H_5)_4 + C_2H_5OH} \tag{3.11}$$

Following synthesis, 1,3-propanediol would then be added after cooling the solution to room temperature. Once mixing of the complex with 1,3-propanediol at this reduced temperature is complete, reduction of the closed system pressure would then lead to ethanol removal:

$$\mathrm{TaC_5H_7O_2(OC_2H_5)_4 + 4\,HOC_3H_6OH \longrightarrow TaC_5H_7O_2(OC_3H_6OH)_4 + 4\,C_2H_5OH} \tag{3.12}$$

More specifically, ideal selection of the distillation temperature and pressure would ensure that alcoholysis of the tantalum(V) β-diketonate complex is reduced and that the vapor pressure of ethanol is higher than the closed system pressure, while the vapor pressure of 1,3-propanediol and the tantalum(v) 1,3-propanediolate β-diketonate complex is lower than the closed system pressure. Following ethanol extraction, the tantalum(v) 1,3-propanediolate β-diketonate solution would be isolated in a liquid form at room temperature.

For example in Figure 3.29, at 23°C the vapor pressure of ethanol is 70 mbar,[213,214] while the vapor pressure of 1,3-propanediol is 0.1 mbar[215,216] (1,3-propanediol data are extrapolated beyond the experimental data range via the literature Antoine parameters). By heating mildly to 40°C, the vapor pressure of ethanol increases to 180 mbar[213,214] and that of 1,3-propanediol to 0.4 mbar[215,216] (the latter still being a theoretical extrapolation). Thus, at 40°C the system pressure should be set above 0.4 mbar and below 180 mbar for ethanol extraction, whereby the tantalum(V) 1,3-propanediolate β-diketonate solution would remain in the flask.

Anhydrous ethanol was selected as the reflux solvent for synthesis of the tantalum(V) ethoxide β-diketonate precursor, since lighter monoalcohols are less likely to undergo alcoholysis than heavier diols in the presence of a metal cation and a β-diketone (where Experiment 3 shows alcoholysis is possible in the absence of ethanol).[196] Thus, higher temperatures with heavier diols should be avoided, in addition to long reflux times with lighter monoalcohols where 8 hours should be sufficient.[150,168,217] Reflux solvents such as benzene[150,168] or tetrahydrofuran[217] could be used, but the former is carcinogenic and the latter may present an explosion hazard after drying on glassware.

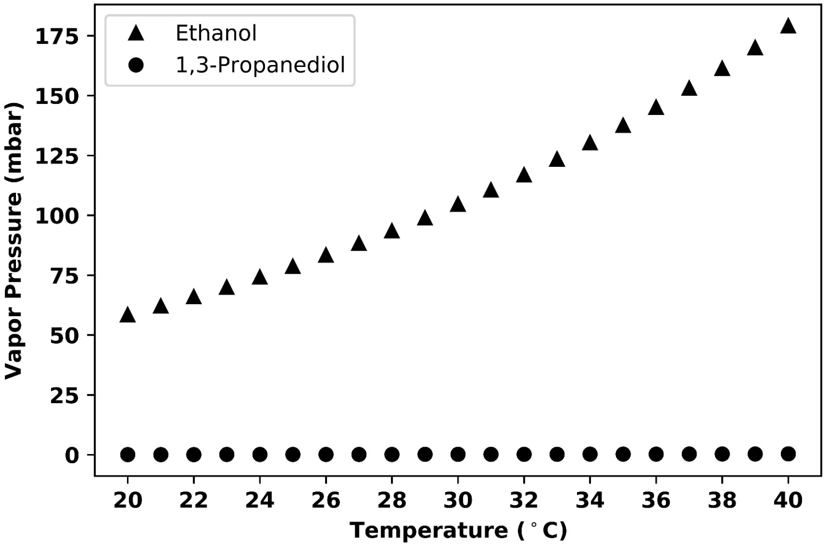

Figure 3.29 Temperature vs. vapor pressure as per the National Institute of Standards and Technology, U.S. Department of Commerce (© The Royal Society of Chemistry 2020).

3.6.1 Synthesis

Anhydrous ethanol (42.33 mmol, 1950 mg [AcrosOrganics, 99.5%, ExtraDry, absolute]), acetylacetone (6.15 mmol, 616 mg [Alfa Aesar, 95%]) and tantalum(V) ethoxide (6.15 mmol, 2499 mg [Alfa Aesar, 99+%]) were mixed in a dried Schlenk flask under argon in a glovebox, after which the Schlenk flask with a magnetic stirring rod was removed from the glovebox and connected to a Schlenk line. The flask was dipped in silicone oil, with the oil temperature being maintained at 80°C over 8 hours in order to promote chelation of acetylacetone to the tantalum cation. The reaction was kept under argon with continuous stirring and a vertical condenser (cold finger), whereby the condenser keeps the acetylacetone in solution.

Following the 8 hour mixing, the silicone oil was cooled to 23°C over a 2 hour period. 1,3-propanediol (42.04 mmol, 3199 mg [Sigma-Aldrich, for synthesis]) was then added to the flask via syringe through the Schlenk valve, and the flask was then returned to argon. After addition, small bubbles appeared which went away over time. The mixing continued for 12 hours, after which the solution was colorless and precipitate free.

As the Schlenk line setup was suboptimal for vacuum distillation, the solution in the Schlenk flask was removed from the Schlenk line, transferred from the Schlenk flask to a round-bottom flask, and the round-bottom flask was connected to a rotary evaporator for ethanol removal from the solution. Once connected, the rotation speed was set to 95 rpm, the system pressure to 30 mbar, and the water bath temperature to 40°C (where the flask would remain submerged). Ethanol removal proceeded for 8 hours, and afterward the measured mass loss of 3236 mg was close to the calculated ethanol loss of 3367 mg.

The entire procedure is displayed in Figure 3.30. NMR of the sample was performed roughly a month later, in order to give a better idea of solution stability. Unfortunately, not enough distillate could be collected for NMR.

3.6.2 NMR Measurements

The ^{1}H NMR spectrum of the product (δ [ppm], Figures 3.31 and 3.32) shows the presence of the expected 1,3-propanediol peaks at δ 1.81 [$HOCH_2CH_2CH_2OH$], δ 3.72 [$HOCH_2CH_2CH_2$-OH], and δ 5.21 [$HOCH_2CH_2CH_2OH$]. Three separate methine acetylacetone-enol peaks appear at δ 5.96, δ 5.87, and δ 5.74 [$H_3C(CO)CH(CO)CH_3$]. The peaks from δ 2.30 to δ 2.14 overlap significantly (with δ 2.21 being the most prominent peak, see Figure 3.32), making the following methyl peak assignments tentative: acetylacetone-keto [$H_3C(CO)CH_2(CO)CH_3$] or acetone [$H_3C(CO)CH_3$] methyl peaks (the latter from alcoholysis)[196,211] occur at δ 2.30 and δ 2.26, and the acetylacetone-enol [$H_3C(CO)CH(CO)CH_3$] methyl peaks around δ 2.21 and δ 2.14. The multiple peaks for the same proton on the acetylacetone-enol tautomer may be due to the different ways in which acetylacetone can bind to the metal cation,[207] or due to possible peak shifts when more than one acetylacetone molecule chelates to the metal cation.

Further downfield, as the δ 4.21 peak resonates at a higher frequency than the alcoholic methylene 1,3-propanediol peak at δ 3.72, in addition to the presence of another overlapping methyl peak at δ 2.14, this likely indicates the acetylation of 1,3-propanediol and the creation of 3-hydroxypropyl acetate,[208] despite the extra steps taken to avoid alcoholysis of the complex. One of the overlapping peaks at δ 2.14 would then correspond to the methyl attached to the ester carbonyl [$HOCH_2CH_2CH_2O(CO)CH_3$], and the peak at δ 4.21 would be the protons on the methylene carbon bound to the ester oxygen [$HOCH_2CH_2CH_2O(CO)CH_3$]. Additionally, the TOCSY spectrum in Figure 3.33 shows three distinct proton groups on three consecutive carbon atoms, and the ^{13}C NMR and HMBC spectra corroborate these findings (discussed below), as well as the literature values for 3-hydroxypropyl acetate.[212] It is not clear whether the δ 4.21 peak occurs as a triplet, and the peak at δ 4.65 is difficult to assign with the available data.

The ^{13}C NMR spectrum of the product (δ [ppm], Figure 3.34) shows the expected

1,3-propanediol peaks at δ 35.2 [$HOCH_2\mathit{C}H_2CH_2OH$] and δ 59.0 [$HO\mathit{C}H_2CH_2\mathit{C}H_2OH$]. Acetylacetone-enol peaks around δ 192.0 [$H_3C(\mathit{C}O)CH(\mathit{C}O)CH_3$], around δ 102.0 [$H_3C(CO)\mathit{C}H(CO)CH_3$], and around δ 26.2 [$H_3\mathit{C}(CO)CH(CO)\mathit{C}H_3$] appear in the spectrum, along with some acetylacetone-keto [$H_3C(\mathit{C}O)CH_2(\mathit{C}O)CH_3$] or acetone[196,209] [$H_3C(\mathit{C}O)CH_3$] peaks at δ 209.2 and δ 204.3, and around δ 31.6 [$H_3\mathit{C}(CO)CH_2(CO)\mathit{C}H_3$] or [$H_3\mathit{C}(CO)\mathit{C}H_3$]; there is possibly an acetylacetone-keto peak around δ 59.0 [$H_3C(CO)\mathit{C}H_2(CO)CH_3$], which is difficult to assign due to the presence of 1,3-propanediol. The peak at δ 171.8 [$HOCH_2CH_2CH_2O(\mathit{C}O)CH_3$], not associated with any of the reagents, is located in the range typically found for ester carbonyl carbons and would support the idea that 1,3-propanediol has been acetylated and that 3-hydroxypropyl acetate has been formed.[208] This is supported by literature[212] and the HMBC spectrum in Figure 3.35, which shows cross-peaks at ^{1}H δ 2.14 – ^{13}C δ 171.8 and ^{1}H δ 4.21 – ^{13}C δ 171.8. HMBC also shows no visible cross-peak at ^{1}H δ 4.65 – ^{13}C δ 171.8, possibly indicating that the compound with the ^{1}H δ 4.65 peak does not contain an acetylated alcohol.

3.6.3 Discussion

As the acetylacetone-enol methyl peaks appear more prominently than the acetylacetone-keto and 3-hydroxypropyl acetate methyl peaks, particularly with respect to Experiment 3, the method appears to reduce alcoholysis. Furthermore, the resulting solution remains stable for at least a month. Therefore, this method will also be tested with benzoylacetone in the next experiment. Interestingly, the resulting solution is much more transparent than the Experiment 1 product, and less yellow than the Experiment 3 product.

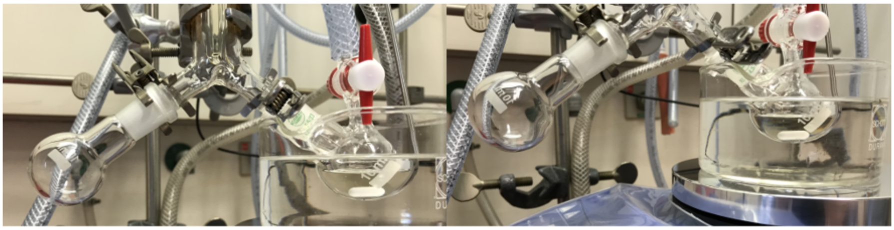

09:37 on 07.05.2019: Start under argon, finger towards reactor (right).

09:51 on 07.05.2019: 80°C reached.

17:53 on 07.05.2019: Begin cooling to room temperature (leave in silicone oil).

19:53 on 07.05.2019: 1,3-Propanediol added via syringe and Schlenk valve.

08:38 on 08.05.2019: Mixing at room temperature ended.

08:52 – Begin 30 mbar at 40°C (rotary evaporator).

13:15 – Checkpoint 30 mbar at 40°C.

16:53 – End, return to atmosphere.

Figure 3.30 Photographic record of Experiment 4, where the extra flask in the Schlenk line (left) was not used and is to keep the system closed (© The Royal Society of Chemistry 2020).[136,137]

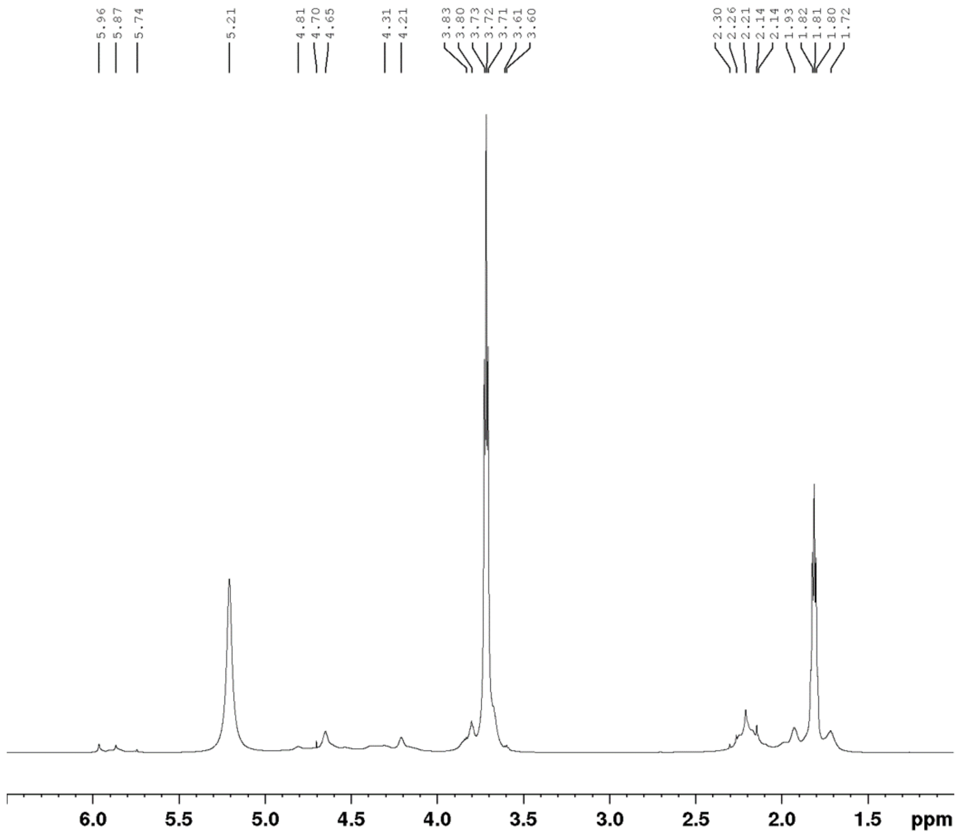

Figure 3.31 ^{1}H NMR [External D_2O]: Experiment 4 – Product (© The Royal Society of Chemistry 2020).[136,137]

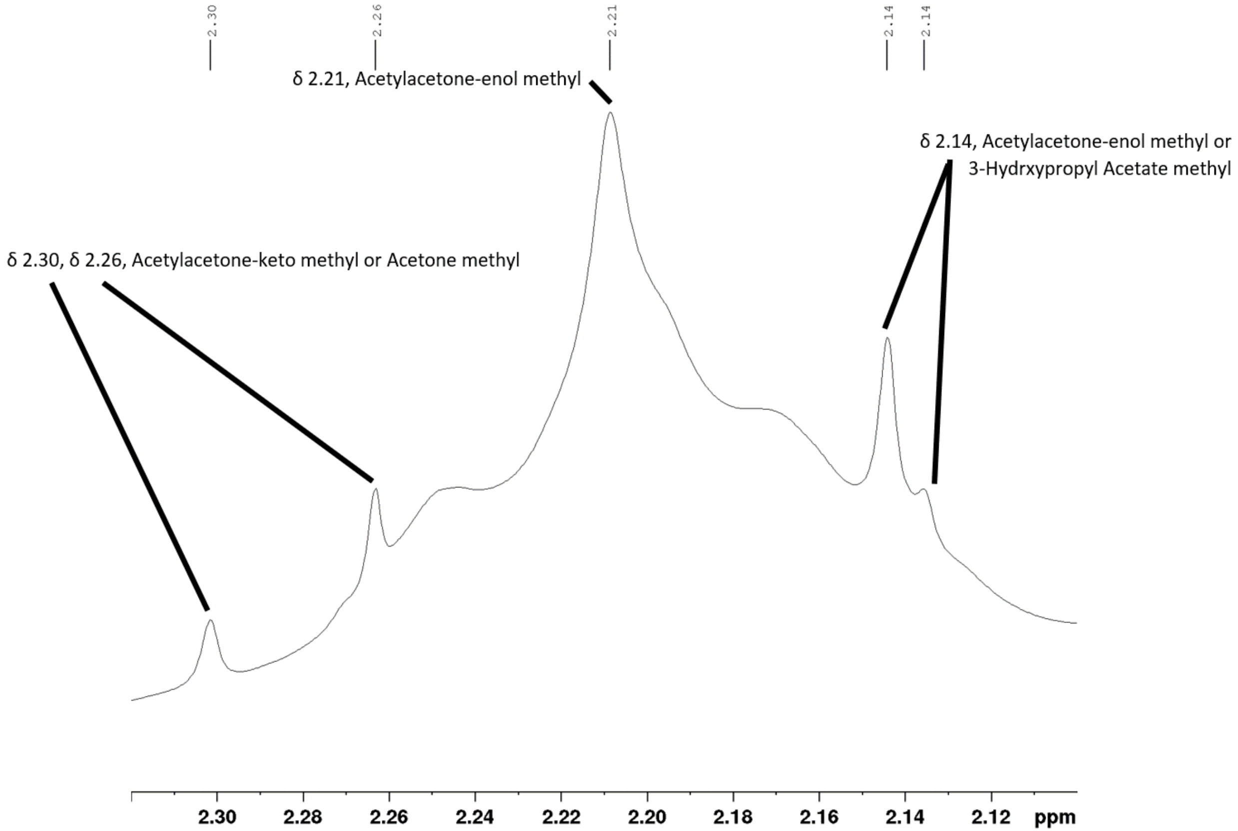

Figure 3.32 ^{1}H NMR [External D_2O]: Experiment 4 – Product (© The Royal Society of Chemistry 2020).[136,137]

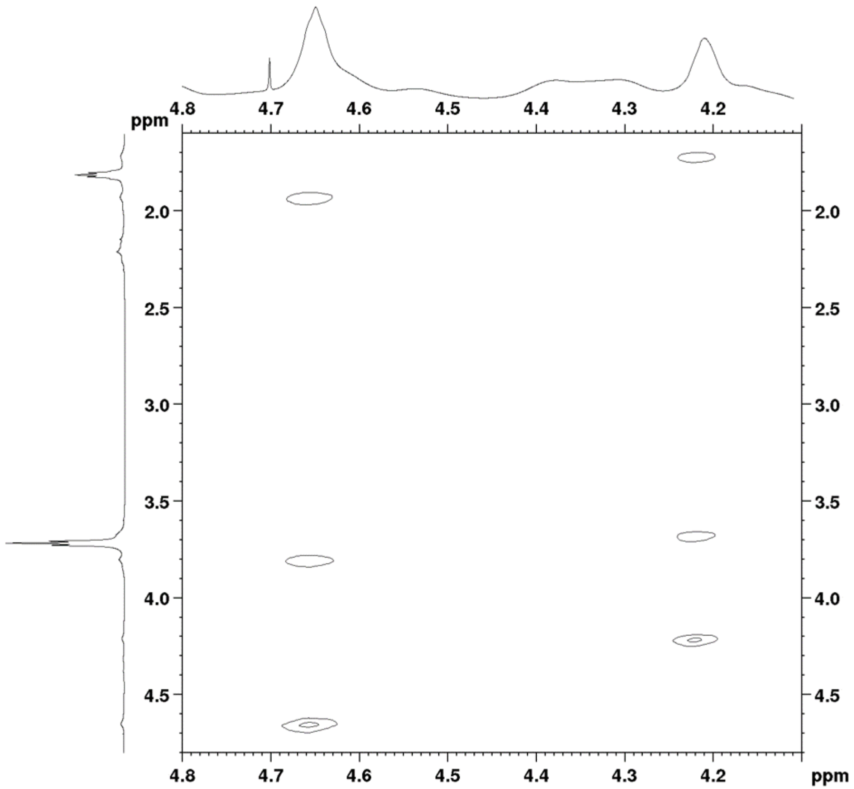

Figure 3.33 TOCSY [External D_2O]: Experiment 4 – Product (© The Royal Society of Chemistry 2020).[136,137]

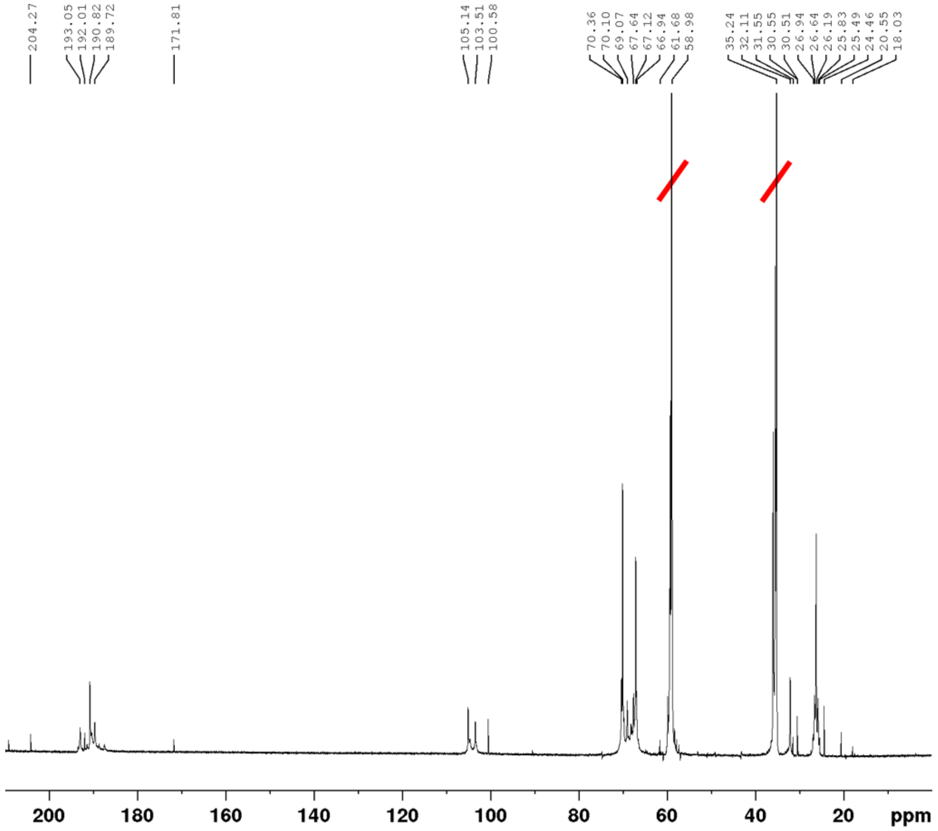

Figure 3.34 ^{13}C NMR [External D_2O]: Experiment 4 – Product (© The Royal Society of Chemistry 2020).[136,137]

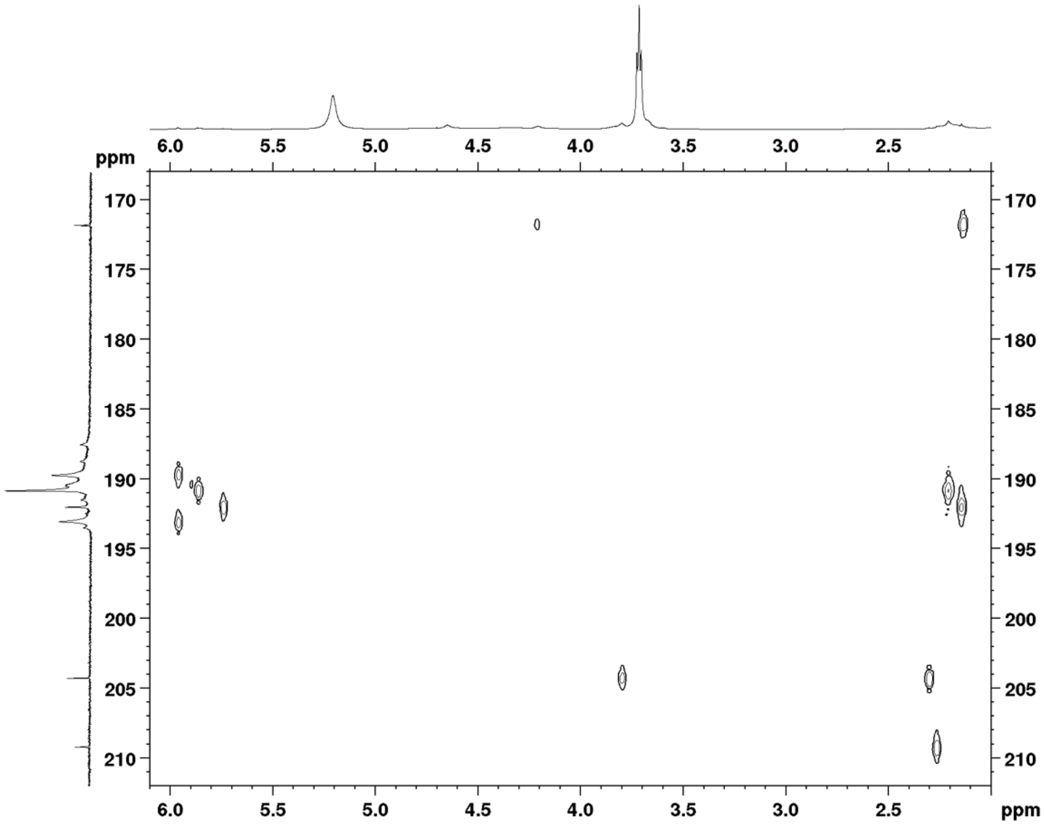

Figure 3.35 HMBC [External D_2O]: Experiment 4 – Product (© The Royal Society of Chemistry 2020).[136,137]

3.7 Experiment 5 - Proposed Method with Benzoylacetone

As the proposed method appeared successful with acetylacetone, the procedure will be attempted here with benzoylacetone, where in the case of using benzoylacetone as the β-diketone in a 1:1 molar ratio with tantalum(V) ethoxide for synthesis, the reaction would proceed as shown under reflux at an elevated temperature:

$$\mathrm{Ta(OC_2H_5)_5 + C_{10}H_{10}O_2 \longrightarrow TaC_{10}H_9O_2(OC_2H_5)_4 + C_2H_5OH} \tag{3.13}$$

Following synthesis, 1,3-propanediol would then be added after cooling the solution to room temperature. Once mixing of the complex with 1,3-propanediol at this reduced temperature is complete, reduction of the closed system pressure would then lead to ethanol removal:

$$\mathrm{TaC_{10}H_9O_2(OC_2H_5)_4 + 4\,HOC_3H_6OH \longrightarrow TaC_{10}H_9O_2(OC_3H_6OH)_4 + 4\,C_2H_5OH} \tag{3.14}$$

3.7.1 Synthesis

The synthesis steps from Experiment 4 will be repeated here for clarity. Anhydrous ethanol (54.24 mmol, 2499 mg [AcrosOrganics, 99.5%, ExtraDry, absolute]), benzoylacetone (5.99 mmol, 972 mg [Sigma Aldrich, 99%]) and tantalum(V) ethoxide (6.12 mmol, 2486 mg [Alfa Aesar, 99+%]) were mixed in a dried Schlenk flask under argon in a glovebox, after which the Schlenk flask with a magnetic stirring rod was removed from the glovebox and connected to a Schlenk line. The flask was dipped in silicone oil, with the oil temperature being maintained at 80°C over 8 hours in order to promote chelation of benzoylacetone to the tantalum cation. The reaction was kept under argon with continuous stirring and a vertical condenser (cold finger), whereby the condenser keeps the benzoylacetone in solution.

Following the 8 hour mixing, the silicone oil was cooled to 23°C over a 2 hour period. 1,3-propanediol (42.16 mmol, 3208 mg [Sigma-Aldrich, for synthesis]) was then added to the flask via syringe through the Schlenk valve, and the flask was then returned to argon. After addition, small bubbles appeared which went away over time. The mixing continued for 12 hours, after which the solution had a slight yellow hue and was precipitate free.

As the Schlenk line setup was suboptimal for vacuum distillation, the solution in the Schlenk flask was removed from the Schlenk line, transferred from the Schlenk flask to a round-bottom flask, and the round-bottom flask was connected to a rotary evaporator for ethanol removal from the solution. Once connected, the rotation speed was set to 95 rpm, the system pressure to 30 mbar, and the water bath temperature to 40°C (where the flask would remain submerged). Ethanol removal proceeded for 8 hours, and afterward the measured mass loss of 3681 mg was close to the calculated ethanol loss of 3909 mg.

The entire procedure is displayed in Figure 3.36. NMR of the sample was performed roughly a month later, in order to give a better idea of solution stability. Unfortunately, not enough distillate could be collected for NMR.

3.7.2 NMR Measurements

The ^{1}H NMR spectrum of the product (δ [ppm], Figures 3.37 and 3.38) shows the presence of the expected 1,3-propanediol peaks at δ 1.68 [$HOCH_2C\mathit{H}_2CH_2OH$], δ 3.59 [$HOC\mathit{H}_2CH_2C\mathit{H}_2$-OH], and δ 5.11 [$\mathit{H}OCH_2CH_2CH_2O\mathit{H}$]. Three separate methine benzoylacetone-enol peaks appear at δ 6.53, δ 6.44, and δ 6.24 (Ph = phenyl group) [$Ph(CO)C\mathit{H}(CO)CH_3$]. The peaks from δ 2.50 to δ 2.00 overlap significantly (with δ 2.22 being the most prominent peak), with the following tentative assignments: δ 2.46 for the benzoylacetone-keto methyl [$Ph(CO)CH_2(CO)C\mathit{H}_3$] and around δ 2.22 for the enol methyl [$Ph(CO)CH(CO)C\mathit{H}_3$]. Peaks in the δ 8.00 to δ 7.30 range belong to the phenyl group protons on benzoylacetone [$\mathit{Ph}(CO)C$ -$H(CO)CH_3$]. Many unassigned peaks are present, possibly associated with different alcoholysis products. As for acetylacetone, benzoylacetone may be bound to the metal cation in different ways,[207] resulting in multiple peaks for the same proton; alternatively, this may be due to possible peak shifts when more than one benzoylacetone molecule chelates to the metal cation.

The ^{13}C NMR spectrum of the product (δ [ppm], Figure 3.39) shows the expected 1,3-propanediol peaks at δ 35.1 [$HOCH_2\mathit{C}H_2CH_2OH$] and δ 58.9 [$HO\mathit{C}H_2CH_2\mathit{C}H_2OH$]. Benzoylacetone-enol peaks around δ 193.0 [$Ph(CO)CH(\mathit{C}O)CH_3$], around δ 182.0 [$Ph(\mathit{C}O)CH(CO)CH_3$], around δ 100.0 [$Ph(CO)\mathit{C}H(CO)CH_3$], peak(s) within the range δ 28.0 to δ 25.0 [$Ph(CO)CH(CO)\mathit{C}H_3$] (difficult to assign exact peak), and the multiple phenyl ring carbon peaks (likely mixed in with those of the keto tautomer) in the range δ 140.0 to δ 125.0 [$\mathit{Ph}(CO)CH(CO)CH_3$] appear in the spectrum, along with some benzoylacetone-keto peaks at δ 199.2 [$Ph(CO)CH_2(\mathit{C}O)CH_3$], a carbonyl peak likely overshadowed by enol peaks in the range δ 195.0 to δ 190.0 [$Ph(\mathit{C}O)CH_2(CO)CH_3$], around δ 59.0 [$Ph(CO)\mathit{C}H_2(CO)CH_3$] (difficult to assign exact peak), and peak(s) within the range δ 33.0 to δ 30.0 [$Ph(CO)CH_2(CO)\mathit{C}H_3$] (difficult to assign exact peak). The peak at δ 171.7, not associated with any of the reagents, is located in the range typically found for ester carbonyl carbons and would support the idea that acetylation of an alcohol group has occurred.[208]

3.7.3 Discussion

As the benzoylacetone-enol methyl peaks appear more prominently than the benzoylacetone-keto and possibly 3-hydroxypropyl acetate methyl peaks, the method appears to reduce alcoholysis. Furthermore, the resulting solution remains stable for at least a month. Like the Experiment 4 product relative to Experiment 1, the resulting solution here with benzoylacetone is much more transparent than the Experiment 2 product.

10:09 on 08.05.2019: Start under argon, finger towards reactor (right).

10:30 on 08.05.2019: 80°C reached.

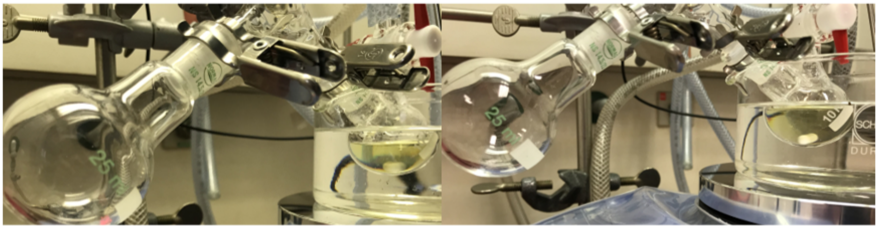

18:31 on 08.05.2019: Begin cooling to room temperature (leave in silicone oil).

20:31 on 08.05.2019: 1,3-Propanediol added via syringe and Schlenk valve.

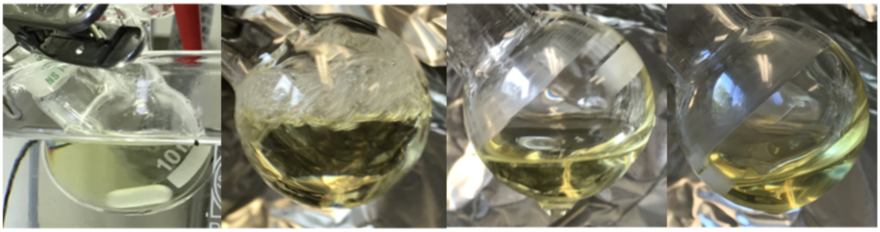

09:22 on 09.05.2019: Mixing at room temperature ended.

09:36 – Begin 30 mbar at 40°C (rotary evaporator).

12:04 – Checkpoint 30 mbar at 40°C.

17:37 – End, return to atmosphere.

Figure 3.36 Photographic record of Experiment 5, where the extra flask in the Schlenk line (left) was not used and is to keep the system closed (© The Royal Society of Chemistry 2020).[136,137].

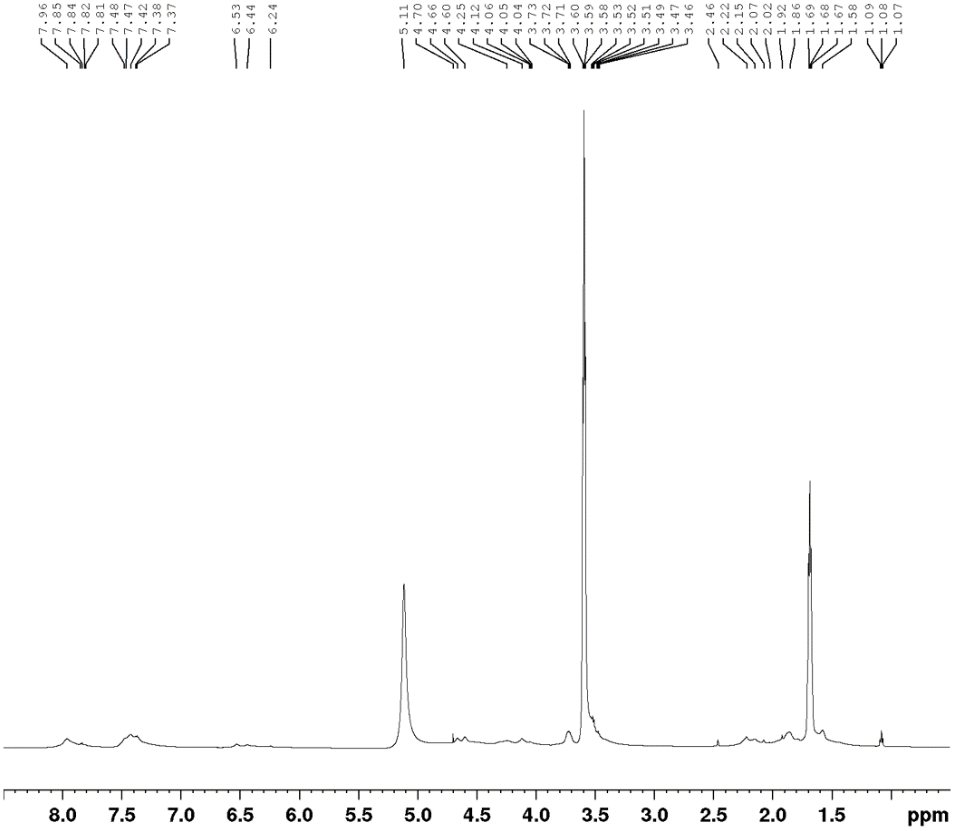

Figure 3.37 ^{1}H NMR [External D_2O]: Experiment 5 – Product (© The Royal Society of Chemistry 2020).[136,137]

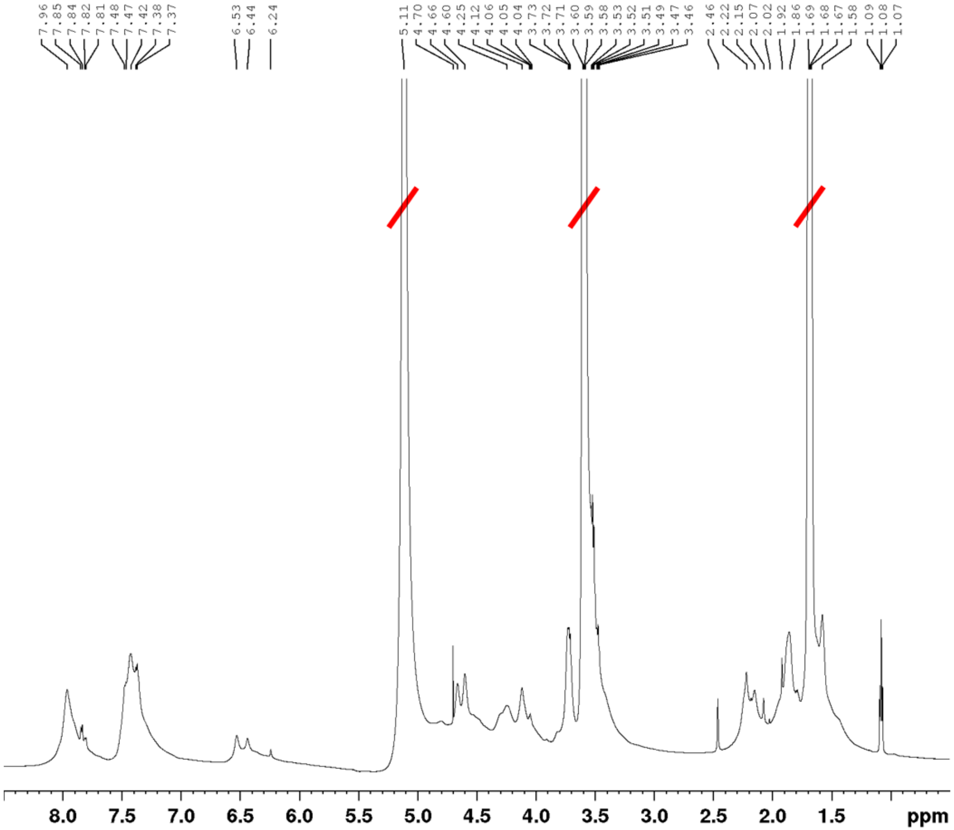

Figure 3.38 ^{1}H NMR [External D_2O]: Experiment 5 – Product (© The Royal Society of Chemistry 2020).[136,137]

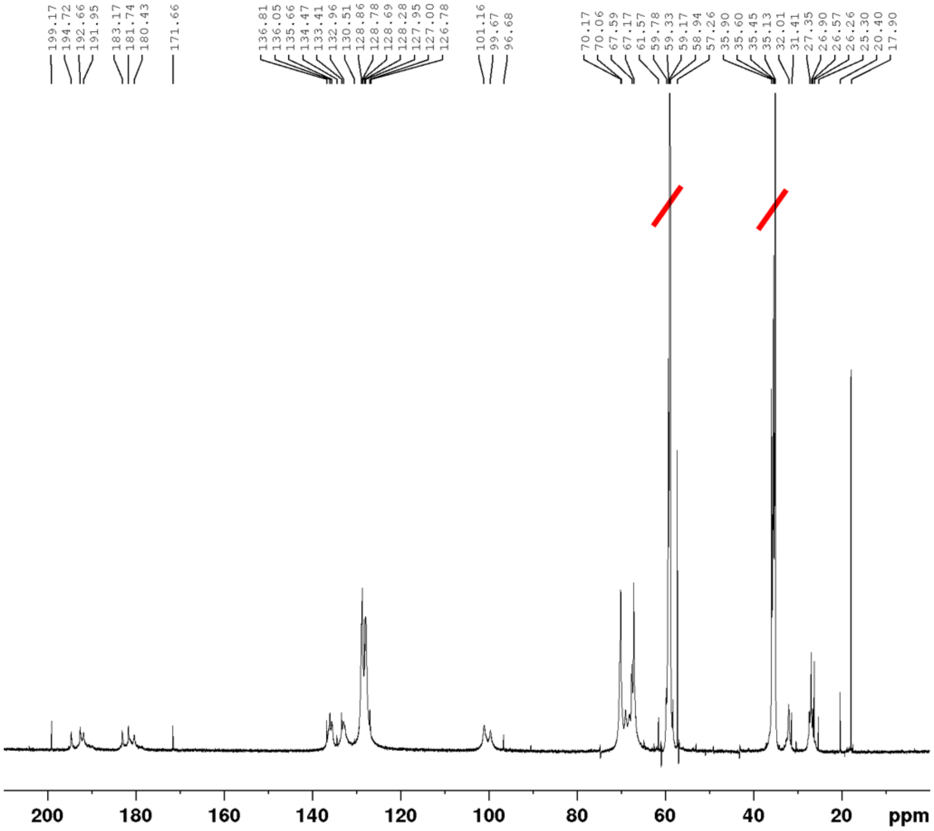

Figure 3.39 ^{13}C NMR [External D_2O]: Experiment 5 – Product (© The Royal Society of Chemistry 2020).[136,137]

3.8 Proposed Method - Discussion and Repeated Synthesis

Upon storing the solution products from Experiments 4 and 5 in atmosphere, visible precipitates do not form over the course of 2 months, and the solutions largely keep their color as shown in Figure 3.40 (the 10.05.2019 photo is from a few days after synthesis, and the 31.05.2019 photo is shortly before NMR measurements). Considering the solution stability and the NMR results, further repetition of this synthesis method is warranted in order to confirm its reproducibility.

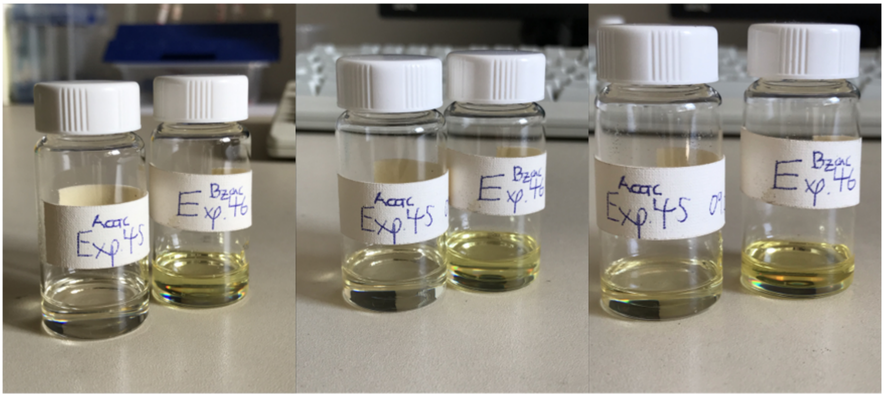

10.05.2019 31.05.2019 04.07.2019

Figure 3.40 Experiment 4 with acetylacetone (Acac, left) and Experiment 5 with benzoylacetone (Bzac, right) compared over time.

Therefore, the proposed method was repeated for methyl acetoacetate, ethyl acetoacetate, acetylacetone, benzoylacetone, and dibenzoylmethane (the first two being β-ketoesters, and the latter three β-diketones), with the reagent and distillate masses listed below:

- **Experiment 6** - Methyl acetoacetate (6.05 mmol, 702 mg [Sigma-Aldrich, ReagentPlus®, 99%]), anhydrous ethanol (42.02 mmol, 1936 mg [AcrosOrganics, 99.5%, ExtraDry, absolute]), tantalum(V) ethoxide (6.03 mmol, 2451 mg [Alfa Aesar, 99+%]), and 1,3-propanediol (42.24 mmol, 3214 mg [Sigma-Aldrich, for synthesis]) as the reagents, with a measured mass loss of 3405 mg upon distillation (calculated ethanol loss of 3325 mg, which is unexpectedly less than the measured loss).

- **Experiment 7** - Ethyl acetoacetate (6.17 mmol, 803 mg [Sigma-Aldrich, puriss. p.a., ≥99.0% (GC)]), anhydrous ethanol (42.04 mmol, 1937 mg [AcrosOrganics, 99.5%, ExtraDry, absolute]), tantalum(V) ethoxide (6.15 mmol, 2498 mg [Alfa Aesar, 99+%]), and 1,3-propanediol (43.11 mmol, 3280 mg [Sigma-Aldrich, for synthesis]) as the reagents, with a measured mass loss of 3320 mg upon distillation (calculated ethanol loss of 3353 mg).

- **Experiment 8** - Acetylacetone (6.04 mmol, 605 mg [Alfa Aesar, 95%]), anhydrous ethanol (42.65 mmol, 1965 mg [AcrosOrganics, 99.5%, ExtraDry, absolute]), tantalum(V) ethoxide (6.01 mmol, 2440 mg [Alfa Aesar, 99+%]), and 1,3-propanediol (42.11 mmol, 3204 mg [Sigma-Aldrich, for synthesis]) as the reagents, with a measured mass loss of 3216 mg upon distillation (calculated ethanol loss of 3349 mg).

- **Experiment 9** - Benzoylacetone (6.00 mmol, 973 mg [Sigma Aldrich, 99%]), anhydrous ethanol (54.27 mmol, 2500 mg [AcrosOrganics, 99.5%, ExtraDry, absolute]), tantalum(V) ethoxide (6.02 mmol, 2445 mg [Alfa Aesar, 99+%]), and 1,3-propanediol (42.06 mmol, 3200 mg [Sigma-Aldrich, for synthesis]) as the reagents, with a measured mass loss of 3577 mg upon distillation (calculated ethanol loss of 3887 mg).

- **Experiment 10** - Dibenzoylmethane (6.26 mmol, 1403 mg [Sigma-Aldrich, 98%]), anhydrous ethanol (54.27 mmol, 2500 mg [AcrosOrganics, 99.5%, ExtraDry, absolute]), tantalum(V) ethoxide (6.23 mmol, 2532 mg [Alfa Aesar, 99+%]), and 1,3-propanediol (43.99 mmol, 3347 mg [Sigma-Aldrich, for synthesis]) as the reagents, with a measured mass loss of 3623 mg upon distillation (calculated ethanol loss of 3935 mg).

During distillation in all experiments, the pressure was set to 30 mbar but would fluctuate from 30 mbar to 60 mbar throughout the 8 hour distillation. As with Experiments 4 and 5, stable solutions were obtained for all experiments, and are shown in Figure 3.41.

Considering the reproducibility of the proposed synthesis method, along with the results from Experiments 1 - 3, one can observe that alcoholysis of the complex by 1,3-propanediol can be avoided during ethanol removal. As stated in Experiment 4, this can be accomplished through adjustments in the system temperature and pressure. Therefore, when beginning with 1,3-propanediol and a tantalum(v) tetraethoxide β-diketonate complex or a tantalum(V) tetraethoxide β-ketoester complex, the desired substitution may proceed as shown in Figure 3.42, with A in the equation below being the chelated β-diketone or β-ketoester:

$$\mathrm{TaA(OC_2H_5)_4} + 4\,\mathrm{HOC_3H_6OH} \longrightarrow \mathrm{TaA(OC_3H_6OH)_4} + 4\,\mathrm{C_2H_5OH} \tag{3.15}$$

If the temperature is set too high and for too long, then undesired alcoholysis of the complex is more probable, with the proposed reaction mechanism[207] also shown in Figure 3.42. However, when using the optimal parameters and by replacing tantalum(V) ethoxide with titanium(IV) isopropoxide, this resulted in a cloudy solution (see Figure A.1 in the Appendix) and was also reported by Kemmitt and Daglish with their methods.[196] Therefore, the procedure may only work for tantalum(V) with its odd valency, and possibly niobium(V), based solutions.

The resulting tantalum solutions can be modified with diethylene glycol monoethyl ether (DEGEE) (Sigma-Aldrich, ReagentPlus 99%) in order to achieve the proper viscosity and surface tension for inkjet printing,[218] with the results tabulated in Table 3.1, where the solution products from Experiments 6 - 10 were used. The viscosity (2 minute mark) was measured with a DV3T rheometer (AMETEK Brookfield, USA), and surface tension (average of n = 10, except for dibenzoylmethane where n = 1) with a surface tensiometer model A3 (KINO Industry Co., Ltd., USA).

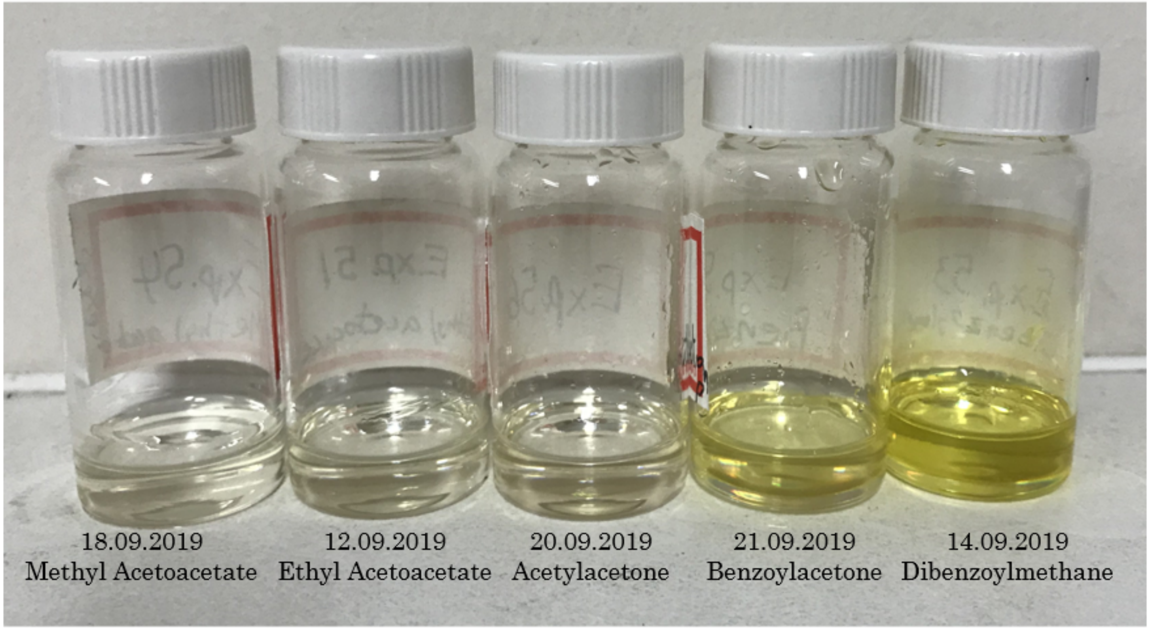

21.09.2019

Figure 3.41 Method repeated and compared with different chelating molecules (labeled individually with production date, and observed together at date below), going from left to right from Experiment 6 to Experiment 10.

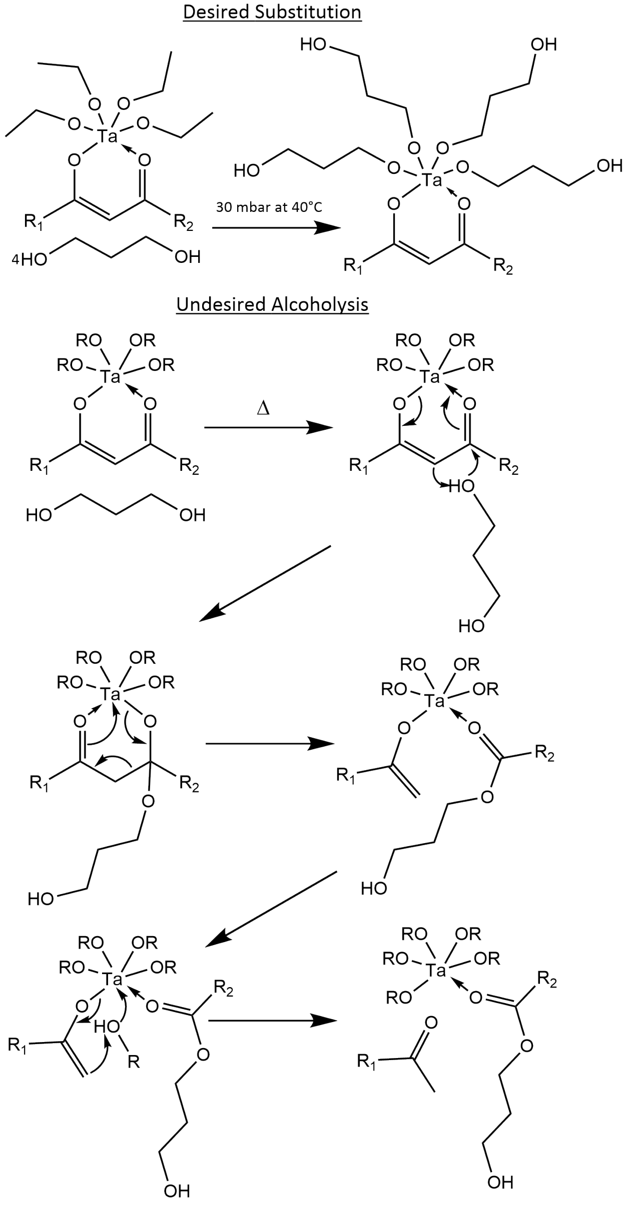

Figure 3.42 Desired substitution (above) and the undesired mechanism of alcoholysis (below), the latter of which results in the formation of acetone and 3-hydroxypropyl acetate through the alcoholysis of acetylacetone. R_1 and R_2 are both methyl groups for acetylacetone, and would change for other β-diketones/β-ketoesters (© The Royal Society of Chemistry 2020).[136,137]

Table 3.1 Viscosity and surface tension at 23°C in atmosphere for products and dilutions from proposed synthesis in Experiments 6 - 10 (DEGEE = diethylene glycol monoethyl ether; MeOAc = methyl acetoacetate; EtOAc = ethyl acetoacetate; Acac = acetylacetone; Bzac = benzoylacetone; DBM = dibenzoylmethane).

Solutions at 23°C	Viscosity (mPa s)	Surface Tension (mN m^{-1})
1,3-propanediol	48.1	44
DEGEE	4.60	31
MeOAc product	218	40
30 wt% MeOAc prod.	10.4	33
EtOAc product	188	39
30 wt% EtOAc prod.	9.70	32
Acac product	347	45
40 wt% Acac prod.	15.4	34
30 wt% Acac prod.	10.3	33
Bzac product	850	45
30 wt% Bzac prod.	10.0	33
DBM product	2600	35
30 wt% DBM prod.	12.2	34

In order to see if the solution can be mixed with a small amount of iridium, with the possible goal of later obtaining a more pH sensitive layer,[38] the experiment was repeated again for acetylacetone and then diluted to 40 wt% product. The diluting solution was DEGEE with 1 wt% iridium(III) acetylacetonate (Sigma-Aldrich, 97%); the solution was made by vortexing 117 mg of iridium(III) acetylacetonate with 11583 mg of DEGEE for a total of 11700 mg, followed by sonicating for 30 minutes with the Emmi-35HC-Q ultrasonic cleaner (EMAG AG, Germany). This resulted in a precipitate free, bright yellow solution. Future research could involve deposition and testing of such iridium-tantalum solutions. The tantalum solution synthesis reagents are listed below with the measured ethanol loss, along with images of before and after vortexing the product with the iridium(III) acetylacetonate solution in Figure 3.43.

- **Experiment 11** - Acetylacetone (6.61 mmol, 662 mg [Alfa Aesar, 95%]), anhydrous ethanol (42.07 mmol, 1938 mg [AcrosOrganics, 99.5%, ExtraDry, absolute]), tantalum(V) ethoxide (6.60 mmol, 2682 mg [Alfa Aesar, 99+%]), and 1,3-propanediol (46.42 mmol, 3532 mg [Sigma-Aldrich, for synthesis]) as the reagents, with a measured mass loss of 3363 mg upon distillation (calculated ethanol loss of 3458 mg).

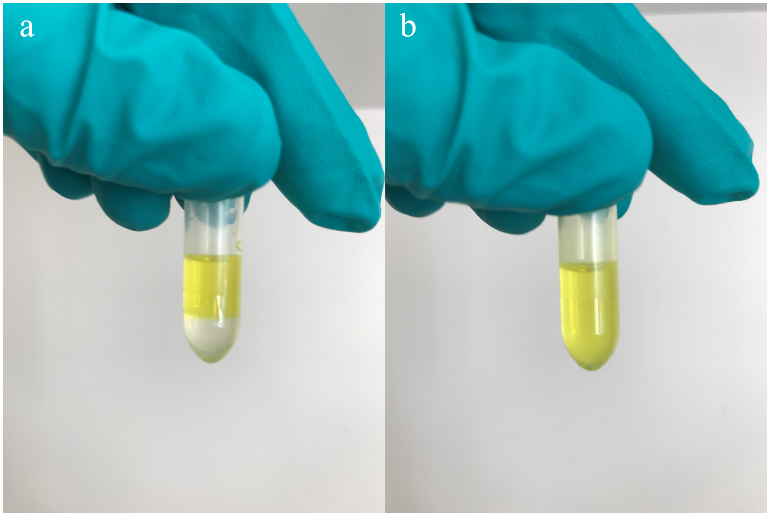

Figure 3.43 Ink before vortexing with phase separation, with 1 wt% iridium(III) acetylacetonate in DEGEE above as bright yellow and the product below as a very light yellow (a), and ink after vortexing and sonicating (b).

3.9 Experiment 12 - “Fast” Proposed Method with Acetylacetone

The final experiment concerns whether the synthesis process with acetylacetone from Experiments 4, 8, and 11 can be sped up, namely by shortening the overnight mixing time after 1,3-propanediol addition. Synthesis was followed by sending a sample directly for NMR measurements.

3.9.1 Synthesis

Anhydrous ethanol (42.35 mmol, 1951 mg [AcrosOrganics, 99.5%, ExtraDry, absolute]), acetylacetone (6.62 mmol, 663 mg [Alfa Aesar, 95%]) and tantalum(V) ethoxide (6.42 mmol, 2607 mg [Sigma-Aldrich, 99.98% trace metals basis]) were mixed in a dried Schlenk flask under argon in a glovebox, after which the Schlenk flask with a magnetic stirring rod was removed from the glovebox and connected to a Schlenk line. The flask was dipped in silicone oil, with the oil temperature being maintained at 80°C over 8 hours in order to promote chelation of acetylacetone to the tantalum cation. The reaction was kept under argon with continuous stirring and a vertical condenser (cold finger), whereby the condenser keeps the acetylacetone in solution. The tantalum(V) ethoxide from Sigma-Aldrich, which was used in this experiment (there were delivery problems from Alfa Aesar), gives the solution a more yellow hue than when tantalum(V) ethoxide from Alfa Aesar was used in Experiments 4, 8, and 11.

Following the 8 hour mixing, the silicone oil was cooled to 23°C over a 1.5 hour period. 1,3-propanediol (45.10 mmol, 3432 mg [Sigma-Aldrich, for synthesis]) was then added to the flask via syringe through the Schlenk valve, and the flask was then returned to argon. After addition, small bubbles appeared which went away over time. The mixing continued for 1 hour, a much shorter time than the 12 hours for Experiments 4 - 11, after which the solution was colorless and precipitate free.

As the Schlenk line setup was suboptimal for vacuum distillation, the solution in the Schlenk flask was removed from the Schlenk line, transferred from the Schlenk flask to a round-bottom flask, and the round-bottom flask was connected to a rotary evaporator for ethanol removal from the solution. Once connected, the rotation speed was set to 95 rpm, the system pressure to 30 mbar, and the water bath temperature to 40°C (where the flask would remain submerged). Ethanol removal proceeded for 8.75 hours, and afterward the measured mass loss of 3073 mg was close to the calculated ethanol loss of 3430 mg. Once ethanol removal was completed, a sample of the product was sent directly to NMR; however, not enough distillate could be collected for NMR. The entire procedure is displayed in Figure 3.44.

3.9.2 NMR Measurements

The ^{1}H NMR spectrum of the product (δ [ppm], Figures 3.45 and 3.46) shows the presence of the expected 1,3-propanediol peaks at δ 1.80 [$HOCH_2CH_2CH_2OH$], δ 3.70 [$HOCH_2CH_2CH_2$-OH], and δ 5.25 [$HOCH_2CH_2CH_2OH$]. Three separate methine acetylacetone-enol peaks appear at δ 5.95, δ 5.85, and δ 5.73 [$H_3C(CO)CH(CO)CH_3$]. The peaks from δ 2.35 to δ 2.10 overlap significantly (with δ 2.19 and δ 2.13 being the most prominent peaks, see Figure 3.46), making the following methyl peak assignments tentative: acetylacetone-keto [$H_3C(CO)CH_2(CO)CH_3$] or acetone [$H_3C(CO)CH_3$] methyl peaks (the latter from alcoholysis)[196,211] occur at δ 2.32 and δ 2.29, and the acetylacetone-enol [$H_3C(CO)CH(CO)CH_3$] methyl peaks around δ 2.19 and δ 2.13. The multiple peaks for the same proton on the acetylacetone-enol tautomer may be due to the different ways in which acetylacetone can bind to the metal cation,[207] or due to possible peak shifts when more than one acetylacetone molecule chelates to the metal cation.

Further downfield, as the δ 4.20 peak resonates at a higher frequency than the alcoholic methylene 1,3-propanediol peak at δ 3.70, this likely indicates the acetylation of 1,3-propanediol and the creation of 3-hydroxypropyl acetate as in Experiment 4,[208] despite the extra steps taken to avoid alcoholysis of the complex. A possible overlapping peak at δ 2.13 would then correspond to the methyl attached to the ester carbonyl [$HOCH_2CH_2CH_2O(CO)CH_3$], and the peak at δ 4.20 would be the protons on the methylene carbon bound to the ester oxygen [$HOCH_2CH_2CH_2O(CO)CH_3$]. Additionally, the TOCSY spectrum in Figure 3.47 shows three distinct proton groups on three consecutive carbon atoms, and the ^{13}C NMR and HMBC spectra corroborate these findings (discussed below), as well as the literature values for 3-hydroxypropyl acetate.[212] It is not clear whether the δ 4.20 peak occurs as a triplet, and the peak at δ 4.64 is difficult to assign with the available data.

The ^{13}C NMR spectrum of the product (δ [ppm], Figure 3.48) shows the expected 1,3-propanediol peaks at δ 35.2 [$HOCH_2\mathit{C}H_2CH_2OH$] and δ 58.9 [$HO\mathit{C}H_2CH_2\mathit{C}H_2OH$]. Acetylacetone-enol peaks around δ 192.0 [$H_3C(\mathit{C}O)CH(\mathit{C}O)CH_3$], around δ 102.0 [$H_3C(CO)\mathit{C}H(CO)CH_3$], and around δ 26.1 [$H_3\mathit{C}(CO)CH(CO)\mathit{C}H_3$] appear in the spectrum, along with some acetylacetone-keto [$H_3C(\mathit{C}O)CH_2(\mathit{C}O)CH_3$] or acetone[196,209] [$H_3C(\mathit{C}O)CH_3$] peaks at δ 204.4, and around δ 30.5 [$H_3\mathit{C}(CO)CH_2(CO)\mathit{C}H_3$] or [$H_3\mathit{C}(CO)\mathit{C}H_3$]; there is possibly an acetylacetone-keto peak around δ 59.0 [$H_3C(CO)\mathit{C}H_2(CO)CH_3$], which is difficult to assign due to the presence of 1,3-propanediol. The peak at δ 172.0 [$HOCH_2CH_2CH_2O(\mathit{C}O)CH_3$], not associated with any of the reagents, is located in the range typically found for ester carbonyl carbons and would support the idea that 1,3-propanediol has been acetylated and that 3-hydroxypropyl acetate has been formed.[208] This is supported by literature[212] and the HMBC spectrum in Figure 3.49, which shows a cross-peak at ^{1}H δ 2.13 – ^{13}C δ 172.0 (although unlike Experiment 4, there is no visible cross-peak at ^{1}H δ 4.20 – ^{13}C δ 172.0).

3.9.3 Discussion

Aside from the more unclear 3-hydroxypropyl acetate peaks and cross-peaks, these results are largely consistent with those of Experiment 4. Therefore, shortening the mixing time after 1,3-propanediol addition from 12 hours to 1 hour appears to give the same results. The 12 hour mixing time in Experiments 4, 8, and 11 was less a matter of science and more of convenience, as that allows for 8 hour chelation during the day, mixing overnight, and then 8 hour ethanol removal the following day. The 1 hour mixing time, although faster, would require a 19 hour working day (or two closely placed shifts).

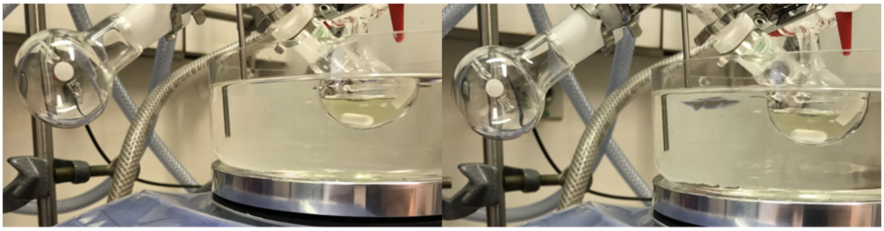

11:08 on 06.08.2019: Start under argon, finger towards reactor (right).

11:31 on 06.08.2019: 80°C reached.

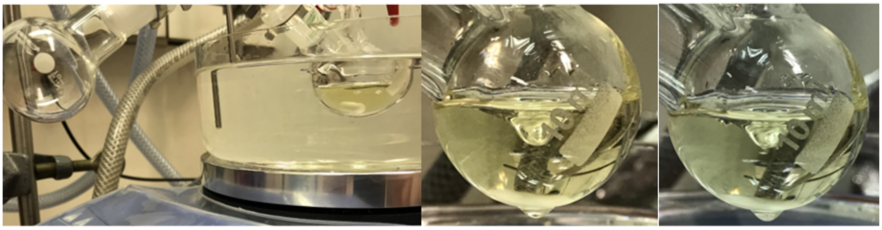

19:30 on 06.08.2019: Begin cooling to room temperature (leave in silicone oil).

21:05 – 1000 RPM, 1,3-propanediol added.

22:06 – 1000 RPM, bubbles gone.

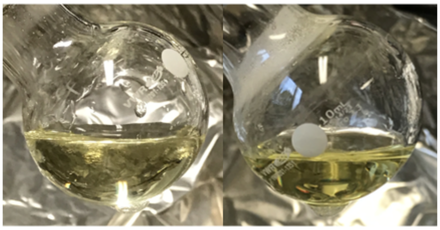

22:32 – Begin 50 mbar at 40°C, on 06.08.2019 (rotary evaporator).

07:15 – End, send directly to NMR, on 07.08.2019

Figure 3.44 Photographic record of Experiment 12, where the extra flask in the Schlenk line (left) was not used and is to keep the system closed (the observed pressure of 50 mbar was with the rotary evaporator set to 30 mbar).

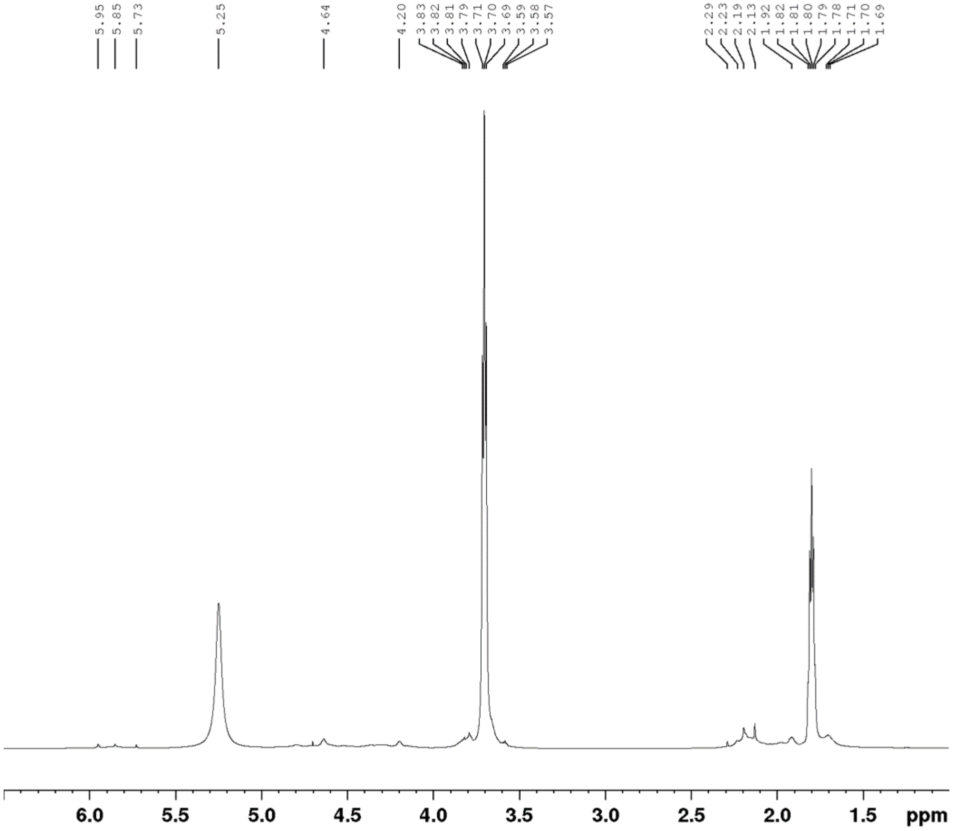

Figure 3.45 ^{1}H NMR [External D_2O]: Experiment 12 – Product.

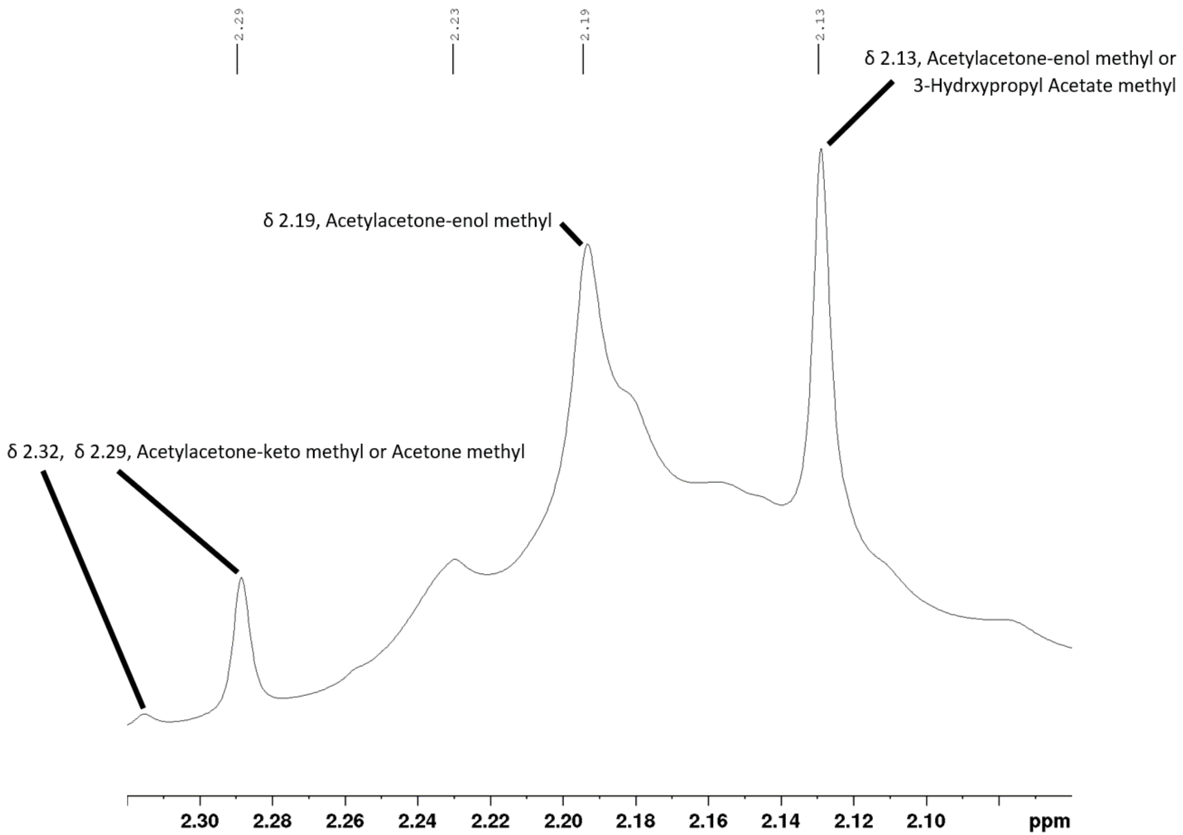

Figure 3.46 ^{1}H NMR [External D_2O]: Experiment 12 – Product.

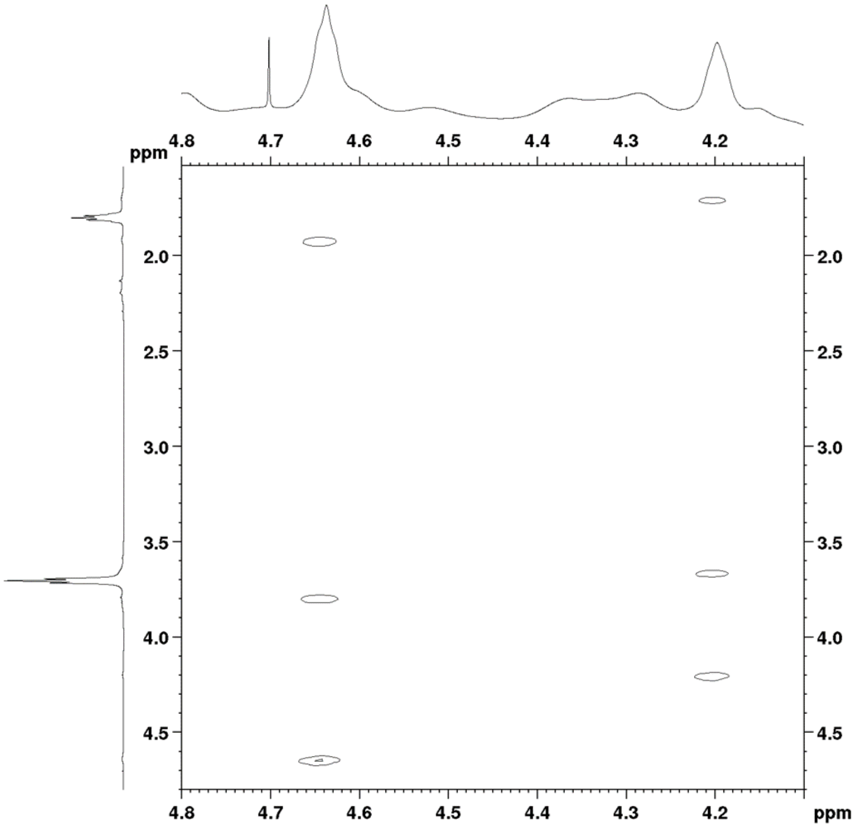

Figure 3.47 TOCSY [External D_2O]: Experiment 12 – Product.

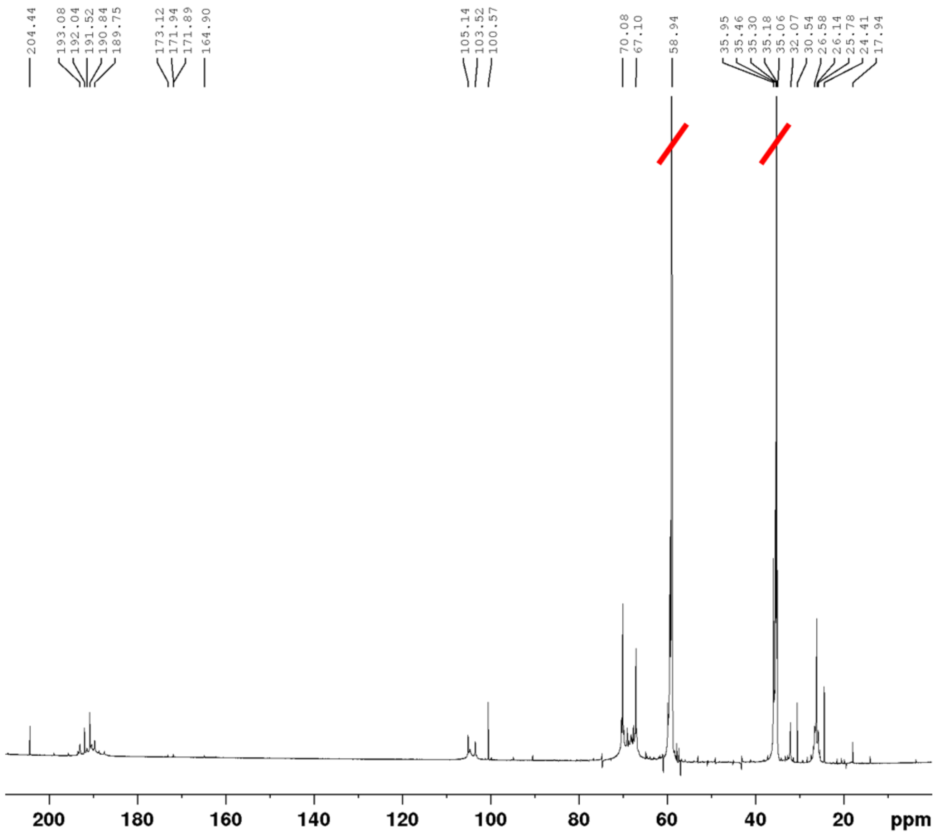

Figure 3.48 ^{13}C NMR [External D_2O]: Experiment 12 – Product.

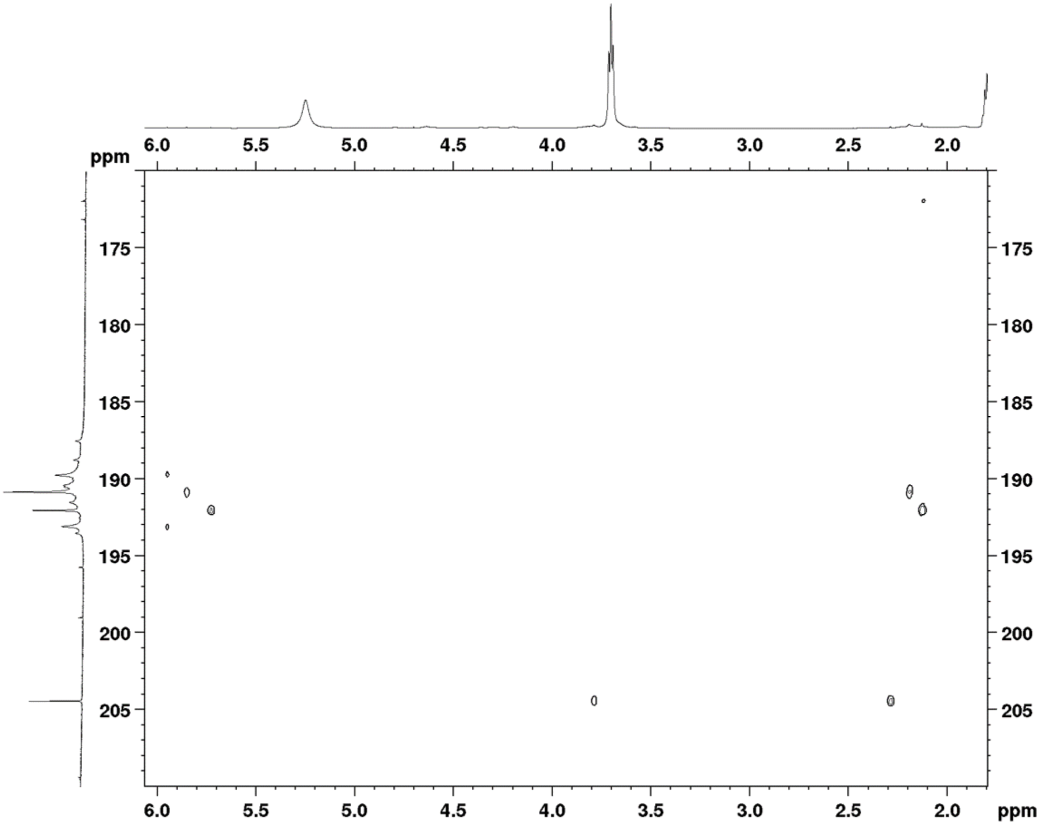

Figure 3.49 HMBC [External D_2O]: Experiment 12 – Product.

Chapter Four

Sensor Fabrication

As flash lamp annealing is highly compatible with roll-to-roll processing, when compared to other annealing techniques,[219] investigations into photocuring tantalum oxide layers with a flash lamp will be conducted in this chapter. This chapter will begin with finding the optimal photocuring parameters with a flash lamp, which are then used to fabricate the capacitive pH sensor described in Chapter 5. The following experiment will show how the flash lamp cured material remains on the gold electrode after exposure to acidic and basic solutions in an extended-gate field-effect transistor (EGFET) measuring configuration. In the final experiment, solutions from the optimized solution synthesis will be flash lamp cured and characterized by various spectroscopy techniques. Parts of this chapter have been published[135–137,220] and discussed in German patent application DE 10 2019 006 976.5 filed on October 8, 2019.[138]

4.1 Flash Lamp Annealing

Most of this section will be taken from Chapter 2 of the recently published *Flash Lamp Annealing: From Basics to Applications*,[221] which provides a very thorough review of the topic.

Considering a black body which absorbs all incident radiation, its emitted energy per unit area as a function of wavelength and temperature can be determined using Planck's law,[222] with h being Planck's constant, c being the speed of light, k being Boltzmann's constant, λ being the emitted wavelength, and T being the temperature of the black body:

$$B_\lambda\left(\lambda, T\right) = \frac{2hc^2}{\lambda^5}\frac{1}{\exp\left(hc/\left[\lambda k T\right]\right) - 1} \tag{4.1}$$

The peak wavelength for any black body can be calculated using Wien's displacement law, with b being Wien's constant, demonstrating that an increase in temperature will lead to a decrease in the peak wavelength:

$$\lambda_{\text{peak}} = \frac{b}{T} \tag{4.2}$$

Thus, by assuming a star as a black body, the star's surface temperature can be used to estimate its spectral output, as shown in Figure 4.1 for Alpha Centauri,[223,224] our closest neighbor.[225,226] As the surface temperature of the star increases from Proxima Centauri, then to Alpha Centauri B, and finally to Alpha Centauri A, the peak emitting wavelength blueshifts, thereby allowing for more photon emission in the UV range.

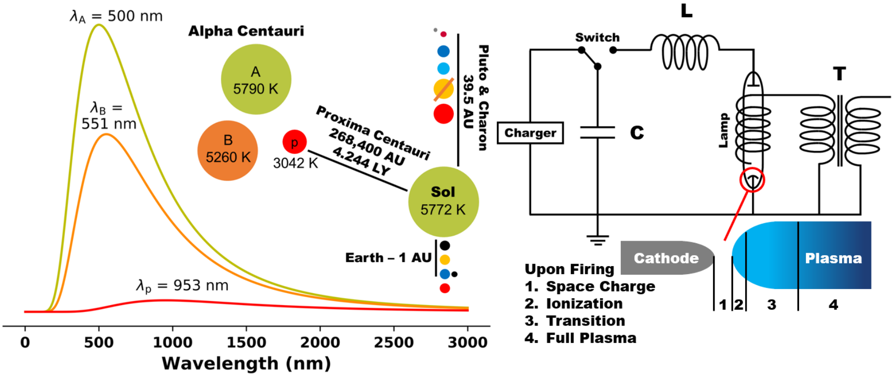

Figure 4.1 Left: spectral output of stars in the Alpha Centauri system, assuming they are black bodies where an increase in surface temperature leads to a blueshift in the peak wavelength - Sol and Alpha Centauri A have a similar spectral output.[223,227] Right: simplified LC circuit with external triggering (via a transformer) and a grounded cathode, with a reference coil wrapped around the lamp to ensure reliable triggering. The optional switch is to protect the charger during discharge.[221]

By assuming Planck's law for a flash lamp, containing a noble gas (He, Ne, Ar, Kr, Xe) which can be ionized to produce light, an increase in plasma temperature would lead to more emitted photons for photocuring a material in the UV range. For the quick delivery of energy required for a flash lamp to achieve this, a charged capacitor with capacitance, C, can be used where the square of the voltage, V, across the capacitor is proportional to the stored energy, E:

$$E = \frac{1}{2} C V^2 \tag{4.3}$$

Upon discharge, the current, I, as a function of time, t, is governed by the rate of the voltage change:

$$I\left(t\right) = C \frac{dV\left(t\right)}{dt} \tag{4.4}$$

The current density profile in the lamp, j, is a function of I and the time-dependent plasma arc diameter, d_{a}:

$$j\left(t\right) = \frac{4I\left(t\right)}{\pi d_a^2} \tag{4.5}$$

In relating the temperature, T, to j, the following equation can be used where p_{R} is the reference pressure of the filling gas (element specific), p_0 the filling gas pressure, p the working pressure, and E_{i} the ionization energy (element specific):

$$j^3 = 1.064 \times 10^{19} \left(\frac{p_{\mathrm{R}}}{p_0}\right)^{0.4} p^2 \exp\left(-2 \times 10^4 \frac{E_{\mathrm{i}}}{T}\right) \tag{4.6}$$

When attempting to correct for deviations from the ideal gas model, the following equation can be used instead:

$$j = 11 p^{0.5} T^{1.25} E_{\mathrm{i}}^{-0.5} \exp\left(-5000 \frac{E_{\mathrm{i}}}{T}\right) \tag{4.7}$$

In either case, an increase in E from Equation 4.3, and thereby j, leads to an increase in T. Additionally, for the same value of E, an increase in the discharge rate of the capacitor from Equation 4.4 leads to a higher I, and therefore a higher j. Thus a higher input energy and a shorter discharge, or pulse, time would lead to a higher plasma temperature; however, if the pulse time is too short, then the capacitor may not be able to release the required amount of energy, meaning that the lamp operator needs to balance these variables to achieve the optimum energy and pulse length for UV light emission.

Typically, the pulse is modulated with a series LC circuit, as shown in Figure 4.1. In this case, a transformer triggers the circuit via external circuitry. In a simplified circuit, the time constant, τ, and the impedance, Z, are a function of L and C, which governs the pulse shape:

$$\tau = \sqrt{LC} \text{ with } Z = \sqrt{\frac{L}{C}} \tag{4.8}$$

For the lamp gas, conversion efficiency increases with atomic mass of the gas, and therefore xenon is often used. The lamp's output spectrum, regardless of filling gas, is a broad continuum from UV to near IR, with element specific spectral lines. The spectral lines are more visible with a low flash energy, while the continuum is more visible at higher energy. In attempting to apply Planck's law, however, the emissivity of the the lamp initially increases monotonically with wavelength, leading to an underestimate with Planck's law for emitted UV. Furthermore, energy increases lead only to small increases in the plasma temperature, as other losses in the plasma consume some of the energy. However, with a further increase in energy, the emissivity increases and converges towards a black body, and this increase is observed to be stronger in the UV range than in the visible and IR range. Therefore, an increase in the input energy and the plasma temperature is desired for curing UV absorbing layers.

Additionally, the absorption and thermal properties of the material receiving the irradiation need to be taken into account.[228] Although it is difficult to measure the temperature accurately during processing, the material temperature can be simulated. For example, by using a transient 1-D heat conduction model, the heat conduction equation can be discretized using finite element analysis. This equation requires knowing the density, ρ, the specific heat at constant pressure, c_p, and the thermal conductivity, κ, of the material receiving the irradiation:

$$\rho c_p \frac{\delta T}{\delta t} = \frac{\delta}{\delta x}\left(\kappa \frac{\delta T}{\delta x}\right) + S \tag{4.9}$$

In this case, S is a volumetric source term, and the equation would be used over a material depth, L. Depending on the absorption properties of the material, the heat pulse after receiving irradiation can be treated either as a surface heat flux or a volumetric source term, the latter of which being based on the absorptivity. For the case of surface flux, while considering the boundary conditions $x = 0$ (4.10) and $x = L$ (4.11):

$$q_0''(t) = q_p''(t) - h_{\infty,0}\left(T_0 - T_{\infty,0}\right) - \epsilon\sigma T_0^4 \tag{4.10}$$

$$q_L''(t) = h_{\infty,L}\left(T_L - T_{\infty,L}\right) \tag{4.11}$$

Here, $q_p''(t)$ is the pulse waveform, σ is the Stefan-Boltzmann constant, ϵ is the emmisivity, $h_{\infty,0}$ is the convective heat transfer coefficient, T_0 is the surface temperature, and $T_{\infty,0}$ is the ambient surface temperature above the film stack (the values for L are the same as those for 0 but for below the film stack). However, if a volumetric source term is used instead, $q_p''(t)$ is omitted and Beer's law is used, with q_0'' as the incident heat flux, q'' as the transmitted flux through a planar volume of depth l, and α as the absorption coefficient:

$$\frac{q''}{q_0''} = \exp\left(-\alpha l\right) \tag{4.12}$$

Beer's law is then used to calculate the fraction of the surface heating pulse, $q_p''(t)$, absorbed in each cell. The PulseForge (Novacentrix, USA), which uses a xenon flash lamp for photonic sintering and curing, uses these relations in its SimPulse software. In this way, the operator can predict the heat profile in each layer after irradiation. By knowing the thermal profile, a pulse can be made so as to properly cure or sinter the desired material, without damaging the substrate beneath it. However, if the properties of the material to be sintered are unknown, then an Edisonian approach towards finding the best pulse, which will be followed in the experimental section, may be required.

4.2 Deposition and Spectroscopy Methods

Inkjet Printing and Plasma Treatment

Viscosity was measured with a DV3T rheometer (AMETEK Brookfield, USA) at the 2 minute mark, and surface tension with a surface tensiometer model A3 (KINO Industry Co., Ltd., USA) being an average of n = 10. Ink sonication was performed with a Emmi-35HC-Q ultrasonic cleaner (EMAG AG, Germany). Plasma substrate treatment used the NANO plasma oven (Diener electronic GmbH + Co. KG, Germany), with parameters later specified for each experiment. All inkjet printing was performed with an OmniJet 300 printer (Unijet Co., Ltd., South Korea), using 10 pL Dimatix cartridges (FUJIFILM Dimatix, Inc., USA) with detailed parameters for each case in the experimental section.

Annealing

Thermal annealing used a programmable, precision hot plate with the Programmer PR 5 (Harry Gestigkeit GmbH, Germany), where a glass Petri dish was placed over the samples (lip contacting the hot plate) to prevent contamination from the environment. Flash lamp annealing was carried out with the PulseForge 1200 (Novacentrix, USA) with an output spectrum from roughly 230 nm – 1000 nm at the set voltages,[229] with the procedure detailed for each case in the experimental methods (a working distance of 25 mm was used in all cases, with photocuring being run at room temperature).

Parylene C Deposition for Feed Line Passivation

Parylene C was chosen as a chemically inert and biocompatible passivation layer, where over a thickness of 100 nm the material is pinhole free.[230] In order to deposit the material, the SCS Labcoter 2 - Parylene Deposition System 2010 (Specialty Coating Systems, Inc., USA) with default system settings was used. The dimer dichloro-p-cyclophane (DPX-C, Specialty Coating Systems, Inc.) was pyrolyzed to form the layer, and γ-methyacryloxypropyltrimethoxysilane (A-174 Silane, Specialty Coating Systems, Inc.) was used for adhesion to the substrate. A tape mask, guided by the naked eye and utilizing clean room dicing tape (1008R-11.5, Ultron Systems, Inc.), was cut with scissors and taped on the sensor contact pads and the cured tantalum oxide layer - after parylene C deposition, the tape was carefully removed with the aid of a scalpel, leaving a passivation layer covering the feedlines.

See Figure B.1 (Appendix) for a visual of sample placement in the chamber with an example of tape mask removal. A modified, visual description of the deposition process from the manufacturer[231] is shown in Figure B.2 (Appendix).

UV/Visible Spectrophotometry

UV/Vis spectra of the films on a-SiO_2 were measured versus a 0.5 mm thick a-SiO_2 reference, with a 1 nm step in the 200 nm to 400 nm range. The device used was a Lambda 900 spectrometer (PerkinElmer, USA).

Confocal Raman Microscopy

Confocal Raman microscopy was performed using an alpha300 R setup (WITec, Germany). Illumination of the sample was performed using a 532 nm excitation line from a single-mode frequency doubled Nd:YAG laser via a 100 µm single-mode glass fiber. A LD EC Epiplan-Neofluar 50 × 0.55 objective (Carl Zeiss AG, Germany) was used and the laser power at the sample behind the objective was 12 mW.

An edge filter was used to separate the Raman signal from the excitation line. Confocality of the Raman signal was achieved via a 50 µm multi-mode fiber glass between the microscope and the Raman spectrometer, where the fiber serves as a pin-hole. The Raman spectrometer was equipped with a holographic grating of 600 lines per mm. For the detector, a Newton 970 EMCCD camera (Andor Technology Ltd, United Kingdom) with 1600 × 200 pixels was used, where this configuration allows a spectral resolution of about 2 cm^{-1} to be obtained.

An integration time of roughly 0.1 s per spectrum and pixel was used to improve the signal-to-noise ratio (S/N). For Raman depth scans, 100 pixel × 80 pixel scans were used for covering an area of 50 µm × 40 µm. All data sets were analyzed using cluster analysis and non-negative matrix factorization.

X-Ray Diffraction (XRD)

X-ray measurements were accomplished with a high-resolution D8 diffractometer (Bruker Corporation, USA), using the CuKα1 wavelength ($\lambda = 1.54016$ Å) collimated and filtered by means of a Göbel mirror and a Ge-220 four-crystal monochromator. On the detector side, a scintillator with a mechanical slit of 3 mm was employed. The $2\theta/\theta$ scans were carried out in a range from $2\theta = 3°–120°$ with angular resolutions of 0.1°. Each data point was measured for 10 s.

X-Ray Photoelectron Spectroscopy (XPS)

Spectra were obtained using a Phi5000 VersaProbe II (ULVAC-Phi Inc., USA). The source was AlKα, monochromatic (1.486 keV) with X-ray settings of 50 W, 15 kV in a 200 µm spot. Survey spectra were obtained with a 187.5 eV pass energy, with a 0.8 eV step and 100 ms per step. Detailed spectra used a 23.5 eV pass energy, with a 0.1 eV step and 100 ms per step.

Atomic quantification assumed a homogeneous volume, using atomic% (at%) with a 15% relative error. Quantification was normalized to 100 at%. The Shirley-background was subtracted and empirical relative sensitivity factors were used. Charge compensation was performed by setting the main peak of the C 1s signal to 285 eV.

Ion Beam Analysis

Rutherford backscattering spectrometry (RBS) and nuclear reaction analysis (NRA) were performed using 1.43 MeV deuterons. A beam spot diameter of about 200 µm was set up using a triple-focus. A 20 µm resolution imaging camera together with a piezo manipulator enabled positioning of the beam spot on the regions of interest on each sample. Each sample spot was integrated for about 2000 s to about 3 µC of ion charge for sufficient counting statistics. Signals were acquired using a 100 µm thick PIPS detector with 11 keV FWHM resolution at 150° reaction angle.

RBS and NRA data were analyzed using SimNRA 7.02 with Rutherford cross-sections for all elements except for C and O which were analyzed using the $^{16}O(d,p_0)^{17}O$ and $^{12}C(d,p_0)^{13}C$ reactions and Sigmacalc 2.0 cross-sections. The measurement achieves a total uncertainty of 10% originating from the Particle*Sr value determined from the substrate RBS and NRA counting statistics. The good counting statistics of tantalum results in negligible uncertainties for this element.

LCR Meter Measurements (Experiment 3)

After the 125°C preliminary anneal, the layers were exposed to the xenon flash lamp, with the parallel capacitance (with parasitic capacitance subtracted) and the parallel resistance measured at 1000 Hz every 50 shots, using a DE-5000 LCR meter with TL-22 probes (DER-EE, Taiwan). Plotted values were an average from 5 structures, with the error bar reporting the standard deviation.

Focused Ion Beam (FIB) Sectioning and Scanning Electron Microscopy (SEM)

FIB sectioning and subsequent SEM imaging was carried out with a HELIOS 600i NanoLab (FEI, Thermo Fisher Scientific, USA). First the region of interest on the sample was covered in situ with protective Pt/C layers. Rough milling was processed with Ga^+ ions at 0.43 nA or 0.79 nA and 30 kV followed by a fine polishing step at 40 pA and 30 kV. SEM imaging was performed at 21 pA and 3 kV using the TL detector for secondary electrons.

4.3 Experiment 1 - Flash Lamp Annealing

The first solution for flash lamp testing involved refluxing 618 mg tantalum(V) ethoxide (Alfa Aesar, 99+%), 637 mg acetylacetone (Alfa Aesar, 95%), and 1725 mg 1,3-propanediol (Sigma-Aldrich, for synthesis) in 120°C silicone oil for 8 hours in air (23.07.2018), followed by removal of the vertical condenser (cold finger) for 2 hours to allow for ethanol removal (this assumption was made before the nuclear magnetic resonance (NMR) experiments in Chapter 3 were run). This product had a dark amber appearance, similar to Experiment 1 in Chapter 3, and was then diluted with 1-butanol (99.9%, Sigma-Aldrich) in order to achieve the proper viscosity and surface tension for inkjet printing. However, dilution with 1-butanol led to the need to constantly purge (flood the nozzles to remove blockage) during printing, possibly due to the formation of tantala glass particles (i.e., the ink was not air stable, perhaps caused by 1-butanol evaporation). Thus, diethylene glycol monoethyl ether (DEGEE) (Sigma-Aldrich, ReagentPlus 99%) was used instead and led to better results, likely because of DEGEE's lower vapor pressure. In both cases, vortexing was required to obtain a homogeneous ink.

Table 4.1 Viscosity and surface tension for diluted product.

Ink	Viscosity (mPa s)	Surface Tension (mN m^{-1})
504 mg Product, 500 mg 1-Butanol	8.42	27
782 mg Product, 825 mg DEGEE	11.5	32

In order to make more solution after viscosity and surface tension measurements, another reflux was run with 610 mg tantalum(V) ethoxide (Alfa Aesar, 99+%), 603 mg acetylacetone (Alfa Aesar, 95%), and 1751 mg 1,3-propanediol (Sigma-Aldrich, for synthesis) in 120°C silicone oil overnight (starting at 20:22 on 01.08.2018). Unfortunately, the camera used to take the pictures, where the file timestamp was used to mark reaction duration, was dropped on the asphalt and broke, so the exact reaction time is not clear - however, the reaction was stopped the next day in the morning (with the condenser removed for 2 hours for assumed ethanol removal), and the product had a dark amber appearance like the previous experiment. A 50 wt% product dilution in DEGEE (filtered with a Whatman Puradisc 13, GF/B, 1.0 µm glass filter [GE Healthcare, USA]) was then used for inkjet printing on laser ablated, gold interdigitated electrodes (IDEs) on PET (see Table 4.2 for laser ablation parameters and substrate specifications). These IDEs consisted of 40 digits, being ~2000 µm long, ~55 µm wide, and with a gap spacing of about ~25 µm. The plasma parameters are in Table 4.3, and the printing parameters in Table 4.4.

Table 4.2 Laser ablation of 50 nm thick gold, 5 nm thick titanium adhesion layer (gold and titanium deposited via electron-beam physical vapor deposition), on 80 µm thick DuPont PCS (PET) with an RDX 500 Laser Machine (Pulsar Photonics GmbH, Germany).

Installed Laser Source		
Focus Objective (mm)	Pulse Width (ps)	Wavelength (nm)
100	12	532
Ablation Settings		
Repetition Rate (MHz)	Laser Power (W)	Mark/Scanner Speed (mm s^{-1})
5	30	1000

Table 4.3 Surface plasma treatment for laser ablated IDEs.

Gas	Pressure (mbar)	Power (W)	Time (s)
Argon	0.6	150	120

Table 4.4 Printing parameters for laser ablated IDEs (head height not noted).

Waveform (µs)	Voltage (V)	Frequency (Hz)	Pitch (µm)	Dimensions (Drops)
1 - 10 - 1	25	1000	30	140 × 140

After printing, all samples were annealed for approximately 10 hours at 125°C on a hot plate. For finding the best shot parameters with the PulseForge 1200 (Novacentrix, USA), each pulse would be tested and then adapted for improvement. The tests proceeded with the following assumptions: large pulse envelopes shock the material, and may lead to unwanted fracturing and cracking; higher voltages (maximum output of 450 V with the PulseForge 1200) emit more photons in the UV range (as discussed in the previous section and reported by the manufacturer),[229] which is necessary for oxides and chelated β-diketonates. Parallel capacitance was measured with a RLC 200 Meter (Grundig, Germany) at 1000 Hz, and microscope images were taken with the Keyence X-150 Laser Microscope (Keyence, Japan). Composite images were made with a machine controlled stage and the microscope software, where some “before” images were only taken of part of the sensor, as a false assumption was made that only part of the sensor needed to be imaged to save time.

4.3.1 Finding the Right Pulse

Sample 1 in Figure 4.2 (also Figure C.1 in the Appendix) shows an example of where with too large of a pulse envelope at 350 V, the gold/titanium/PET substrate absorbs too much heat, which leads to the undesired cracking. Therefore, various tests at 450 V were run with divided pulse envelopes and are tabulated in Table 4.5, where a higher voltage from Equation 4.3 would theoretically yield more UV photons. Each listed group of shot parameters was tested for a different sample, where the images are shown in Figures C.2 - C.14 in the Appendix. The final sample (Sample 14) listed at the bottom of Table 4.5 is shown here in Figure 4.3 and in the Appendix in Figure C.14, which shows a color change and a slight capacitance increase after photocuring. From these tests, the best results occurred with multiple, short pulses at a high voltage, with each pulse divided into "µpulses" as they are referred to by the manufacturer.

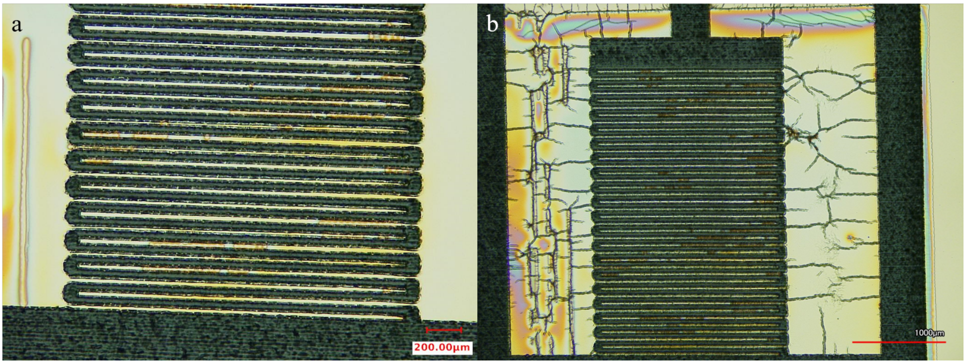

Figure 4.2 Sample 1 Firing Parameters - 1x 770 mJ cm^{-2}, 350 V, 500 µs, 1 undivided pulse, no capacitance change (a - before flash lamp, b - after flash lamp).

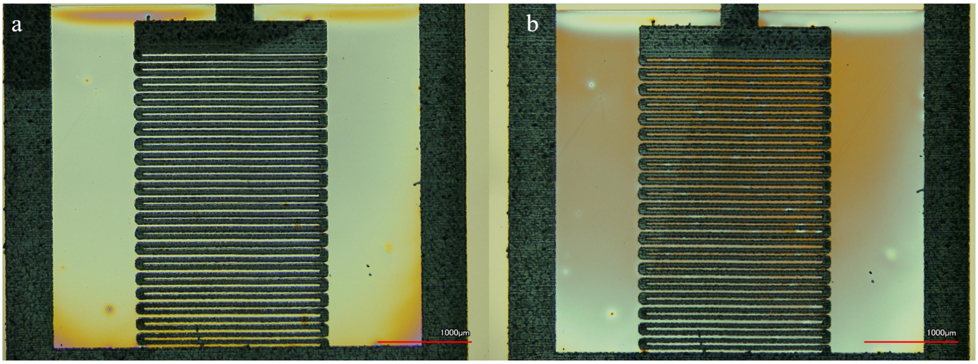

Figure 4.3 Sample 14 Firing Parameters - 2400x at 2 Hz, 663 mJ cm^{-2}, 450 V, 500 µs, 7 µpulses with 40% duty cycle, [3.5 pF before, 5.0 pF after, 1.2 pF parasitics] (a - before flash lamp, b - after flash lamp). The estimated surface temperature of the substrate, according to the SimPulse 2.5 software, plateaus at the following temperatures (with an operating temperature of 25°C): 80 µm thick PET, ∼30°C; 80 µm thick PET with 5 nm Ti adhesion layer and 50 nm Au layer, ∼390°C.

Table 4.5 Shot parameters for successive samples, starting from the top and arriving at the optimal parameters at the bottom, where an underline denotes a change from the previous treatment (above) and where an absence of an underline indicates an attempt to recreate the previous result. For the "Changes" column, the following denote a particular change: X = cracks, C = color change, x pF = parallel capacitance increase.

Shots	Frequency (Hz)	Energy (mJ cm^{-2})	Voltage (V)	Envelope (µs)	µpulses	Duty Cycle (%)	Changes	Figure
1	-	558	450	400	5	50	None	C.2
20	2	558	450	400	5	50	None	C.3
20	2	1130	450	800	5	50	X	C.4
20	2	862	450	600	5	50	X	C.5
20	2	692	450	500	5	50	None	C.6
20	2	692	450	500	5	50	None	C.7
120	2	692	450	500	5	50	None	C.8
120	2	739	450	500	7	50	None	C.9
1200	2	739	450	500	7	50	C	C.10
2400	2	739	450	500	7	50	X, C, 0.8 pF	C.11
2400	2	739	450	500	7	50	X, C, 0.8 pF	C.12
2400	2	663	450	500	7	40	C, 1.7 pF	C.13
2400	2	663	450	500	7	40	C, 1.5 pF	4.3

Being relatively defect free when compared to the other samples, Sample 14 in Figure 4.3 was then compared to a gold negative control with no deposited tantalum oxide layer for pH versus impedance sensitivity, with pH buffer solutions pipetted onto the IDEs. Merck Titrisol buffers of pH 5 (citrate and sodium hydroxide), pH 7 (potassium dihydrogen phosphate and disodium hydrogen phosphate), and pH 9 (boric acid, potassium chloride, and sodium hydroxide) were used for the measurements. Before measuring, both samples were conditioned for two hours in Britton-Robinson's universal pH buffer[232] (0.04 M acetic acid [Glacial, PhEur, SAFC], 0.04 M phosphoric acid [85%, Reag. Ph. Eur, KMF optiChem], 0.04 M boric acid [GR, Merck]) with no addition of sodium hydroxide, giving the buffer a pH of ~1.9. Impedance was measured at a 10 mV amplitude (rms) from 1 Hz to 1 MHz (10 measurements per decade) with the PalmSens 4 (PalmSens BV, The Netherlands), with the counter and reference electrodes shorted and connected to one digit array, and the working electrode to the opposite digit array. On both the negative control sample and the tantalum oxide sample, the pH was cycled from pH 5 to pH 7 to pH 9 a total of 5 times (rinsed with Milli-Q water and N_2 between measurements), with the Bode spectra averaged and plotted in Figure 4.4 for the negative control and Figure 4.5 for Sample 14 having tantalum oxide covering the gold.

The negative control appears to have no clear pH sensitivity. However, when comparing the impedance modulus around 10 kHz for the tantalum oxide sample, the deposited layer appears to have an increasing impedance with pH. However, this experiment is flawed, as the droplet size may change from measurement to measurement. Nonetheless, the results support further investigation of this phenomenon, which will be discussed in more detail in Chapter 5 with Sensor 7-7.

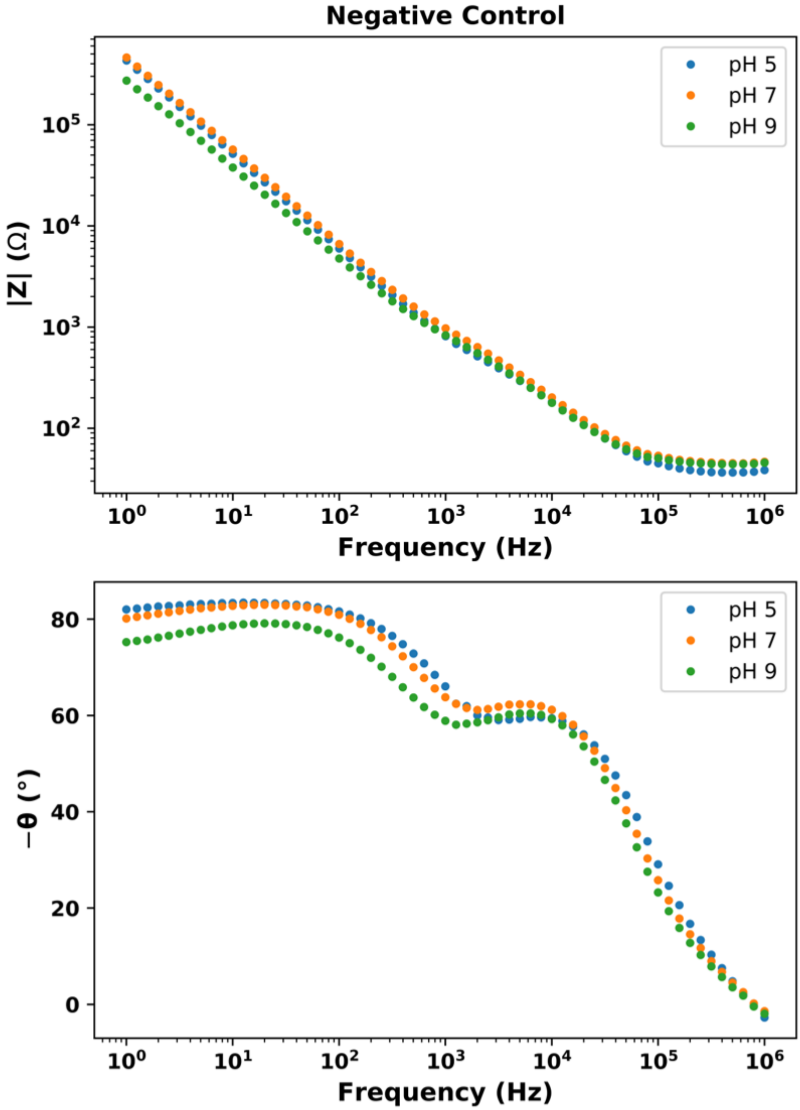

Figure 4.4 Average spectra (n = 5) for pH buffer solution dropped on bare gold electrodes.

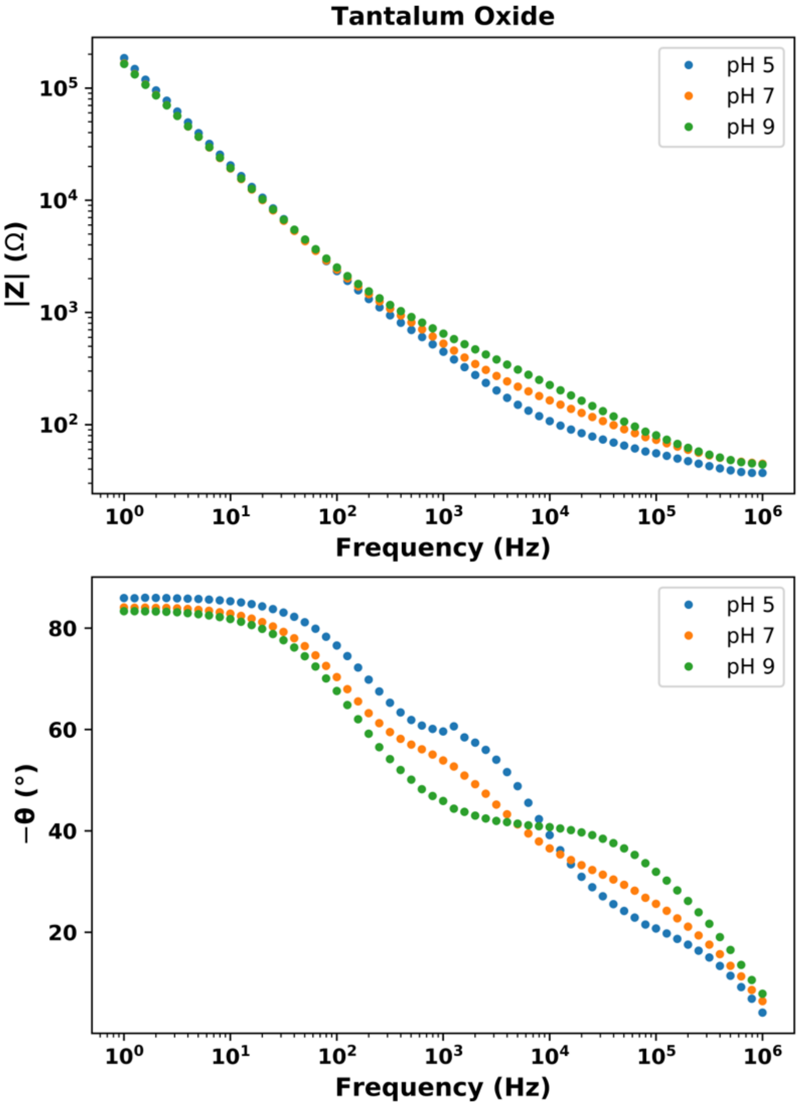

Figure 4.5 Average spectra (n = 5) for pH buffer solution dropped on tantalum oxide covered electrodes for Sample 14.

4.3.2 XPS for Oxidation State and Carbon Content

For a similar experiment (Sample 15), reflux was conducted with 815 mg tantalum(V) ethoxide (Alfa Aesar, 99+%), 203 mg acetylacetone (Alfa Aesar, 95%), and 1010 mg 1,3-propanediol (Sigma-Aldrich, for synthesis) for 24 hours (04.12.2018 - 05.12.2018) in silicone oil at 100°C in air, where the vertical condenser (cold finger) was removed for 2 hours under heat (after the 24 hour reflux). The ink product was then diluted to make a 55 wt% DEGEE ink, and subsequently filtered with a Whatman Puradisc 13, GF/F, 0.7 µm glass syringe filter (GE Healthcare, USA). The ink was then printed on laser ablated gold IDEs on PET, with 40 digits having a length of ∼3500 µm, a gap of ∼50 µm, and a width of ∼50 µm (see Table 4.2 for laser ablation parameters and substrate specifications). Before printing, the IDEs were sonicated with 1 v/v % Aquet detergent (concentrate, Scienceware) in Milli-Q water for 10 minutes, followed by 10 minute sonication in isopropanol. The plasma parameters are in Table 4.6, and the printing parameters in Table 4.7.

Table 4.6 Surface plasma treatment for laser ablated IDEs.

Gas	Pressure (mbar)	Power (W)	Time (s)
1) Argon	0.6	150	180
2) Oxygen	0.3	150	30

Table 4.7 Printing parameters for laser ablated IDEs (head height at 0.5 mm).

Waveform (µs)	Voltage (V)	Frequency (Hz)	Pitch (µm)	Dimensions (Drops)
1 - 10 - 1	25	1000	150	32 × 32

After printing, a 125°C pre-anneal (30 minute ramp, 2 hour hold) was performed on a hot plate. The thermally annealed layers were then photocured with 4000 shots at 0.333

Hz, with the shot parameters in Table 4.8. The shot parameters were further modified from that of Sample 14, in order to avoid machine failure and for more reproducible pulses. The estimated surface temperature of the substrate, according to the SimPulse 2.5 software, plateaus at the following temperatures and an operating temperature of 25°C: 80 µm thick PET, ∼25°C; 80 µm thick PET with 5 nm Ti adhesion layer and 50 nm Au layer, ∼250°C.

Table 4.8 Shot parameters for flash lamp curing of tantalum oxide layers for Sample 15 and Sensor 7-7, where a total of 4000 shots were fired at a frequency of 0.333 Hz.

Pulse Shape	Energy (mJ cm^{-2})	Voltage (V)	µpulses	µpulse rise − fall (µs)
	456	400	3	75 − 150

The XPS survey spectrum in Figure 4.6 and the Ta 4f and O 1s spectra in Figure 4.7 show the formation of stochiometric Ta_2O_5, where the O/Ta ratio is 2.4 which is within the expected error for a O/Ta ratio of 2.5. The detected silicon in Table 4.9 may be from the laser ablation of PET with siloxane contamination,[233] while the detected carbon is affected by surface contamination and is not an indicator of bulk carbon content.

Table 4.9 XPS for Sample 15.

At% C 1s	At% O 1s	At% Si 2p	At% Ta 4f	At% Au 4f
13.8	62.5	7.2	15.4	1.2

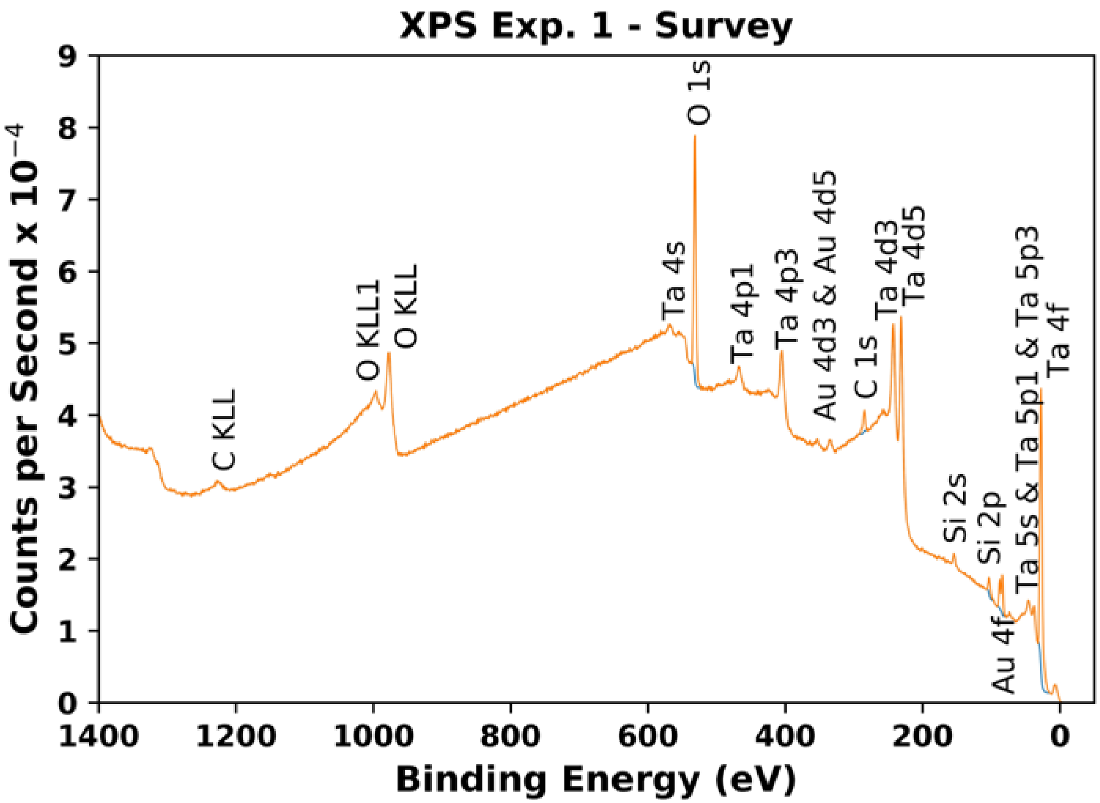

Figure 4.6 XPS survey spectrum of Sample 15 (© 2022 Elsevier B.V. All rights reserved.).[220]

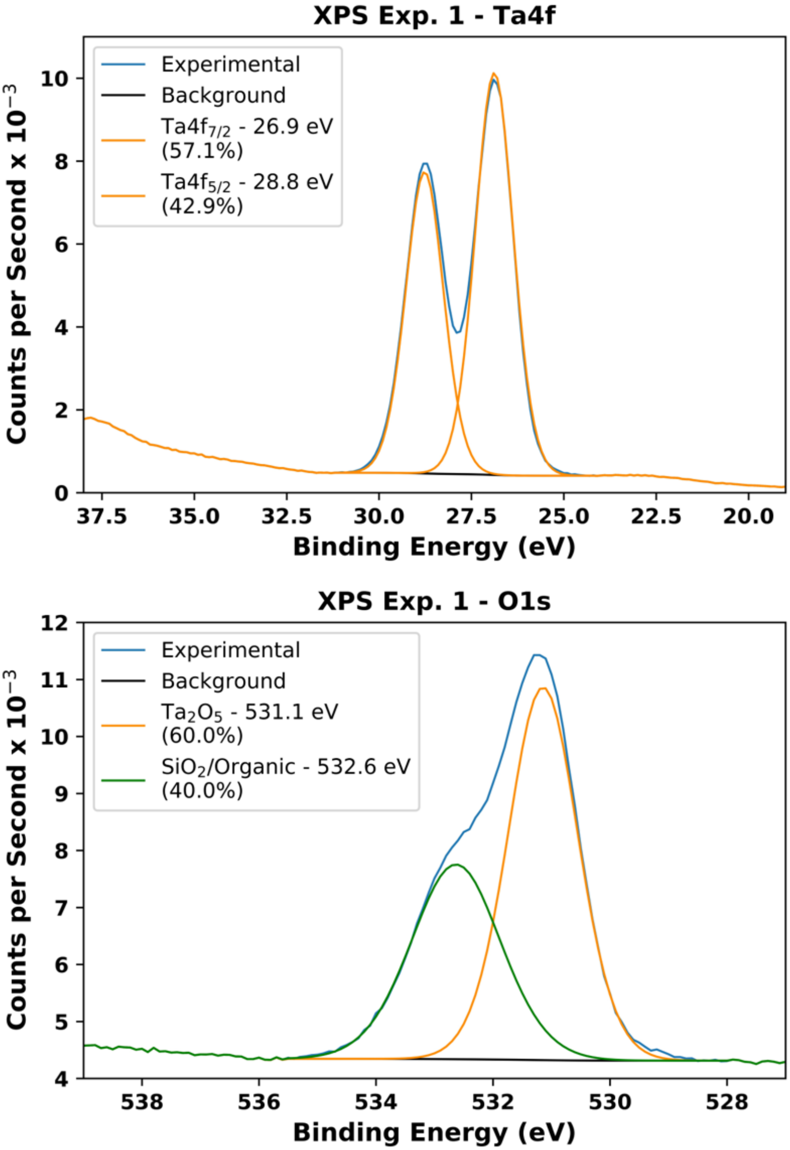

Figure 4.7 XPS Ta 4f and O 1s spectra of Sample 15 (© 2022 Elsevier B.V. All rights reserved.).[220]

4.3.3 Sensor 7-7 Fabrication

In making the tantalum ink for the immittance spectroscopy study in Chapter 5 with Sensor 7-7, reflux was conducted with 813 mg tantalum(V) ethoxide (Alfa Aesar, 99+%), 209 mg acetylacetone (Alfa Aesar, 95%), and 1037 mg 1,3-propanediol (Sigma-Aldrich, for synthesis) for 24 hours (27.10.2018 - 28.10.2018) in silicone oil at 100°C in air, where the vertical condenser (cold finger) was removed for 2 hours under heat (after the 24 hour reflux). The ink product was then diluted to make a 60 wt% DEGEE (Sigma-Aldrich, ReagentPlus 99%) ink, and subsequently filtered with a Whatman Puradisc 13, GF/F, 0.7 µm glass syringe filter. The ink was then printed on laser ablated gold IDEs on PET (see Table 4.2 for laser ablation parameters and substrate specifications), with 40 digits having a length of ~3500 µm, a gap of ~50 µm, and a width of ~50 µm. Before printing, the IDEs were sonicated with 1 v/v % Aquet detergent (concentrate, Scienceware) in Milli-Q water for 10 minutes, followed by 10 minute sonication in isopropanol. The plasma parameters are in Table 4.10, and the printing parameters in Table 4.11.

Table 4.10 Surface plasma treatment for laser ablated IDEs.

Gas	Pressure (mbar)	Power (W)	Time (s)
1) Argon	0.6	150	180
2) Oxygen	0.3	~105	30

Table 4.11 Printing parameters for laser ablated IDEs (head height at 0.8 mm).

Waveform (µs)	Voltage (V)	Frequency (Hz)	Pitch (µm)	Dimensions (Drops)
1 - 10 - 1	25	1000	190	25 × 25

After printing, a 125°C pre-anneal (1 hour ramp, 4 hour hold) was performed on a hot plate. The annealed layers were photocured with the shot parameters in Table 4.8, for a total of 4000 shots at a firing frequency of 0.333 Hz. Following photocuring (no thermal post-anneal), parylene C was deposited with 6.0 g of dichloro-p-cyclophane (DPX-C, Specialty Coating Systems, Inc.), with silane used for adhesion to the substrate, leaving an estimated 3 µm layer covering the feedlines after tape mask removal; the process of removing the tape mask from Sensor 7-7 is shown in Figure B.1 in the Appendix. The immittance spectra measurements are reported and discussed in Chapter 5.

4.4 Experiment 2 - pH Buffer Resistance

After determining that the synthesized solutions can be photocured to form tantalum oxide films on gold/titanium/PET foil, this experiment will investigate whether prolonged exposure to acidic and basic solutions, through pH measurements in an EGFET configuration, can remove the tantalum oxide from the gold electrode.

The product from Experiment 1 of Chapter 3 was used for this experiment, with ink preparation and printed layers shown in Figure 4.8. The ink product was diluted to make a 55 wt% DEGEE (Sigma-Aldrich, ReagentPlus 99%) ink, and subsequently filtered with a Whatman Puradisc 13, GF/F, 0.7 µm glass syringe filter (GE Healthcare, USA). The ink was then printed on laser ablated gold IDEs on PET, with 62 digits having a length of ∼4800 µm, a gap of ∼25 µm, and a width of ∼50 µm (see Table 4.2 for laser ablation parameters and substrate specifications). The series capacitance at 1 Hz versus pH for these sensors in Britton-Robinson buffer solutions[232] with 0.28 M NaCl is shown in Figure 5.31 at the end of Chapter 5, and the immittance spectra are shown in the Appendix (Figures F.1 - F.8), where the solutions have a salinity similar to "low sodium Kimchi."[11] The ink was also printed on 5 mm x 5 mm gold PET electrodes for EGFET testing (also laser ablated to form gold strips shown in Figure 4.9). Before printing, the gold PET substrate was rinsed with toluene to remove gold particles, sonicated with 1 v/v % Aquet detergent (concentrate, Scienceware) in Milli-Q water for 10 minutes, and lastly sonicated for 10 minutes in isopropanol. The plasma parameters are in Table 4.12, and the printing parameters in Table 4.13.

Table 4.12 Surface plasma treatment for laser ablated IDEs.

Gas	Pressure (mbar)	Power (W)	Time (s)
1) Argon	0.6	150	300
2) Oxygen	0.6	150	120

Table 4.13 Printing parameters for laser ablated IDEs (head height at 1.1 mm).

Waveform (µs)	Voltage (V)	Frequency (Hz)	Pitch (µm)	Dimensions (Drops)
1 - 10 - 1	40	1000	150	40 × 40

Table 4.14 Shot parameters for flash lamp curing of tantalum oxide layers in Experiment 2 and Experiment 3, where for Experiment 2 a total of 5000 shots were fired at a frequency of 0.333 Hz.

Pulse Shape	Energy (mJ cm^{-2})	Voltage (V)	µpulses	µpulse rise − fall (µs)
	623	400	3	100 − 200

After printing, a 125°C pre-anneal (1 hour ramp, 2 hour hold) was performed on a hot plate. The annealed layers were photocured with the shot parameters in Table 4.14, for a total of 5000 shots at a firing frequency of 0.333 Hz; this pulse was further improved from prior experiments, where the longer rise and fall times at a lower voltage and frequency were found to be more reproducible. The estimated surface temperature of the substrate, according to the SimPulse 2.5 software, plateaus at the following temperatures and an operating temperature of 25°C: 80 µm thick PET, ~25°C; 80 µm thick PET with 5 nm Ti adhesion layer and 50 nm Au layer, ~300°C.

A 125°C post-anneal (1 hour ramp, 2 hour hold) was then performed, followed by parylene C deposition to passivate the feedlines. 6.1 g of dichloro-p-cyclophane dimer (DPX-C, Specialty Coating Systems, Inc.) was used to deposit an estimated 3 µm thick layer covering the feedlines, with silane used for adhesion. Figure 4.9 shows the prepared sensing electrodes before and after tape mask removal.

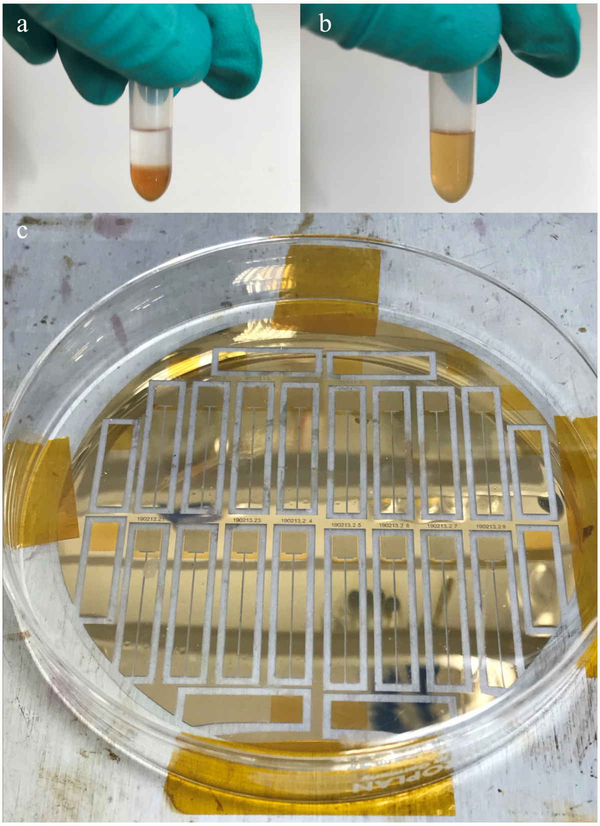

Figure 4.8 Ink before vortexing with phase separation, with DEGEE above as clear and the product below as amber (a), ink after vortexing (b), and ink printed on gold PET foil (c) annealing on the hot plate, with the darker areas being the printed layer.

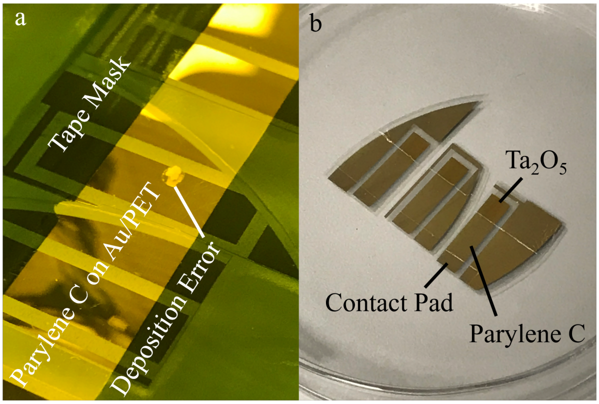

Figure 4.9 Tape mask on tantalum oxide and contact pads after parylene C deposition (a) and tape mask removal (b).

4.4.1 EGFET pH Measurement

A pioneering use of Ta_2O_5-EGFETs in 1971 by Lagow et al.[234] involved anodizing tantalum metal to form an oxide film, cutting the anodized metal into circles which were "crimped into the shape of bottle caps with a face diameter of 1/4 inch," and attaching the metal side to a field-effect transistor for use as chloride resistant, long-term electrocardiogram (EKG) electrodes intended for astronauts and patients in intensive care. Namely, the tantalum oxide film would contact the patient's skin, who is grounded by ohmic contact, for low-impedance recording and transmission. Ta_2O_5-EGFETs have also been investigated for pH sensing with Ta_2O_5 sputtered onto gold metallized PET foils,[121] and the flash lamp annealed films used here will be examined as a sensing material for this configuration.

The EGFET pH sensing experiment in this work followed that of Ghoneim et al.,[235] due to their extensive characterization of the experimental setup. Therefore with the goal of reproducibility, their procedure was replicated as much as possible with a diagram shown in Figure 4.10. The setup, run in a dark Faraday cage, used a CD4007UBE nMos transistor (Texas Instruments, USA), a BASi RE-6 Ag/AgCl reference electrode containing a 3

M NaCl gel (Bioanalytical Systems, Inc., USA), and the prepared tantalum oxide sensing layer. Measurements were run in saturation mode with the 4200A-SCS Parameter Analyzer (Keithley Instruments, USA) with a V_{DS} bias of 5 V and a V_{GS} bias of 3 V. Saturation mode was chosen since Ghoneim et al. were able to achieve a Nernstian response with zinc oxide, unlike in linear mode. The intrinsic drift of the transistor (Figure D.1), the drift of the reference electrode (Figure D.2), and the transistor sensitivity (Figure D.3) for a mV pH^{-1} conversion are shown in the Appendix, which also followed the procedure of Ghoneim et al.

Test solutions were made with Britton-Robinson's universal pH buffer[232] (0.04 M acetic acid [Glacial, PhEur, SAFC], 0.04 M phosphoric acid [85%, Reag. Ph. Eur, KMF optiChem], 0.04 M boric acid [GR, Merck]) by adding 1 M sodium hydroxide (pellets, Sigma-Aldrich) to adjust the pH. A 2 hour conditioning of the sensing electrode in the buffer without added sodium hydroxide (pH ∼1.9) was performed; in support of this conditioning step, the zeta potential of Ta_2O_5, deposited via atomic layer deposition (ALD), stabilized after 1 hour at pH 5.6 in 1 mM KCl, where ozone activation was performed before solution exposure.[236] For measuring the solution pH and conductivity, a MPC227 pH/Conductivity Meter (Mettler-Toledo, USA) was used with the InLab RoutinePro pH electrode (Mettler-Toledo, USA) and the InLab 731-ISM-2m conductivity electrode (Mettler-Toledo, USA). The pH was measured both before and after placement of the tantalum oxide electrode in the buffer solution, with the measured pH after removal of the tantalum oxide electrode from the solution taken for the EGFET plots. Solution conductivity was measured after the EGFET experiment was run. All pH and conductivity values are tabulated in Table 4.15.

Due to the insulative nature of tantalum oxide, and the high input impedance of the transistor, the drain current was recorded for 60 minutes after the tantalum oxide sensing layer and reference electrode were placed into solution. The tantalum oxide electrode and reference electrode were also shorted beforehand, in order to equalize the charge on the electrodes.

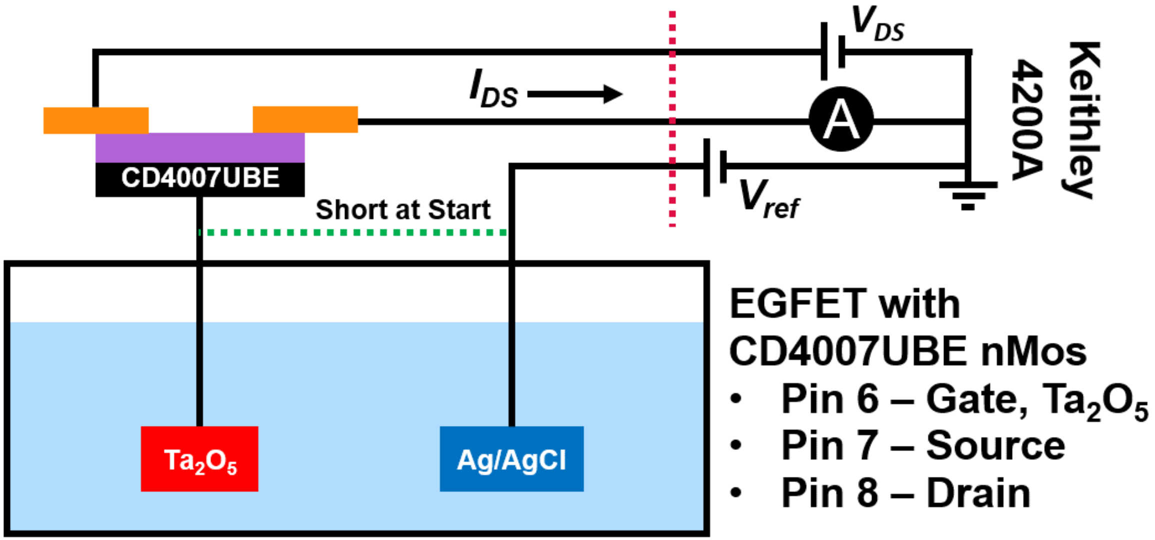

Figure 4.10 EGFET setup[235] in a dark Faraday cage with a CD4007UBE nMos transistor run in saturation mode with the Keithley 4200A-SCS Parameter Analyzer, using a V_{DS} bias of 5 V and a V_{GS} bias of 3 V. For resetting before measurement, the BASi RE-6 Ag/AgCl reference electrode containing a 3 M NaCl gel was shorted with the fabricated tantalum oxide extended-gate, where the extended-gate was connected to the gate pin of the transistor.

Table 4.15 pH and conductivity measurement of Britton-Robinson solutions, with values during the increase from pH **2** to pH **12** in blue, and the decrease from pH **12** to pH **2** in red. Solution conductivity measurements were made after the entire experiment was run.

Approximate pH	pH at $t = 0$ s	pH at $t = 3600$ s	Conductivity (mS cm^{-1})
2	2.01	2.01	3.53
3	3.06	2.96	1.71
4	4.01	3.96	2.00
5	5.05	5.02	3.47
6	5.98	6.00	4.29
7	7.00	7.00	5.07
8	8.02	8.01	5.75
9	8.97	9.01	6.48
10	10.05	10.06	7.45
11	11.11	11.03	7.95
12	12.06	12.04	10.54
11	11.09	11.1	7.95
10	10.06	9.96	7.45
9	9.03	9.07	6.48
8	8.09	8.03	5.75
7	7.04	7.01	5.07
6	6.05	5.96	4.29
5	5.07	5.01	3.47
4	4.02	4.02	2.00
3	3.04	3.01	1.71
2	2.05	2.02	3.53

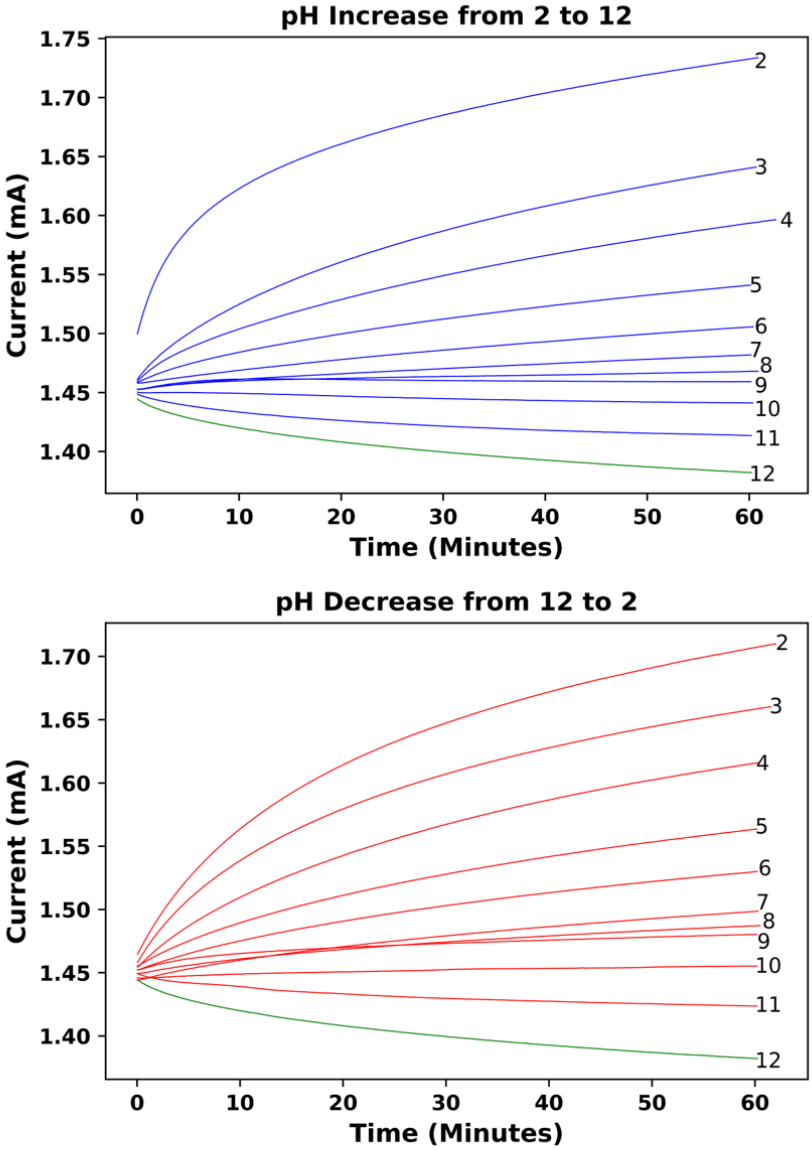

Figure 4.11 Continuous measurement of drain current from pH 2 to pH 12, and back to pH 2 (only one measurement at pH 12). After the 1 hour measuring period, the sensing electrode was rinsed with Milli-Q and N_2, and the circuit was reset in the new solution (sensing and reference electrodes shorted).

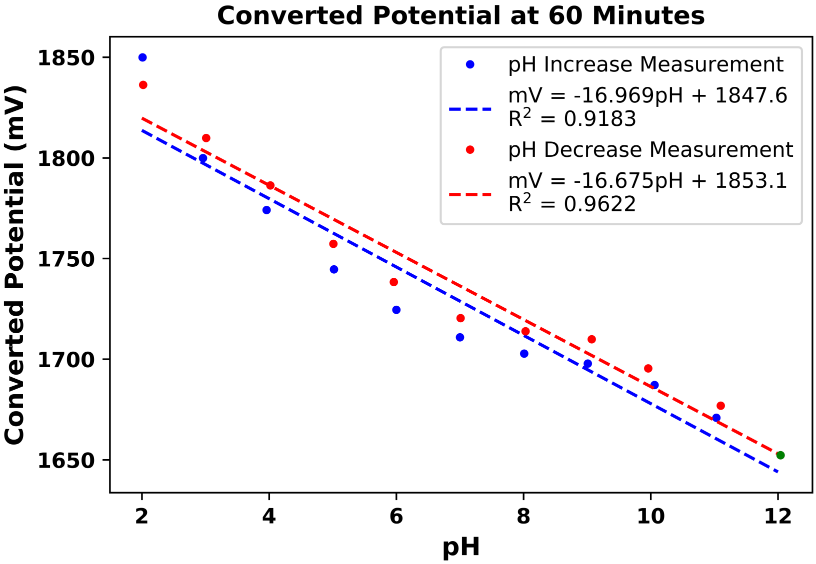

Figure 4.12 Drain current measurement taken at 1 hour, and then converted to mV in order to see linear sensitivity. After the 1 hour measuring period, the sensing electrode was rinsed with Milli-Q and N_2, and the circuit was reset in the new solution (sensing and reference electrodes shorted).

In measuring the drain current from pH 2 to pH 12, and back to pH 2, a pH sensitive slope takes more than 30 minutes as shown in Figure 4.11 (see pH 7, pH 8, and pH 9). The current drift appears to be much larger than the drift of the transistor or the reference electrode (see Figures D.1 and D.2 in the Appendix), showing that the sensing layer is largely responsible for the drift. Using the calculated transistor sensitivity value of $2.25 \times 10^{-5}\ \sqrt{\mathrm{A}}\ \mathrm{mV}^{-1}$ (see Figure D.3 in the Appendix), the pH sensitivity in mV was determined and plotted at 1 hour in Figure 4.12. Although the response time (at least 30 minutes) is much longer than for the more conductive zinc oxide sensor from Ghoneim et al. (about 2 minutes at pH 6, pH 7, and pH 8), the layer appears to show linear pH sensitivity, which is supported by the fact that the pH 3 solution has a lower conductivity than the pH 2 and pH 4 solutions. Using insulating oxides in an EGFET construction has been observed to reduce their pH response with respect to more conductive oxides,[237] although EGFET configurations can vary significantly. Given the linear sensitivity observed here, further investigations with an impedimetric sensor are warranted, and will be discussed in Chapter 5.

4.4.2 XPS for pH Buffer Resistance

XPS for a 125°C pre-anneal sample (Figure 4.13), a sample with photocuring and pre-/post-Annealing (Figure 4.14), and a sample with annealing, photocuring, tape mask removal, and solution exposure during the EGFET experiment (Figure 4.15) have tabulated atomic percentages in Table 4.16; 24 hours includes the 2 hour conditioning time, the 21 hour consecutive measurement time, and time taken in cleaning the electrodes and changing solutions. The XPS data shows that carbon decreases after photocuring and a post-anneal, and that tantalum oxide remains present after tape mask removal and buffer exposure. Furthermore, the oxidation state appears to be +5 for Ta_2O_5[238] in all steps of the process, showing a chemically stable tantalum oxide layer on the gold, even after the EGFET experiment. As with Experiment 1, the detected silicon in Table 4.16 may be from the laser ablation of PET with siloxane contamination.[233]

Table 4.16 XPS for Experiment 2.

Treatment	At% C 1s	At% O 1s	At% Si 2p	At% Ta 4f	At% P 2p
125°C Pre-Anneal	40.8	46.0	2.9	10.3	-
hv with Pre-/Post-Anneal	17.9	62.9	3.2	16.0	-
24 Hour pH Buffer	11.5	66.2	3.9	15.5	2.9

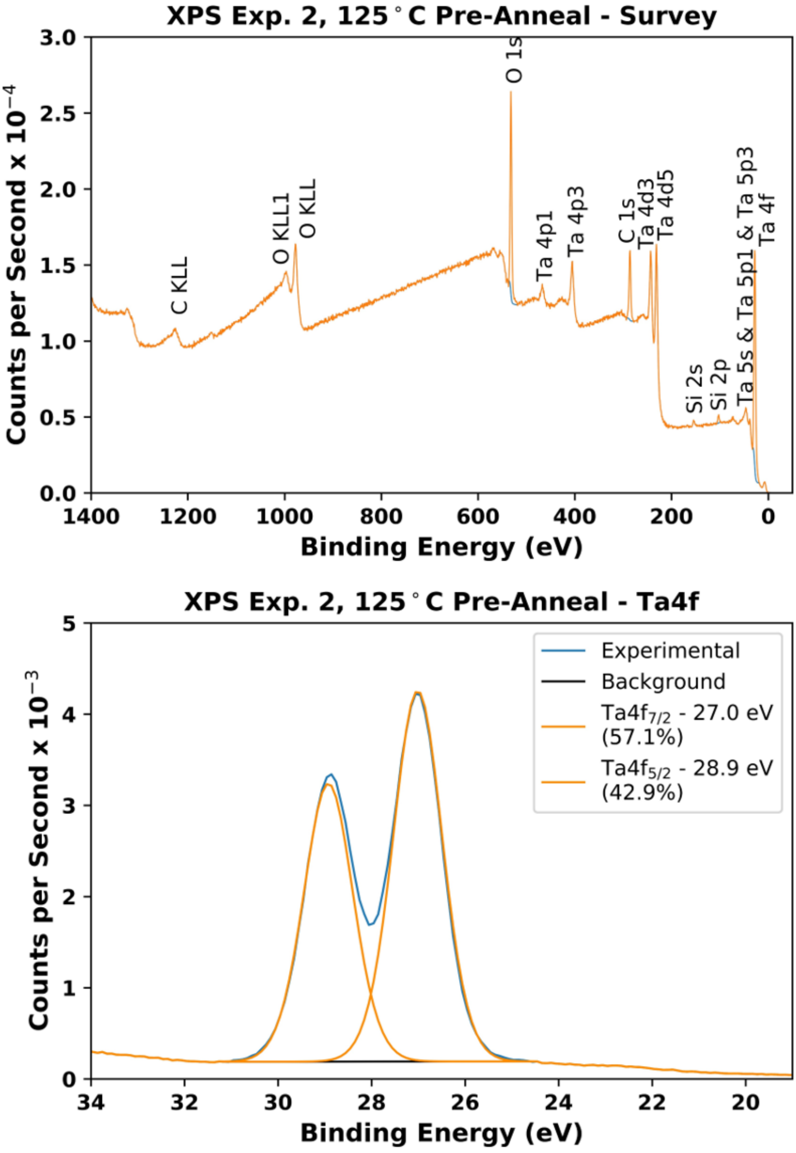

Figure 4.13 XPS after initial thermal anneal at 125°C.

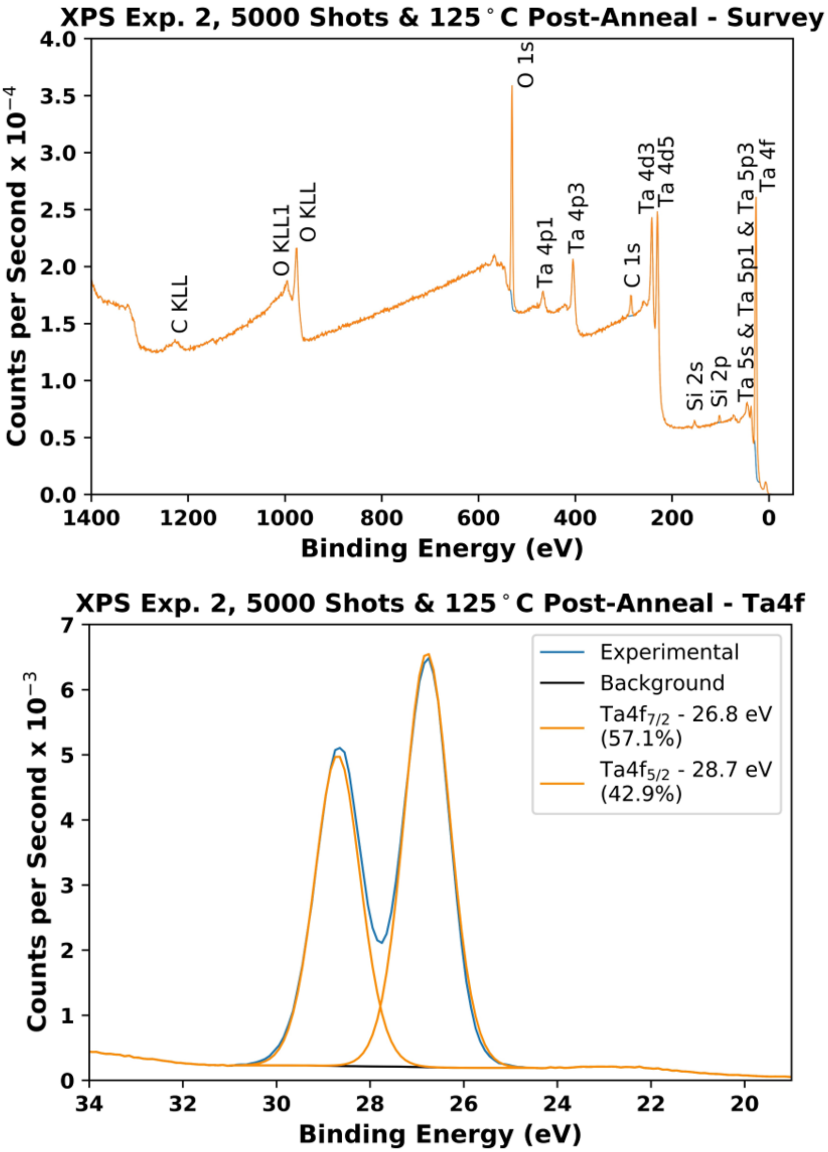

Figure 4.14 XPS after flash lamp annealing followed by another thermal anneal at 125°C.

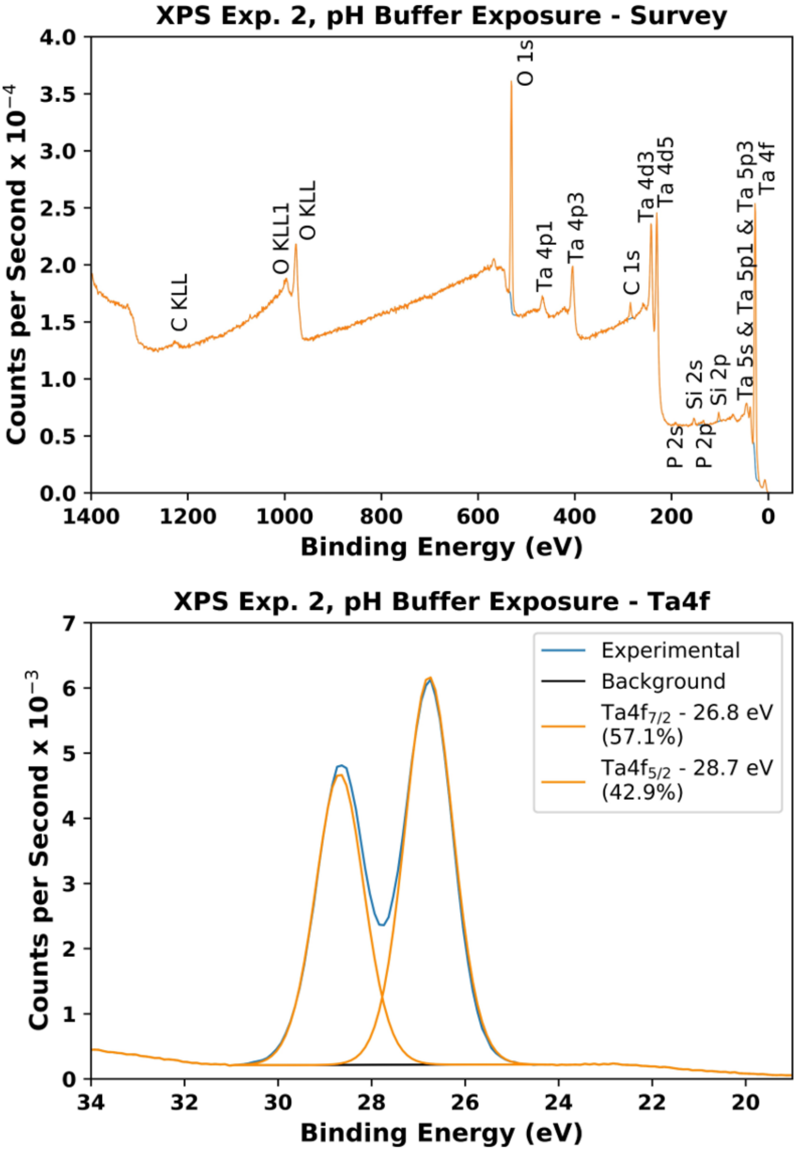

Figure 4.15 XPS after 24 hour pH buffer exposure and EGFET measurement.

4.5 Experiment 3 - Optimized Deposition

The inks used to deposit the layers for the final experiment are from Experiments 4 and 5 of Chapter 3, which describe the proposed optimal synthesis methods for the acetylacetone solution and the benzoylacetone solution, respectively. However, the benzoylacetone layers were only examined using UV-Vis, since benzoylacetone is a larger molecule than acetylacetone, and where the use of benzoylacetone would likely lead to more unwanted carbon impurities.[185] The viscosity and surface tension measurements for the inks are from separate syntheses in Chapter 3 (Experiment 8 for acetylacetone and Experiment 9 for benzoylacetone) and are shown in Table 3.1. Layers were printed to be uniform, where after printing all substrates were thermally annealed on a hot plate at 125°C with a 1 hour ramp and a 2 hour hold, which was followed by photocuring for the phototreated samples.

The surface temperatures of the substrates for the used shot parameters in Table 4.14, estimated by using the SimPulse 2.5 software, plateau at a firing frequency of 0.333 Hz and an operating temperature of 25°C as follows: 500 µm thick a-SiO_2, ∼25°C; 500 µm thick c-Si, ∼60°C; 80 µm thick PET, ∼25°C; 80 µm thick PET with 5 nm Ti adhesion layer and 50 nm Au layer, ∼300°C.

4.5.1 UV-Vis for Acetylacetone and Benzoylacetone Layers

Amorphous silicon dioxide (a-SiO_2), being 0.5 mm thick, was selected as the best substrate for measuring in the near UV range, as PET absorbs substantially more than a-SiO_2 in this range. Before printing, the substrate's surface was plasma treated with the parameters in Table 4.17. Then for printing, the parameters for both the acetylacetone and benzoylacetone based films are shown in Table 4.18. The acetylacetone ink was 706 mg of DEGEE (70 wt%) vortexed with 308 mg of product (30 wt%), while the benzoylacetone ink was 732 mg of DEGEE (69 wt%) vortexed with 328 mg of product (31 wt%).

Table 4.17 Surface plasma treatment for a-SiO_2 used in the UV-Vis measurements.

Gas	Pressure (mbar)	Power (W)	Time (s)
Argon	0.6	150	300

Table 4.18 Printing parameters on 0.5 mm a-SiO_2 for both the acetylacetone and benzoylacetone layers used in the UV-Vis measurements (head height at 1.0 mm).

Waveform (µs)	Voltage (V)	Frequency (Hz)	Pitch (µm)	Dimensions (Drops)
1 - 10 - 1	25	1000	75	400 × 220

UV-Vis absorption spectra are plotted in Figure 4.16 for acetylacetone and Figure 4.17 for benzoylacetone. The absorption peaks for the unbound β-diketones' $\pi \rightarrow \pi^*$ transition peaks,[239] along with the Ta-bound peaks, are shown in Table 4.19. In the acetylacetone layer, exposure to 1000 shots results in the global maximum redshifting to about 212 nm, while for benzoylacetone more than 1000 shots are required. This difference may be due to the benzoylacetone film being denser, or perhaps due to benzoylacetone being less volatile as it is solid at room temperature (acetylacetone is liquid at room temperature). The global maxima peaks[183,184] and the local maxima for the β-diketones' $\pi \rightarrow \pi^*$ transition peaks[185–187] for photocured, tantalum oxide films all agree with literature. As expected, the Ta-bound peaks are redshifted relative to the unbound peaks.

Table 4.19 $\pi \rightarrow \pi^*$ absorption peaks (nm) for acetylacetone and benzoylacetone as unbound molecules,[239] and when bound to tantalum on a-SiO_2.

β-Diketone	$\pi \rightarrow \pi^*$ unbound	$\pi \rightarrow \pi^*$ Ta-bound
Acetylacetone	~270	319
Benzoylacetone	~310	348

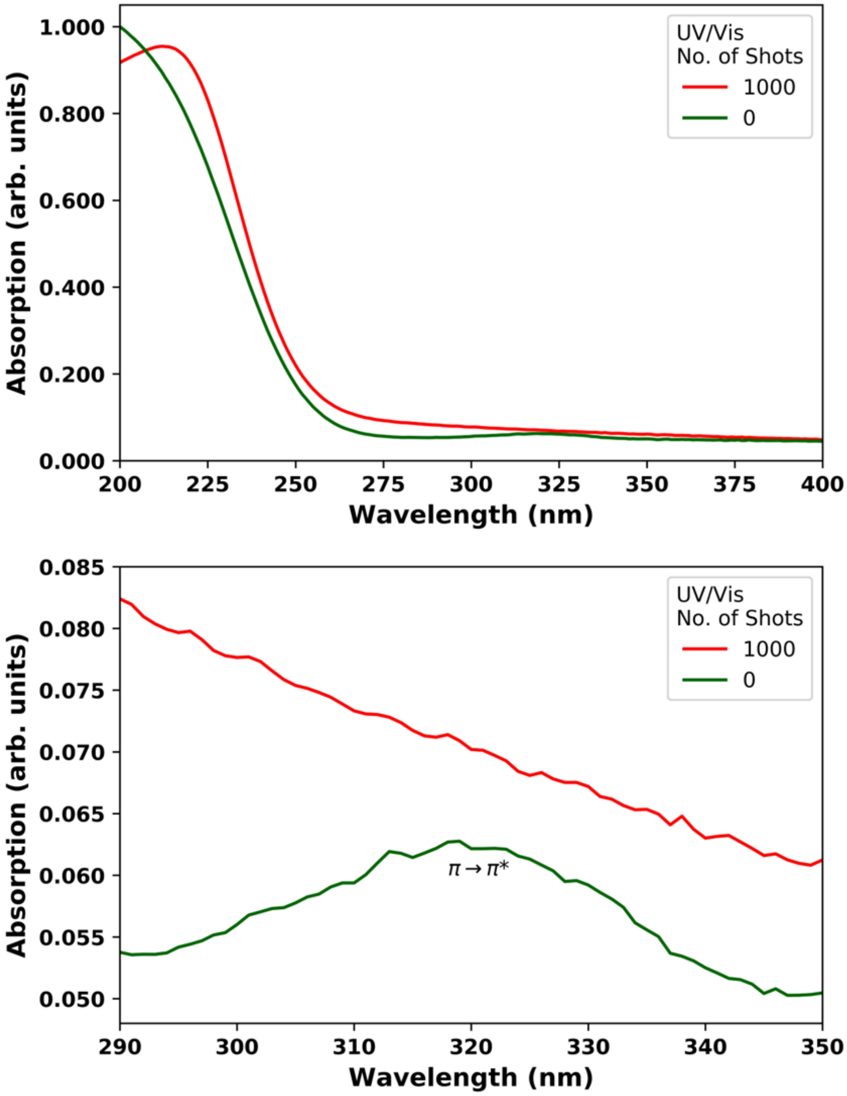

Figure 4.16 UV-Vis absorption spectrum for the acetylacetone based film and different treatments (© The Royal Society of Chemistry 2020).[136,137]

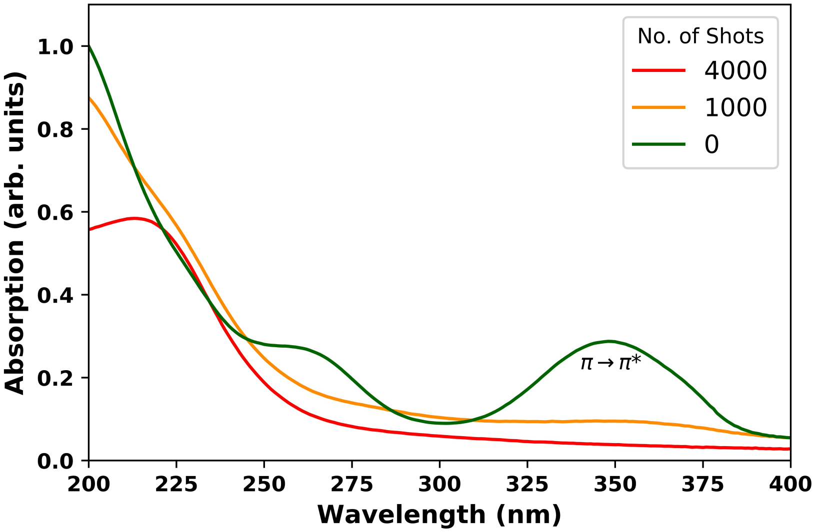

Figure 4.17 UV-Vis absorption spectrum for the benzoylacetone based film and different treatments (© The Royal Society of Chemistry 2020).[136,137]

4.5.2 Raman and XRD for Acetylacetone Layer

Amorphous silicon dioxide (a-SiO_2), being 0.5 mm thick, was selected as having minimal interference for both the Raman and XRD measurements. Before printing, the substrate's surface was plasma treated with the parameters in Table 4.20. The printing parameters are then shown in Table 4.21, where the droplet density was increased from the UV-Vis sample in order to obtain better Raman spectra. The concentration of the product in the ink was also increased for better spectra, where 611 mg of DEGEE (60 wt%) was vortexed with 404 mg of product (40 wt%).

Table 4.20 Surface plasma treatment for a-SiO_2 used in the Raman and XRD measurements.

Gas	Pressure (mbar)	Power (W)	Time (s)
Oxygen	0.6	150	300

Table 4.21 Printing parameters on 0.5 mm a-SiO_2 for the acetylacetone layer used in the Raman and XRD measurements (head height at 1.0 mm).

Waveform (µs)	Voltage (V)	Frequency (Hz)	Pitch (µm)	Dimensions (Drops)
1 - 10 - 1	25	1000	70	450 × 275

Prior studies have indicated that amorphous tantalum oxide films have two characteristic bands, one being the O-3Ta band for the stretching and bending of triple-coordinated oxygen at 670 cm^{-1}, and the other being the O-2Ta band for the stretching of double-coordinated oxygen at 800 cm^{-1}.[240,241] In crystalline samples, other peaks in the 400 cm^{-1} to 900 cm^{-1} range may arise, which is the range for various coupled modes involving the stretching and bending of different Ta-O bonds.

The measured Raman shifts in Table 4.22 and the Raman and XRD spectra in Figure 4.18 appear to indicate that the deposited layer is amorphous after photocuring, where the formation of a crystalline layer would require an annealing temperature of over 600°C.[200,240,241] The Raman spectra were obtained through a hyperspectral analysis of the measured interface and subsequent subtraction of the remnant a-SiO_2 spectrum. The a-SiO_2 spectrum, along with the photocured tantalum oxide layer and the precursors, are shown in Figure 4.19. The depth scans that distinguish the photocured tantalum oxide layer from the a-SiO_2 substrate show an observed thickness which is thicker than the actual value, as the Z-resolution is too low in optical microscopy.

Before photocuring (0 shots), other peaks appear to be present which disappear after photocuring on the same sample (1000 shots), especially where the C-H band at ~2800 cm^{-1} appears to diminish after photocuring. The precursor peaks also appear to be largely absent in the 1000 shot spectrum. In combination with the UV-Vis spectra, these results show that tantalum oxide arises through the decomposition of the acetylacetonate complex.

Table 4.22 Raman shifts (cm^{-1}) for the observed amorphous tantalum oxide bands and with the C-H band indicating the presence of organic molecules.[240,241]

O-3Ta	O-2Ta	C-H
~670	~800	~2800

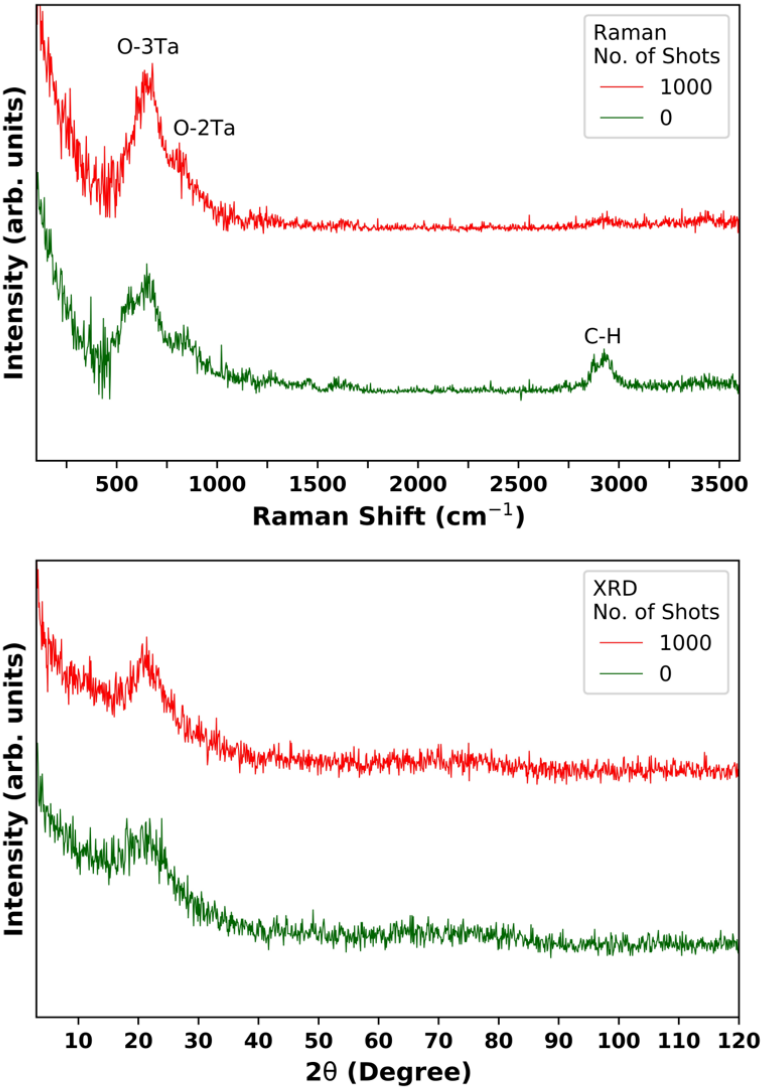

Figure 4.18 Raman and XRD spectra for the acetylacetone based film and different treatments (© The Royal Society of Chemistry 2020).[136,137]

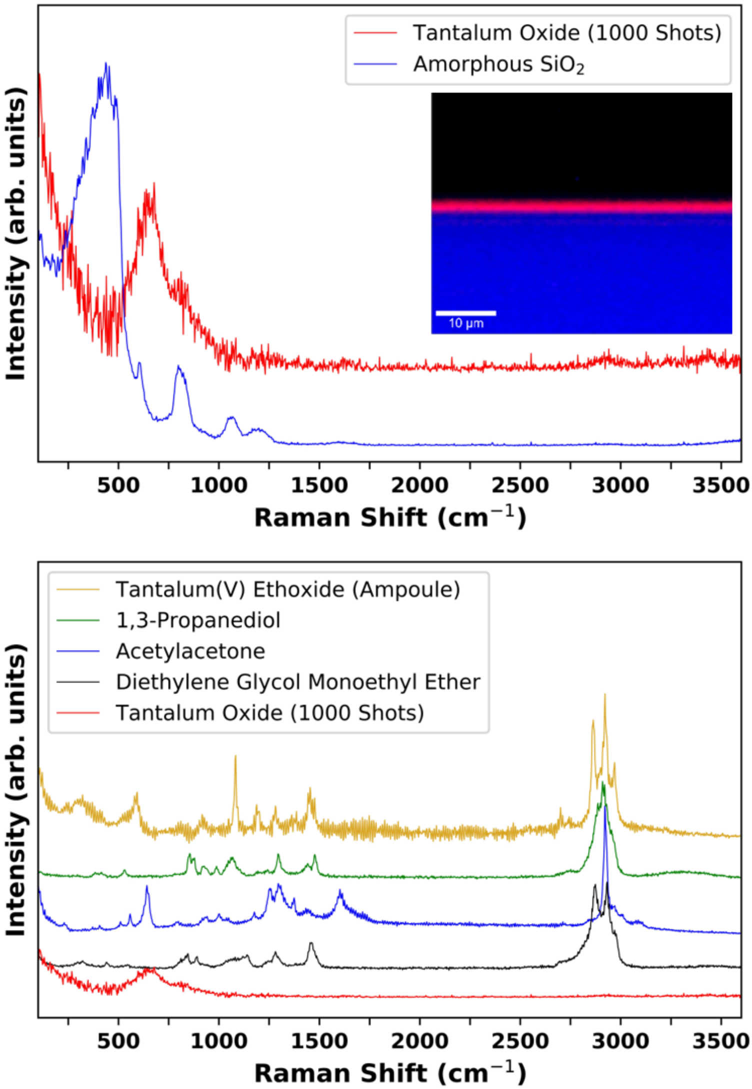

Figure 4.19 Raman spectra of the photocured acetylacetone based film versus a-SiO_2 and solution precursors (© The Royal Society of Chemistry 2020).[136,137]

4.5.3 RBS/NRA for Acetylacetone Layer

Crystalline silicon wafer (c-Si), being 0.5 mm thick, was selected as the best substrate for minimizing excess oxygen and carbon. The substrate is also made of lower mass nuclei than tantalum, which is important for distinguishing peaks in RBS. Before printing, the substrate's surface was plasma treated with the parameters in Table 4.23. The printing parameters are then shown in Table 4.24. The acetylacetone ink was 622 mg of DEGEE (60 wt%) vortexed with 414 mg of product (40 wt%).

Table 4.23 Surface plasma treatment for c-Si used in the RBS/NRA measurements.

Gas	Pressure (mbar)	Power (W)	Time (s)
Argon	0.6	150	300

Table 4.24 Printing parameters on 0.5 mm c-Si for the acetylacetone layer used in the RBS/NRA measurements (head height at 1.0 mm).

Waveform (µs)	Voltage (V)	Frequency (Hz)	Pitch (µm)	Dimensions (Drops)
1 - 10 - 1	25	1000	70	75 × 75

Sharp peak forms are shown for all separate samples in Figures 4.20 and 4.21, with the samples being the 125°C pre-anneal treatment (0 shots), the 1000 shot treatment with pre-anneal, the 5000 shot treatment with pre-anneal, and the 125°C post-anneal treatment (1 hour ramp, 2 hour hold) with a pre-anneal and 5000 shots. All detected material resides in the first resolution bin of 5.5×10^{21} atoms per m^2, with the layer thicknesses being in the range from 1.0×10^{21} atoms per m^2 to 1.5×10^{21} atoms per m^2.

The tabulated atomic percentages for these samples are in Table 4.25, where the carbon content appears to decrease after an initial phototreatment of 1000 shots. However, as these were all different samples, care must be taken in drawing a direct conclusion between photocuring and carbon content. The amount of detected carbon is similar to that of a few monolayers of graphite, but surface contamination may also influence the carbon measurement. The O/Ta values, which ideally would be 2.5, are larger for all samples and exceed the values for anodic tantalum oxide NRA oxygen standards;[242–244] additionally, even though the samples have different O/Ta values, the ratio remains constant within uncertainties. The observed extra oxygen could stem from SiO_2 formation, organic molecules, or adsorbed water. Furthermore, with the limited depth resolution, some of the oxygen may be present near the c-Si surface or within the substrate.

Table 4.25 RBS/NRA observed atom content (10 at% relative uncertainty due to the counting statistics of ^{16}O NRA, assuming homogeneous layer) with a c-Si substrate, where the layer thickness has units of 10^{19} at. per m^3. The O/Ta ratio has an approximate error of ±0.5.

Treatment	at% C	at% O	at% Ta	Thickness	O/Ta
125°C Pre-Anneal	10.9	70.7	18.4	149	3.8
1000 Shots	3.3	76.7	19.9	143	3.9
5000 Shots	5.0	71.8	23.2	113	3.1
125°C Post-Anneal	5.2	73.7	21.1	123	3.5

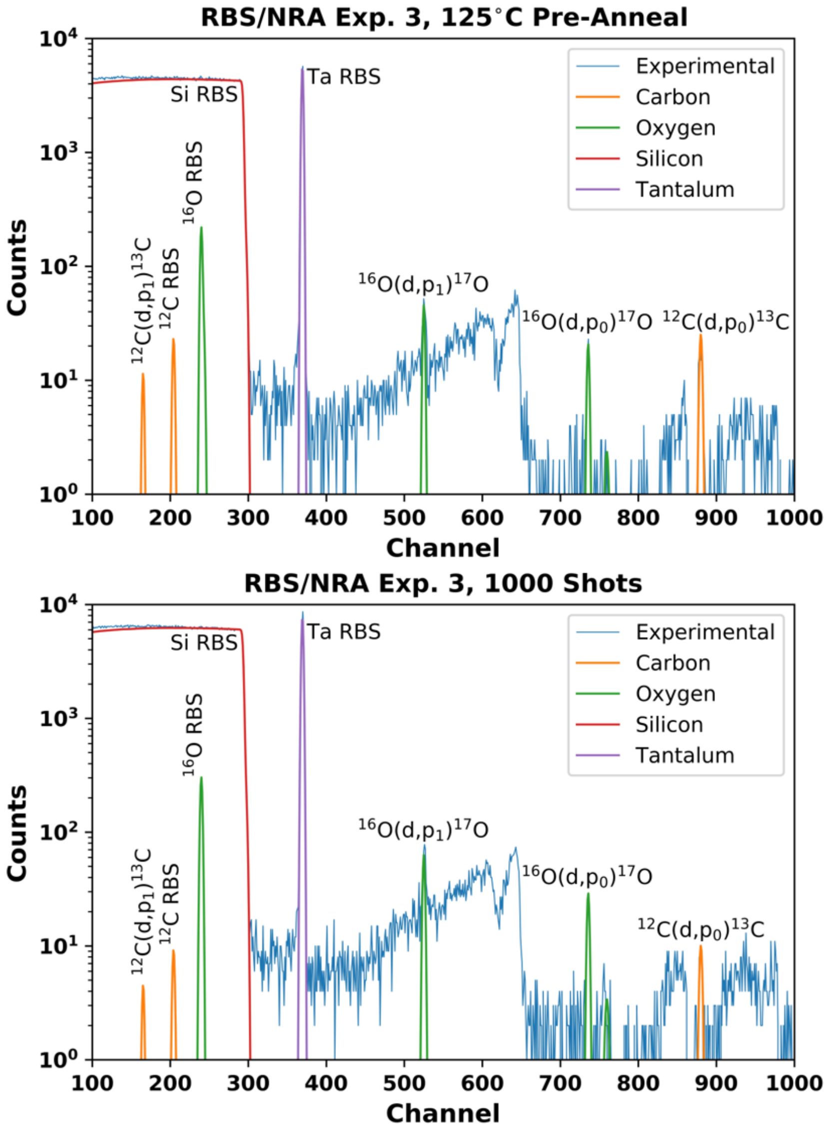

Figure 4.20 RBS/NRA spectra of "125°C pre-anneal" and "1000 shots with pre-anneal" samples (© The Royal Society of Chemistry 2020).[136,137]

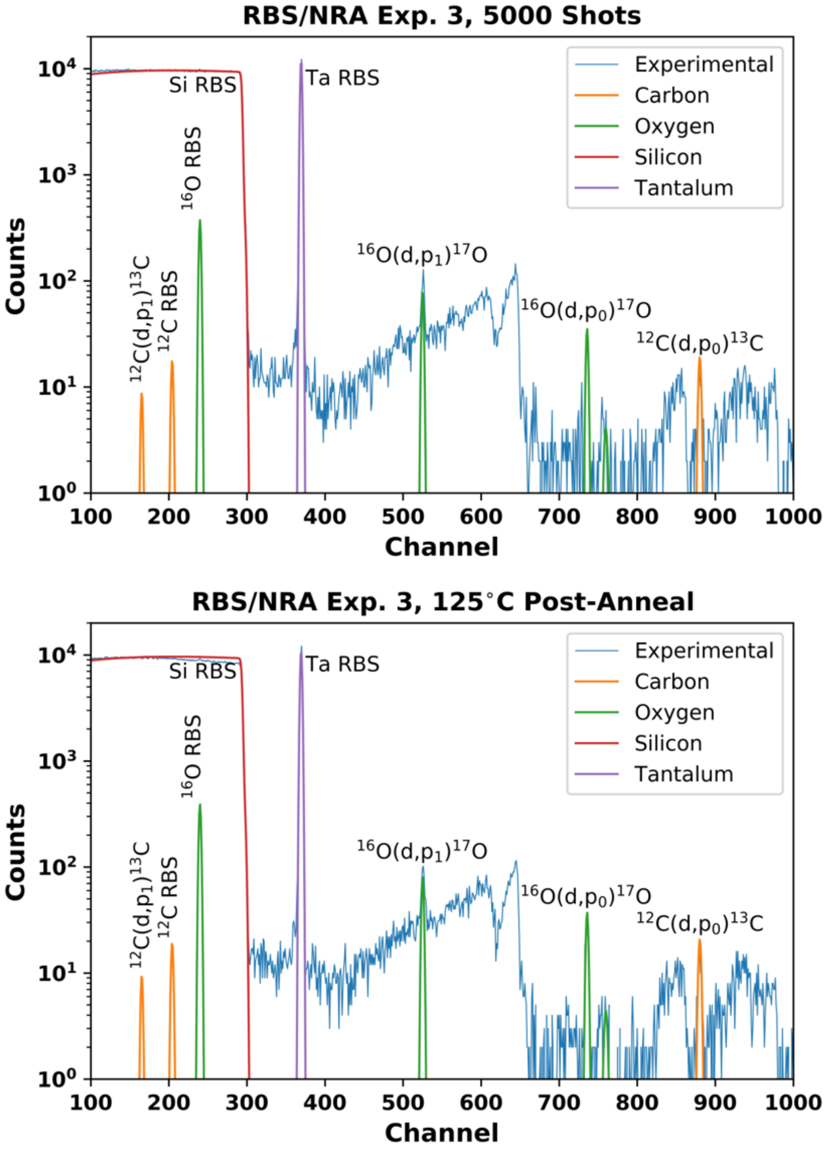

Figure 4.21 RBS/NRA spectra of "5000 shots with pre-anneal" and "125°C post-anneal (pre-anneal and 5000 shots before)" samples.

4.5.4 XPS, LCR Meter, and FIB/SEM for Acetylacetone Layer

Wet-etched Au/Ti/PET foil, with less than 50 nm of gold deposited on a ∼5 nm titanium adhesion layer (metallization via electron-beam physical vapor deposition) on 80 µm PET (DuPont PCS), was the target substrate for the pH sensors as the substrate is flexible enough for roll-to-roll processing. The wet-etched, IDE structures consisted of 250 digits in a 4 mm × 4 mm area, with a digit length of ∼3992 µm and a width/gap length of ∼8 µm. Before printing, the substrate's surface was plasma treated with the parameters in Table 4.26. The printing parameters are then shown in Table 4.27. The acetylacetone ink was 622 mg of DEGEE (60 wt%) vortexed with 414 mg of product (40 wt%).

Table 4.26 Surface plasma treatment for Au/Ti/PET used in the XPS and LCR meter measurements.

Gas	Pressure (mbar)	Power (W)	Time (s)
Oxygen	0.6	150	120

Table 4.27 Printing parameters on Au/Ti/PET for the acetylacetone layer used in the XPS and LCR meter measurements (head height at 1.0 mm).

Waveform (µs)	Voltage (V)	Frequency (Hz)	Pitch (µm)	Dimensions (Drops)
1 - 10 - 1	25	1000	150	35 × 31

The XPS survey spectra for all samples are plotted in Figures 4.22 and 4.23, with the samples being the 125°C pre-anneal treatment (0 shots), the 1000 shot treatment with pre-anneal, the 5000 shot treatment with pre-anneal, and the 125°C post-anneal treatment (1 hour ramp, 2 hour hold) with a pre-anneal and 5000 shots. The atomic quantities obtained from the spectra are listed in Table 4.28.

The binding energies for Ta 4f are plotted in Figures 4.24 and 4.25, where the binding energies at ~26.8 eV for Ta $4f_{7/2}$ (57.1% Ta 4f area) and ~28.7 eV for Ta $4f_{5/2}$ (42.9% Ta 4f area) are visible in all samples, demonstrating that Ta stays at one oxidation state throughout thermal annealing and photocuring, which would be +5 for Ta_2O_5.[238]

The O 1s binding energies are plotted in Figures 4.26 and 4.27, which show an increase in oxide oxygen and a decrease in organic oxygen after 1000 shots.[245] Further treatment at 5000 shots and with a post-anneal do not appear to affect the oxygen and carbon content within error. The oxide O/Ta ratios are listed in Table 4.28, which stay around a value of 3.0 (ideally this value should be 2.5 for Ta_2O_5). The observed oxygen excess may be due to the fact that XPS is a surface characterization technique, which would have a higher oxygen content than the bulk oxide.

The C 1s binding energies are plotted and fitted[246] in Figures 4.28 and 4.29. Acetylated 1,3-propanediol, and thus the formation of 3-hydroxypropyl acetate, may be detected with the ester groups in all samples. However, the surface likely has contamination from the environment, and the ester groups may come from organic contaminants.

Table 4.28 XPS atom content with deposited layer on wet-etched Au/Ti/PET foil (15 at% relative uncertainty, assuming homogeneous layer). XPS is a surface characterization technique, unlike RBS/NRA which penetrates the material further, and is likely why the at% values for both techniques are quite different. The tantalum oxide O/Ta values are in excess (ideally O/Ta = 2.5), but have an error which is difficult to determine due to the overlapping O 1s integrals.

Treatment	At% C 1s	At% O 1s	At% Ta 4f	At% Au 4f	Oxide O/Ta
125°C Pre-Anneal	40.9	47.9	10.7	0.4	3.1
1000 Shots	16.5	64.2	17.4	1.9	3.0
5000 Shots	15.2	65.2	17.4	2.2	3.0
125°C Post-Anneal	20.2	62.4	15.5	1.8	3.1

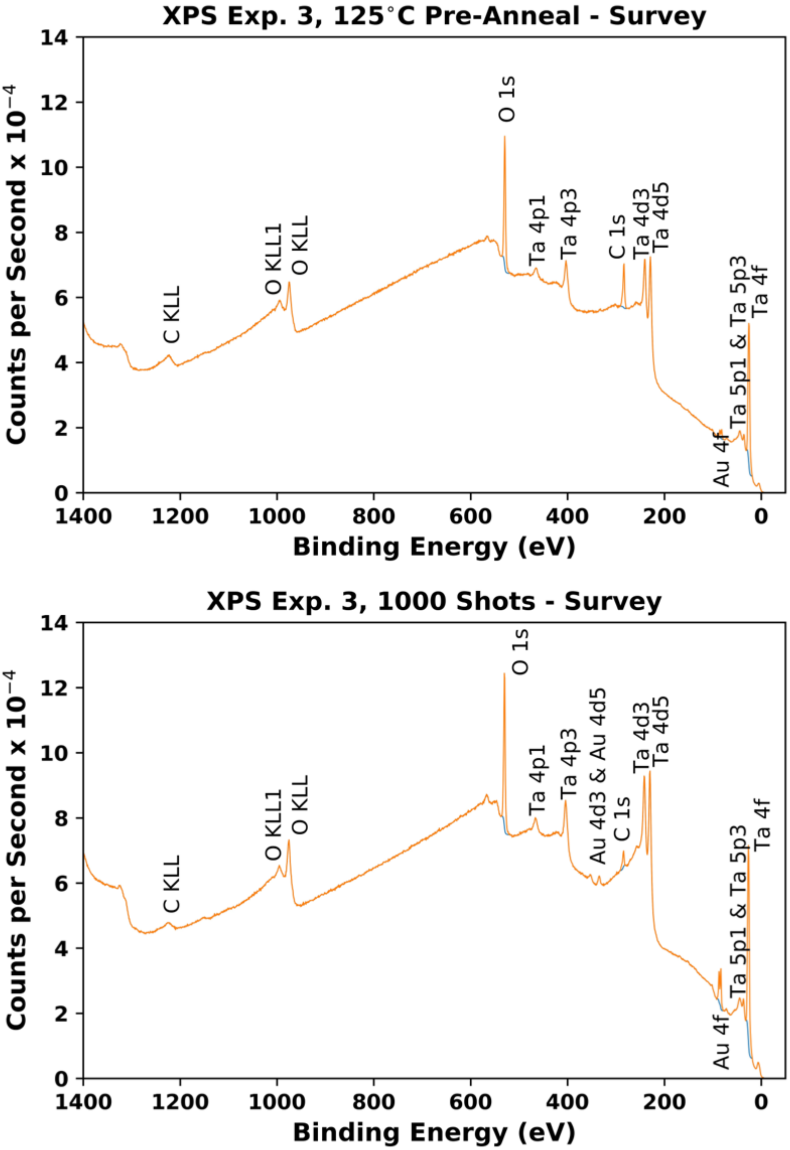

Figure 4.22 XPS survey spectra of "125°C pre-anneal" and "1000 shots with pre-anneal" samples (© The Royal Society of Chemistry 2020).[136,137]

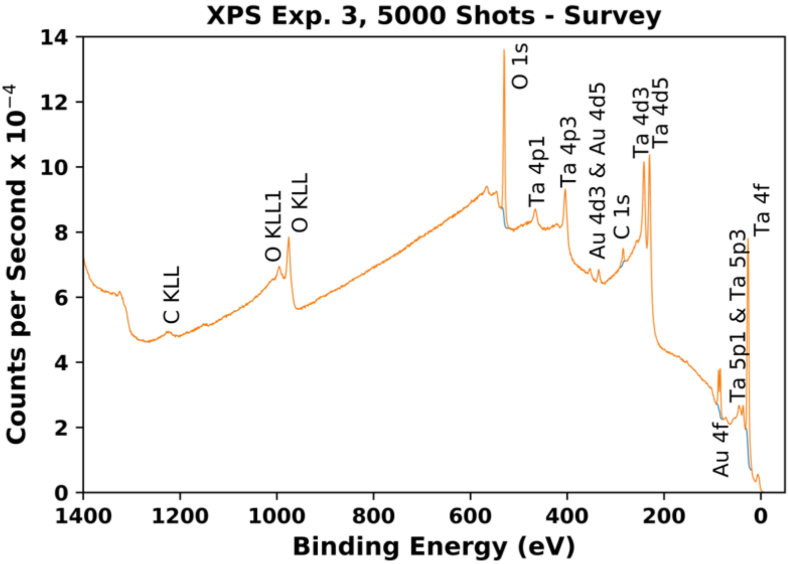

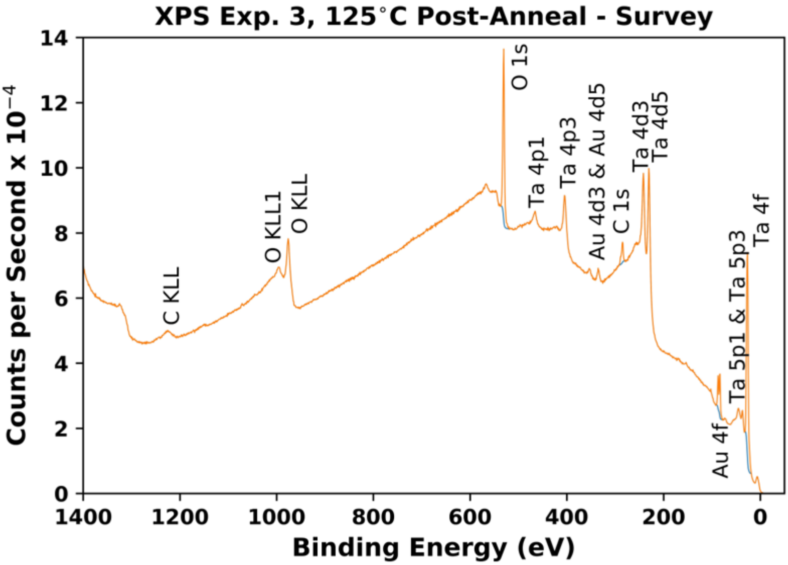

Figure 4.23 XPS survey spectra of "5000 shots with pre-anneal" and "125°C post-anneal (pre-anneal and 5000 shots before)" samples.

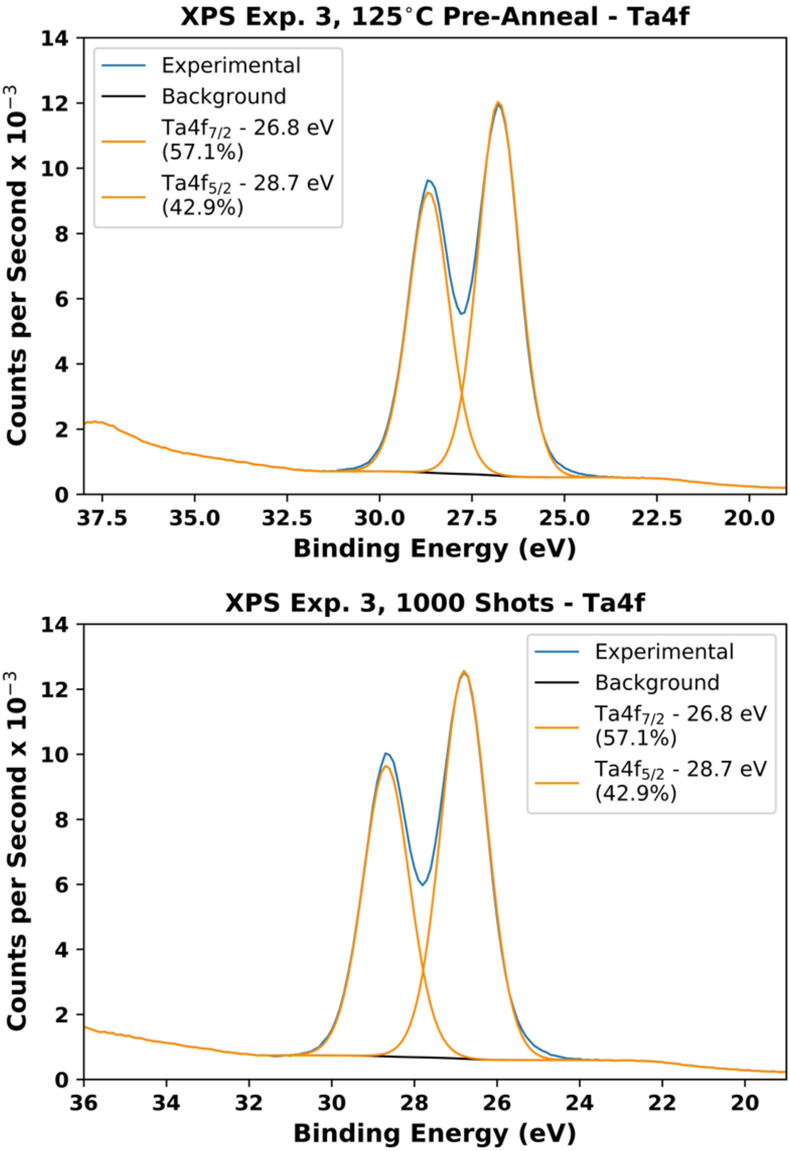

Figure 4.24 XPS Ta 4f spectra of “125°C pre-anneal” and “1000 shots with pre-anneal” samples (© The Royal Society of Chemistry 2020).[136,137]

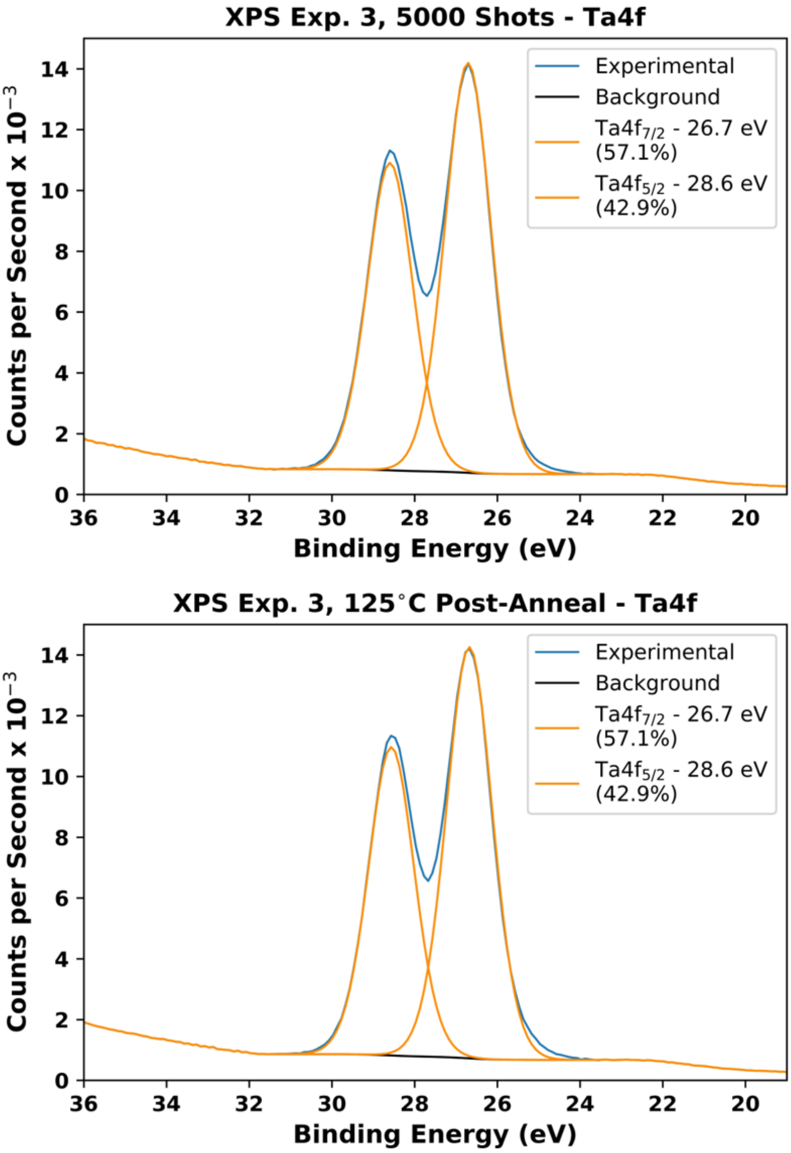

Figure 4.25 XPS Ta 4f spectra of “5000 shots with pre-anneal” and “125°C post-anneal (pre-anneal and 5000 shots before)” samples.

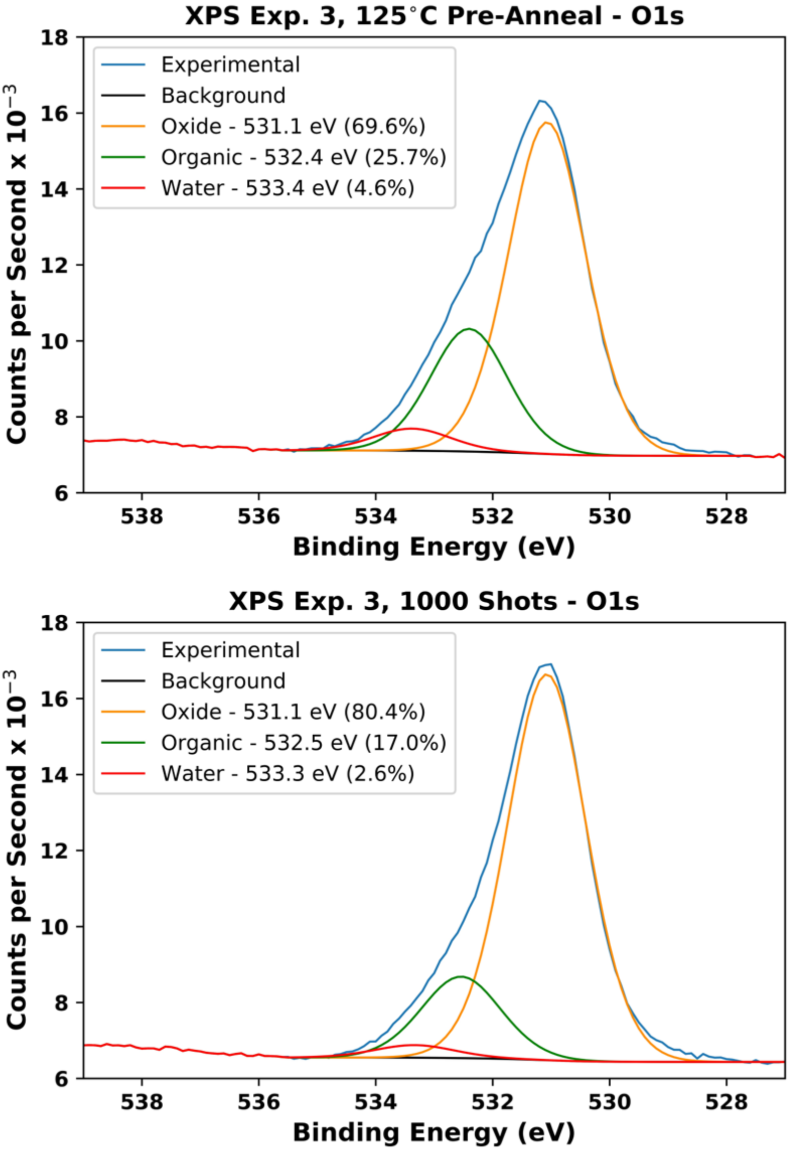

Figure 4.26 XPS O 1s spectra of "125°C pre-anneal" and "1000 shots with pre-anneal" samples (© The Royal Society of Chemistry 2020).[136,137]

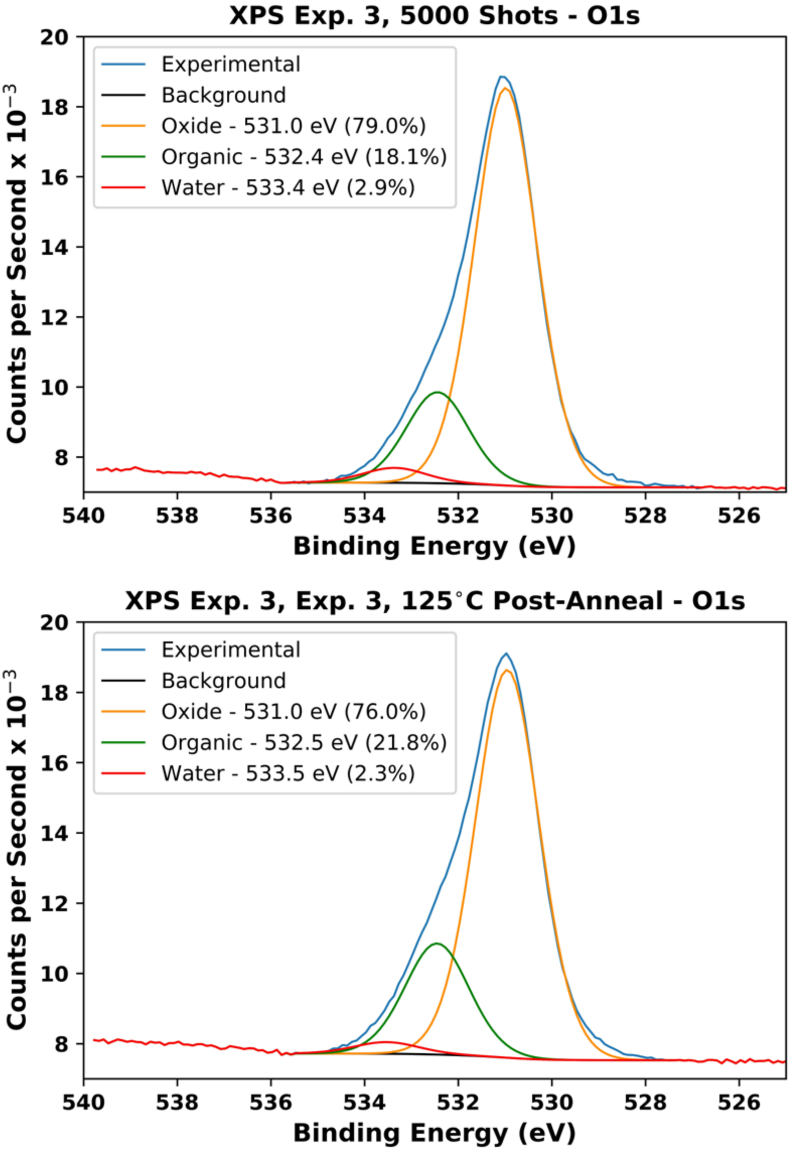

Figure 4.27 XPS O 1s spectra of "5000 shots with pre-anneal" and "125°C post-anneal (pre-anneal and 5000 shots before)" samples.

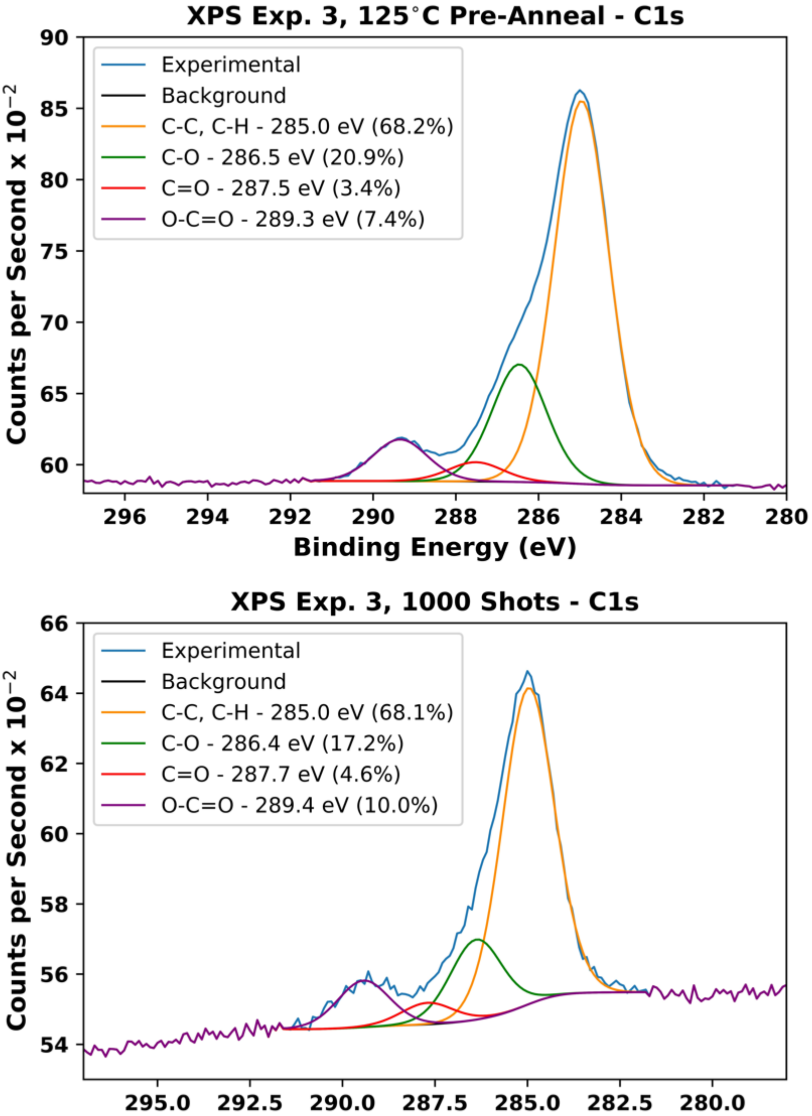

Figure 4.28 XPS C 1s spectra of "125°C pre-anneal" and "1000 shots with pre-anneal" samples (© The Royal Society of Chemistry 2020).[136,137]

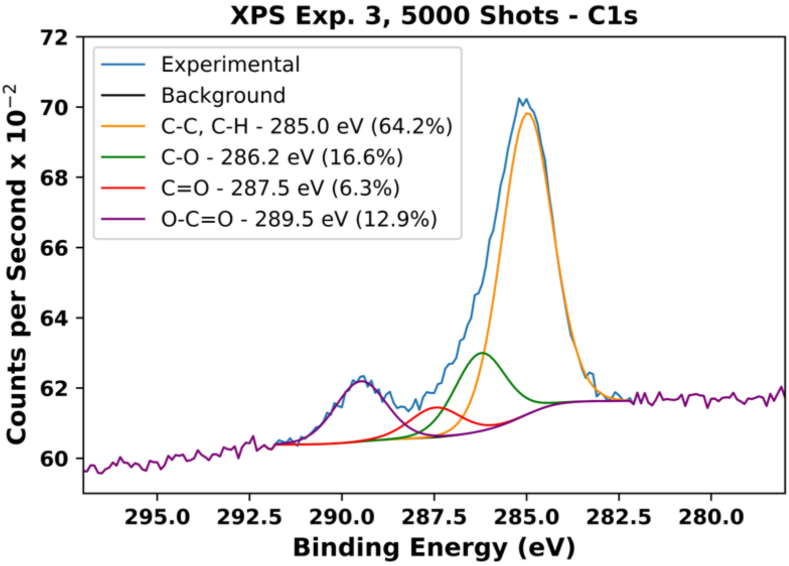

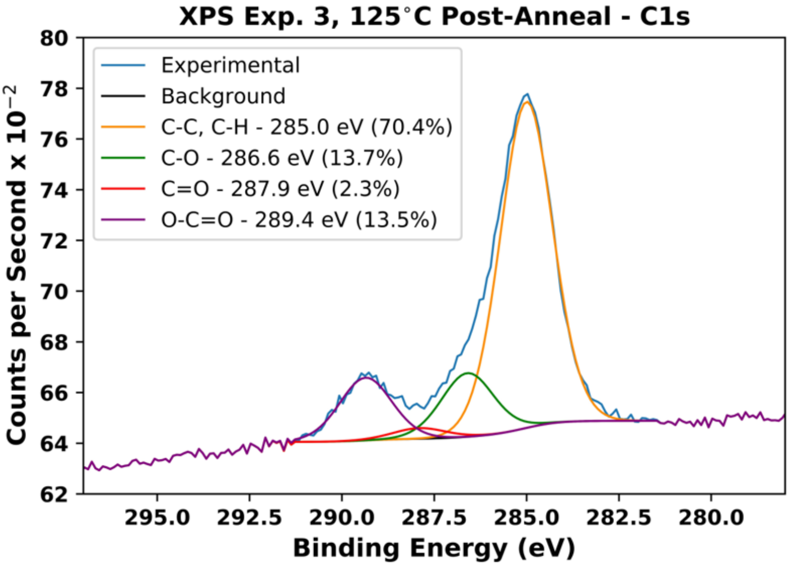

Figure 4.29 XPS C 1s spectra of “5000 shots with pre-anneal” and “125°C post-anneal (pre-anneal and 5000 shots before)” samples.

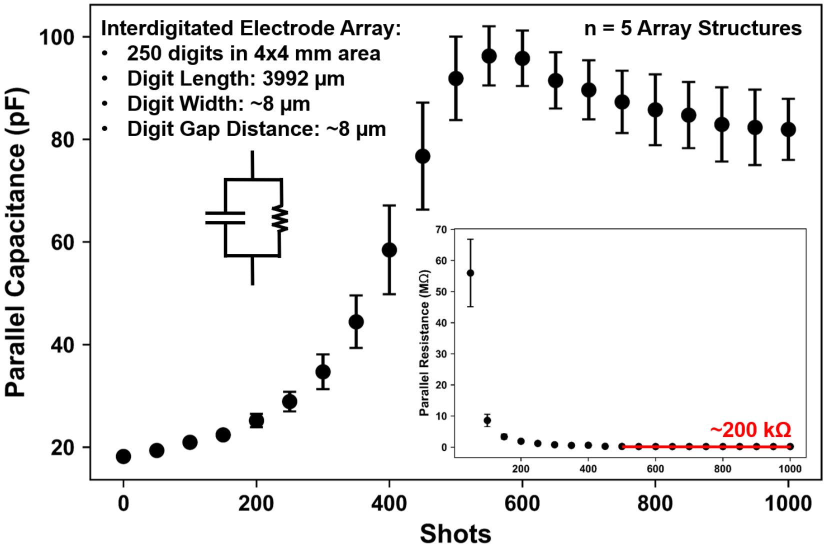

Figure 4.30 Parallel capacitance and parallel resistance measured with an LCR meter (© The Royal Society of Chemistry 2020).[136,137]

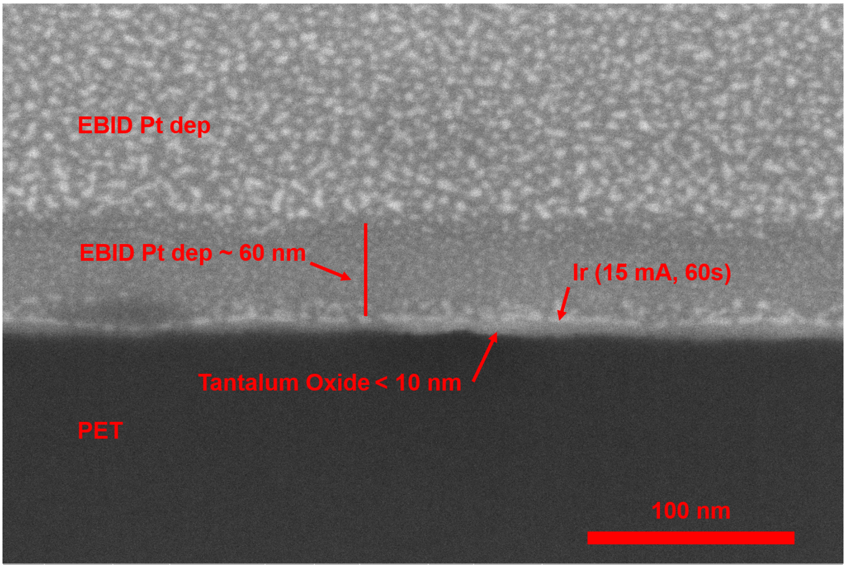

Figure 4.31 FIB/SEM of a sample exposed to a 125°C pre-anneal, 5000 flash lamp shots, and a 125°C post-anneal (© The Royal Society of Chemistry 2020).[136,137]

The parallel capacitance and resistance values are shown in Figure 4.30, where the parallel capacitance peaks after about 500 shots and it then levels off at roughly 80 pF. The parallel resistance decreases to about 200 kΩ and then flattens out, where the leakage current could be caused by oxygen vacancies, defects, or carbon impurities.[183,185,229,247,248]

FIB sectioning and SEM of a sample exposed to all treatments (thermal pre-anneal, 5000 shots, and a thermal post-anneal) is shown in Figure 4.31, with a tantalum oxide layer being less than 10 nm thick on the PET between the gold digits. Due to the “coffee-ring effect” with inkjet printing, the thickness likely varies over the entire sample, where the layer would be thicker at the edges and thinner in the middle.

4.6 Discussion

Through finding the optimal flash lamp shot parameters in Experiment 1 (with subsequent improvements in the parameters for better reproducibility), demonstrating resistance to acidic and basic solutions in Experiment 2, and pursuing more detailed characterizations in Experiment 3 with layers derived from optimally synthesized solutions, a flash lamp annealing procedure for the produced tantalum oxide films has been outlined in this chapter. Future experiments should involve determining the dielectric constant and refractive index of the tantalum oxide layers as a function of flash lamp shots, which would require accurate thickness measurements (which unfortunately due to a lack of instrumentation, were not performed here). One possible way to measure the dielectric constant would be to produce many metal-insulator-metal samples, each with a different amount of flash lamp treatment, and then determine the dielectric constant as Matavž et al. did for inkjet printed, sol-gel derived, and doped tantalum oxide films.[218] However, the exact layer geometry would need to be known for such a determination, and the layer would need to be free of defects. Furthermore, the layer thickness may also affect the rate of diffusion of oxygen into the layer and carbon volatiles out of the layer, which may further affect the layer properties.

Chapter Five

Immittance Analysis for pH Sensing

This chapter will begin with a short introduction to immittance spectroscopy, which encompasses impedance, admittance, complex capacitance, and modulus (the last of which being the inverse of complex capacitance, which is not to be confused with the impedance magnitude in Bode spectra). The derivation of modulus and the calculation of its spectra will not be performed here, since the spectra were not used in the analysis. Following the immittance spectroscopy discussion will be the derivation of the equivalent circuit, the experimental methods, the results, and finally a concluding discussion. Parts of this chapter have been published elsewhere.[220]

5.1 Immittance Spectroscopy

This introduction to immittance spectroscopy will use relevant information from *Immittance Spectroscopy - Applications to Material Systems*,[249] specifically Chapter 1 for derivations, Chapter 4 for interpretation of admittance and complex capacitance, and Chapter 7 for Bode plane analysis.

In order to simplify trigonometric functions used to describe alternating current (AC), Euler's formula can be used where $j = \sqrt{-1}$:

$$\exp(jx) = \cos(x) + j\sin(x) \tag{5.1}$$

Due to this relation, the voltage $V\left(t\right)$ and current $I\left(t\right)$ of a periodic signal can be represented below with t as time, θ as the lag angle between current and voltage, and $\omega = 2\pi f$ with f as frequency:

$$V\left(t\right) = V_0 \exp\left(j\omega t\right) \;\; \text{and} \;\; I\left(t\right) = I_0 \exp\left(j\left[\omega t - \theta\right]\right) = I_0 \exp\left(j\omega t - j\theta\right) \tag{5.2}$$

In a linear system, Ohm's law is able to satisfy the principle of superposition. Therefore, in defining the impedance, $Z\left(t\right)$:

$$Z\left(t\right) = \frac{V_0 \exp\left(j\omega t\right)}{I_0 \exp\left(j\omega t - j\theta\right)} = Z_0 \exp\left(j\theta\right) \tag{5.3}$$

Euler's formula from Equation 5.1 can be used to convert Equation 5.3 to a trigonometric function and allow for a straightforward, graphical representation:

$$Z_0 \exp\left(j\theta\right) = Z_0 \cos\left(\theta\right) + jZ_0 \sin\left(\theta\right) = Z' + jZ'' \tag{5.4}$$

Impedance, Z, is further defined to have two components, resistance, Z' (also known as R), and reactance, Z'' (also known as X):

$$Z = Z' + jZ'' \tag{5.5}$$

Z'' can be affected by an inductive reactance, X_L, or a capacitive reactance, X_C:

$$X_L = \omega L \;\; \text{and} \;\; X_C = -\frac{1}{\omega C} \tag{5.6}$$

Thus, the sign of Z'' determines whether inductive effects (positive) or capacitive effects (negative) are primarily influencing the reactance. Furthermore, these relations allow for the calculation of series inductance or series capacitance at a given frequency.

In a Nyquist plot, the resistance is plotted on the x-axis, and the reactance on the y-axis. However, there are multiple ways to represent impedance. For instance, the impedance magnitude, $|Z|$, and the phase angle, θ, can be derived from the resistance and reactance values:

$$|Z| = \sqrt{\left(Z'\right)^2 + \left(Z''\right)^2} \;\; \text{and} \;\; \theta = \arctan\left(\frac{Z''}{Z'}\right) \tag{5.7}$$

$|Z|$ and θ then allow for plotting versus frequency in the Bode representation, as shown in Figure 5.1. The plotted data assumes a 1 μF capacitor in series with a 100 Ω resistor, where the Bode plot in Figure 5.1 will be used later for a comparison to the experimental data. At high frequencies, the capacitive reactance term goes to zero, and the resistor dominates, thereby having a phase angle approaching 0°. As the frequency decreases, the capacitive reactance term becomes larger, and the phase angle approaches $-90°$ with an increase in $|Z|$ (ideal capacitors have an infinitely large resistance at $f = 0$ Hz, i.e., direct current).

Therefore, when the phase angle is 0°, the device under test is a resistor, and when the phase angle is $-90°$ or 90°, the device under test is a capacitor or inductor, respectively. In the case of a Nyquist plot, a capacitor or inductor would yield a line parallel to the y-axis (Z''), with the x-intercept determined by the series resistance and where a lone resistor would be a dot on the x-axis (Z').

Another way to represent the impedance is by its inverse, admittance:

$$\mathrm{S} = \frac{1}{\Omega} \quad \therefore \quad Y = \frac{1}{Z} = \frac{1}{Z' + jZ''} = \left(\frac{1}{Z' + jZ''}\right)\left(\frac{Z' - jZ''}{Z' - jZ''}\right) = \frac{Z' - jZ''}{(Z')^2 + (Z'')^2} \tag{5.8}$$

The admittance, Y, is defined to have the conductance, Y' (also known as G), and susceptance, Y'' (also known as B):

$$Y = Y' + jY'' \tag{5.9}$$

Then from Equation 5.8, the magnitude of Y' and Y'' can be determined from Z' and Z'':

$$Y' = \frac{Z'}{(Z')^2 + (Z'')^2} \text{ and } Y'' = -\frac{Z''}{(Z')^2 + (Z'')^2} \tag{5.10}$$

Y'' can be affected by an inductive susceptance, B_L, or a capacitive susceptance, B_C:

$$B_L = -\frac{1}{\omega L} \text{ and } B_C = \omega C \tag{5.11}$$

The admittance can be further converted to complex capacitance, C^*, as shown below:

$$\mathrm{F} = \frac{\mathrm{S}}{\mathrm{Hz}} \quad \therefore \quad C^* = \frac{Y}{j\omega} = \frac{Y' + jY''}{j\omega} = \left(\frac{Y' + jY''}{j\omega}\right)\left(\frac{j}{j}\right) = \frac{Y''}{\omega} - j\frac{Y'}{\omega} = C' - jC'' \tag{5.12}$$

Then for the sake of clarity:

$$C' = \frac{Y''}{\omega} \text{ and } C'' = \frac{Y'}{\omega} \tag{5.13}$$

The imaginary capacitance, C'', is related to loss, where an ideal capacitor with no loss effects is a dot on the C' axis at the capacitor's magnitude for all frequencies. Itagaki et al.[250] have simulated the Nyquist plot (Z' versus Z'') and complex capacitance plot (C' versus C'') for various circuits with an electrode in solution.

Along with the Bode representation, the admittance (Y' versus Y'') and complex capacitance will be used for interpreting the experimental impedance data. The Nyquist plot will also be shown, but this representation will prove to be less informative. Furthermore, the y-axis (Z'', Y'', and C'') will be arbitrarily plotted as positive in order to keep the plot in Cartesian quadrant I, as inductive effects are expected to be negligible.

In a series RC circuit, comparing the admittance plot (where higher frequencies are more easily observed) to its respective complex capacitance plot (where lower frequencies are more easily observed) makes it easier to visualize whether there are two series RC elements in parallel. If there is one semicircle in both plots, then the circuit can be modeled as a simple RC series circuit. Another example is shown in Figure 5.2, where the admittance plot shows a clearly visible semicircle, indicating the presence of a capacitor, $\mathrm{C_Y}$, in series with a resistor, $\mathrm{R_Y}$. However in the complex capacitance plot, two clearly visible and neighboring semicircles indicate the presence of two capacitors, $\mathrm{C_1}$ and $\mathrm{C_2}$, in parallel with their respective input resistances of $\mathrm{R_1}$ and $\mathrm{R_2}$, where $\mathrm{C_Y} = \mathrm{C_1} + \mathrm{C_2}$. As both $\mathrm{C_1}$ and $\mathrm{C_2}$ are visible in the complex capacitance plot, their capacitances are close in order of magnitude. However, as only one semicircle is clearly visible in the admittance plot, this would suggest that $\mathrm{R_1}$ and $\mathrm{R_2}$ differ by orders of magnitude (where the smaller resistance dominates in the admittance plane). In the opposite case not shown here, where one semicircle is clearly visible in the complex capacitance plot, and two semicircles are clearly visible in the admittance plot, then the resistors would be close in order of magnitude and the capacitors would differ largely in order of magnitude.

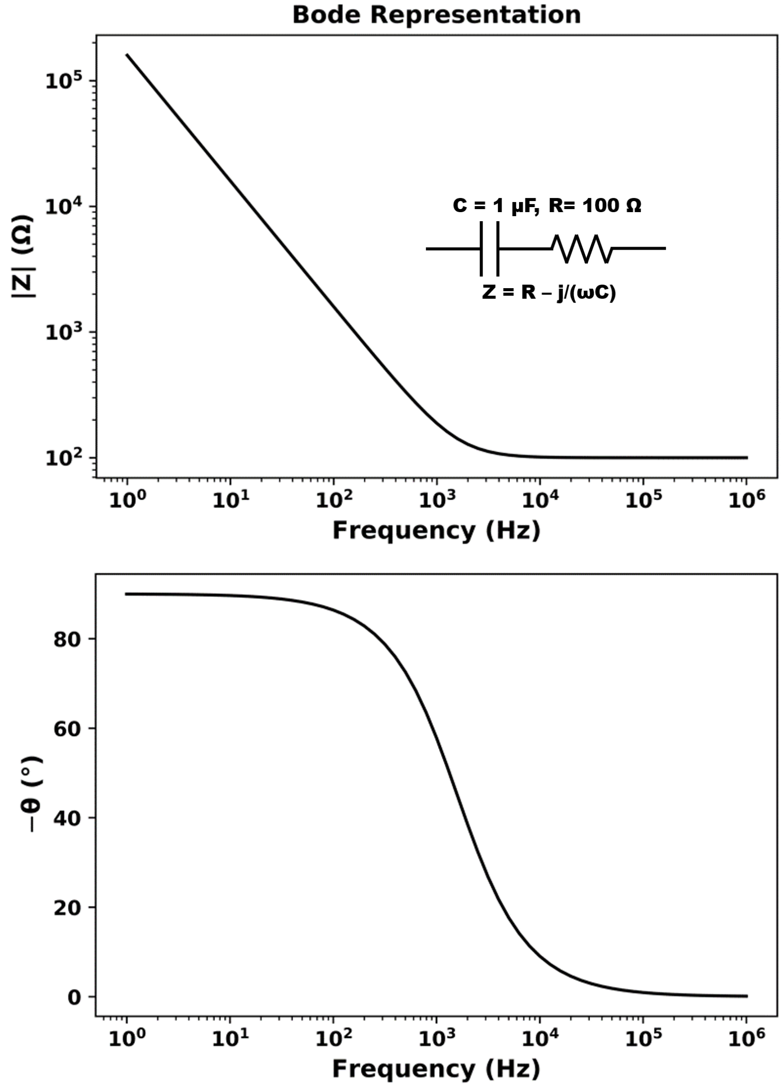

Figure 5.1 Bode plot for a series RC circuit, where R = 100 Ω and C = 1 µF.

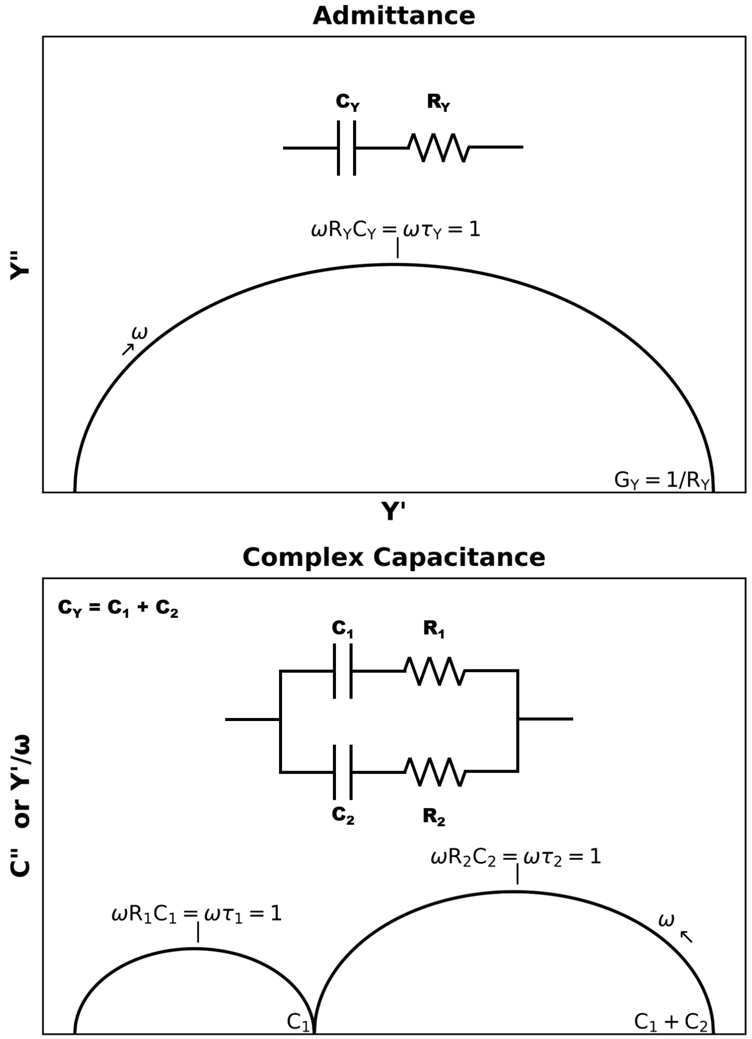

Figure 5.2 Admittance and complex capacitance plots for a series RC circuit, where C_1 and C_2 are roughly the same order of magnitude, while R_1 and R_2 have a large difference in order of magnitude. τ is the respective time constant (with units in s [seconds] when resistance is in Ω and capacitance is in F), being the time to 63% of total charge and thereby the time to 37% of discharge.[251]

5.2 Equivalent Circuit

If desired, impedance data recorded over a range of frequencies can be fitted with an equivalent circuit model. Such models suffer from being based in theory, and may neglect unknown elements in the system. Additionally, a good fit can be obtained simply by adding many elements to the model. Nonetheless, fitting a model based on a simple, grounded theory is accepted practice among scientists and engineers.

However, the system must be linear in order for an equivalent circuit to be fit. The Poisson-Boltzmann equation, based on statistical thermodynamics (the nonlinear, exponential term), describes the potential and the distribution of ions in solution at a charged electrode:[252]

$$\nabla^2\psi = -\frac{F}{\epsilon_w\epsilon_0}\sum_i^n c_{i,\infty} z_i \exp\left(-\frac{z_i F\psi}{RT}\right) \tag{5.14}$$

The equation models a mean field and assumes ions as point charges, where F is Faraday's constant, ϵ_w is the relative permittivity of water, ϵ_0 is the permittivity of vacuum, $c_{i,\infty}$ is the bulk solution species concentration for a total of n species, z_i is the species valency, ψ is the double layer potential when considering an electrical gradient locally parallel to a surface in solution ($\psi = 0$ in the bulk solution), R is the molar gas constant, and T is the temperature. As ψ resides in the exponential function, the operating voltage needs to be kept low in order to assume a linear system.

By ignoring the boundary conditions of Equation 5.14, the potential can be normalized by the thermal voltage, RT/F, which is about 25 mV at room temperature:[253]

$$\psi^* = \frac{F\psi}{RT} \tag{5.15}$$

Then, combining the normalized potential, ψ^*, with Equation 5.14, leads to:

$$\nabla^2\psi^* = -\frac{F^2}{\epsilon_w\epsilon_0 RT}\sum_i^n c_{i,\infty} z_i \exp\left(-z_i\psi^*\right) \tag{5.16}$$

The concentrations of n species can be further normalized by the ionic strength, I_c, of the bulk solution, $I_{c,bulk}$:[253,254]

$$c_{i,\infty}^{*} = \frac{c_{i,\infty}}{I_{c,bulk}} \text{ where } I_c = \frac{1}{2}\sum_{i}^{n} c_i z_i^2 \tag{5.17}$$

By using the normalized concentration in Equation 5.16, and by multiplying the right-hand side by 2/2 to correct for both anions and cations, a characteristic multiplier emerges:

$$\nabla^2 \psi^* = -\frac{1}{2}\frac{2F^2 I_c}{\epsilon_w \epsilon_0 RT}\sum_{i}^{n} c_{i,\infty}^{*} z_i \exp\left(-z_i \psi^*\right) \tag{5.18}$$

Through dimensional analysis, the multiplier's dimensions have units of m^{-2}:

$$\frac{2F^2 I_c}{\epsilon_w \epsilon_0 RT} \rightarrow \frac{\mathrm{C}^2}{\mathrm{mol}^2} \cdot \frac{\mathrm{mol}}{\mathrm{m}^3} \cdot \frac{\mathrm{J\,m}}{\mathrm{C}^2} \cdot \frac{\mathrm{K\,mol}}{\mathrm{J}} \cdot \frac{1}{\mathrm{K}} = \frac{1}{\mathrm{m}^2} \tag{5.19}$$

Therefore, the characteristic length, λ_D, or the Debye length, can be calculated with the following formula:

$$\lambda_D = \sqrt{\frac{\epsilon_w \epsilon_0 RT}{2F^2 I_c}}\Bigg|_{bulk} \tag{5.20}$$

The Debye length is an approximation of the distance where the potential at the electrode decays into the bulk solution.[252] This will be used as the characteristic length of the diffuse layer described below.[255]

In describing the impedance of the $\mathrm{SiO_2}$-electrolyte interface (with the following charges and capacitances being expressed per unit area), Bousse and Bergveld[256] mention in 1983 an insulator surface charge, σ_0, having both a pH contribution, σ_a, and an interfering, specifically adsorbing ion with a partial charge contribution and high capacitance, σ_{ad}:[48–50]

$$\sigma_0 = \sigma_a + \sigma_{ad} \tag{5.21}$$

In deriving the equivalent circuit, contributions will be ignored for now from σ_{ad}, leaving $\sigma_0 = \sigma_a$. When the insulator is deposited on a gold electrode, with the electrode inserted into solution, the insulator with a charge, Q_i, separates the gold electrode from an electrolyte, where the electrolyte has a diffuse layer charge, σ_d. Then for any solid electrode in solution,[257] a charge balance emerges where in this case Q_{Au} is the surface charge of the gold electrode, and $Q_{Au,i}$ is the charge at the gold-insulator interface:[256]

$$Q_{Au} + Q_{Au,i} + Q_i + \sigma_0 + \sigma_d = 0 \tag{5.22}$$

When an external circuit provides an incremental charge, dQ, for a non-conducting insulator, this allows for the assumption that $Q_{Au,i}$ and Q_i are not affected by incremental charge and potential changes. Therefore, the following relation is obtained:[256]

$$dQ = dQ_{Au} = -\left(d\sigma_0 + d\sigma_d\right) \tag{5.23}$$

In this case, the distribution of dQ between $d\sigma_0$ and $d\sigma_d$ from Equation 5.23 hinges on the surface reactions at the insulator-electrolyte interface.

The AC performance of a circuit with a capacitor is regulated by a differential capacitance, in contrast to a total capacitance, with the differential capacitance, C, defined below where q is the positive charge difference and V the positive voltage drop:[255]

$$C = \frac{dq}{dV} \tag{5.24}$$

In considering this definition, the insulator-electrolyte interface impedance, Z_{ie}, can be determined from Equation 5.23 with the potential drop in the electrolyte at the same interface, ψ_0, where $Z^{-1} = Y$ from Equation 5.8 and $Y\left(j\omega\right)^{-1} = C^*$ from Equation 5.12:[256]

$$Z_{ie}^{-1} = j\omega\frac{\Delta Q_{Au}}{\Delta\psi_0} = -j\omega\left(\frac{\Delta\sigma_d}{\Delta\psi_0} + \frac{\Delta\sigma_0}{\Delta\psi_0}\right) \tag{5.25}$$

Thus from Equation 5.25, two parallel capacitive components become apparent.

The first term relates to the electrical double layer which forms at the electrode-electrolyte interface. Again, ignoring specific adsorption of counterions in the condensed area of the double layer, the Gouy-Chapman-Stern theory will be applied. Within this model, the charge of the diffuse part of the double layer is defined in terms of the valence magnitude for symmetric electrolytes, z, the potential over the diffuse layer, ψ_d, and the normalized diffuse layer potential from Equation 5.15, ψ_d^*:[255]

$$\sigma_d = -\frac{\epsilon_w \epsilon_0 \psi_d}{\lambda_D} \left(\frac{2}{z\psi_d^*} \sinh\left[\frac{z\psi_d^*}{2}\right]\right) \tag{5.26}$$

In considering the diffuse layer capacitance per unit area, C_d, the capacitance is defined in terms of the Debye length from Equation 5.20:[255]

$$C_d = \frac{\epsilon_w \epsilon_0}{\lambda_D} \left(\cosh\left[\frac{z\psi_d^*}{2}\right]\right) \tag{5.27}$$

Additionally, the diffuse layer charge from Equation 5.26, σ_d, and its potential drop, ψ_d, can be related to the capacitance in the condensed layer, or the Stern capacitance per unit area, C_{stern}, to arrive at the total interface potential:[256]

$$\psi_0 = \psi_d - \frac{\sigma_d}{C_{stern}} \tag{5.28}$$

The Stern capacitance, which is placed in series with the diffuse layer capacitance, is defined by a characteristic permittivity, ϵ_S, and thickness, λ_S:[255]

$$C_{stern} = \frac{\epsilon_S}{\lambda_S} \tag{5.29}$$

For aqueous electrolyte solutions near electrodes, the usual values for the Stern permittivity are predicted to be between $6\epsilon_0$ and $30\epsilon_0$, with a Stern thickness from 1 Å to 10 Å.[255] The thickness is often related to the hydrated ion radius,[12] as shown in Figure 5.3.

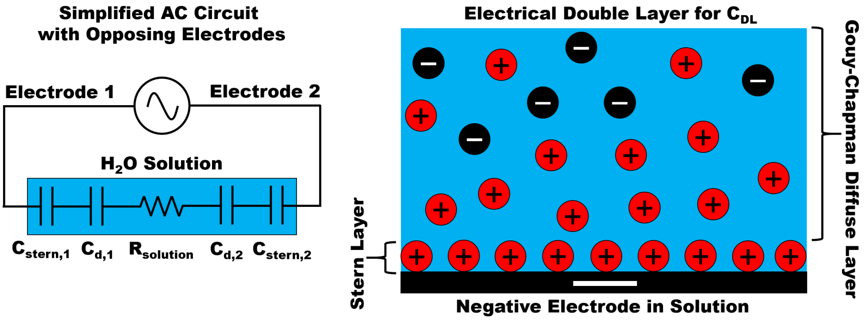

Figure 5.3 Simplified AC circuit for two opposing and chemically inert electrodes in solution, along with a simplified illustration (ignoring the solvation shells and water molecules) of the series combination of the Gouy-Chapman diffuse layer (described with Boltzmann statistics) with the condensed Stern layer.[255]

Finally by adding the diffuse layer capacitance from Equation 5.27, with the stern layer capacitance from Equation 5.29 in series, the following relation for the double layer capacitance per unit area, C_{DL}, is obtained when ignoring steric hindrance:[255]

$$C_{DL}^{-1} = -\frac{d\psi_0}{d\sigma_d} = C_d^{-1} + C_{stern}^{-1} = \left\{ \frac{\epsilon_w \epsilon_0}{\lambda_D} \left(\cosh \left[\frac{z\psi_d^*}{2} \right] \right) \right\}^{-1} + \left\{ \frac{\epsilon_S}{\lambda_S} \right\}^{-1} \tag{5.30}$$

As the Debye length, λ_D, decreases (with an increase in ionic strength from Equation 5.20) and approaches the Stern thickness, λ_S, the total double layer capacitance from Equation 5.30 increases. For sodium chloride solutions, the observed Debye length has been seen to decrease with an increase in concentration up to about 1 M NaCl, whereafter the Debye length increases with a further increase in concentration.[258] Additionally, in relating the Stern thickness, λ_S, to hydrated ion radius, one would expect that a smaller hydrated ion radius would yield a higher Stern capacitance.[12]

In glass systems such as SiO_2, Al_2O_3, and Ta_2O_5, the primary charge determining ions are H^+ and OH^- ions, which affect both the double layer and the specific adsorption layer.[41,45,47,259] Furthermore, the electrophoretic mobilities in water (movement in the solvent in response to an electric field) for H^+ and OH^- ions are about 7× and 4× higher, respectively, than those of K^+, Na^+, and Li^+ at room temperature and at infinite dilution; this faster movement of H^+ and OH^- in water is due to reactive mechanisms which include the Grotthus mechanism, but their mobilities are of roughly the same order as other ions at the glass-water interface.[260]

As H^+ and OH^- are smaller and more able to adsorb than K^+, Na^+, and Li^+ on Ta_2O_5,[47] a prediction could be made that the pH plays a larger role in affecting the double layer capacitance in the presence of interfering cations, especially at shorter Debye lengths (i.e., higher ionic strength with minimal steric hindrance) where the double layer reduces to the Stern layer. This will be further discussed later, where in returning to the pH adsorption term from Equation 5.25, the surface charge of the insulator as a function of pH can be described with the site-binding model[21,44] (while ignoring the the improved model[41,45] for this derivation):[256]

$$\left(\mathrm{pH_{pzc}} - \mathrm{pH}\right)\ln 10 = \frac{e\psi_0}{kT} + \mathrm{arsinh}\left(\frac{\sigma_0}{\gamma e N_s}\right) \tag{5.31}$$

Here, pH is the solution pH, $\mathrm{pH_{pzc}}$ is the solution pH where the insulator surface is electrically neutral (pH 2 for SiO_2, pH 8 for Al_2O_3, and pH 3 for Ta_2O_5),[41,45] γ is the surface reactivity (assumed that $\gamma^2 \ll 1$ for all usual insulators in silicon technology), N_s is the number of reaction sites per unit area on the insulator surface, k is the Boltzmann constant, and e is the elementary charge.

This adsorption effect can be used to determine the capacitance in parallel to the double layer capacitance, where the former branch of the Z_{ie} has two components in series:[256]

$$(j\omega)^{-1}\frac{\Delta\psi_0}{\Delta\sigma_0} = (j\omega)^{-1}\left.\frac{\delta\psi_0}{\delta\sigma_0}\right|_{\mathrm{pH}} + (j\omega)^{-1}\left.\frac{\delta\psi_0}{\delta \mathrm{pH}}\right|_{\sigma_0}\frac{\Delta \mathrm{pH}}{\Delta\sigma_0} \tag{5.32}$$

Evaluating these partial derivatives assumes that the surface reactions can be established on an experimental time-scale, which has been observed in prior studies.[256] Then by taking the first term of Equation 5.32, and relating it to the adsorbed charge of H^+ and OH^- ions, the pH adsorption capacitance, C_a, can be determined:[256]

$$C_a^{-1} = -\frac{d\psi_0}{d\sigma_0} = \frac{kT}{\gamma e^2 N_s}\left(1 + \left[\frac{\sigma_0}{\gamma e N_s}\right]^2\right)^{-\frac{1}{2}} \tag{5.33}$$

By taking the second term of Equation 5.32, and considering semi-infinite linear ion diffusion (i.e., unrestricted diffusion towards a large planar electrode), where the surface pH changes based on the applied AC signal, the Warburg impedance from standard theory can be used:[256,261]

$$W_a = \frac{1}{j\omega}\left(\left.\frac{\delta\psi_0}{\delta \mathrm{pH}}\right|_{\sigma_0}\right)\frac{\Delta \mathrm{pH}}{\Delta\sigma_0} = \frac{kT}{e^2\sqrt{2\omega}}\,\frac{1-j}{[\mathrm{H}^+]\sqrt{D_{\mathrm{H}^+}} + [\mathrm{OH}^-]\sqrt{D_{\mathrm{OH}^-}}} \tag{5.34}$$

Both the ion concentrations, $[H^+]$ and $[OH^-]$, and their respective diffusion coefficients, D_{H^+} and D_{OH^-}, affect the Warburg impedance, W_a. Further note that with $\sqrt{2\omega}$ in the denominator in the first fraction on the right-hand side, W_a becomes larger with a decrease in frequency, where it would be more visible at lower frequencies in the immittance spectra.

As both the double layer capacitance without specific adsorption, C_{DL}, and the pH specific adsorption capacitance, C_a, appear in parallel, then the insulator-electrolyte impedance, Z_{ie}, approaches a pure capacitance with a decrease in frequency ($W \propto \omega^{-1/2}$, $C \propto \omega^{-1}$) with both branches added below:[256]

$$C_{ie0} = \lim_{\omega \to 0} \left(\frac{Z_{ie}^{-1}}{j\omega} \right) = C_{DL} + C_a = C_{DL} \left(1 + \beta \sqrt{1 + \left(\frac{\sigma_0}{\gamma e N_s} \right)^2} \right) \tag{5.35}$$

Here, β is a pH sensitivity parameter at the surface and is shown below, where at high ionic strength the double layer approaches the stern capacitance, C_{stern}, and β is then only insulator dependent:[256]

$$\beta = \frac{\gamma e^2 N_s}{kTC_{DL}} \tag{5.36}$$

However as discussed previously, in the presence of interfering, specifically adsorbing ions at high ionic strength, such as K^+, Na^+, and Li^+,[47] or at a pH far from pH_{pzc}, a separate term for the interfering partial charge adsorption from Equation 5.21, σ_{ad}, may be required:[256]

$$Z_{ie,ad}^{-1} = j\omega \frac{\Delta Q_{Au}}{\Delta \psi_0} = -j\omega \left(\frac{\Delta \sigma_d}{\Delta \psi_0} + \frac{\Delta \sigma_a}{\Delta \psi_0} + \frac{\Delta \sigma_{ad}}{\Delta \psi_0} \right) \tag{5.37}$$

Then at the limit of zero frequency, $Z_{ie,ad}$ would approach the following capacitance:[256]

$$C_{ie0,ad} = \lim_{\omega \to 0} \left(\frac{Z_{ie,ad}^{-1}}{j\omega} \right) = C_{DL} + C_a + C_{ad} \tag{5.38}$$

An example of $\mathrm{C_{DL}}$ in parallel with $\mathrm{C_{ad}}$ is illustrated[257] in Figure 5.4 (the variables' italics are now removed for consistency with the impedance introduction and the fitted data shown later).

Then for building the equivalent circuit by placing $\mathrm{Z_{ie,ad}}$ in series with an insulator capacitance, $\mathrm{C_i}$, the solution resistance, $\mathrm{R_{Sol}}$, and other system impedances, the Bousse-Bergveld circuit with interfering ions is complete and is shown in Figure 5.5.[256] Although some metal oxide insulators, such as SiO_2, have lower pH reactivity (yielding a higher interfacial impedance) and require the $\mathrm{C_a}$—$\mathrm{W_a}$ branch, the pH reactivity of other oxides such as Al_2O_3 and Ta_2O_5 is higher (yielding a lower interfacial impedance), and this branch may prove negligible in the case of the latter two oxides. The C_{ad}—W_{ad} branch may be negligible at low ionic strength or close to pH_{pzc}, whereas at higher ionic strength or far from pH_{pzc} this branch may become more prominent.

In measuring the impedance of an interdigitated electrode (IDE) structure in solutions containing different ion sizes with the same charge, such as for K^+, Na^+, and Li^+, the effect each ion size has on C_{DL} and C_{ad}, particularly for flash lamp annealed tantalum oxide, needs to be understood. In order to explore the effects of interfering ions, this experiment will examine how four different universal pH buffers (using NaOH to increase the pH), one with no added alkali chloride salt, one with 0.5 M KCl, one with 0.5 M NaCl, and one with 0.5 M LiCl would affect the double layer capacitance (namely solvated ions without specific adsorption) and a parallel specific adsorption capacitance. An automated setup with a gold IDE sensor, where the sensor has a sol-gel deposited tantalum oxide layer on the gold structures, will be used for this experiment.

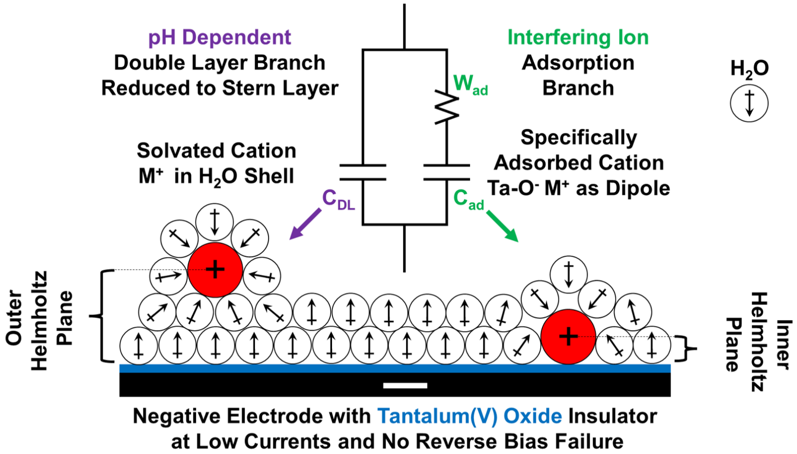

Figure 5.4 Parallel branches of $Z_{ie,ad}$ which omits C_a and reduces C_{DL} to the Stern layer, shown with a simplified illustration of a solvated cation (M^+) in the outer Helmholtz plane for C_{DL}, and a specifically adsorbed cation (M^+) on tantalum(V) oxide in the inner Helmholtz plane for C_{ad}. This illustration was modified and adopted from Bootsma, de Rooij, and van Silfhout[257] (© 2022 Elsevier B.V. All rights reserved.).[220]

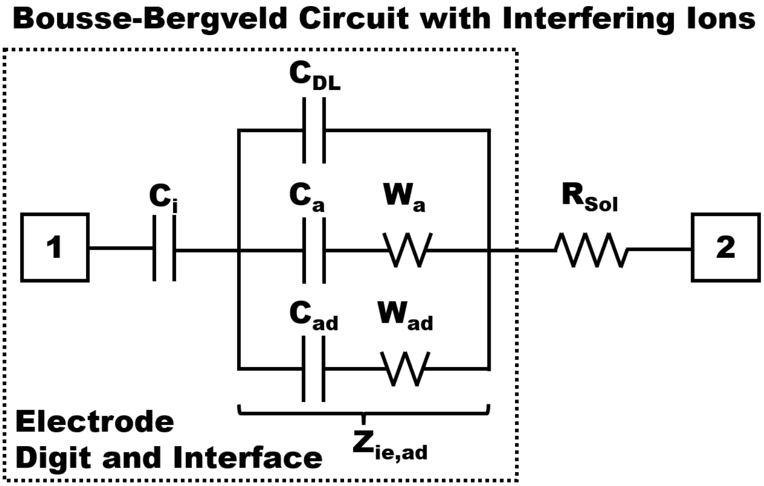

Block	1	2
Vermilyea	Tantalum	Platinum
Bousse-Bergveld	Silicon	Reference Electrode
This Work	Gold	Opposite Digit and Interface

Figure 5.5 Bousse-Bergveld circuit with interfering, specifically adsorbing ions based on prior work from Vermilyea[53,54] and Bousse, Bergveld.[256] C_i is the insulator capacitance, C_{DL} is the double layer capacitance without specific adsorption, C_a is the pH specific adsorption capacitance, W_a is the pH related Warburg element for semi-infinite linear ion diffusion, C_{ad} is the interfering ion specific adsorption capacitance, W_{ad} is the interfering ion related Warburg element, and R_{Sol} is the solution resistance. Additional elements, such as the global capacitance for the interdigitated electrode (IDE) device,[262] were left out for the sake of brevity (© 2022 Elsevier B.V. All rights reserved.).[220]

5.3 Experimental Methods - Automated Setup

Sensor 7-7, from Experiment 1 of Chapter 4 which described sensor fabrication, was used in these measurements. In order to get more data points, and to allow time for ion diffusion in solution and in the sensor, an automated setup was constructed to avoid human error. For avoiding interference between the pH electrode and the IDE sensor, a Braccio robotic arm (Arduino, USA) was used to remove the pH electrode during measurement, as shown in Figure 5.6. The robotic arm was set manually to have the following initial position: carousel at 0°, link 1 (coming out of the carousel) perpendicular to Earth, link 2 (attached to link 1) parallel to Earth, link 3 (attached to link 2) parallel to Earth, the hand (attached to link 3) parallel to Earth, and the grabber with its servo (servo 6) removed. The initial position must be set manually, as the robotic arm jumps to the “safety position” immediately upon being turned on. Coincidentally, the hand has a hole where the InLab RoutinePro pH electrode (Mettler-Toledo, USA) can fit and be held. The hand’s rotating servo (servo 5) was thus deactivated to keep the hand parallel to Earth, and thereby hold the electrode perpendicular to Earth in solution. Finally, the pH electrode cable was taped to link 2 during measurement, and a plastic support was attached to link 2 via cable tie in order to protect the electrode if the power cut out.

The arm was controlled with an Arduino Uno microcontroller (Arduino, USA), with the code in the Appendix. The microcontroller took either one of two byte commands, with 0 being a 3 M potassium chloride (99%, Alfa Aesar) electrode storage solution (carousel rotation at 0°), and 1 for the measurement solution (carousel rotation at 90°). A third beaker containing Milli-Q water as a cleaning solution was placed between the two beakers (carousel rotation at 45°), where the arm would dip the electrode in this solution for 5 seconds before moving to either the storage or measurement solutions. 400 mL plastic PMP Griffin beakers with printed red scale (VITLAB, Germany) were used to store the solutions; glass beakers were not used, as glass beakers may lead to increased pH electrode damage when compared to plastic beakers upon accidental collision.

The measurement beaker contained 200 mL of Britton-Robinson's universal pH buffer[232] (0.04 M acetic acid [Glacial, PhEur, SAFC], 0.04 M phosphoric acid [85%, Reag. Ph. Eur, KMF optiChem], 0.04 M boric acid [GR, Merck]), where 1 M sodium hydroxide [pellets, Sigma-Aldrich] was added dropwise to increase the pH. Base addition was controlled with a separate Arduino Uno microcontroller (Arduino, USA) and ALA-VM8 solenoid valves (Scientific Instruments, USA), where the valves would pinch a silicone tube with a 0.7 mm inner diameter and a 2.0 mm outer diameter. The tube was connected to an open syringe containing the base, and when the solenoid valve opened, the base was fed via gravity to the measurement beaker at an approximate rate of $\sim$1.5 drops s^{-1}.

A Python 3 "command script" (see Appendix) controlled the robot arm and the solenoid valves, while also running a measurement script on request for the PalmSens 4 impedance analyzer (PalmSens BV, The Netherlands). Once the measurement script was run, the "command script" would close (or more technically in Python parlance, "kill") the PalmSens PSTrace software, which was required for performing another measurement later. Additionally, the computer operating system sleep was turned off, or else the setup would freeze in position upon sleeping.

The IDE sensor was held in the measurement beaker, where its impedance was measured at a 10 mV amplitude (rms) from 1 Hz to 1 MHz (10 measurements per decade) with the PalmSens 4 potentiostat and impedance analyzer, with the counter and reference electrodes shorted and connected to the digit array on one side of the sensor, and the working electrode to the opposite array. Before the impedance measurement, a 2 hour conditioning step in the beaker was performed, where sensor drift was observed largely to cease after this period; in support of this conditioning step, the zeta potential of Ta_2O_5, deposited via atomic layer deposition (ALD), stabilized after 1 hour at pH 5.6 in 1 mM KCl, where ozone activation was performed before solution exposure.[236] After the impedance measurement, base was added to the measurement beaker by opening the solenoid valve for 30 seconds, in order to increase the pH of the measurement solution. After 30 seconds, the valve was closed and the pH electrode was moved from the storage beaker to the measurement beaker, where pH and temperature were measured for 30 minutes before the next measurement. The pH and temperature data were recorded in a separate program about every second by using output from the MPC227 pH/Conductivity Meter (Mettler-Toledo, USA). No stirring was performed over the 30 minute period, as solution movement can affect the pH measurement via changes in the streaming potential[263] and electromagnetic interference needed to be avoided as much as possible. After 30 minutes, the robot arm would move the pH electrode back to the storage beaker, and another impedance measurement would be performed. This process was repeated for each measurement, with the entire setup in a dark Faraday cage.

Sensor 7-7 was used in four different buffer solutions, in order to determine the effects of the Debye length and ion size on the measured impedance.[258] These solutions were all Britton-Robinson buffers,[232] the first being with no added alkali chloride salt, the second with 0.5 M potassium chloride (99%, Alfa Aesar), the third with 0.5 M sodium chloride (BioXtra, ≥99.5% (AT), Sigma-Aldrich), and the fourth with 0.5 M lithium chloride (anhydrous, Fluka BioChemika). The impedance was measured at 25 pH points (24 base additions). Plotted impedance was labeled with the pH immediately before electrode removal, and equivalent circuit fitting was performed with the Levenberg-Marquardt algorithm (error bars indicate percent error) with the PalmSens PSTrace software.

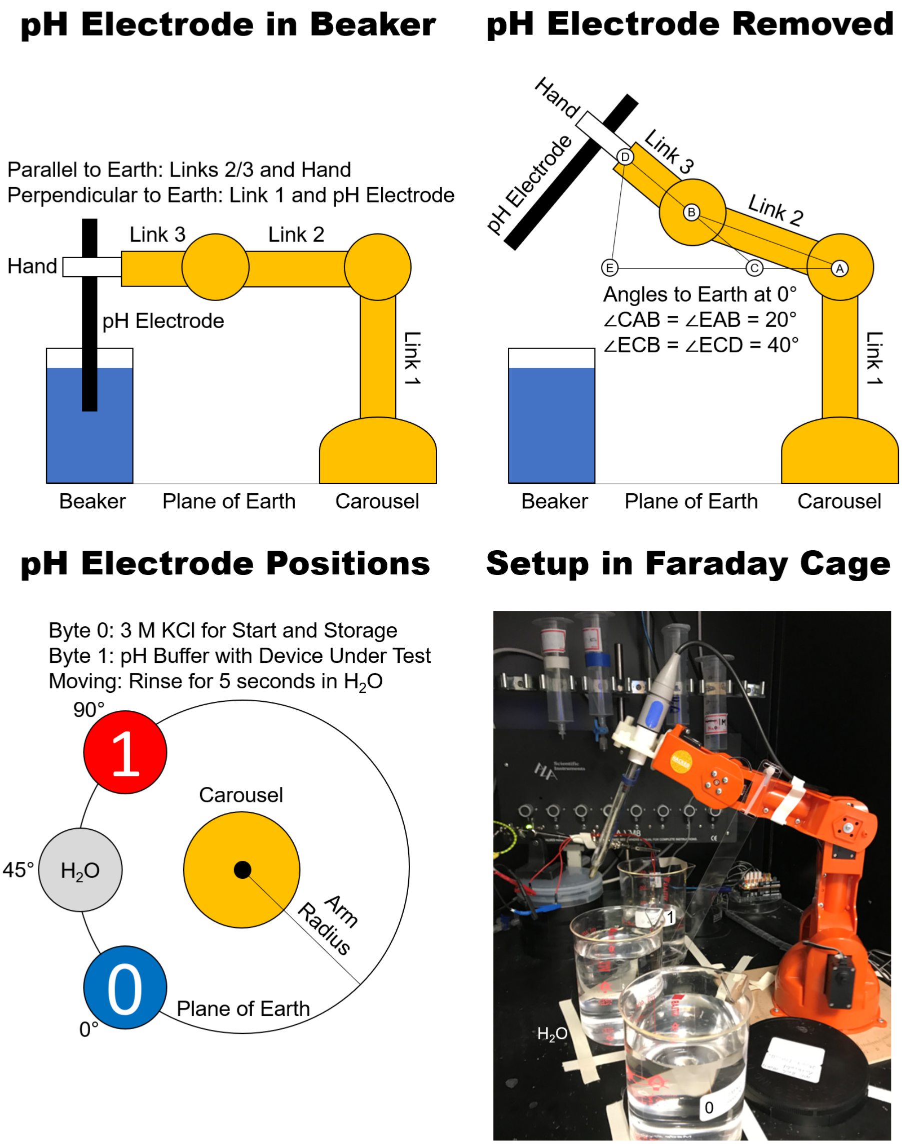
pH Electrode in Beaker

pH Electrode Removed

pH Electrode Positions

Setup in Faraday Cage

Figure 5.6 Diagram of the arm holding the pH electrode perpendicular to Earth in solution (upper left), along with the arm position for removing the electrode (upper right) and the beaker positions (lower left). The image of the automated setup in the Faraday cage (lower right) shows the arm moving the pH electrode from beaker to beaker (© 2022 Elsevier B.V. All rights reserved.).[220]

5.4 Results

pH and temperature over time are plotted in this section, where the "spikes and dips" between the 30 minute measurement times are when the pH electrode is removed from the measurement beaker. The pH at room temperature tends to drift much more in the high ionic strength solutions, especially at low pH; the addition of neutral salts to solution has been observed to affect ion activity and may reduce the the buffering ability of the solutions.[264,265] Furthermore in the high ionic strength solutions, the change in the liquid junction potential with respect to the calibration buffers may affect the pH, in addition to alkaline error of the glass electrode. Thus, the impedance versus pH, which was measured over roughly 1 minute, will assume that the pH does not change over this relatively short time period; this again goes back to the assumption of measuring on an experimental time scale,[256] which for practical purposes in this case limited the measurement from 1 Hz to 1 MHz.

The Bode plots (Figures E.1 - E.4), the Nyquist plots and admittance plots (Figures E.5 - E.8), and the series RC plots (Figures E.9 - E.12) are shown in the Appendix, while the complex capacitance plots are shown in Figure 5.14. The Bode plots have a similar characteristic shape and order of magnitude as the example discussed previously in the impedance introduction in Figure 5.1. The Nyquist plots are relatively vertical when comparing the magnitude of the x-axis and the y-axis, thus approaching a vertical line for a capacitor. The admittance plots appear to show one semicircle, while in approaching infinitely low frequency the complex capacitance plots appear to show two neighboring semicircles (although this is inconclusive for the low ionic strength and 0.5 M KCl solutions); this behavior was also discussed previously for the example in Figure 5.2.

In observing the assumed circuits for both low ionic strength (Figure 5.12) and high ionic strength solutions (Figure 5.13), a pH dependent $C_{\mathrm{Ta_2O_5}}$, possibly caused by a "proton space charge" as has been observed in anodic Ta_2O_5 films,[54] is observable in the series capacitance plots at high frequencies and in all solutions (after the double layer effects diminish at ∼10 kHz and before the inductive effects begin after ~50 kHz),[266] where the series capacitance decreases with an increase in pH. At most frequencies in the high ionic strength solutions, the same pH dependence is observed, where both C_{DL} and $C_{Ta_2O_5}$ have been observed to be pH sensitive by Vermilyea for anodic Ta_2O_5, but this pH dependence varies with the solution constituents.[53,54]

Due to the low, primarily H^+/OH^- driven interfacial impedance for Ta_2O_5,[53,256,262,266–268] $C_{Ta_2O_5}$ with an assumed leakage current (see Figure 4.30), R_{Au}, and R_{Sol} are lumped into R_1 as a series resistance for both simplified circuits, which allows for better fitting with the Levenberg-Marquardt algorithm. In regard to $C_{Ta_2O_5}$, Vermilyea also noted that in KCl solutions of varying concentration, the thickness of the Ta_2O_5 layer appeared to have no significant effect on the change in magnitude for the insulator-electrolyte interface capacitance versus pH.[53] Then for the interface, C_1, also present in both simplified circuits, is attributed to the double layer capacitance without specific adsorption, C_{DL}, and is placed in series with R_1. The pH dependent specific adsorption capacitance, C_a, is expected to be negligible for Ta_2O_5,[256] particularly between pH 4 and pH 10 for thin, anodic Ta_2O_5 where the impedance is thought to be "diffusion controlled" rather than an adsorption capacitance.[53] Therefore, C_2 (the low frequency semicircle on the right) is attributed to the interfering ion specific adsorption capacitance, C_{ad}, in series with a Warburg impedance, W_1, attributed to W_{ad}; this branch was only fitted to the 0.5 M NaCl and 0.5 M LiCl solutions, since for the 0.5 M KCl solutions the frequency would need to go lower than 1 Hz for more data points and a realistic fit with the provided software. Thus, the simplified circuit for low ionic strength was fitted to the 0.5 M KCl solution at higher frequencies (100 Hz to 1 MHz), in order to obtain a more accurate fit for C_1, while the same circuit was fitted to the "no added chloride salt," low ionic strength solution from 1 Hz to 1 MHz. Example fits in the complex capacitance plane are shown in Figure 5.15, and fitted values for R_1, C_1, C_2, and W_1 are then plotted versus pH in their own subsection, where the results will be discussed further in the next section.

5.4.1 Time versus pH and Temperature

In the "no added alkali chloride salt" solution shown in Figure 5.8, the pH values appear stable after 30 minutes of mixing by diffusion, with the temperature cooling slowly overnight from ~20.8°C to ~20.2°C. However, for the 0.5 M KCl solution in Figure 5.9, the pH values are not as stable after 30 minutes of mixing by diffusion, unlike for the solution with no added chloride salt. Thus, the added 0.5 M KCl appears to affect the buffering ability of the solution, as with the 0.5 M NaCl (Figure 5.10) and 0.5 M LiCl (Figure 5.11) solutions, with possible causes discussed at the beginning of this section. The 0.5 M KCl solution temperature cooled slowly overnight from ~21.5°C to ~20.2°C, while both the 0.5 M NaCl solution and 0.5 M LiCl solution temperature hovered at ~20.6°C overnight.

In observing the recorded pH values, Figure 5.7 serves as a reference from the original buffer first reported in 1931.[232] As 0.2 M NaOH was added to the universal pH buffer, the pH increases almost linearly. These plotted values allow for an estimated NaOH molarity with each addition (see Table G.1 in the Appendix).

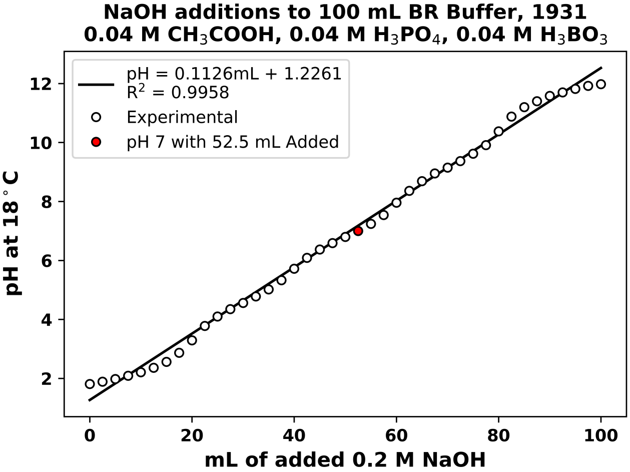

Figure 5.7 Original data plotted for 0.2 M NaOH additions to 0.04 M phosphoric acid, 0.04 M acetic acid, and 0.04 M boric acid.[232]

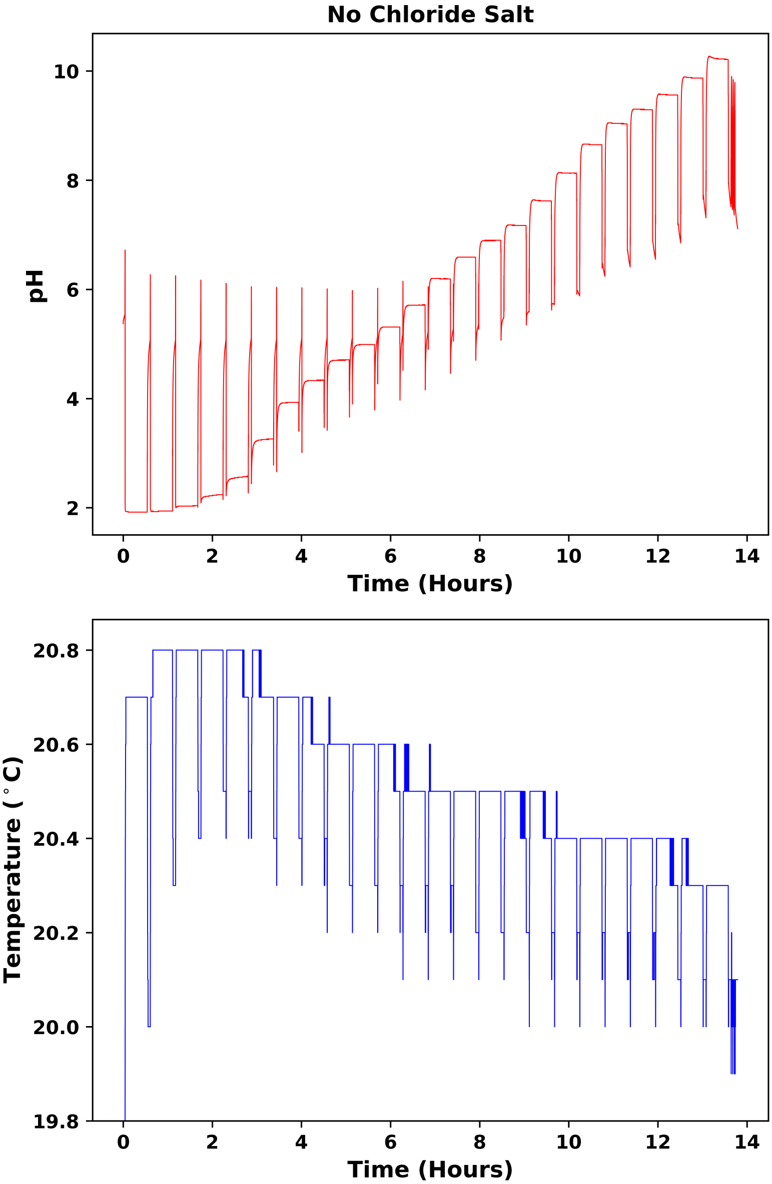

Figure 5.8 pH and temperature for the "no added alkali chloride salt" buffer, with "spikes and dips" between the 30 minute pH measurement intervals being when the pH electrode was removed from the measurement solution (© 2022 Elsevier B.V. All rights reserved.).[220]

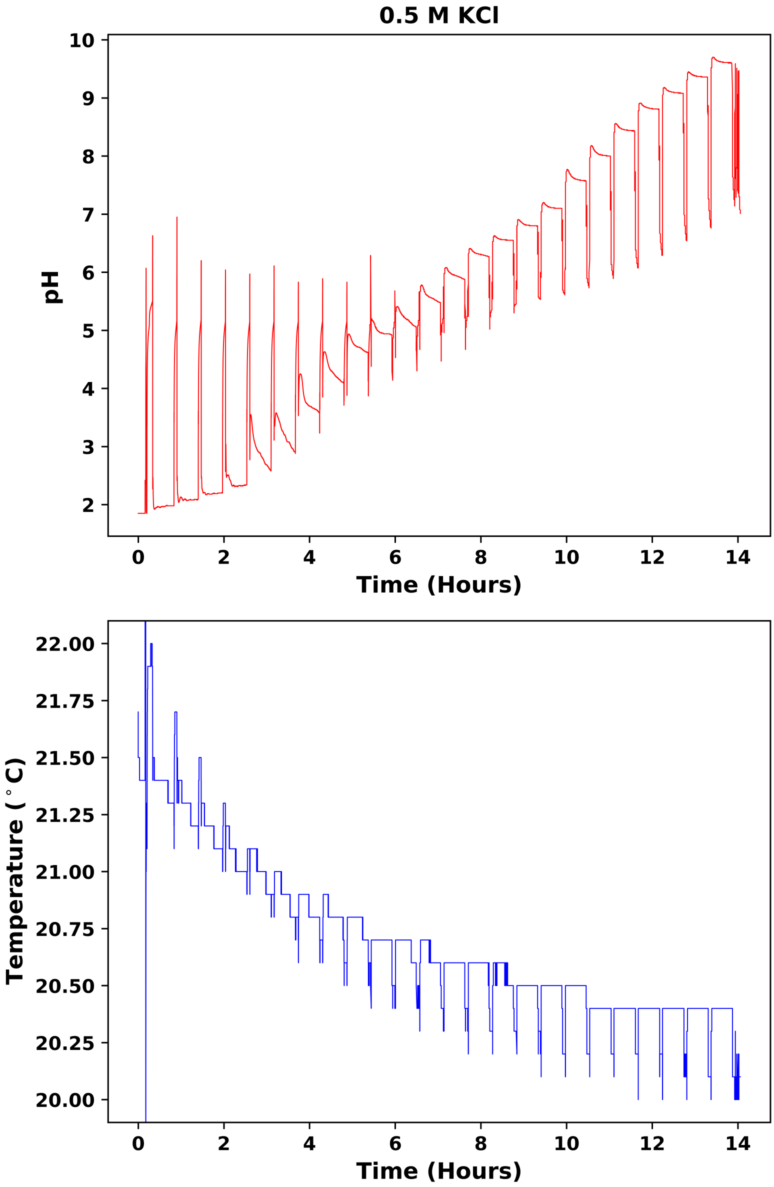

Figure 5.9 pH and temperature for the 0.5 M KCl buffer, with "spikes and dips" between the 30 minute pH measurement intervals being when the pH electrode was removed from the measurement solution (© 2022 Elsevier B.V. All rights reserved.).[220]

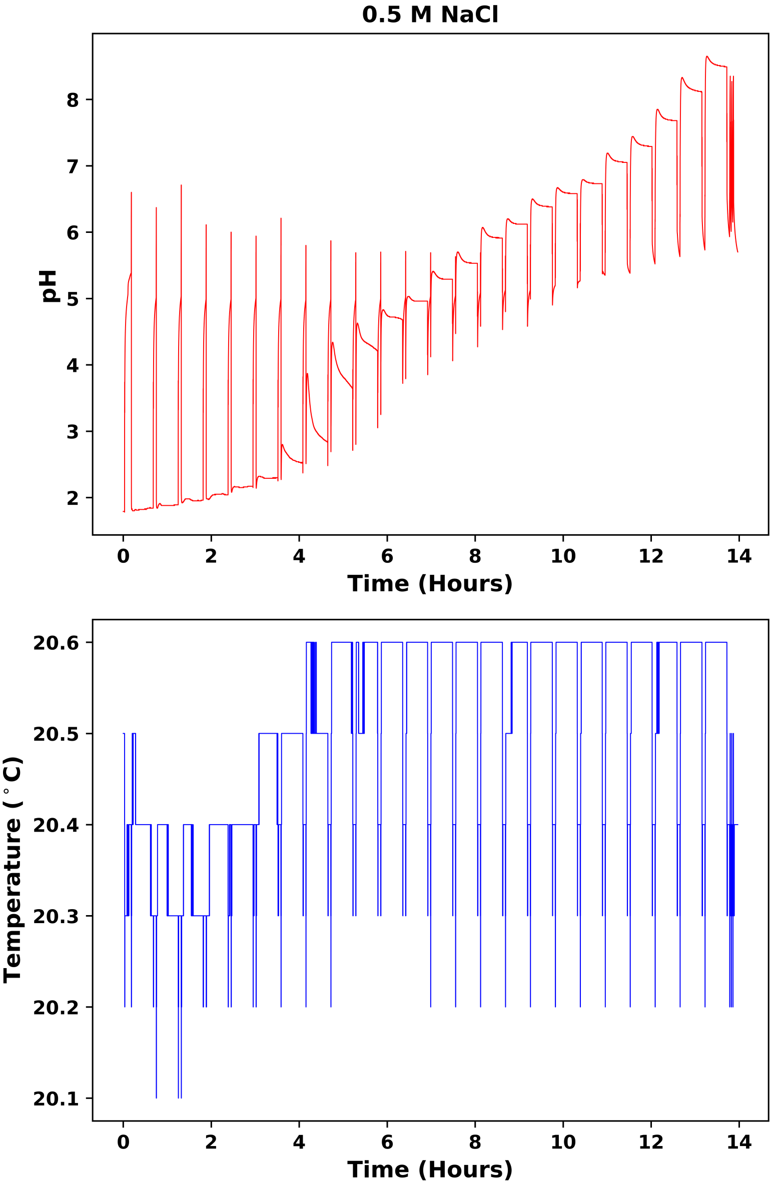

Figure 5.10 pH and temperature for the 0.5 M NaCl buffer, with "spikes and dips" between the 30 minute pH measurement intervals being when the pH electrode was removed from the measurement solution (© 2022 Elsevier B.V. All rights reserved.).[220]

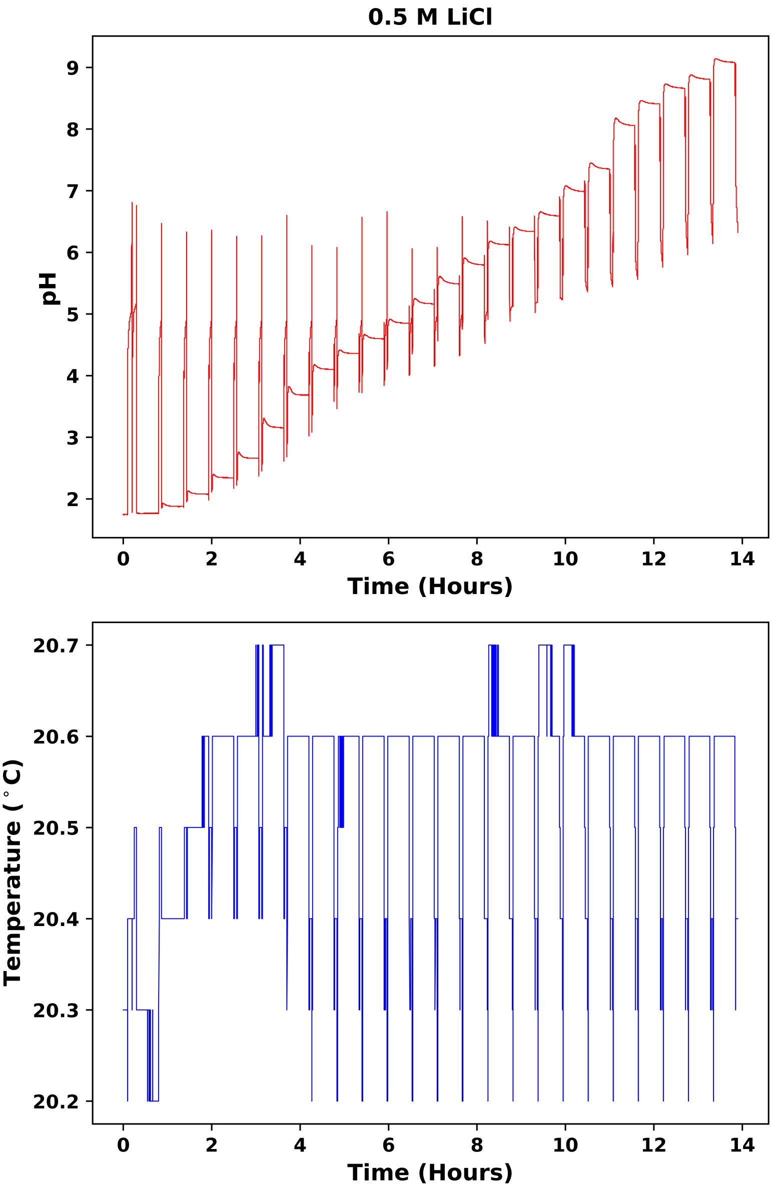

Figure 5.11 pH and temperature for the 0.5 M LiCl buffer, with “spikes and dips” between the 30 minute pH measurement intervals being when the pH electrode was removed from the measurement solution (© 2022 Elsevier B.V. All rights reserved.).[220]

5.4.2 Complex Capacitance Plots with Fits

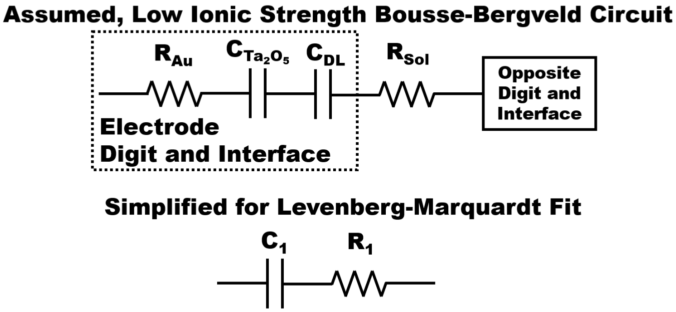

Figure 5.12 Assumed and simplified circuit for the "no added alkali chloride salt," low ionic strength solution. The simplified circuit was fitted to the "no added alkali chloride salt" solution from 1 Hz to 1 MHz, while the same circuit was fitted to the 0.5 M KCl solution from 100 Hz to 1 MHz, with the latter solution likely needing to go below 1 Hz for an accurate, high ionic strength circuit fit.

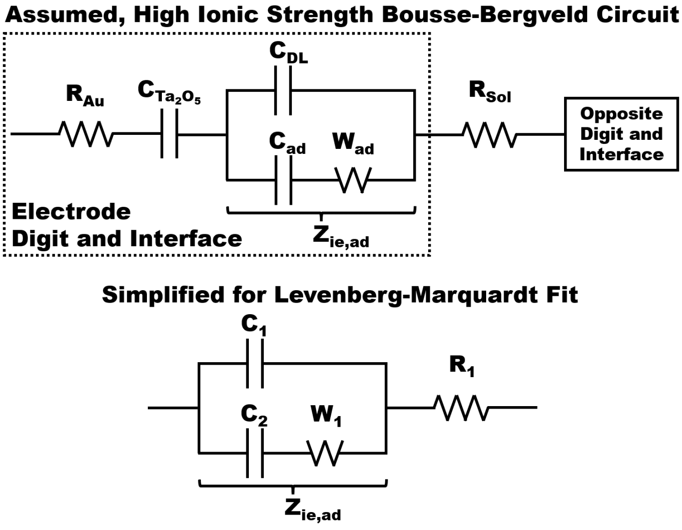

Figure 5.13 Assumed and simplified circuit for high ionic strength solutions. In fitting the simplified circuit to the 0.5 M KCl solution, the $C_2 - W_1$ branch was omitted, reducing it to $C_1 - R_1$ and fitting from 100 Hz to 1 MHz.

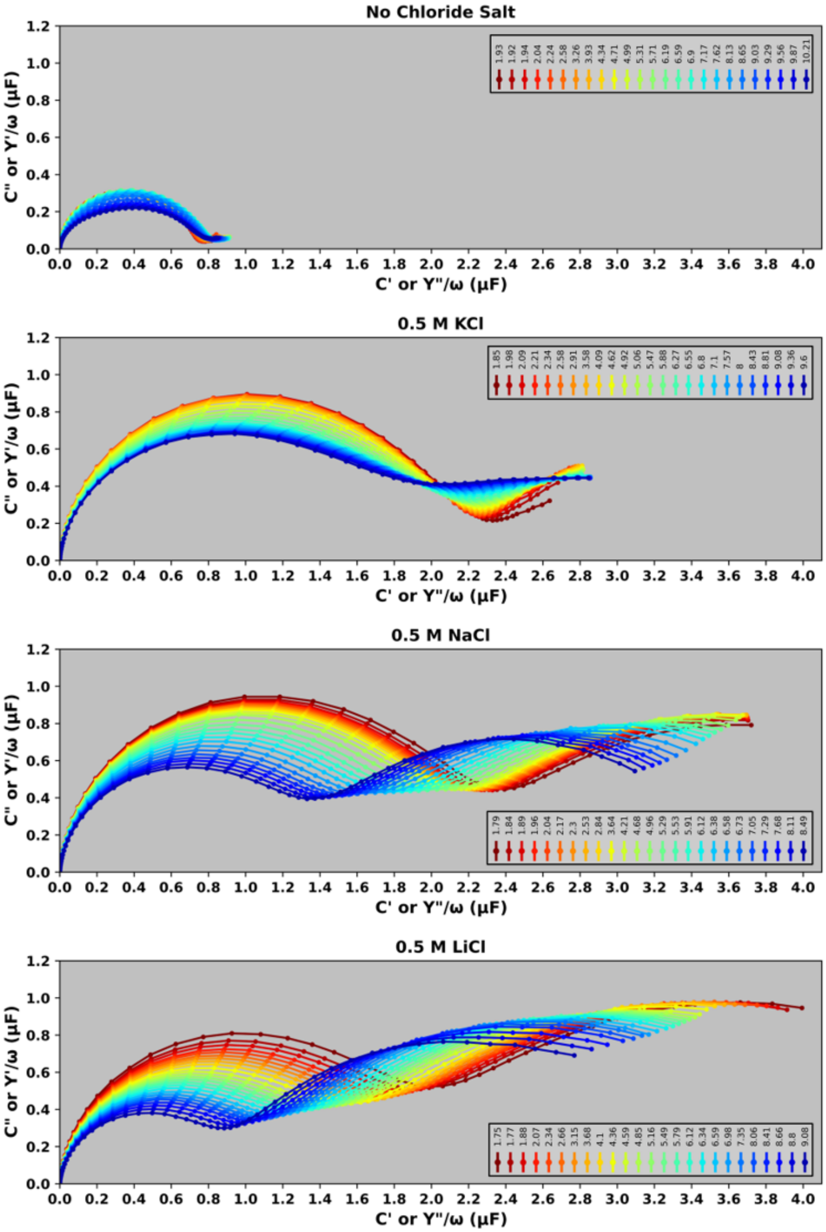

Figure 5.14 Complex capacitance plots with the measured data from 1 Hz to 1 MHz for all solutions, with each pH point color coded from red (acidic) to more basic (blue) (© 2022 Elsevier B.V. All rights reserved.).[220]

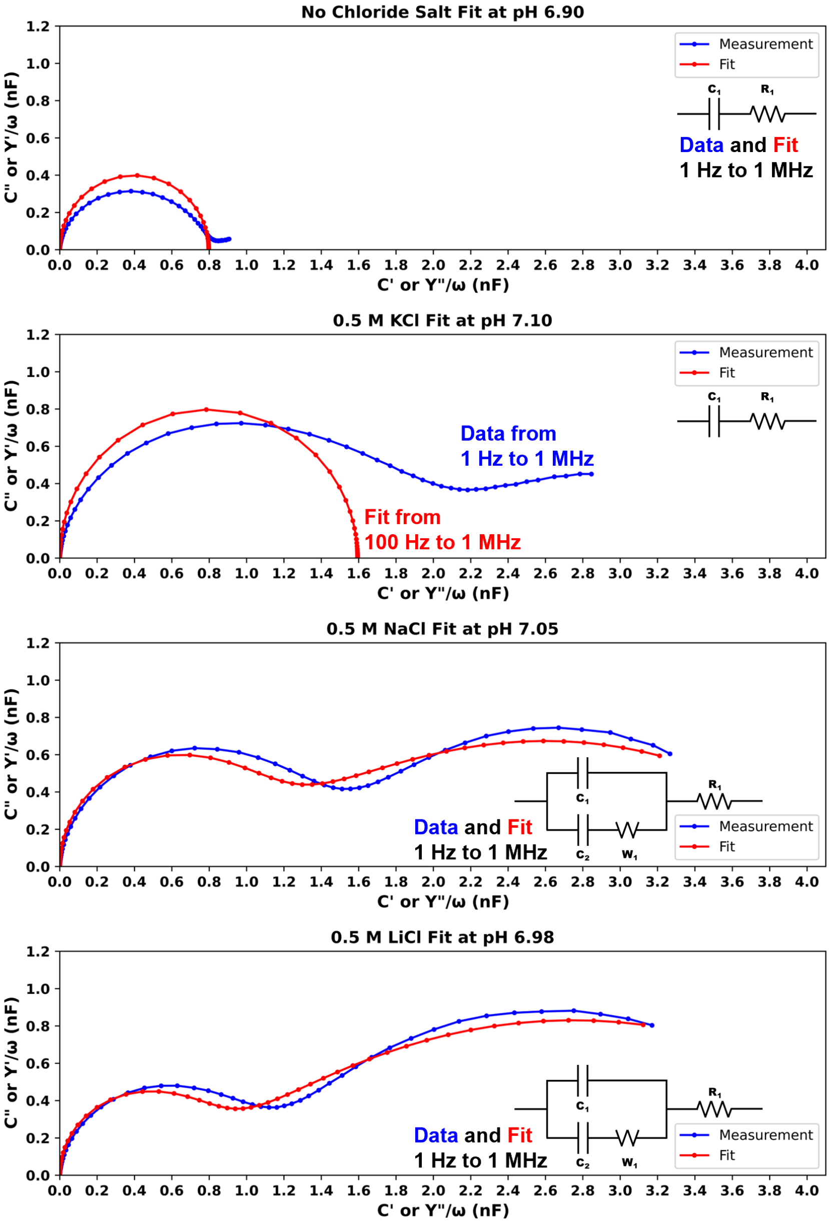

Figure 5.15 Levenberg-Marquardt fit examples for all solutions at roughly pH 7.

5.4.3 pH versus Resistance in Series with Interface

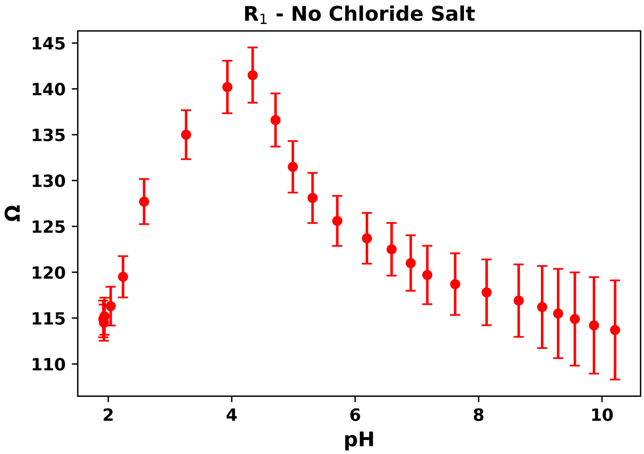

Figure 5.16 C_1 in series with R_1 for "no added alkali chloride salt" solution, where R_1 peaks around pH 4.5.

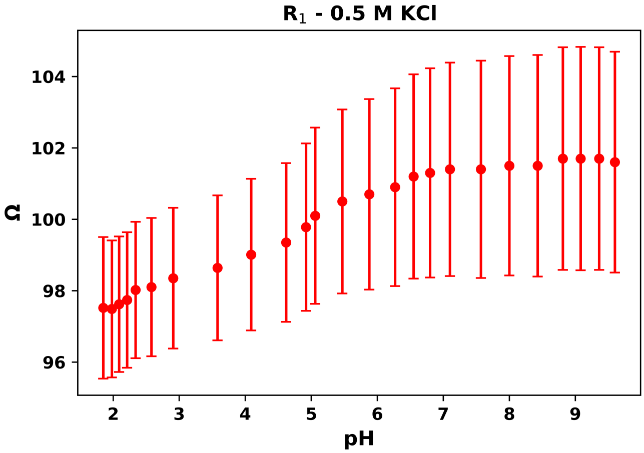

Figure 5.17 C_1 in series with R_1 from 100 Hz to 1 MHz for 0.5 M KCl, where R_1 hovers around 100 Ω.

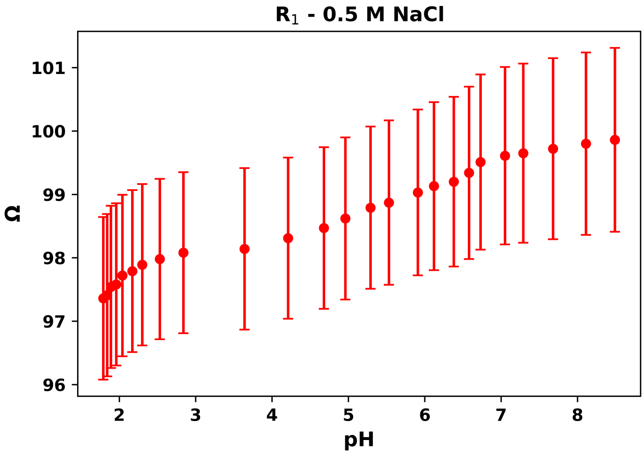

Figure 5.18 R$_1$ in the simplified, high ionic strength circuit for 0.5 M NaCl, with no clear pH dependence while considering error (© 2022 Elsevier B.V. All rights reserved.).[220]

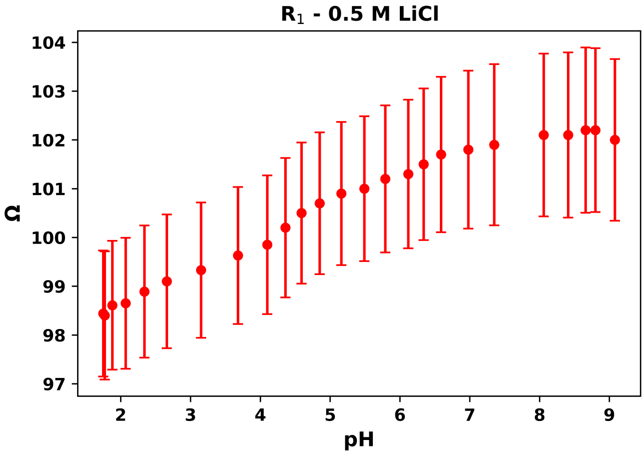

Figure 5.19 R$_1$ in the simplified, high ionic strength circuit for 0.5 M LiCl, with no clear pH dependence while considering error (© 2022 Elsevier B.V. All rights reserved.).[220]

5.4.4 pH versus Double Layer Capacitance

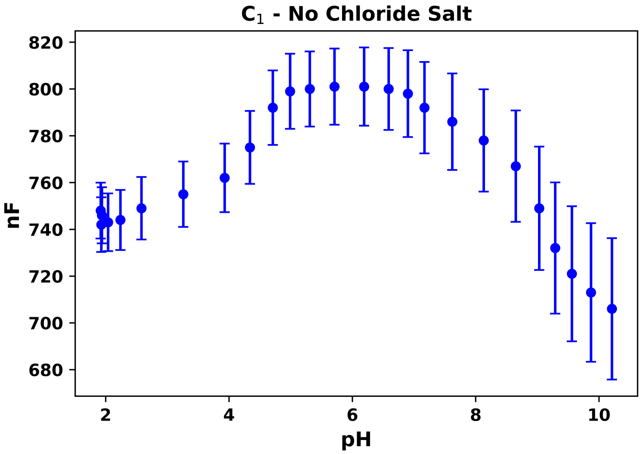

Figure 5.20 C_1 in series with R_1 for "no added alkali chloride salt" solution, where C_1 peaks around pH 6 but with significant error.

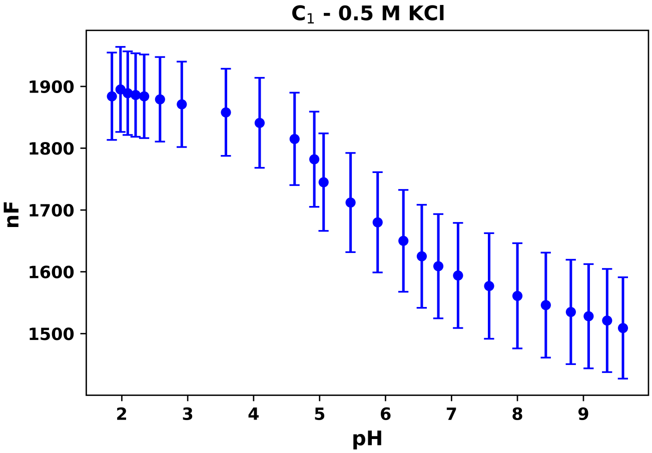

Figure 5.21 C_1 in series with R_1 from 100 Hz to 1 MHz for 0.5 M KCl, where C_1 appears pH dependent but with significant error.

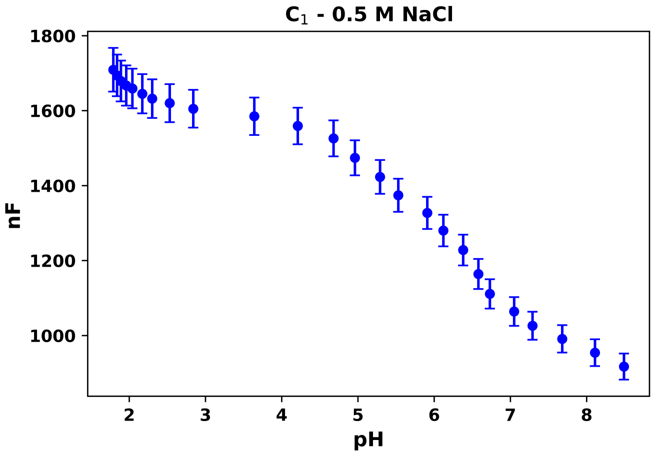

Figure 5.22 C_1 in the simplified, high ionic strength circuit for 0.5 M NaCl, where C_1 appears pH dependent. The C_1 double layer capacitance magnitude for 0.5 M NaCl here appears larger than for 0.5 M LiCl in Figure 5.23 (the opposite is true for C_2) (© 2022 Elsevier B.V. All rights reserved.).[220]

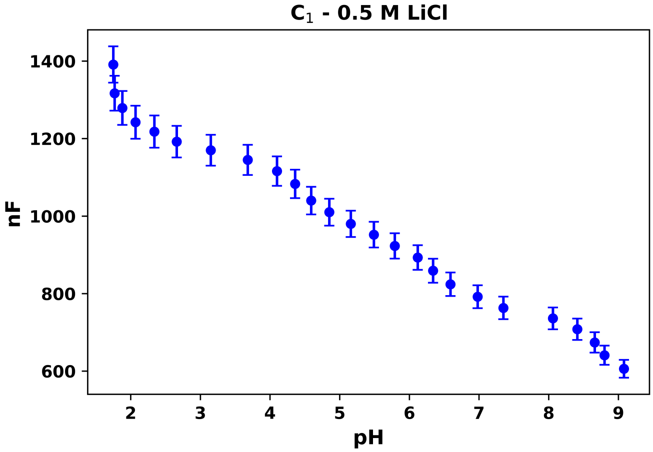

Figure 5.23 C_1 in the simplified, high ionic strength circuit for 0.5 M LiCl, where C_1 appears pH dependent. The C_1 double layer capacitance magnitude for 0.5 M LiCl here appears smaller than for 0.5 M NaCl in Figure 5.22 (the opposite is true for C_2) (© 2022 Elsevier B.V. All rights reserved.).[220]

5.4.5 pH versus Interfering Ion Specific Adsorption Capacitance

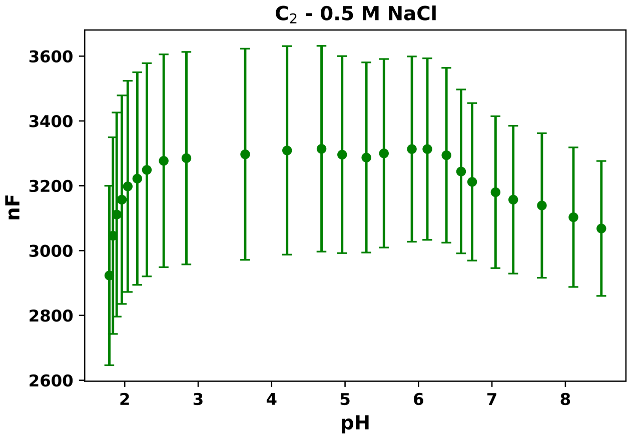

Figure 5.24 C_2 in the simplified, high ionic strength circuit for 0.5 M NaCl, with no clear pH dependence while considering error. The C_2 specific adsorption capacitance magnitude for 0.5 M NaCl here appears smaller than for 0.5 M LiCl in Figure 5.25 (the opposite is true for C_1) (© 2022 Elsevier B.V. All rights reserved.).[220]

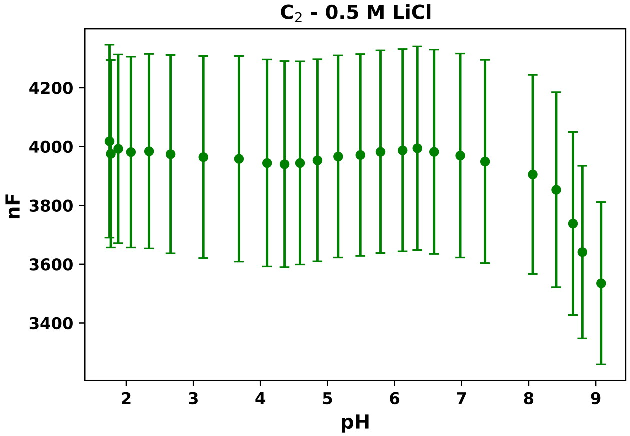

Figure 5.25 C_2 in the simplified, high ionic strength circuit for 0.5 M LiCl, which appears to decrease at high pH (and with increasing NaOH and larger Na^+ ions). The C_2 specific adsorption capacitance magnitude for 0.5 M LiCl here appears larger than for 0.5 M NaCl in Figure 5.24 (the opposite is true for C_1) (© 2022 Elsevier B.V. All rights reserved.).[220]

5.4.6 pH versus Interfering Ion Warburg Impedance

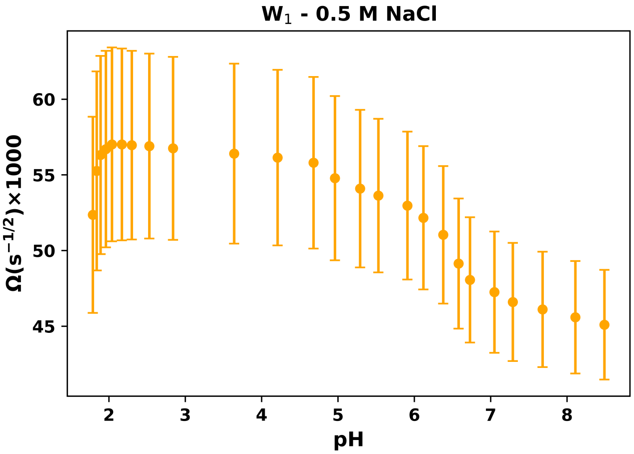

Figure 5.26 W$_1$ in the simplified, high ionic strength circuit for 0.5 M NaCl, with no clear pH dependence while considering error (© 2022 Elsevier B.V. All rights reserved.).[220]

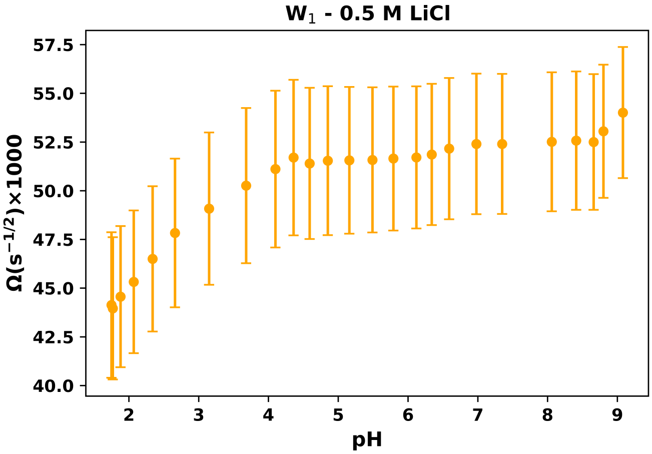

Figure 5.27 W$_1$ in the simplified, high ionic strength circuit for 0.5 M LiCl, which may increase with pH but with significant error (© 2022 Elsevier B.V. All rights reserved.).[220]

5.5 Discussion

5.5.1 No Added Alkali Chloride Salt

The fitted and plotted values versus pH (Figure 5.16 for R_1 and Figure 5.20 for C_1) appear to show that the device has a lossy capacitance in this solution, with no clear pH dependence. However as discussed previously, a pH dependence is visible in the series capacitance from roughly 10 kHz to 50 kHz in Figure E.9, where the double layer effects are diminished and the insulator capacitance is visible.[266] This pH dependence could be caused by the "proton space charge" which Vermilyea detected in anodic tantalum oxide;[54] in a later publication however, Vermilyea mentioned that this space charge may not be directly caused by protons.[55]

Additionally, knowing from Table 4.15 that pH 3 Britton-Robinson buffer has the highest solution resistance, and that R_1 is highest between pH 4 and pH 5 here, the effects of the tantalum oxide layer on R_1 are visible. A similar peak in the series resistance was also observed by Vermilyea with anodic tantalum oxide, although in a 2 M KCl solution at pH ~3.5.[53] His theoretical model did, however, predict a peak around pH 4 (in contrast to Bousse and Bergveld,[256] Vermilyea[53] appears to have placed the capacitances in series).

5.5.2 0.5 M KCl

The fitted and plotted values versus pH (Figure 5.17 for R_1 and Figure 5.21 for C_1) appear to show that the double layer capacitance is pH dependent, although the error is quite large with the limited frequency range and the omission of C_2 and W_1 from the circuit. Nonetheless, C_1 is decreasing with an increase in pH over large increases in basicity. Furthermore, at frequencies greater than 100 Hz a pH dependence is visible in the series capacitance in Figure E.10.

5.5.3 0.5 M NaCl

The fitted and plotted values versus pH (Figure 5.18 for R_1, Figure 5.22 for C_1, Figure 5.24 for C_2, and Figure 5.26 for W_1) show a clear pH dependence with C_1, where a low pH yields a higher capacitance. Furthermore, a pH dependence is visible over most frequencies in the series capacitance in Figure E.11. For examples of real world applications, the 2.9 wt% / 0.5 M NaCl solution measured here would be considered "high sodium kimchi"[11] (a Korean food staple), and is also similar to ocean salinity.[9,10] The IDE sensors made with the EGFET sensing layers in Experiment 2 of Chapter 4 were used to measure a 1.6 wt% / 0.28 M NaCl solution, which is similar in concentration to "low sodium kimchi,"[11] and the results are discussed at the end of this chapter with a plot of the series capacitance at 1 Hz in Figure 5.31. The series resistance and series capacitance spectra for the 0.28 M NaCl solutions are in the Appendix (Figures F.1 - F.8), which similarly show a decrease in series capacitance with in increase in pH at most frequencies.

5.5.4 0.5 M LiCl

The fitted and plotted values versus pH (Figure 5.19 for R_1, Figure 5.23 for C_1, Figure 5.25 for C_2, and Figure 5.27 for W_1) show a clear pH dependence with C_1, where a low pH yields a higher capacitance. Furthermore, a pH dependence is visible over most frequencies in the series capacitance in Figure E.12, which could prove informative in battery applications using aqueous electrolytes.[269] In 2019, Pan et al.[270] examined sol-gel derived, tantalum oxide aerogels as anodes in both lithium and sodium ion battery applications, where the reaction mechanism will be shortly described before comparing the effects ion size has on C_1 and C_2.

5.5.5 Redox Effects

Before this discussion is continued, possible redox effects need to be considered. For example, when placed in aqueous alkali, the electrochromic reaction for thin films of tantalum oxide is as follows:[271]

$$\mathrm{Ta_2^{5+}O_5(s) + H_2O + e^- \longrightarrow 2\,Ta^{4+}O_2(s) + 2\,OH^-(aq)} \tag{5.39}$$

The reduction of Ta^{5+} (colorless) to Ta^{4+} (very pale blue) allows for electrochromic applications and requires an energy input. However, since the thin film only has a slight color change, Ta_2O_5 is usually used as an ion-conductive electrolyte which is deposited in a stack, generally with different oxide layers which emit more potent colors.[271,272] For sol-gel derived electrolytes, Ozer[52] studied both Ta_2O_5 and Nb_2O_5 as proton conductors stacked on WO_3/ITO, where a minimum in transmittance at 550 nm was observed around −0.4 V.

Additionally, lithium tantalate has been investigated as an electrolyte for anodes in lithium ion batteries,[273,274] where insertion/extraction is as follows (where $x = 8$ is the maximum value):[270,275]

$$\mathrm{Ta_2O_5 + x(Li^+ + e^-) \longleftrightarrow Li_xTa_2O_5} \tag{5.40}$$

A similar reaction has been observed for sodium ion battery applications. However, the potentials required for insertion/extraction in a sol-gel derived, Ta_2O_5 aerogel are ∼0.8/1 V (cathodic/anodic) for lithium and 0.86/0.91 V (cathodic/anodic) for sodium. The disordered aerogel is a network of Ta_2O_5 nanoparticles, thereby increasing surface area and making insertion easier. Vermilyea[53] may have observed something similar when 1 V was applied across a 10 nm thick anodic Ta_2O_5 film, where potential hysteresis versus pH in NaCl and LiCl solutions was found; Vermilyea then concluded that these smaller alkali cations can adsorb on the surface.

Given that in this experiment, a thin (although possibly nanoporous) film was studied in an aqueous solution at a low operating potential amplitude of 10 mV (rms), redox effects for both protons and other alkali ions can be considered to be negligible, which is supported by the XPS results for the EGFET sensor showing one oxidation state of +5. Thus, we can attribute the observed phenomena in the immittance spectra to be largely a result of the double layer and specific adsorption of interfering ions on the oxide surface.

5.5.6 Effects of Ion Size on the Insulator-Electrolyte Impedance

In considering mobile ions on the insulator surface, fit deviations with the selected equivalent circuit may be due to metal oxide insulators following the "Discrete Helmholtz" model in solution, where the electric field is not uniform and diffusely distributed as is normally modeled with conductive electrodes.[276] Namely, ions in the electrolyte are correlated to "anchor points" on the insulator rather than being paired to specific counterions, and where the cations move over the insulator surface among these "anchor points." These points can appear closer to each other than in a diffuse charge distribution model, and thereby create their own parallel potential gradient. Parallel electric field vectors, present in IDE devices,[262] can also encourage the cations to move among these "anchor points" on insulators.

Formation of the double layer on IDEs is also time dependent and nonuniform over the electrode surface, and the applied electric field leads to fluid flow where the frequency at peak velocity is position and geometry dependent.[255,277–280] In a two electrode system, similar to the previously reported indium tin oxide impedimetric pH sensor (one working electrode between two counter electrodes),[281] the electrical double layer forms first on the electrode edges at the gap, and with longer charging times forms further away from the edge.[255,280] Measurement in aqueous KCl with two coplanar electrodes, covered with a thin TiO_2 layer, indicated that the double layer is not a pure capacity at low frequencies. This could not be ascribed to ion diffusion effects or Faradaic current, and remains a debated topic.[280]

Fit deviations may also be due to influences from $C_{Ta_2O_5}$, the insulator capacitance in series to the insulator-electrolyte interface with an assumed leakage current.[185] $C_{Ta_2O_5}$ was ignored in the simplified equivalent circuit and where anodic Ta_2O_5 has been observed to have a pH dependent "proton space charge."[54,55] In measuring with coplanar titanium electrodes covered with a thin TiO_2 layer, the insulator was mentioned as reducing the potential drop across the diffuse layer and thus ion velocity in solution.[280]

Prior Studies with Interfering Ions

In shortly returning to ion interference for pH sensing in the ISFET configuration, the theoretical sensitivity of Ta_2O_5-ISFETs within the range of pH 2 to pH 12, based on the improved model by van Hal, Eijkel, and Bergveld,[41,45] do not have significant pH deviations in high ionic strength solutions (aside from an increased response time).[282] Such deviations grow larger with an increasing ionic strength (Equations 5.17 and 5.20) and thereby an increasing differential double layer capacitance per unit area, C_{dif} from Chapter 2 of this thesis, which theoretically reduces the response of the electrolyte potential drop at the insulator-electrolyte interface, ψ_0, to changes in the bulk solution pH, $\mathrm{pH_B}$:

$$\frac{\delta\psi_0}{\delta \mathrm{pH_B}} = -\frac{kT\ln 10}{e}\left(\frac{kTC_{dif}\ln 10}{e^2\beta_{int}} + 1\right)^{-1} \tag{5.41}$$

However, the relatively high intrinsic buffer capacity of Ta_2O_5, β_{int}, is able to mitigate the effects of the double layer capacitance and interfering ions, as explained by van Kerkhof, Eijkel, and Bergveld in detail.[282] The buffering response of Ta_2O_5 follows a decrease in $|\psi_0|$ after addition of electrolyte to solution, as the diffuse layer capacitance, and thereby the integral double layer capacitance per unit area, C_{DL}, increases quickly with a decrease in the Debye length, λ_D:

$$\downarrow|\psi_0| = \frac{|\sigma_0|}{\uparrow C_{DL}} \tag{5.42}$$

This is gradually followed by a change in the surface charge, σ_0, by Ta_2O_5 adjusting the surface pH, $\mathrm{pH_S}$ from Equation 2.21 in Chapter 2, through adsorbing or desorbing H^+ and "correcting" ψ_0 to equilibrium with the value before electrolyte addition:

$$\uparrow|\psi_0| = \frac{\uparrow|\sigma_0|}{C_{DL}} \tag{5.43}$$

Nonetheless, Equation 5.41 indicates that the double layer capacitance will always have some effect on the pH response. In the case of a capacitive pH sensor in high ionic strength solutions, however, the shorter Debye length provides advantages for measuring a larger double layer capacitance driven primarily by H^+ and OH^- ions.[53]

In other experimental observations with Ta_2O_5-ISFETs, deviations above pH 12 were observed by Bobrov et al.[47] in 1991 for Na^+ and K^+ solutions, while for Li^+ solutions these began above pH 7 where a "pLi" response was observed. Above pH 12, the pLi response becomes Nernstian, thus showing the effects ion size has on interfering with pH sensing (Li^+ is the smallest and K^+ is the largest, while the opposite is true when the cations are hydrated).[12,283,284] Overall, Bobrov et al. found a decrease in pH sensitivity in the basic region with interfering cations, with the decrease in pH sensitivity ranked from most to least interference: $Li^+ > Na^+ > K^+$. Due to these ion sensitivities, Bobrov et al. proposed that Ta_2O_5-ISFETs do not follow the site-binding model as proposed by Bousse, de Rooij, and Bergveld[21] but rather that of chemical glass electrodes, where due to the Nernstian pH response and response to alkali ions, that the ion-exchange theory of glass electrodes is more appropriate for Ta_2O_5. Unfortunately, when van Hal et al. derived and reported the improved model from that of Bousse et al., four years after the report of Bobrov et al., the experimental observations of Bobrov et al. were not present in the discussion; however, unlike the model presented by Bousse et al., van Hal et al. considered the influence of ionic strength over the entire pH range in their derivation of the improved model. Thus, although the exact pH sensing mechanism remains unclear, there appears to be consensus that pH sensing with Ta_2O_5 can be affected by the ionic strength of the solution.

As this experiment is largely based on observations, with the theory only acting as an aid in explaining these observations, the results reported by Bobrov et al. will be used as the base for the discussion. Returning to ion size and its effects on the immittance spectra, Bobrov et al. concluded that the smallest ion, lithium, is mobile only at the surface of Ta_2O_5, which allows for the most likely assumption that lithium insertion is not happening, as discussed previously for lithium tantalate. Therefore, a comparison for C_1 and C_2 among different ion sizes, including their respective hydration shells, can be made for the double layer capacitance and the specific adsorption capacitance from interfering ions, respectively.

In considering the double layer capacitance, C_{DL}, from Equation 5.30 for C_1, the Stern distance, λ_S, has a significant influence at high ionic strength as the Debye length, λ_D, is reduced. X-ray photoelectron spectroscopy (XPS) methods by Brown et al.[285] have also shown that higher concentrations of NaCl can reduce the Stern length on SiO_2 nanoparticles, where the number of water molecules separating solvated ions from the surface is reduced, indicating that both λ_D and λ_S decrease with an increase in ionic strength. Furthermore, roughly 85% to 90% of the potential drop occurs over the Stern layer on SiO_2 nanoparticles for NaCl solutions, ranging from 0.01 M NaCl to 0.1 M NaCl in concentration, thus illustrating the importance of the Stern layer in affecting the double layer capacitance. As explained above in Equations 5.42 and 5.43, when van Kerkhof et al.[282] started with larger concentrations of interfering ions for Ta_2O_5-ISFETs, and then increased the concentration 5×, the immediate ψ_0 response decreased relative to starting at a lower interfering ion concentration; in order to explain these observations, only a change in λ_D and the diffuse layer capacitance was mentioned in influencing ψ_0, and the findings of Brown et al.[285] should also be considered whereby changes in λ_S from interfering ions, each having their own effective hydration radius,[283,284] also influences the immediate ψ_0 response to electrolyte addition.

Furthermore, negatively charged glass surfaces, such as SiO_2 and Ta_2O_5,[236,286] have more cations near the oxide surface than in the bulk, while anions such as Cl^- are concentrated further away from the surface.[12,49] Additional XPS measurements with alkali chloride salts at a concentration of 50 mM (0.05 M) were able to measure λ_S for particular alkali cations, and thereby C_{stern} per unit area, on SiO_2 nanoparticles while assuming a constant dielectric constant. λ_S was ranked among cations and calculated from the measured surface potential and surface charge density, both measured at pH 10, as being roughly the hydration radius plus one water molecule hydrating the SiO_2 surface: $Li^+ > Na^+ > K^+ > Cs^+$; C_{stern} per unit area was then computed and ranked inversely: $Li^+ < Na^+ < K^+ < Cs^+$.[12] Thus, the measurements and calculations revealed that no specific adsorption of alkali cations occurred at 50 mM in the inner Helmholtz plane. The measured ψ_0 from the XPS method largely followed the SiO_2-ISFET results of Bousse and Bergveld[21] and the SiO_2-impedance results of

Diot et al.,[287] thus illustrating the relevance of the XPS findings[12,285] to the results reported here for Ta_2O_5.

Similarly, the observations of Bobrov et al.,[47] with interference on Ta_2O_5-ISFETs being ranked as $Li^+ > Na^+ > K^+$, follow those of the XPS measurements[12] where an increased Stern length in the outer Helmholtz plane, and thereby a decreased C_{DL}, with an increased interfering ion hydration radius would increase the measured ψ_0 response:

$$\uparrow |\psi_0| = \frac{|\sigma_0|}{\downarrow C_{DL}} \tag{5.44}$$

However, the opposite trend with specifically adsorbed cation radius in the inner Helmholtz plane, with $Li^+ < Na^+ < K^+$, should also be considered as more specifically adsorbed charges (via partial charge transfer) may possibly increase with a smaller adsorption radius for a cation without the hydration shell,[288] where specifically adsorbed alkali cations and chloride anions act as dipoles in their own plane of charge separate from that of specifically adsorbed H^+.[48–50] Using immittance spectroscopy, as was performed in this work, the effects of interfering ions on the surface of Ta_2O_5 should become more apparent, and thus visible in the double layer capacitance, C_{DL} or C_1, and the interfering ion specific adsorption capacitance, C_{ad} or C_2.

Comparison of Prior Studies to Results

Figure 5.28 displays the impedance magnitude around 100 Hz for the 0.5 M NaCl and 0.5 M LiCl buffer solutions, with the magnitude shown to increase with an increase in pH (similar to Sample 14 in Experiment 1 of Chapter 4, with pH 5, pH 7, and pH 9 at ~10 kHz in Figure 4.5). 100 Hz was chosen since the greatest change in series capacitance (Figures E.11 and E.12 in the Appendix) versus pH occurs at that frequency for the 0.5 M NaCl solution, along with the phase angle being a similar value over the entire pH range while approaching a maximum of $-70°$ to $-80°$ in both solutions, where $-90°$ is the value for an ideal capacitor (Figures E.3 and E.4 in the Appendix). 100 Hz is also the approximate boundary between C_1

at high frequencies and C_2 at low frequencies, with the boundary being denoted by the local minimum on the C''-axis in the complex capacitance plane. The series capacitance vs. pH in Figure 5.29 shows an approximate slope of -110 nF/pH at 100 Hz in both 0.5 M LiCl and 0.5 M NaCl over the entire pH range, with the impedance magnitude having almost the same inverse relative change vs pH. Thus, whether impedance magnitude or series capacitance is used for pH sensing, the sensor fundamentally works in solutions of high ionic strength.

The double layer capacitance without specific adsorption, C_1, appears to increase with a decrease in hydrated ion size from Li^+ to K^+. However, the fit for the 0.5 M KCl solution followed a different procedure, since a realistic fit could not be performed using the provided software with the C_2—W_1 specific adsorption branch for the 0.5 M KCl solution. Therefore, only a proper comparison for the 0.5 M NaCl and 0.5 M LiCl solutions can be made here. Nonetheless, this increase in C_1 with a decrease in Stern length in the outer Helmholtz plane follows the XPS results on SiO_2 nanoparticles with 50 mM (0.05 M) solutions of LiCl, NaCl, KCl, and CsCl. Thus, the results reported here, particularly for Li^+ and Na^+, are largely in accordance with the Gouy-Chapman-Stern theory. However, the calculated Stern capacitance per unit area increase from the XPS study, increasing from Li^+ to Na^+, is only about 6% (from Li^+ to K^+ the increase is about 31%). On the other hand, the fitted C_1 values in Figure 5.29, when going from Li^+ to Na^+, show roughly a 34% capacitance increase at pH 2 and roughly a 30% capacitance increase at pH 8. Therefore, effects other than the Stern length in the outer Helmholtz plane may also be influencing the double layer capacitance represented by C_1, particularly as the fitted values are not per unit area.

In order to account for the area dependence, Brown et al.[12] measured the charge per unit area at pH 10 as the surface charge density, with the absolute magnitude ranked as LiCl < NaCl < KCl < CsCl at 50 mM (0.05 M) on SiO_2. These surface charge density variations were attributed to hydrated ion interactions in the outer Helmholtz plane. Although Brown et al. compared the measured surface potential to a theoretical model which included interactions between hydrated ions, and thereby showed that the measurements approximately follow the theory, a varying dielectric constant was ignored in the Stern distance and Stern capacitance calculation. In simplifying these calculations with a fixed dielectric constant, Brown et al. took the relative permittivity value at the SiO_2 interface from a simplified model applied by Sverjensky[289] in a geology context. Namely, Sverjensky placed all capacitances in series while keeping the permittivity constant throughout the insulator-electrolyte interface, in order to account for different oxides, electrolyte ions, ion hydration states, and adsorption behaviors as well as to make predictions for minerals which had no experimental data.[289,290] Sverjensky further notes that the model does not fit the data for all examined minerals and electrolytes,[289] and that there is debate within the geology community between a series and a parallel model.[290,291] However in this work, the parallel model at the insulator-electrolyte interface, proposed by Bousse and Bergveld[21] for electrolyte-insulator-semiconductor devices, appears to match the data obtained for sol-gel derived Ta_2O_5 in aqueous solution. Bousse et al.[49] also stated that "due to the rapidly varying dielectric constant in this region of the double layer these capacitances are not simply inversely proportional to distance."

In further considering surface charge density differences between this work and those of Brown et al.,[12] the measurements with Ta_2O_5 here used a higher alkali chloride salt concentration (0.5 M) than Brown et al. (0.05 M), while Ta_2O_5 also has a larger number of charged binding sites than SiO_2 which could attract cations towards the surface.[41,45] Thus, both of these factors may possibly lead to more charges per unit area in the outer Helmholtz plane of the Stern layer than was measured by Brown et al. for SiO_2. Other factors can affect the charge density and dielectric constant, and thereby the double layer capacitance, where for example Nakayama and Andelman[13] considered sterics and dielectric decrement.

In the case of steric effects, at high surface charge density the ions approach a concentration limit estimated to be proportional to $(2r)^{-3}$, with r being the hydrated ion radius.[13] Calculated effective hydrated radii are shown in Table 5.1, whose actual values are under debate,[288] but nonetheless rank as $Li^+ > Na^+ > K^+$. Thus in the limit of close-packing, Li^+ would have a lower charge density in the outer Helmholtz plane of the Stern layer than Na^+

and K^+, thereby decreasing the Stern capacitance. Brown et al.[12] also showed with their theoretical model that cation distance away from the surface ranks as $Li^+ > Na^+ > K^+ > Cs^+$, which incorporated hydrated ion interactions. Brown discusses hydration interactions in more detail with Caetano et al.,[292] while stating that the effects of electrode polarization on dielectric discontinuity[293] and a changing dielectric constant from the ions themselves[13] were ignored.

Hasted et al.[294] in 1948 investigated ion specific effects in bulk aqueous electrolyte, and were able to measure a dielectric decrement which is a linear function of ion concentration from 0.5 M to 2 M. In the case of an electrode in solution, the local ion concentration, $n(z)$, as a function of distance from the electrode, z, with the subscript denoting the sign of the ion charge, determines the dielectric decrement along with a coefficient for the respective ion, γ:[13]

$$\epsilon\left(n_{\pm}\right) = \epsilon_w - \gamma_+ n_+(z) - \gamma_- n_-(z) \tag{5.45}$$

Here, ϵ_w is the relative permittivity of water, where in the case of anion depletion in the Stern layer, and where linear decrement is considered, the change in the relative Stern permittivity, ϵ_S, is as follows:

$$\Delta\epsilon_S = \epsilon_S - \gamma_+ n_S^+ = \epsilon_w - 2\gamma_+ n_S^+ \tag{5.46}$$

Important to note is that the cation concentration in the Stern layer, n_S^+, may be reduced by steric effects or hydrated ion interactions in the outer Helmholtz plane. The ion specific γ values are shown in Table 5.1.

Dielectric decrement is caused by the creation of ion holes and polarity changes in the electrolyte.[13,294–297] Hydrated cation polarity ranks as $Li^+ > Na^+ > K^+$, where a smaller cation is able to polarize water molecules more through a reduced radius, and thereby reduce the permittivity as water molecules are able to respond less to external electric fields.[298] Additionally, as the number of water molecules hydrating the ion increases, the polarity decreases as the influence of other water molecules increases. Although Li^+ has been observed to decrease the permittivity more than Na^+ and K^+, a lower ion concentration in the Stern layer for Li^+ may reduce the effect of dielectric decrement in comparison to Na^+ and K^+ according to Equation 5.46. This illustrates the complexity in attempting to estimate the Stern capacitance. Nonetheless, a lower double layer capacitance measured in 0.5 M LiCl with respect to 0.5 M NaCl is likely caused by a longer Stern distance, a lower charge density, and a reduced permittivity in the outer Helmholtz plane at the insulator-electrolyte interface.

Furthermore, recent models and experimental data indicate that in supercapacitor applications in aqueous electrolyte, the dielectric permittivity at the Stern layer changes as a function of distance, time, local ion concentration, and ion type, which complicates the matter further.[297] In considering these effects in the outer Helmholtz plane, the measured double layer capacitance (not per unit area) in this work, with a larger magnitude change between cations, does not necessarily contradict the calculated Stern capacitance per unit area by Brown et al.[12] with a smaller magnitude change between cations, particularly where the latter used a fixed dielectric constant in the calculation.

Then in considering the specific adsorption capacitance in the inner Helmholtz plane, C_2, the larger magnitude observed with the LiCl solution is likely due to the smaller ion size of Li^+ when adsorbed on the surface, which would give Li^+ a higher specific adsorption capacitance with a smaller distance, d, than Na^+; this may be supported by an observed decreasing C_2 at high pH in the LiCl solution, where there is increasing NaOH and larger Na^+ cations. Due to this added NaOH, C_2 is compared in Table 5.2 between the 0.5 M LiCl and 0.5 M NaCl solutions at pH 5.5, where above pH 4 the H^+ adsorption capacitance is negligible for anodic Ta_2O_5,[53] and where the two solutions had a similar pH value with the least amount of added NaOH. In understanding specific adsorption, Bousse et al.[48] noted that specific adsorption of alkali cations (M^+) would have a high capacitance, namely behaving as dipoles with a partial charge contribution to the insulator surface charge:[49,50]

$$\mathrm{Ta{-}OH} + \mathrm{M}^+ \rightleftharpoons \mathrm{Ta{-}O^-\ M^+} + \mathrm{H}^+ \qquad (5.47)$$

Although the M−O adsorption distance at the insulator-electrolyte interface (M−O−Ta, where M = Na^+, Li^+) is not known, an estimate is made here with hydrated Li^+ and Na^+ cations in aqueous solution, with the respective M−O distances for d_{Li^+} and d_{Na^+} with water in Table 5.3. Using these values, the specific adsorption capacitance increase from Na^+ to Li^+ is estimated in Table 5.4, which is close to the observed 20% increase in this work. The change could also be affected by steric and dielectric effects, as with the double layer capacitance, although the fixed number of specific adsorption binding sites may mean these effects are not as prominent. For possible permittivity effects, the adsorption of alkali on gold has shown that polarity increases with an increase in cation radius, namely with the polarity ranked as $Li^+ < Na^+ < K^+$, which is due to the increased partial charge transfer to cations with a smaller radius.[288] However, this may not directly translate to adsorption on Ta_2O_5. As the specific adsorption capacitance remains relatively constant over the measured pH range, specific adsorption effects may need to be considered at high ionic strength along with the double layer capacitance, which may require a modification of the theory proposed by van Hal et al.[41,45] Such a modification would support the observations of Bobrov et al.[47] with ISFETs and Bousse et al.[48] with light-addressable potentiometric sensors (LAPS).

For the case where the frequency is fixed at 100 Hz (thus fixing a variable for a varying dielectric constant), which is where the phase angle approaches a maximum of −70° to −80° (with −90° being an ideal capacitor) and where the series capacitance responds the most to a change in pH for the 0.5 M NaCl solution, the equivalent series resistance (ESR, not to be confused with R_1) and the series capacitance at 100 Hz are tabulated at similar pH values in Table 5.5; a comparison at all pH values between C_1 and the series capacitance at 100 Hz is plotted in Figure 5.29, and the ESR with the series capacitance at 100 Hz are plotted in Figure 5.30 for 0.5 M KCl, 0.5 M NaCl, and 0.5 M LiCl. The ESR and series capacitance values at 100 Hz indicate that the device can be used for capacitive pH sensing when integrated into a simpler electronic circuit for read-out, particularly when the use of an impedance analyzer is not possible.

The higher ESR at 100 Hz for Li^+ may be related to the ion's higher viscosity in solution (i.e., kosmotropic effects with $\mathrm{Li}^+ > \mathrm{Na}^+$, while K^+ and Cl^- are chaotropic and decrease solution viscosity),[299–301] or other unknown effects. In considering fluid velocity, v, as ions move approximately parallel to the electrode surface after applying direct current (DC) between coplanar electrodes, the zeta potential is proportional to the surface charge density in the diffuse layer, σ_q, allowing for the linear approximation of v:[277]

$$v = \frac{E_t \sigma_q \lambda_D}{\eta} \tag{5.48}$$

Here, E_t is the electric field tangential to the electrode surface, η is the medium viscosity, and λ_D is the Debye length. However, when applying an AC electric field, the fluid velocity also becomes frequency dependent. Since the measured 0.5 M LiCl solution likely has a lower surface charge density in the diffuse layer and a higher viscosity than the measured 0.5 M NaCl and 0.5 M KCl solutions, then the difference in ESR at 100 Hz may be influenced by a lower fluid velocity for Li^+ with respect to Na^+ and K^+ (thus following the electrophoretic mobility).[260]

Important to note is that as the pH increases, Na^+ increases in concentration with each NaOH addition for all solutions, where the NaOH molarity increase for each addition is estimated in Table G.1 in the Appendix. Future experiments could be performed with KOH, NaOH, and LiOH for KCl, NaCl, and LiCl solutions, respectively, in order to make the experiment more robust. Resources permitting, measurements in aqueous RbCl and CsCl solutions would also be informative.

Table 5.1 Dielectric decrement coefficients (± 1 M^{-1}) from Hasted et al. (1948), and effective hydration radii for the listed ions. Nakayama and Andelman[13] refer to radii from Nightingale (1959), while Brown et al.[12] refer to radii from Kielland (1937). Waegele et al.[288] (2019) doubt the accuracy of the effective hydration radii in the context of catalysis and electrode adsorption.

Hydrated Ion	γ (M^{-1}) Hasted et al.[294]	r (Å) Nightingale[284]	r (Å) Kielland[283]
H^+	17	2.82	-
OH^-	13	3.00	-
Li^+	11	3.82	5.3
Na^+	8	3.58	4.7
K^+	8	3.31	3.9
Cl^-	3	3.32	3.9

Table 5.2 $C_{2,\mathrm{LiCl}}/C_{2,\mathrm{NaCl}}$ ratio at pH 5.5 with minimum, no error, and maximum values while considering percent error, where the "no error" value is close to the estimates in Table 5.4.

$C_{2,\mathrm{NaCl}}$ at pH 5.53	$C_{2,\mathrm{LiCl}}$ at pH 5.49	Min	No Error	Max
3300 ± 291 nF	3971 ± 343 nF	1.010	1.203	1.434

Table 5.3 M−O distance in Å of hydrated Li^+ and Na^+ as a function of hydration number, or coordination number, N_c, with Avg. being the average distance for the respective ion. These values have been obtained from structure databases in 2012, where $N_c = 4$ for Li^+ and $N_c = 6$ for Na^+ are suspected to be the most common coordination numbers for these cations in aqueous solution.[302] The average distances are close to the previously published values by Marcus in 1988.[303]

N_c	4	5	6	Avg.
Li^+	1.942		2.132	2.037
Na^+		2.358	2.415	2.387

Table 5.4 Estimated specific adsorption capacitance (C_2) increase from Na^+ to Li^+ using the literature values[302] for M−O distances in aqueous solution from Table 5.3, calculated as $d_{Li^+}^{-1}/d_{Na^+}^{-1}$. Each value is calculated from the intersection of the Li^+ and Na^+ ions of a given hydration number, and includes an average of the 4 values. $N_c = 4$ for Li^+ and $N_c = 6$ for Na^+ may yield the most appropriate estimation.

M^+ N_c	Li^+ 4	Li^+ 6	Li^+ Avg
Na^+ 5	1.214	1.106	
Na^+ 6	1.244	1.133	
Na^+ Avg			1.174

Table 5.5 Equivalent series resistance (ESR) and series capacitance values at 100 Hz for Li^+ and Na^+ solutions at a particular pH value, reported with the R_{Li^+}/R_{Na^+} and C_{Na^+}/C_{Li^+} ratios (note the flipped ion labels between R and C).

pH Li^+ | pH Na^+	R Li^+ (Ω)	R Na^+ (Ω)	R Li^+ / R Na^+	C Li^+ (nF)	C Na^+ (nF)	C Na^+ / C Li^+
1.77 | 1.79	256	200	1.28	1919	2236	1.17
1.88 | 1.89	262	204	1.28	1874	2175	1.16
2.34 | 2.30	272	208	1.31	1792	2120	1.18
3.68 | 3.64	286	213	1.34	1680	2072	1.23
5.49 | 5.53	334	237	1.41	1457	1867	1.28
6.12 | 6.12	353	251	1.41	1393	1779	1.28
6.34 | 6.38	365	259	1.41	1353	1732	1.28
6.59 | 6.58	379	270	1.40	1313	1678	1.28
6.98 | 7.05	391	290	1.35	1276	1586	1.24
8.06 | 8.11	416	316	1.32	1213	1482	1.22
8.41 | 8.49	431	326	1.32	1182	1447	1.22

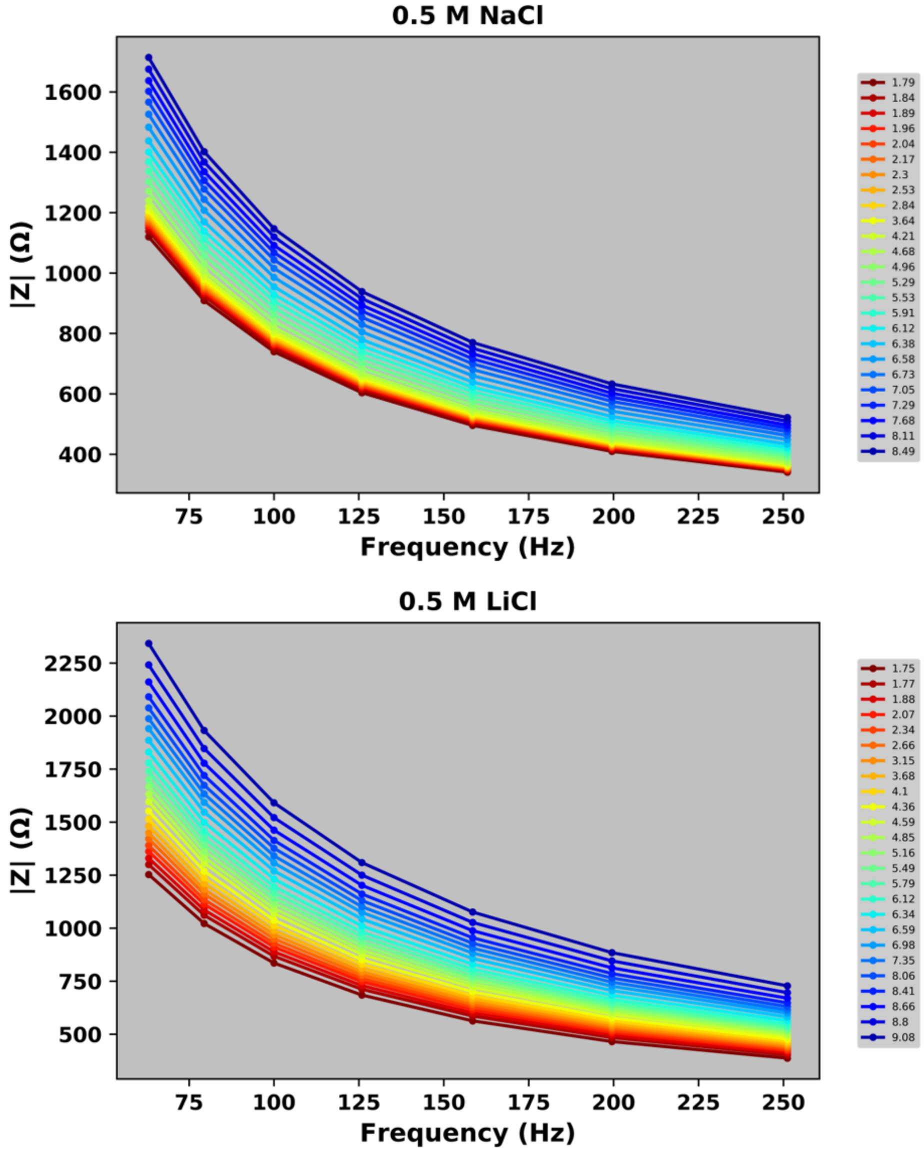

Figure 5.28 Impedance magnitude increasing with pH around 100 Hz for both the 0.5 M NaCl and 0.5 M LiCl solutions. The impedance magnitude change versus pH appears larger in the 0.5 M LiCl solution than in the 0.5 M NaCl solution (© 2022 Elsevier B.V. All rights reserved.).[220]

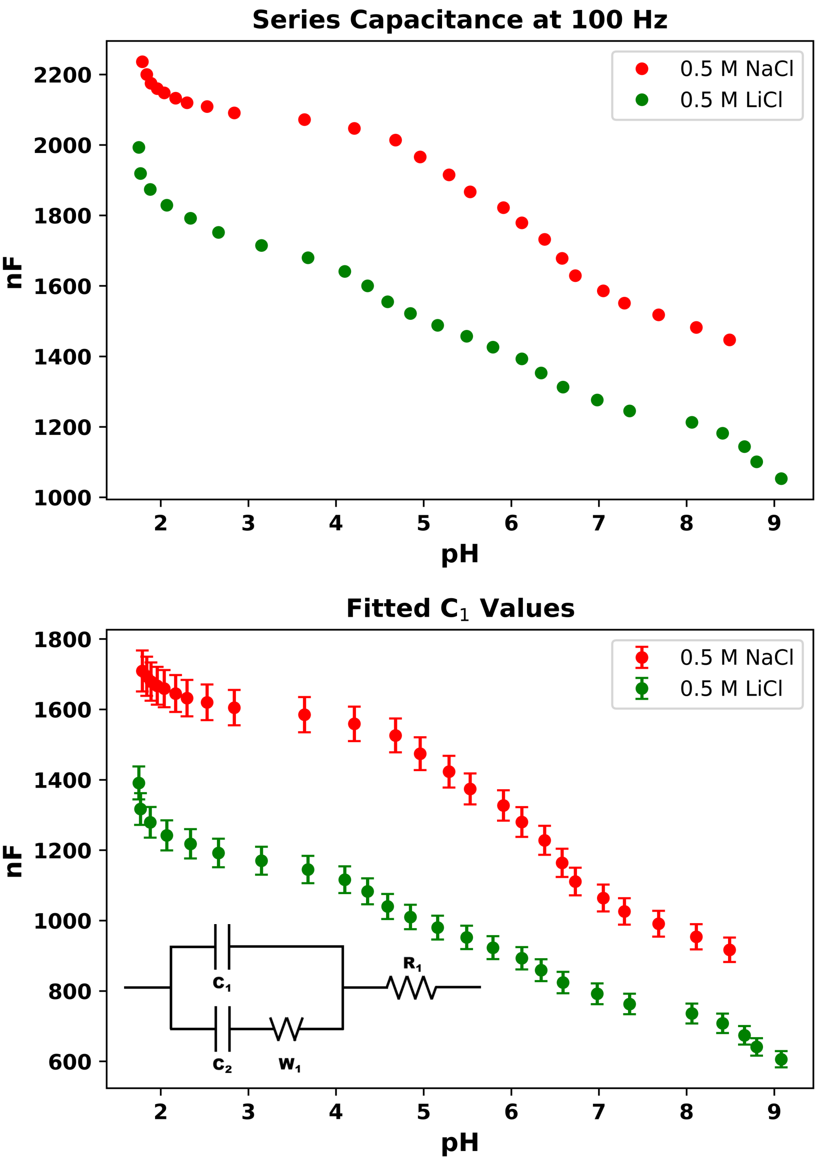

Figure 5.29 Series capacitance at 100 Hz for Na^+ and Li^+ solutions, compared with C_1 values from Figure 5.22 for Na^+ and Figure 5.23 for Li^+, where similar behavior occurs (© 2022 Elsevier B.V. All rights reserved.).[220]

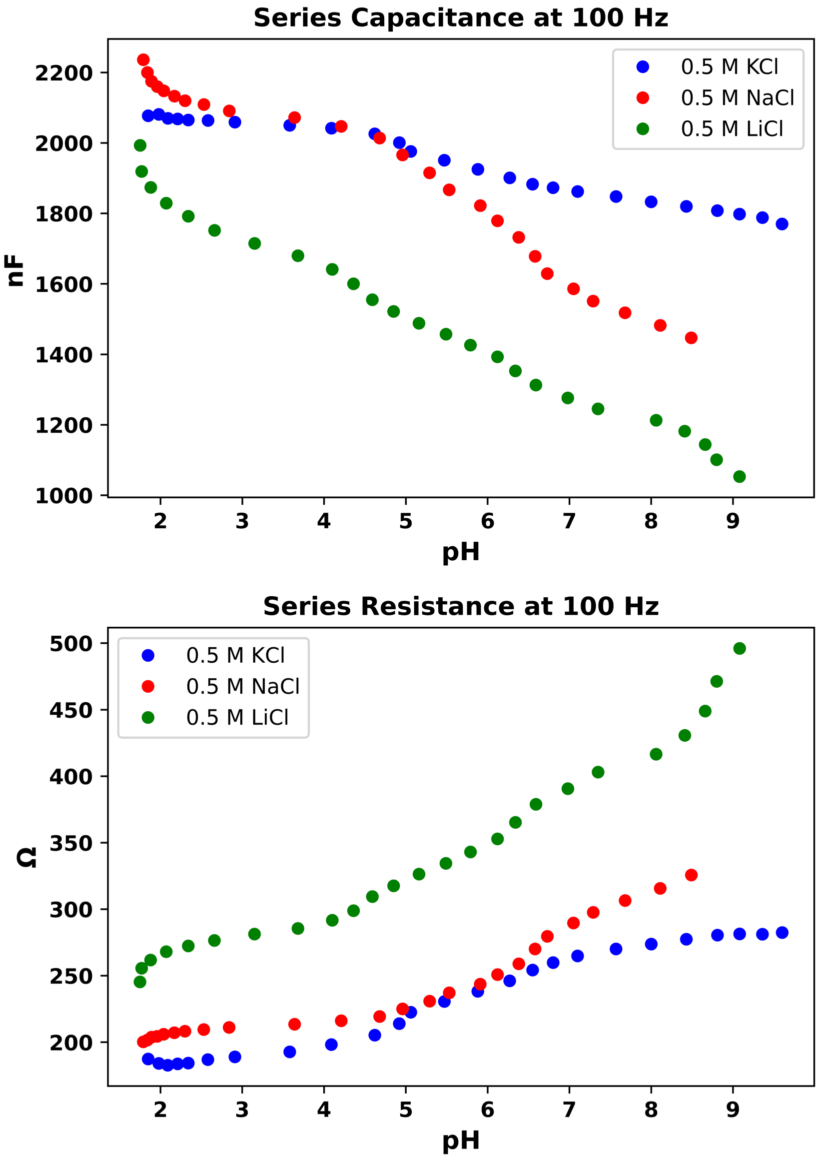

Figure 5.30 Equivalent series resistance (ESR, not to be confused with R_1) and series capacitance plotted versus pH at 100 Hz for K^+ (-40 nF/pH), Na^+ (-110 nF/pH), and Li^+ (-110 nF/pH) cations. The Li^+ solution has a higher ESR and a lower series capacitance than the Na^+ solution over the entire pH range (© 2022 Elsevier B.V. All rights reserved.).[220]

5.5.7 0.28 M NaCl with Sensors 1-8, 1-7, 1-6, and 1-5

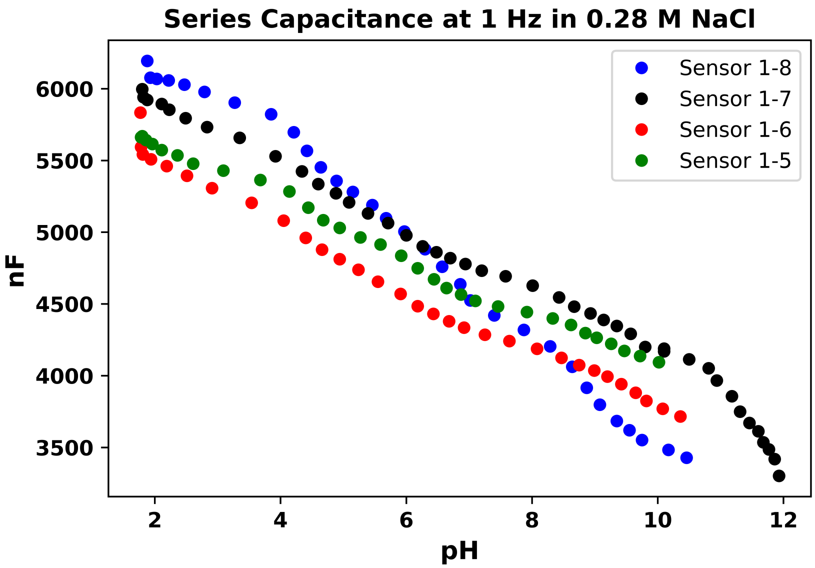

Figure 5.31 The series capacitance plotted at 1 Hz in 0.28 M NaCl.

As seen in the series capacitance spectra for Sensors 1-8 in Figure F.2, 1-7 in Figure F.4, 1-6 in Figure F.6, and 1-5 in Figure F.8, the largest change in the series capacitance in 0.28 M NaCl occurs at 1 Hz and is plotted in Figure 5.31, where Sensors 1-8, 1-6, and 1-5 were measured from about pH 2 to pH 10.5, while Sensor 1-7 was measured from about pH 2 to pH 12. In the pH range from pH 2 to pH 11, the slopes for Sensors 1-8, 1-7, 1-6, and 1-5 are about -336 nF/pH, -214 nF/pH, -219 nF/pH, and -196 nF/pH, respectively; from pH 11 to pH 12, the slope is about -635 nF/pH for Sensor 1-7. The larger slopes seen here, with respect to Sensor 7-7 in 0.5 M NaCl at 100 Hz with -110 nF/pH, could be due to the lower frequency, the larger geometry, or a possibly larger change in the Debye length as the NaOH concentration is increased. Variations among sensors could be due to differences in the deposited tantalum oxide layers. 0.28 M NaCl is similar to “low sodium kimchi.”[11]

Chapter Six

Thermistor

Recall the standard definition of pH below, where the pH of the measurement standard S, pH(S), can be used to determine the pH of a solution X, pH(X):[15,17]

$$\mathrm{pH(X)} = \mathrm{pH(S)} + \frac{(E_\mathrm{X} - E_\mathrm{S})F}{RT \ln 10} \tag{6.1}$$

Here, the difference in e.m.f. between the standard potential, E_S, and the solution potential in question, E_X, needs to be known; additionally, F is Faraday's constant, R is the molar gas constant, and T is the system temperature. In light of this pH dependence on temperature, where temperature represents an average of the kinetic energy of particles in matter, a temperature sensor which could be fabricated via roll-to-roll processing is vital for an operational pH sensor fabricated in the same manner.

Thus, an observed layer resistivity dependence on temperature with synthesized ruthenium-tantalum oxide films will be examined as a possible temperature sensor, which could be integrated with fabricated tantalum oxide pH sensors. Parts of this chapter have been discussed in German patent application DE 10 2019 006 976.5 filed on October 8, 2019.[138]

6.1 $\mathrm{RuO_2}$ Thermistor

A negative temperature coefficient (NTC) effect is known to occur for disordered ruthenium dioxide,[304] and is caused by localization of the electron wave function and other quantum effects which are outside the scope of this thesis.[305] However, a short discussion on past experimental observations is warranted.

In 1967 Iles and Casale from British industry,[306,307] in reporting screen printed ruthenium-niobium resistors with an added insulating glass, justified mixing the two elements as a way to control the resistivity and the temperature coefficient in manufacturing resistors. In particular, niobium pentoxide was found to be able to be incorporated up to 50% molecular into the ruthenium dioxide lattice. The desired effect in mixing the two oxides, as quoted from the authors, is as follows:[306,307]

> Since the temperature coefficient of resistance of ruthenium dioxide is metallic in nature and strongly positive, introduction of a non-conducting oxide might be expected to exert a negative influence on the temperature coefficient. Thus control of temperature coefficient in addition to resistivity might be achieved.

A similar description for mixing group 5 elements with ruthenium dioxide, resulting in a material with different conductive properties, was reported in Russian research in the 1980s. Their findings are quoted below:[308]

> One of the methods of controlling the electrical properties of RuO_2 is its alloying with d-elements of the fifth group, which is possible due to the presence of wide ranges of solid solutions based on RuO_2 in the Ru-M-O (M = V, Nb) systems...
>
> ...Alloying of RuO_2 with vanadium or ~~rubidium~~ [translation error: niobium] is related to inter-cation interactions leading to a change in the valence-electron density in the Ru-O π^*- and M-O π^* bands [M = V, Nb], which directly influences the electrical conductivity of the solid solutions.

Remember from the history of tantalum discussed earlier that the Soviet Union was not able to acquire tantalum easily, which may be why the Russian group only investigated mixing with vanadium and niobium. The same group later measured the NTC observed in such materials, although they noticed the NTC diminished after adding more of the dopant. Their discussion is quoted below to retain accuracy:[309]

> In RuO_2 and $Ru_{(1-x)}M_xO_2$ the d band of the cation sublattice, which is formed by the $2t_{2g}$ orbitals, is located near the Fermi level, and the energy levels of the metal-oxygen bonds are located in the lower part of the valence band. When RuO_2 is doped to x = 0.05-0.1, the $2t_{2g}$ band moves to a deeper position along the energy scale as a consequence of the Ru-M cation-cation interaction, and the density of the "metallic" ruthenium 4d states undergoes a decrease, which results in a sharp increase in ρ [resistivity] (in this case, W > Nb > V).
>
> As the content of M is increased ($x > 0.1$), the position of the $2t_{2g}$ level is stabilized, but the lowering of the oxygen 2p density in the Ru-O π bond in response to the appearance of the M-O π bond results in delocalization of the corresponding 4d electrons and a certain decrease in ρ.

As the Russian group was annealing at over 800°C in air, this allowed for lattice incorporation for both metals. Similarly, calcining of sol-gel prepared ruthenium-titanium oxide (using ruthenium(III) acetylacetonate and titanium(IV) isopropoxide) at 1300°C resulted in a positive temperature coefficient, possibly because both form an ordered rutile lattice.[210] Thus, a low temperature sol-gel approach with ruthenium and tantalum may not result in lattice incorporation, but rather a mixture of conducting RuO_2 with an insulating Ta_2O_5 glass, potentially leading to localization and a negative temperature coefficient, as is the case for disordered RuO_2,[304] RuO_2 and/or IrO_2 in a disordered Al_2O_3 matrix,[310] and amorphous lanthanum-ruthenium oxide.[311] Fabrication of the latter material via chemical solution deposition (CSD) is discussed in a patent, where the lanthanum assures a disordered material, even after annealing at high temperatures where crystalline ruthenium dioxide would normally form. A similar experiment, where lanthanum is replaced with tantalum, will be described and discussed below.

6.2 Experiment 1 - NTC Effect Observed

In an attempt at creating a 30 Ru : 70 Ta material for pH sensing[312,313] (where due to instabilities as discussed in the background, investigations for pH measurements were abandoned), 1,3-propanediol (120 mmol, 9138 mg [Sigma-Aldrich, for synthesis]), ruthenium(III) acetylacetonate (1.44 mmol, 575 mg [Merck, for synthesis]), and tantalum(V) ethoxide (2.62 mmol, 1066 mg [Alfa Aesar, 99+%]) were added to a Schlenk flask in air, with the flask subsequently connected to an argon line and a vertical condenser (cold finger). The flask was then placed in a heating mantle at 190°C, where mixing via magnetic stirring was carried out for about 13.5 hours. A greenish/black solution resulted, where filtering the entire solution with 6 Minisart 1.20 μm cellulose acetate filters (Sartorius AG, Germany) resulted in a homogeneous, red-yellow solution. After examining the filtered solution material (2 hour oven treatment at 250°C) via energy-dispersive X-ray spectroscopy (EDX) (Oxford Instruments X-Max 80 mm^2, UK; Software - INCA 4.15, The Microanalysis Suite Issue 18d; average of 5 points) on a carbon stage, a 59 Ru : 41 Ta material resulted, thus missing the original mark with an input of 35 Ru : 65 Ta.

In order to make an ink, 1 mL of filtered product was then diluted in 1.6 mL of 1-pentanol (Sigma-Aldrich, ACS reagent, ≥99%), where the ink had a viscosity of 11.4 mPa s and a surface tension of 27 mN m^{-1} (see Chapter 4 for viscosity and surface tension measurement procedure). The ink was then printed on interdigitated electrodes (IDEs) with 36 digits, having a length of 3000 μm, a width of 40 μm, and a gap of 15 μm. These IDEs were 200 nm thick gold on 20 nm thick titanium, with a 500 μm thick borofloat wafer as the substrate. The plasma and printing parameters (see Chapter 4 for device descriptions) are shown in Tables 6.1 and 6.2, respectively. After printing, the chip was then placed on a hot plate for 2 hours at 250°C.

Table 6.1 Surface plasma treatment for gold IDEs on borofloat wafer.

Gas	Pressure (mbar)	Power (W)	Time (s)
Oxygen	0.6	150	18

Table 6.2 Printing parameters for laser ablated IDEs (head height at 1.1 mm).

Waveform (µs)	Voltage (V)	Frequency (Hz)	Pitch (µm)	Dimensions (Drops)
1 - 10 - 1	25	1000	100	40 × 40

Upon soldering the chip to the carrier, and checking the solder joints via a resistance measurement on the hot plate, it was noticed that the resistance changed when the chip was removed from the hot plate. In order to investigate this further, wires were soldered to the gold contacts on the carriers for the 4 sensors. The wires were then connected to the PalmSens 4 potentiostat via the MUX8 multiplexer (PalmSens BV, The Netherlands), and the impedance at 100 Hz and 100 mV amplitude (rms, phase angle of 0°) was taken as the resistance. The chip was placed on a RCT Basic hot plate (IKA, Germany), where the temperature was measured with a GMH 3300 meter (Greisinger, Germany), with the thermocouple taped to the hot plate. Such a setup provides an inaccurate temperature reading, as the hot plate likely does not have uniform heating. Nonetheless, the setup allows for an initial determination of temperature sensitivity. The ink synthesis, dilution, cured layer on IDEs (for the sensor connected to channel 3), and temperature setup are shown in Figure 6.1.

The hot plate temperature was then cycled (heat-cool) twice with temperatures of approximately 20°C, 30°C, 40°C, 50°C, and 60°C. This was followed by 3 cycles (heat-cool) at 20°C, 30°C, 40°C, 50°C, 60°C, 70°C, 80°C, 90°C, and 100°C. The resistance was measured 3 times at each temperature, and averaged with the standard deviation as the error bar shown in Figure 6.2.

As a NTC was noted in the 20°C to 100°C range, the chip was then placed in a cryostat to test at cooler temperatures. Measurements were performed in a standard He flow cryostat (Oxford Cryosystems, United Kingdom). The sample was mounted on a "sample stick" with a temperature sensor attached and cooled down in flowing gas of cold He (with a typical gas pressure of a few mBar). At the bottom of the cryostat, the He is at 4.2 K in the heat exchanger and can be heated in the exchanger to a given temperature. The sample holder and sample were then cooled down to (approximately) that temperature. Upon cooling, the resistance values for channels 2, 3, and 4 in Figure 6.3 change from those in Figure 6.2, possibly due to the solder joints changing under the temperature change. The samples were further shown to have ohmic behavior at low voltages. Due to an observed NTC over the entire temperature range, a reverse engineering attempt was performed in the next experiment.

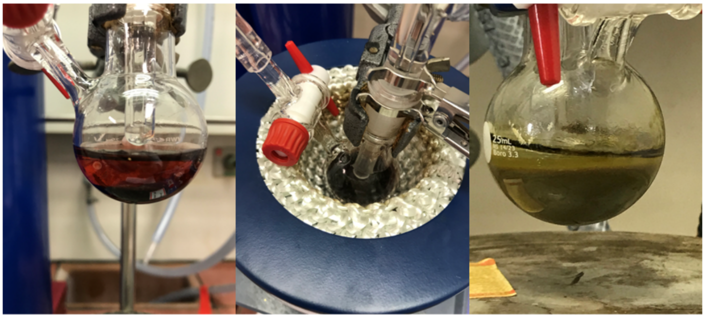

20:27 on 19.02.2018: Reagents mixed.

20:34 on 19.02.2018: Set to 190°C overnight.

09:58 on 20.02.2018: End after more than 13 hours.

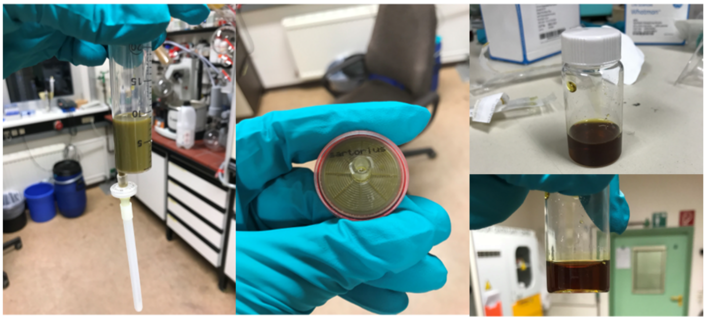

Solution in syringe, with a filter that's too small.

6 Minisart 1.20 µm Cellulose Acetate Filters

Filtered, precipitate-free final product.

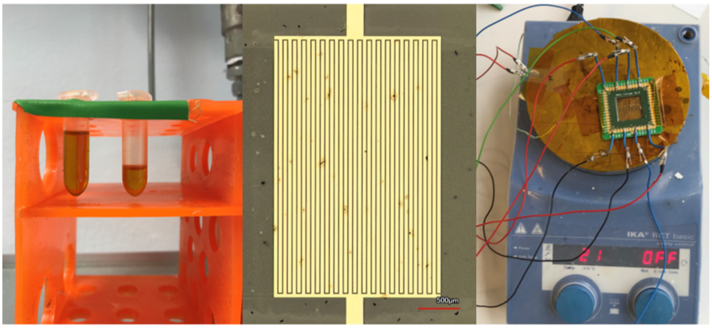

1.0 mL of product diluted in 1.6 mL of 1-pentanol.

Layer cured on IDEs; scale bar = 500 µm.

Chip soldered onto carrier, and placed on hot plate.

Figure 6.1 Synthesis and fabrication of temperature sensors for Experiment 1.

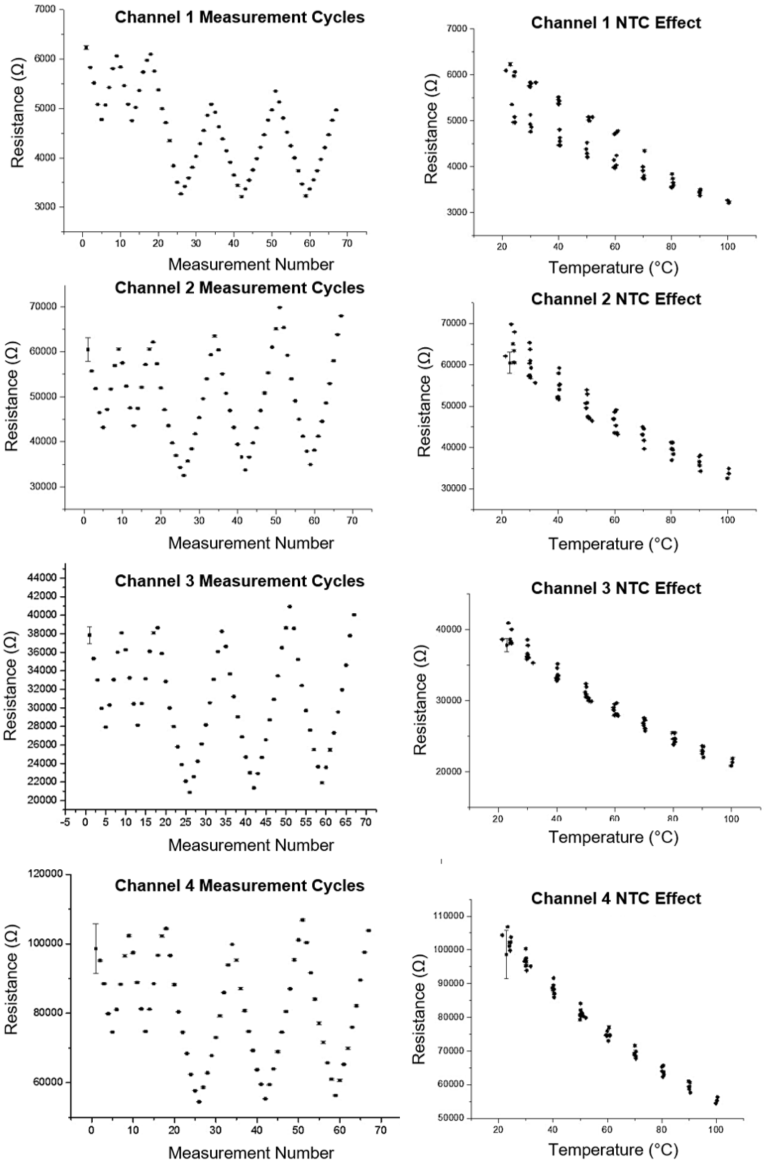
Channel 1 Measurement Cycles

Channel 1 NTC Effect

Channel 2 Measurement Cycles

Channel 2 NTC Effect

Channel 3 Measurement Cycles

Channel 3 NTC Effect

Channel 4 Measurement Cycles

Channel 4 NTC Effect

Figure 6.2 Manual temperature measurements on a hot plate for RuTaOx material from Experiment 1. Resistance taken as the impedance at 100 Hz (with a phase angle of 0°), and amplitude of 100 mV (rms). The measurement number starts at 0, and was taken once the hot plate arrived at the desired temperature. Error bars are the standard deviation of 3 impedance values.

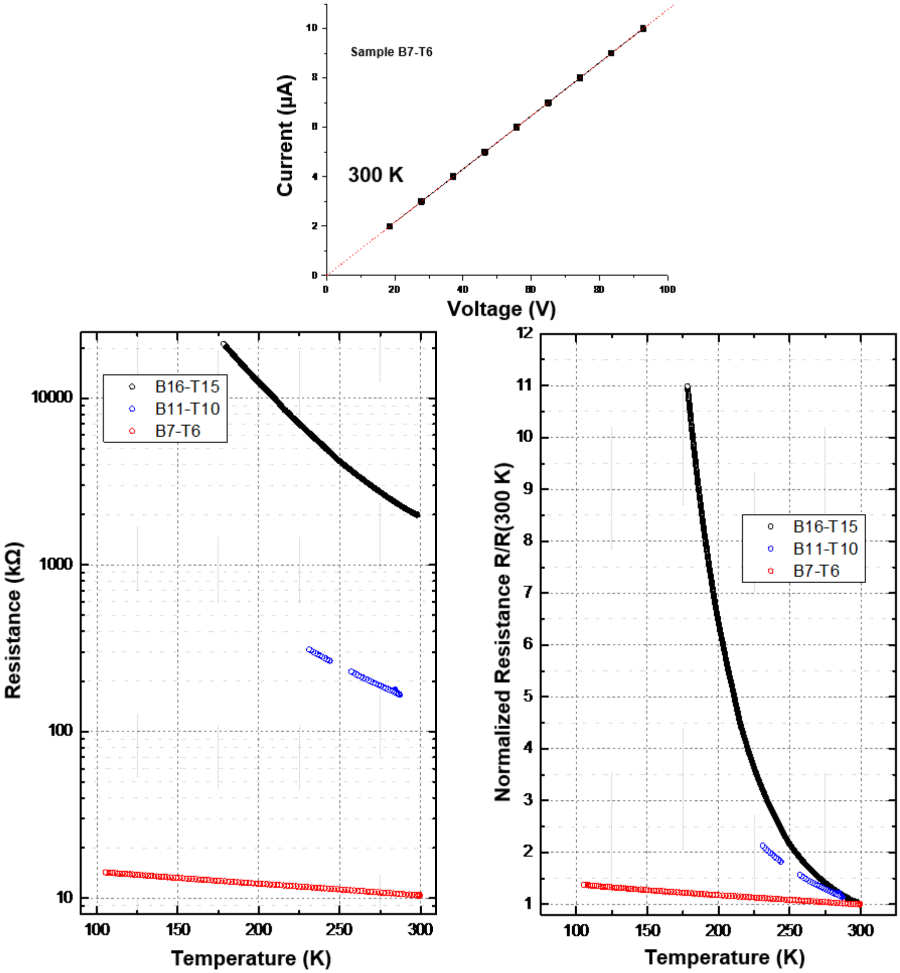

Figure 6.3 Resistance measurements at temperatures less than 300 K for RuTaOx material from Experiment 1. Channel 2 is contacts B7-T6, channel 3 is contacts B11-T10, and channel 4 is contacts B16-T15. All three channels showed an ohmic response at low voltages, with those for channel 2 shown above.

6.3 Experiment 2 - Recreation Attempt

1,3-Propanediol (37.06 mmol, 2820 mg [Sigma-Aldrich, for synthesis]), ruthenium(III) acetylacetonate (0.13 mmol, 53 mg [Merck, for synthesis]), and tantalum(V) ethoxide (0.11 mmol, 45 mg [Alfa Aesar, 99+%]) were added to a Schlenk flask in air, with the flask subsequently connected to an argon line and a vertical condenser (cold finger). The flask was then placed in silicone oil, where mixing via magnetic stirring was carried out for about 49 hours. The oil temperature was maintained at 100°C, and the flask was filled with argon attached to a Schlenk line. After the two day reaction, either precipitate or bubbles were present (not clear which to the naked eye), but these disappeared with time. The synthesis and a comparison to the prior experiment are shown in Figure 6.4.

About 9 months layer, ∼400 mg of product was vortexed with ∼600 mg of diethylene glycol monoethyl ether (DEGEE) (Sigma-Aldrich, ReagentPlus 99%). This was then spin coated at 3000 RPM onto 15 interdigitated electrode structures on one chip (with the feedlines covered with tape) consisting of 18 digits which were 40 µm wide and having a 15 µm gap between digits, where the digit length was 3000 µm long. The digits were made of 200 nm of gold, and adhered with a 20 nm titanium adhesion layer to a 500 µm thick borofloat wafer. After deposition, the chip was heat treated at 250°C for 2 hours on a hot plate. The chip was then mounted to a carrier, where wires were soldered to the carrier to perform resistance measurements, with the construction shown in Figure 6.4.

For measurements, the automated temperature setup used a TEG 127-230-32 Peltier element, (Thermalforce, Germany) which was glued on a liquid cooler to keep the bottom of the element at a constant temperature of 8°C. The top of the element was powered for varying the potential to heat or cool the top side. The heating and cooling was programmed so as to vary the temperature within the range of -20°C to 60°C. Each temperature point was kept constant for 180 s before moving to the next point. These temperature points were cycled in 10°C steps 11 times. In order to accurately measure the temperature, a reference thermocouple device was fixed on top of the element, where the thermocouple was connected to a computer for recording. Additionally, the chip was placed on top of the element and heated/cooled accordingly. All sensors were connected to a PalmSens 4 potentiostat via the MUX8 multiplexer (PalmSens BV, The Netherlands). The Peltier element and the chip were located in a closed box that was flushed with nitrogen to prevent condensation in the chamber at lower temperatures. For determining the resistance, the current was measured for 2 s at 100 mV, which was then averaged and converted to resistance; resistance and temperature data were then matched via time stamp and plotted. Current measurements were performed every ~13.5 seconds, for a total of 2585 data points.

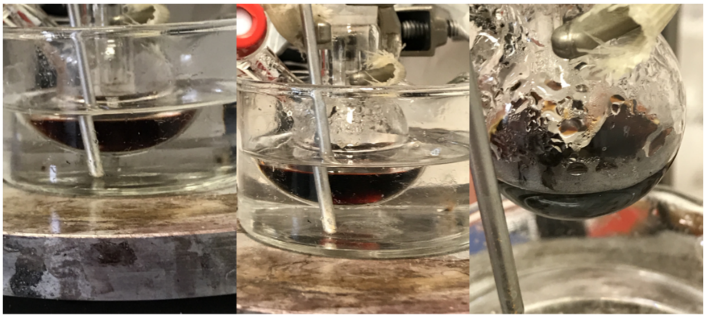

14:16 on 30.07.2018: Set silicone oil to 100°C.

14:53 on 31.07.2018: Continues at 100°C.

15:53 on 01.08.2018: Reaction ended.

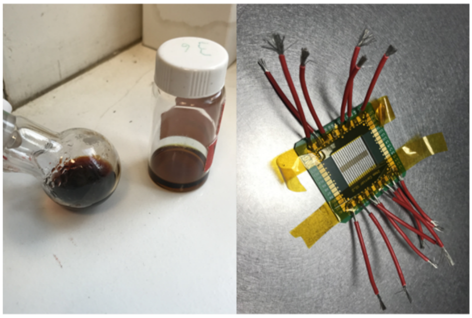

20:02 on 01.08.2018: Exp. 2 (left) with Exp. 1 (right).

Layer spin coated onto chip, with chip on carrier.

Figure 6.4 Synthesis and fabrication of temperature sensors for Experiment 2.

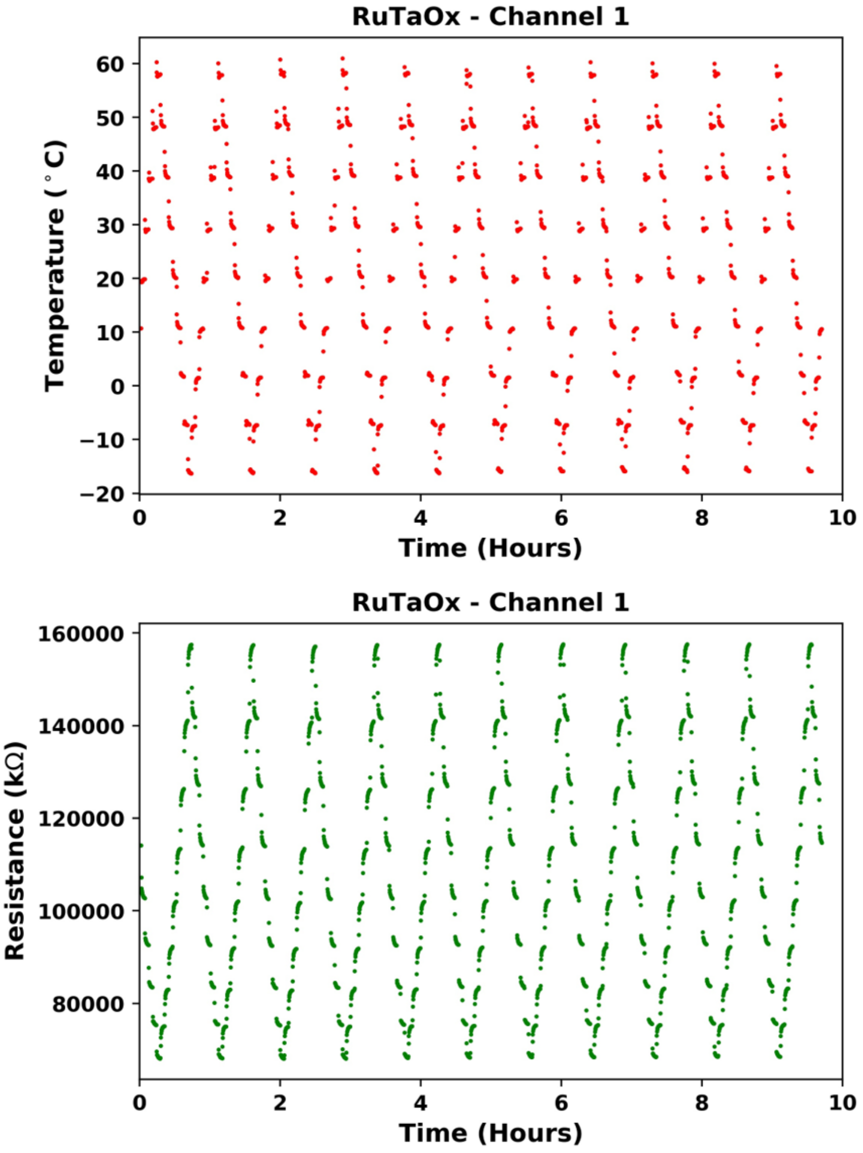

Figure 6.5 Temperature and resistance over time for channel 1 and RuTaOx material from Experiment 2.

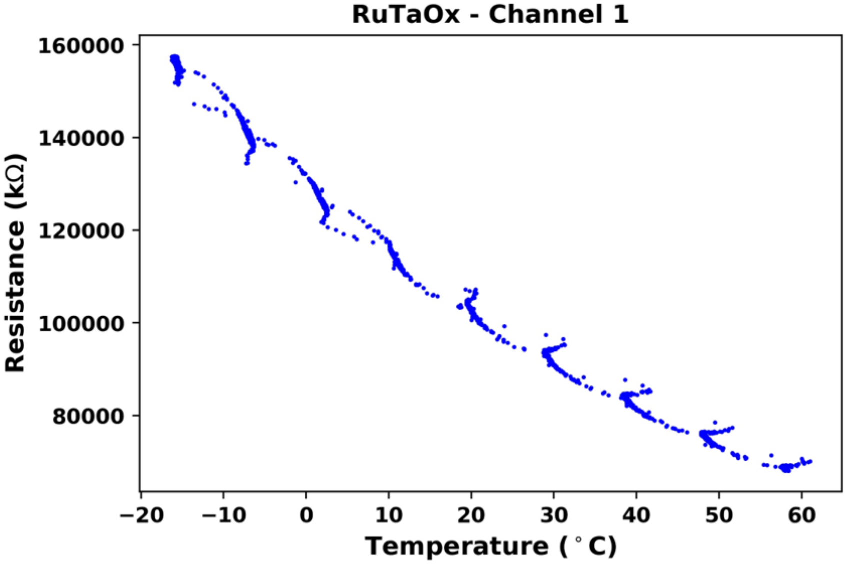

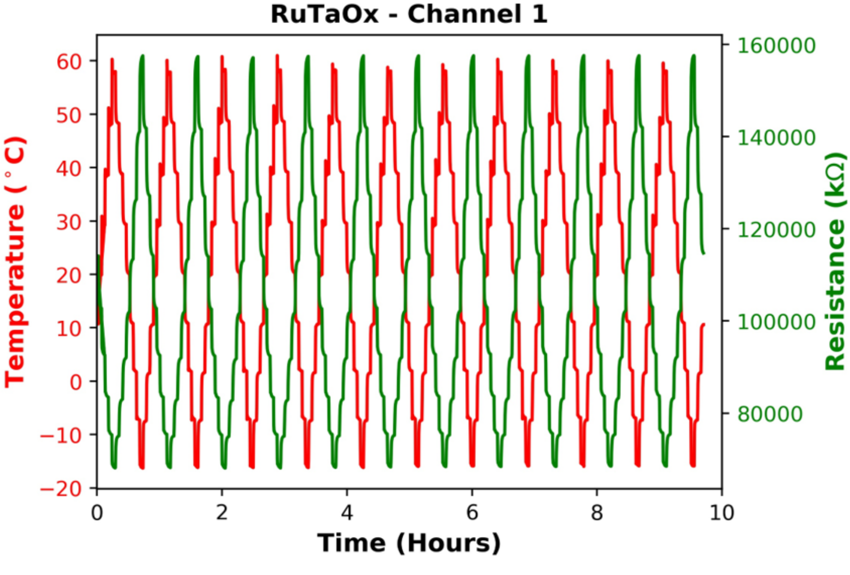

Figure 6.6 Temperature versus resistance for channel 1 and RuTaOx material from Experiment 2.

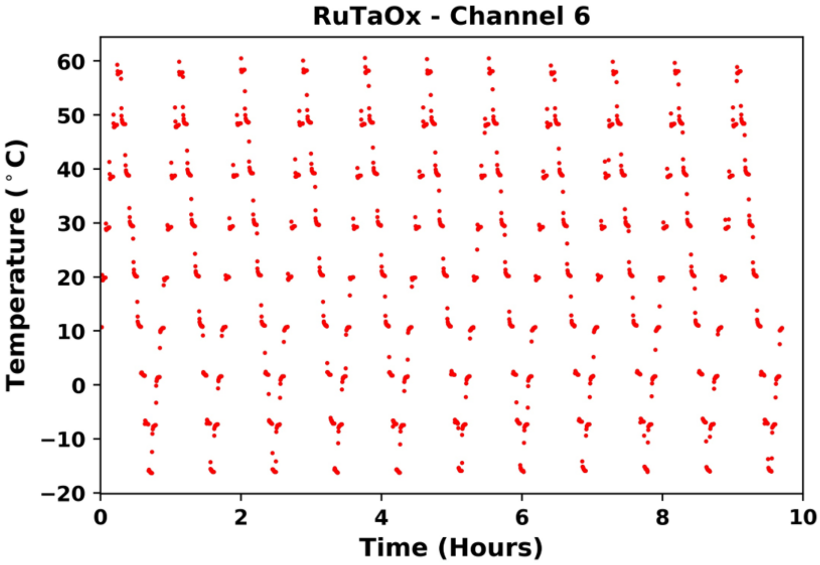

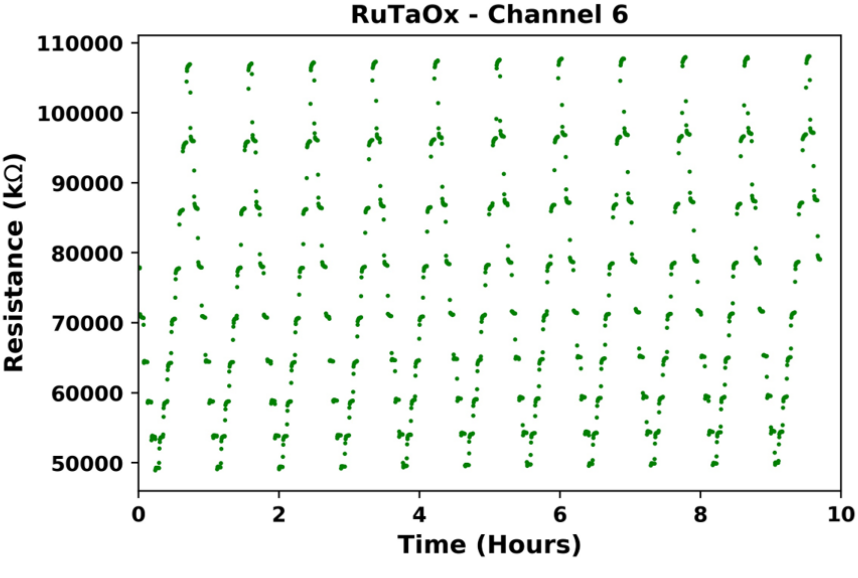

Figure 6.7 Temperature and resistance over time for channel 6 and RuTaOx material from Experiment 2.

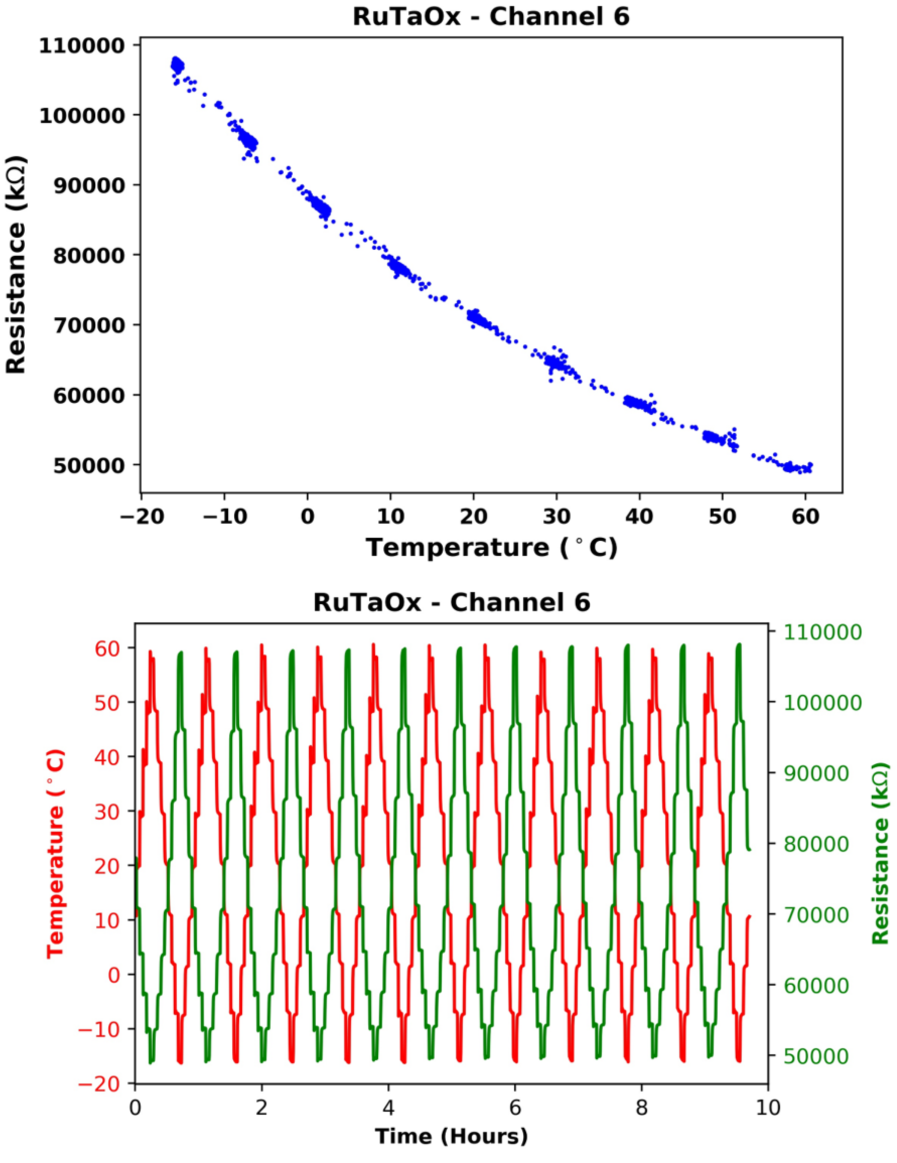

Figure 6.8 Temperature versus resistance for channel 6 and RuTaOx material from Experiment 2.

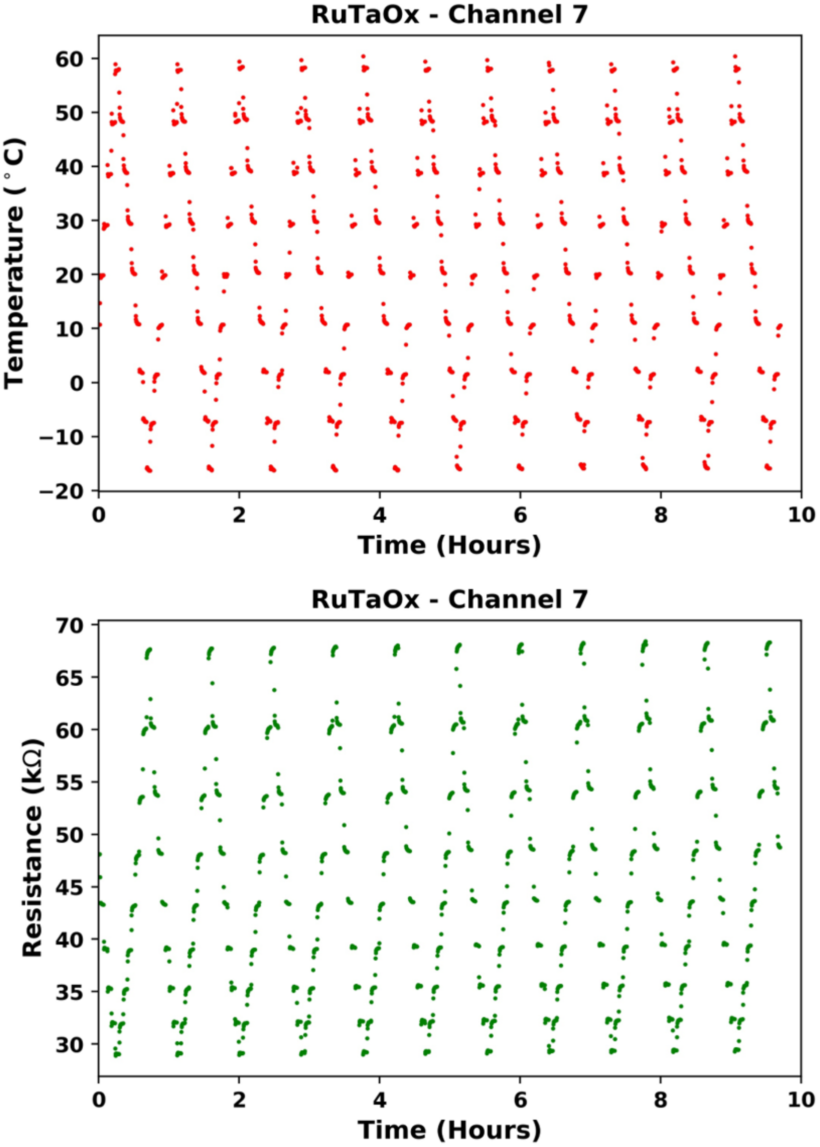

Figure 6.9 Temperature and resistance over time for channel 7 and RuTaOx material from Experiment 2.

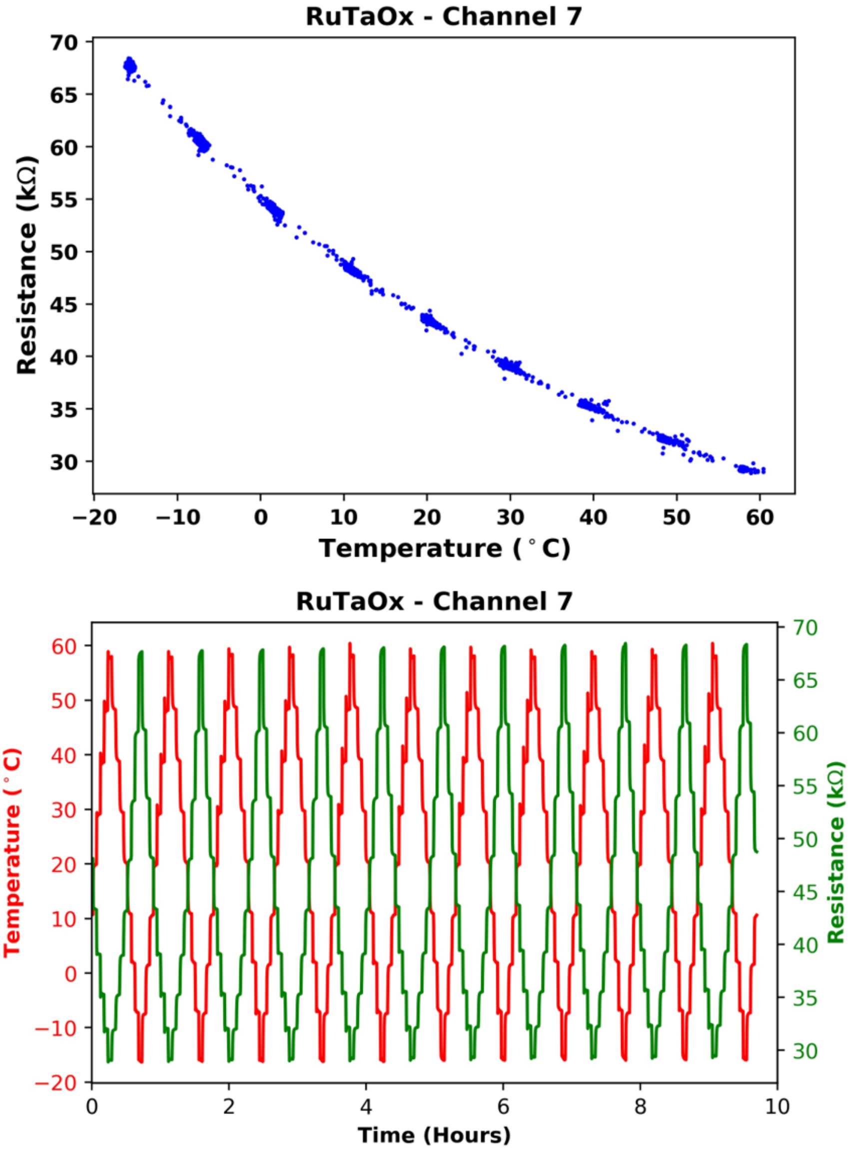

Figure 6.10 Temperature versus resistance for channel 7 and RuTaOx material from Experiment 2.

6.4 Discussion

The results of Experiments 1 and 2 generally show reproducible resistance measurements over multiple cycles. The order of magnitude change among sensors could be due to inherent differences between the layers, or a change in the quantity of material which bridges the gap between digits. Either way, each sensor would need to be calibrated before use as a temperature sensor.

Keeping the observed temperature effect in mind, along with the fact that RuO_2 crystallizes at 200°C (resulting in “metallic” conductive effects with a positive temperature coefficient),[304,314] the added tantalum appears to keep RuO_2 disordered after thermal annealing at 250°C (as with lanthanum at relatively high annealing temperatures).[311] However, this would require additional experiments, such as obtaining XRD spectra, in order to know for sure.

An additional possibility could be that Ru^{3+} is reduced to Ru^0 via polyol reduction,[315] resulting in a disordered distribution of conductive metal nanoparticles. However, Murakami et al.[316] pointed out that upon annealing the metal, oxide formation results unless annealing is performed in a reducing atmosphere (e.g., hydrogen), thus indicating that the layers studied here are likely a disordered metal oxide material. Thus, in explaining how the ruthenium(III) acetylacetonate complex becomes more soluble after heating the solution for prolonged periods of time, a more soluble ruthenium(II) acetylacetonate complex could be created via polyol reduction,[317,318] whereupon in depositing and annealing the material a disordered, conductive oxide results. Nonetheless, this is purely conjecture without experiments such as XPS, which could confirm the oxidation state of the material.

Aside from thermistors, this material could have potential uses in supercapacitors,[319] pH sensors,[312,313] and dimensionally stable anodes for oxygen evolution.[320] Considering these applications, the results reported here could inspire future experiments which examine the solution synthesis and the resulting material further.

Chapter Seven

Conclusion and Outlook

The results of this thesis leave many unanswered questions, with many possible research directions for future projects. To that end, proposed studies for further examination will be discussed below.

Solution Synthesis

Considering the similar alkoxide chemistry for niobium and tantalum, future experiments should investigate whether niobium(V) ethoxide can be used in place of tantalum(V) ethoxide in order to make a niobium(V) 1,3-propanediolate β-diketonate/β-ketoester solution. Extending this procedure to create a sol-gel precursor to niobium oxide films could prove valuable to the manufacturing of devices containing such films. Then for both the tantalum and niobium solutions, further investigations with other β-diketones and β-ketoesters having different functional groups would also help narrow down which chelating molecules could be used with this procedure.

In the suboptimal synthesis procedures, the darker solution color which emerges during prolonged exposure to heat needs to be investigated, possibly by using dynamic light scattering to see if nanoparticles are forming. Additionally, the ambiguous nuclear magnetic resonance (NMR) peaks in the optimized synthesis could also be investigated further, where for the purposes of this work the NMR spectra served mainly as a comparison to the reported results of Calzada and González for the tantalum(V) 1,3-propanediolate precursor solution.[198,200] The effect storage time and temperature has on the photosensitivity of the solutions is also worthy of further investigation.

Thin Film Deposition

In listing only the print resolution for the deposited films, many other factors such as droplet size upon ejection from the nozzle (which can vary depending on how much the printing nozzles have been used), humidity, and the surface energy of the substrate are ignored, which makes reproducibility of the printed layers more difficult. Therefore, in the fabrication of these thin films, future studies must include reliable thickness and surface roughness measurements. A stylus profilometer, or even an atomic force microscope, would likely be the best options for measuring the thickness. However, a 2D profile would not be sufficient, as the "coffee-ring effect" can cause nonuniform ink distributions on the substrate, pushing more material to the edges.[218] Thus, a 3D profile should be obtained, which is then correlated to all material characterization spectra.

Furthermore, the thickness and roughness of the material as a function of heat treatment and photocuring would provide valuable data. Nonetheless, performing such measurements on flexible substrates presents another challenge that would need to be addressed. Along with proper thickness measurements, characteristic material properties should be determined as a function of flash lamp exposure. Both the refractive index and the dielectric constant would be important values in characterizing these films.[155,218,321,322]

In attempting to scale up to roll-to-roll manufacturing, other flash lamp devices more suitable to the job should be investigated. For example, in contrast to the PulseForge 1200 (Novacentrix, USA) which is primarily a research device, the PulseForge 3300 is designed for roll-to-roll processing and can operate at higher voltages for increased UV emission.[229,323] The synthesized solutions could also be optimized for highly scaled gravure printing, which would allow for smaller feature sizes with a high throughput.[132] However, care would need to be taken with the tantalum solutions filling in the grooves in the gravure plates with tantalum oxide over time, as the dissolving of tantalum oxide often requires acidic or caustic solutions, which may damage the plates.

pH Sensing

The optimized synthesis for the tantalum solutions, and possibly even for niobium solutions, should have the films derived from these solutions be tested for pH sensing, which due to time constraints was unfortunately not tested here. Furthermore, any difference in pH sensing ability between the suboptimal and optimal solution synthesis procedures should be looked into. Also, the effect any exposed gold has on pH sensing could be investigated further.

For the extended-gate field-effect transistor (EGFET) pH sensor, future experiments should use a lower impedance reference electrode, as the higher impedance gel-filled electrode used here may have contributed to the long response time for the pH sensor. Other factors, such as the thickness of the tantalum oxide layer or the presence of exposed gold, should also be examined for any potential effects on sensor drift.

In capacitive pH sensing, the effects of the sensor geometry and the fabrication procedure should be correlated to the observed pH sensitivity in the immittance spectra. Furthermore, the contrary results of Manjakkal et al.,[324] showing a decrease in impedance and an increase in capacitance with an increase in pH, needs to be resolved. Two main differences between their procedure and the procedure presented here are apparent: first, Manjakkal et al. used a silver/palladium paste for the conductive interdigitated electrode (IDE) structures, where silver is known not to be chemically inert in solution, and in the experiments presented here less reactive gold electrodes were used; second, Manjakkal et al. used crystalline Ta_2O_5 as a pH sensing layer, in contrast to the amorphous layers examined here. Although crystalline Ta_2O_5 films have been shown to have a lower light induced drift in ion-sensitive field-effect transistor (ISFET) and electrolyte-insulator-silicon structures,[325] grain boundaries in the crystalline film lead to increased leakage currents and sensor hysteresis when compared to amorphous films (with a study including a sol-gel deposited, amorphous Ta_2O_5 film).[118,325–327] Schöning et al.[118] further noted that grain boundaries present defects which can be exploited by diffusing solutions, leading to eventual erosion and damage of the tantalum oxide layer. However, measurement differences could simply be influenced by the ionic strength of the solutions used for measurement, thus making it difficult to compare the results.

As Vermilyea[53–55] reported similar results for amorphous, anodic tantalum oxide films to the results reported here, showing an increase in tantalum oxide "proton space charge" and an increase in the double layer capacitance with a decrease in pH, the results of Vermilyea should be considered as the best comparison to the phenomena observed in this work. Investigation of this pH sensitive behavior could also be continued in real-world applications such as the ocean[9,10] and high salinity foodstuffs such as kimchi.[11]

RuTaOx Thermistor

As characterizing the negative temperature coefficient (NTC) for the RuTaOx thermistors was not the primary goal for this thesis, there remains much to be investigated and understood in future studies. Whether the NTC is due to the localization of the electron wave function, or other effects such as the possibility that the material is a semiconductor, could be explored in more detail. Furthermore, the sheet resistance of the deposited material (with a standardized deposition and fabrication procedure) versus temperature, over multiple samples, would provide a better measure of temperature sensitivity. Finally, a setup that would be more robust at cryogenic temperatures would allow for more accurate characterization of the NTC effect.

Concluding Remarks

In this work, photochemical solution deposition (PCSD) of tantalum oxide via a 1,3-propanediol and β-diketonate route was investigated, where the new method can be adopted in industry for use in mass manufacturing. Through photocuring on flexible gold/titanium/PET foils, deposition of the air-stable solution could be scaled up in future studies to mass manufacturing and roll-to-roll processing. Films deposited on these foils result in tantalum oxide films after photocuring, which are able to be used in pH sensing. Deposition on other substrates, such as a-SiO_2 and c-Si, was also successful and indicates that the procedure could be extended to many applications.

The decrease in capacitance with an increase in pH for the tantalum oxide IDE sensors, particularly in high ionic strength solutions, should be examined further and especially in different electrolytes for different applications. Tantalum oxide should also be compared to other oxides, for example niobium oxide where Vermilyea observed similar phenomena,[53,54] in order to see how the immittance behavior for other oxides on gold IDEs compares to the Bousse-Bergveld model derived for the electrolyte-insulator interface.[256] Additionally, the thermistor effect in RuTaOx films deserves more scrutiny, and could prove valuable in resistor and thermistor applications.

The main takeaway from this work is that contributions from diverse fields in chemistry and physics led to the successful fabrication of a chemically stable, flexible pH sensor. The combination of sol-gel chemistry, inkjet printing, photonic curing, immittance spectroscopy, and pH buffer behavior (with a tangent to NTC thermistors) shows how narrow concepts in science and engineering can be put together to create a device which can be used by society at large. Hopefully, the results presented here do not represent a “capstone” in depositing tantalum oxide films via additive manufacturing, particularly for pH sensing and flexible electronics. Rather, these results should inspire further improvements in synthesis, fabrication, and sensing through future research for applications in Industry 4.0 and the Internet of Things.

REFERENCES

[1] CODATA Internationally recommended 2018 values of the Fundamental Physical Constants. https://physics.nist.gov/cuu/Constants/index.html.

[2] Eisler, P. *My Life with the Printed Circuit*; Lehigh University Press: London, 1989.

[3] Eisler, P. US2441960 Manufacture of electric circuit components. 1948.

[4] Sherwood, E. T.; White, H. L.; Rubinstein, H. W.; Ehlers, G. M. US3369488 Electronically energized device. 1968.

[5] Cohen, T. J. Harry W . Rubinstein , ex-9EEV (SK) Inventor of the Printed Circuit. *CQ Amateur Radio* **1998**, May pp. 22, 24.

[6] Chang, J. S.; Facchetti, A. F.; Reuss, R. A Circuits and Systems Perspective of Organic/Printed Electronics: Review, Challenges, and Contemporary and Emerging Design Approaches. *IEEE Journal on Emerging and Selected Topics in Circuits and Systems* **2017**, *7*, 7–26.

[7] Das, R.; He, X.; Ghaffarzadeh, K. Printed, Organic and Flexible Electronics 2020-2030: Forecasts, Technologies, Markets. 2020; http://www.idtechex.com/en/research-report/printed-organic-and-flexible-electronics-2020-2030-forecasts-technologies-markets/687.

[8] Ghoneim, M. T.; Nguyen, A.; Dereje, N.; Huang, J.; Moore, G. C.; Murzynowski, P. J.; Dagdeviren, C. Recent Progress in Electrochemical pH-Sensing Materials and Configurations for Biomedical Applications. *Chemical Reviews* **2019**, *119*, 5248–5297.

[9] Kester, D. R.; Duedall, I. W.; Connors, D. N.; Pytkowicz, R. M. Preparation of Artificial Seawater. *Limnology and Oceanography* **1967**, *12*, 176–179.

[10] Briggs, E. M.; Sandoval, S.; Erten, A.; Takeshita, Y.; Kummel, A. C.; Martz, T. R. Solid State Sensor for Simultaneous Measurement of Total Alkalinity and pH of Seawater. *ACS Sensors* **2017**, *2*, 1302–1309.

[11] Lee, S.-M.; Cho, Y.; Chung, H.-K.; Shin, D.-H.; Ha, W.-K.; Lee, S.-C.; Shin, M.-J. Effects of kimchi supplementation on blood pressure and cardiac hypertrophy with varying sodium content in spontaneously hypertensive rats. *Nutrition Research and Practice* **2012**, *6*, 315.

[12] Brown, M. A.; Abbas, Z.; Kleibert, A.; Green, R. G.; Goel, A.; May, S.; Squires, T. M. Determination of Surface Potential and Electrical Double-Layer Structure at the Aqueous Electrolyte-Nanoparticle Interface. *Physical Review X* **2016**, *6*, 011007.

[13] Nakayama, Y.; Andelman, D. Differential capacitance of the electric double layer: The interplay between ion finite size and dielectric decrement. *The Journal of Chemical Physics* **2015**, *142*, 044706.

[14] Sørensen, S. P. L. Über die Messung und die Bedeutung der Wasserstoffionenkonzentration bei enzymatischen Prozessen. *Biochemische Zeitschrift* **1909**, 131–200.

[15] Bates, R. G. *Determination of pH: Theory and Practice*, 2nd ed.; John Wiley & Sons, Inc.: New York, 1973; Chapter 2, pp 15–30.

[16] Buck, R. P.; Rondinini, S.; Covington, A. K.; Baucke, F. G. K.; Brett, C. M. A.; Camoes, M. F.; Milton, M. J. T.; Mussini, T.; Naumann, R.; Pratt, K. W.; Spitzer, P.;

Wilson, G. S. Measurement of pH. Definition, standards, and procedures (IUPAC Recommendations 2002). *Pure and Applied Chemistry* **2002**, *74*, 2169–2200.

[17] MacInnes, D. A. Criticism of a Definition of pH. *Science* **1948**, *108*, 693–693.

[18] Bates, R. G.; Guggenheim, E. A. Report on the standardization of pH and related terminology. *Pure and Applied Chemistry* **1960**, *1*, 163–168.

[19] Manjakkal, L.; Szwagierczak, D.; Dahiya, R. Metal oxides based electrochemical pH sensors: Current progress and future perspectives. *Progress in Materials Science* **2020**, *109*, 100635.

[20] Manjakkal, L.; Dervin, S.; Dahiya, R. Flexible potentiometric pH sensors for wearable systems. *RSC Advances* **2020**, *10*, 8594–8617.

[21] Bousse, L.; De Rooij, N.; Bergveld, P. Operation of chemically sensitive field-effect sensors as a function of the insulator-electrolyte interface. *IEEE Transactions on Electron Devices* **1983**, *30*, 1263–1270.

[22] Fog, A.; Buck, R. P. Electronic semiconducting oxides as pH sensors. *Sensors and Actuators* **1984**, *5*, 137–146.

[23] Lonsdale, W. Development, manufacture and application of a solid-state pH sensor using ruthenium oxide. Ph.D. thesis, Edith Cowan University, 2018.

[24] Cammilli, L.; Alcidi, L.; Papeschi, G.; Wiechmann, V.; Padeletti, L.; Grassi, G. Preliminary Experience with the pH-triggered Pacemaker. *Pacing and Clinical Electrophysiology* **1978**, *1*, 448–457.

[25] Lonsdale, W.; Maurya, D.; Wajrak, M.; Alameh, K. Effect of ordered mesoporous carbon contact layer on the sensing performance of sputtered RuO2 thin film pH sensor. *Talanta* **2017**, *164*, 52–56.

[26] Lonsdale, W.; Wajrak, M.; Alameh, K. Effect of conditioning protocol, redox species and material thickness on the pH sensitivity and hysteresis of sputtered RuO2 electrodes. *Sensors and Actuators B: Chemical* **2017**, *252*, 251–256.

[27] Lonsdale, W.; Wajrak, M.; Alameh, K. RuO2 pH Sensor with Super-Glue-Inspired Reference Electrode. *Sensors* **2017**, *17*, 2036.

[28] Lonsdale, W.; Maurya, D.; Wajrak, M.; Tay, C.; Marshall, B.; Alameh, K. Rapid measurement of urease activity using a potentiometric RuO2 pH sensor for detection of Helicobacter pylori. *Sensors and Actuators B: Chemical* **2017**, *242*, 1305–1308.

[29] Lonsdale, W.; Wajrak, M.; Alameh, K. Manufacture and application of RuO2 solid-state metal-oxide pH sensor to common beverages. *Talanta* **2018**, *180*, 277–281.

[30] Lonsdale, W.; Shylendra, S. P.; Wajrak, M.; Alameh, K. Application of all solid-state 3D printed pH sensor to beverage samples using matrix matched standard. *Talanta* **2019**, *196*, 18–21.

[31] Głab, S.; Hulanicki, A.; Edwall, G.; Ingman, F. Metal-Metal Oxide and Metal Oxide Electrodes as pH Sensors. *Critical Reviews in Analytical Chemistry* **1989**, *21*, 29–47.

[32] Bates, R. G. *Determination of pH: Theory and Practice*, 2nd ed.; John Wiley & Sons, Inc.: New York, 1973; Chapter 1, pp 1–14.

[33] Olthuis, W.; Robben, M.; Bergveld, P.; Bos, M.; van der Linden, W. pH sensor properties of electrochemically grown iridium oxide. *Sensors and Actuators B: Chemical* **1990**, *2*, 247–256.

[34] Katsube, T.; Lauks, I.; Zemel, J. pH-sensitive sputtered iridium oxide films. *Sensors and Actuators* **1981**, *2*, 399–410.

[35] Carroll, S.; Baldwin, R. P. Self-Calibrating Microfabricated Iridium Oxide pH Electrode Array for Remote Monitoring. *Analytical Chemistry* **2010**, *82*, 878–885.

[36] Kinlen, P. J.; Heider, J. E.; Hubbard, D. E. A solid-state pH sensor based on a Nafion-coated iridium oxide indicator electrode and a polymer-based silver chloride reference electrode. *Sensors and Actuators B: Chemical* **1994**, *22*, 13–25.

[37] Kuo, L. M.; Chou, Y. C.; Chen, K. N.; Lu, C. C.; Chao, S. A precise pH microsensor using RF-sputtering IrO2and Ta2O5films on Pt-electrode. *Sensors and Actuators, B: Chemical* **2014**, *193*, 687–691.

[38] Lauks, I. R. US5009766 Metal oxide electrodes. 1991.

[39] Bergveld, P. Development of an Ion-Sensitive Solid-State Device for Neurophysiological Measurements. *IEEE Transactions on Biomedical Engineering* **1970**, *BME-17*, 70–71.

[40] Toumazou, C.; Georgiou, P. Piet Bergveld - 40 years of ISFET technology: From neuronal sensing to DNA sequencing. *Electronics Letters* **2011**, *47*, S7.

[41] van Hal, R.; Eijkel, J.; Bergveld, P. A novel description of ISFET sensitivity with the buffer capacity and double-layer capacitance as key parameters. *Sensors and Actuators B: Chemical* **1995**, *24*, 201–205.

[42] Chiang, J. L.; Chen, Y. C.; Chou, J. C. Simulation and experimental study of the pH-sensing property for AlN thin films. *Japanese Journal of Applied Physics, Part 1: Regular Papers and Short Notes and Review Papers* **2001**, *40*, 5900–5904.

[43] Dutta, J. C. Ion sensitive field effect transistor for applications in bioelectronic sensors: A research review. 2012 2nd National Conference on Computational Intelligence and Signal Processing (CISP). 2012; pp 185–191.

[44] Yates, D. E.; Levine, S.; Healy, T. W. Site-binding model of the electrical double layer at the oxide/water interface. *Journal of the Chemical Society, Faraday Transactions 1: Physical Chemistry in Condensed Phases* **1974**, *70*, 1807.

[45] van Hal, R.; Eijkel, J.; Bergveld, P. A general model to describe the electrostatic potential at electrolyte oxide interfaces. *Advances in Colloid and Interface Science* **1996**, *69*, 31–62.

[46] Bergveld, P. Thirty years of ISFETOLOGY. *Sensors and Actuators B: Chemical* **2003**, *88*, 1–20.

[47] Bobrov, P. V.; Tarantov, Y. A.; Krause, S.; Moritz, W. Chemical sensitivity of an ISFET with Ta2O5 membrane in strong acid and alkaline solutions. *Sensors and Actuators: B. Chemical* **1991**, *3*, 75–81.

[48] Bousse, L.; Mostarshed, S.; van der Schoot, B.; de Rooij, N. Comparison of the hysteresis of Ta2O5 and Si3N4 pH-sensing insulators. *Sensors and Actuators B: Chemical* **1994**, *17*, 157–164.

[49] Bousse, L.; De Rooij, N. F.; Bergveld, P. The influence of counter-ion adsorption on the $\psi0$/pH characteristics of insulator surfaces. *Surface Science* **1983**, *135*, 479–496.

[50] Bousse, L.; Meindl, J. D. *Surface Potential-pH Characteristics in the Theory of the Oxide-Electrolyte Interface*; 1987; pp 79–98.

[51] Anderson, M. D.; Aitchison, B.; Johnson, D. C. Corrosion Resistance of Atomic Layer Deposition-Generated Amorphous Thin Films. *ACS Applied Materials & Interfaces* **2016**, *8*, 30644–30648.

[52] Özer, N.; Lampert, C. M. Sol-gel deposited amorphous tantalum oxide and niobium oxide films as protonic conductors. 1995.

[53] Vermilyea, D. Proton exchange at the Ta2O5 — electrolytic solution double layer. *Surface Science* **1964**, *2*, 444–455.

[54] Vermilyea, D. Proton space charge in anodic oxide films. *Journal of Physics and Chemistry of Solids* **1965**, *26*, 133–141.

[55] Vermilyea, D. A. Anodic Films, Protons, and Electrolytic Rectification. *Journal of The Electrochemical Society* **1968**, *115*, 177.

[56] Greenwood, N. N.; Earnshaw, A. *Chemistry of the Elements*, 2nd ed.; Elsevier Butterworth-Heinemann: Burlington, 1997; Chapter 1, pp 1–19.

[57] Munker, C. Evolution of Planetary Cores and the Earth-Moon System from Nb/Ta Systematics. *Science* **2003**, *301*, 84–87.

[58] Palme, H.; Lodders, K.; Jones, A. *Treatise on Geochemistry*; Elsevier, 2014; pp 15–36.

[59] Pfeifer, M. The Tantalum Isotope Inventory of Terrestrial and Early Solar System Materials. Ph.D. thesis, University of Cologne, Cologne, 2017.

[60] Cano, E. J.; Sharp, Z. D.; Shearer, C. K. Distinct oxygen isotope compositions of the Earth and Moon. *Nature Geoscience* **2020**, *13*, 270–274.

[61] Yokota, S.; Terada, K.; Saito, Y.; Kato, D.; Asamura, K.; Nishino, M. N.; Shimizu, H.; Takahashi, F.; Shibuya, H.; Matsushima, M.; Tsunakawa, H. KAGUYA observation of global emissions of indigenous carbon ions from the Moon. *Science Advances* **2020**, *6*, eaba1050.

[62] Tang, M.; Lee, C.-T. A.; Chen, K.; Erdman, M.; Costin, G.; Jiang, H. Nb/Ta systematics in arc magma differentiation and the role of arclogites in continent formation. *Nature Communications* **2019**, *10*, 235.

[63] Tantalum-Niobium International Study Center. https://www.tanb.org/index.

[64] Hatchett, C. III. An analysis of a mineral substance from North America, containing a metal hitherto unknown. *Philosophical Transactions of the Royal Society of London* **1802**, *92*, 49–66.

[65] Crell, L. F. F. *Chemische Annalen für die Freunde der Naturlehre, Arzneygelahrtheit, Haushaltungskunst und Manufakturen*; Fleckeisen: Helmstädt ; Leipzig, 1802; pp 257–270.

[66] Ekeberg, A. G. *Kongl. Vetenskaps Academiens .NYA Handlingar*; Johan Pehr Lindh: Stockholm, 1802; pp 68–83.

[67] Crell, L. F. F. *Chemische Annalen für die Freunde der Naturlehre, Arzneygelahrtheit, Haushaltungskunst und Manufakturen*; Fleckeisen: Helmstädt ; Leipzig, 1803; pp 3–21.

[68] Rose, H. Ueber die Zusammensetzung der Tantalite und ein im Tantalite von Baiern enthaltenes neues Metall. *Annalen der Physik und Chemie* **1844**, *139*, 317–341.

[69] Usselman, M. C. William Hyde Wollaston. 2020; https://www.britannica.com/biography/William-Hyde-Wollaston.

[70] Wollaston, H. XV. On the identity of Columbium and Tantalum. *Philosophical Transactions of the Royal Society of London* **1809**, *99*, 246–252.

[71] Marignac,; Blomstrand,; Deville, H.; Troost, L.; Hermann, R. Tantalsäure, Niobsäure, (Ilmensäure) und Titansäure. *Zeitschrift für Analytische Chemie* **1866**, *5*, 384–389.

[72] Marignac, Trennung der Niobsäure und Tantalsäure. *Zeitschrift für Analytische Chemie* **1866**, *5*, 389–391.

[73] Rayner-Canham, G.; Zheng, Z. Naming elements after scientists: An account of a controversy. *Foundations of Chemistry* **2008**, *10*, 13–18.

[74] von Bolton, W. Das Tantal und die Tantallampe von Siemens & Halske. *Zeitschrift für Elektrotechnik und Elektrochemie* **1905**, *11*, 722–725.

[75] Hirst, H. Recent progress in tungsten metallic filament lamps. *Journal of the Institution of Electrical Engineers* **1908**, *41*, 636–661.

[76] Balke, C. W. Columbium and Tantalum. *Industrial & Engineering Chemistry* **1935**, *27*, 1166–1169.

[77] Flanigan, P.; Kshettry, V. R.; Benzel, E. C. World War II, tantalum, and the evolution of modern cranioplasty technique. *Neurosurgical Focus* **2014**, *36*, E22.

[78] Fulcher, O. H. Tantalum as a metallic implant to repair cranial defects. *Journal of the American Medical Association* **1943**, *121*, 931.

[79] Burke, G. L. The corrosion of metals in tissues; and an introduction to tantalum. *Canadian Medical Association journal* **1940**, *43*, 125–8.

[80] Pudenz, R. H. The repair of cranial defects with tantalum. *Journal of the American Medical Association* **1943**, *121*, 478.

[81] Spurling, R. G. The use of tantalum wire and foil in the repair of peripheral nerves. *Surgical Clinics of North America* **1943**, 1491–504.

[82] Weiss, P. Sutureless reunion of severed nerves with elastic cuffs of tantalum. *Journal of Neurosurgery* **1944**, *1*, 219–225.

[83] Norcross, N. C.; Bakody, J. T. Observations on the use of tantalum foil in peripheral nerve surgery. *Journal of Neurosurgery* **1947**, *4*, 69–71.

[84] Cunningham, L. D.; United States Department of the Interior, B. o. M. *Tantalum: Mineral Commodity Profiles*; 1983.

[85] Freeman, Y. *Tantalum and Niobium-Based Capacitors*; Springer International Publishing: Cham, 2018.

[86] Nest, M. *Coltan*; Polity press: Cambridge, UK, 2011.

[87] Greenwood, N. N.; Earnshaw, A. *Chemistry of the Elements*, 2nd ed.; Butterworth-Heinemann: Oxford, 1997; Chapter 22, pp 976–1001.

[88] Melcher, F.; Sitnikova, M. A.; Graupner, T.; Martin, N.; Oberthür, T.; Henjes-Kunst, F.; Gäbler, E.; Gerdes, A.; Brätz, H.; Davis, D. W.; Dewaele, S. Fingerprinting of conflict minerals: columbite-tantalite ("coltan") ores. *Society for Geology Applied to Mineral Deposits* **2008**, 1, 7–14.

[89] Gäbler, H.-E.; Melcher, F.; Graupner, T.; Bahr, A.; Sitnikova, M. A.; Henjes-Kunst, F.; Oberthür, T.; Brätz, H.; Gerdes, A. Speeding Up the Analytical Workflow for Coltan Fingerprinting by an Integrated Mineral Liberation Analysis/LA-ICP-MS Approach. *Geostandards and Geoanalytical Research* **2011**, *35*, 431–448.

[90] Wallwork, P. Challenges Facing the Tantalum Industry. Minor Metals and Rare Earths Conference. Hong Kong, 2008.

[91] Mancheri, N. A.; Sprecher, B.; Deetman, S.; Young, S. B.; Bleischwitz, R.; Dong, L.; Kleijn, R.; Tukker, A. Resources , Conservation & Recycling Resilience in the tantalum supply chain. *Resources, Conservation & Recycling* **2018**, *129*, 56–69.

[92] Schulz, K. J.; Piatak, N. M.; Papp, J. F. *Niobium and Tantalum Chapter M of Critical Mineral Resources of the United States - Economic and Environmental Geology and Prospects for Future Supply*; 2017; Vol. 1802-M.

[93] Norton, J. D.; Crespi, A. M.; Untereker, D. F. US8280519B2 Method of maintaining wet-tantalum electrolytic capacitors. 2012.

[94] Papakyriacou, M. Effects of surface treatments on high cycle corrosion fatigue of metallic implant materials. *International Journal of Fatigue* **2000**, *22*, 873–886.

[95] Bobyn, J. D.; Stackpool, G. J.; Hacking, S. A.; Tanzer, M.; Krygier, J. J. Characteristics of bone ingrowth and interface mechanics of a new porous tantalum biomaterial. *The Journal of Bone and Joint Surgery* **1999**, *81*, 907–914.

[96] Bobyn, J. D.; Poggie, R.; Krygier, J.; Lewallen, D.; Hanssen, A.; Lewis, R.; Unger, A.; O Keefe, T.; Christie, M.; Nasser, S.; Wood, J.; Stulberg, S.; Tanzer, M. Clinical Validation of a Structural Porous Tantalum Biomaterial for Adult Reconstruction. *The Journal of Bone & Joint Surgery* **2004**, *86*, 123–129.

[97] Sun, Y. S.; Chang, J. H.; Huang, H. H. Corrosion resistance and biocompatibility of titanium surface coated with amorphous tantalum pentoxide. *Thin Solid Films* **2013**, *528*, 130–135.

[98] Fraser, D.; Mendonca, G.; Sartori, E.; Funkenbusch, P.; Ercoli, C.; Meirelles, L. Bone response to porous tantalum implants in a gap-healing model. *Clinical Oral Implants Research* **2019**, *30*, 156–168.

[99] Zykova, A.; Safonov, V.; Goltsev, A.; Dubrava, T.; Rossokha, I.; Donkov, N.; Yakovin, S.; Kolesnikov, D.; Goncharov, I.; Georgieva, V. Surface modification of tantalum pentoxide coatings deposited by magnetron sputtering and correlation with cell adhesion and proliferation in in vitro tests. *Journal of Physics: Conference Series* **2016**, *700*.

[100] Song, G.; Chen, Y.; Liang, C.; Yi, X.; Liu, J.; Sun, X.; Shen, S.; Yang, K.; Liu, Z. Catalase-Loaded TaOx Nanoshells as Bio-Nanoreactors Combining High-Z Element and Enzyme Delivery for Enhancing Radiotherapy. *Advanced Materials* **2016**, *28*, 7143–7148.

[101] Samudrala, R. K.; Azeem, P. A. Preliminary biological evaluation of tantalum containing soda lime borosilicate bioactive glasses. *Journal of Alloys and Compounds* **2019**, 151853.

[102] Li, R.; Wei, Y.; Gu, L.; Qin, Y.; Li, D. Sol–gel-assisted micro-arc oxidation synthesis and characterization of a hierarchically rough structured Ta–Sr coating for biomaterials. *RSC Advances* **2020**, *10*, 20020–20027.

[103] McCreery, D. B.; Agnew, W. F.; Yuen, T. G. H.; Bullara, L. A. Comparison of neural damage induced by electrical stimulation with faradaic and capacitor electrodes. *Annals of Biomedical Engineering* **1988**, *16*, 463–481.

[104] Martinez, G.; Laske, T. G.; Marshall, M. T. US9468754B2 Leads for selective sensing and virtual electrodes. 2016.

[105] De Vittorio, M.; Martiradonna, L.; Assad, J. In *Nanotechnology and Neuroscience: Nano-Electronic, Photonic and Mechanical Neuronal Interfacing*; De Vittorio, M., Martiradonna, L., Assad, J., Eds.; Springer New York: New York, NY, 2014; pp v–vii.

[106] Munshi, M. Z. A.; Bonnerup, C. A. US5654030 Method of making implantable stimulation electrodes. 1997.

[107] Biednov, M.; Lebyedyeva, T.; Shpylovyy, P. Gold and aluminum based surface plasmon resonance biosensors: sensitivity enhancement. Optical Sensors 2015. 2015; p 95061P.

[108] Li, D.; Zhang, W.; Liu, H.; Hu, J.; Zhou, G. High Sensitivity Refractive Index Sensor Based on Multicoating Photonic Crystal Fiber With Surface Plasmon Resonance at Near-Infrared Wavelength. *IEEE Photonics Journal* **2017**, *9*, 1–8.

[109] Hasan, M. R.; Akter, S.; Ahmed, K.; Abbott, D. Plasmonic Refractive Index Sensor Employing Niobium Nanofilm on Photonic Crystal Fiber. *IEEE Photonics Technology Letters* **2018**, *30*, 315–318.

[110] Kruise, J.; Rispens, J.; Bergveld, P.; Kremer, F.; Starmans, D.; Haak, J.; Feijen, J.; Reinhoudt, D. Detection of charged proteins by means of impedance measurements. *Sensors and Actuators B: Chemical* **1992**, *6*, 101–105.

[111] Poghossian, A.; Schöning, M. J. Detecting Both Physical and (Bio-)Chemical Parameters by Means of ISFET Devices. *Electroanalysis* **2004**, *16*, 1863–1872.

[112] Poghossian, A.; Abouzar, M.; Sakkari, M.; Kassab, T.; Han, Y.; Ingebrandt, S.; Offenhäusser, A.; Schöning, M. Field-effect sensors for monitoring the layer-by-layer adsorption of charged macromolecules. *Sensors and Actuators B: Chemical* **2006**, *118*, 163–170.

[113] Rothberg, J. M. et al. An integrated semiconductor device enabling non-optical genome sequencing. *Nature* **2011**, *475*, 348–352.

[114] Veigas, B.; Pinto, J.; Vinhas, R.; Calmeiro, T.; Martins, R.; Fortunato, E.; Baptista, P. V. Quantitative real-time monitoring of RCA amplification of cancer biomarkers mediated by a flexible ion sensitive platform. *Biosensors and Bioelectronics* **2017**, *91*, 788–795.

[115] Andrianova, M.; Kuznetsov, E.; Grudtsov, V.; Kuznetsov, A. CMOS-compatible biosensor for L-carnitine detection. *Biosensors and Bioelectronics* **2018**, *119*, 48–54.

[116] Uria, N.; Abramova, N.; Bratov, A.; Muñoz-Pascual, F.-X.; Baldrich, E. Miniaturized metal oxide pH sensors for bacteria detection. *Talanta* **2016**, *147*, 364–369.

[117] Satake, H.; Sakata, T. Cell Adhesion Characteristics on Tantalum Pentoxide Gate Insulator for Cultured-Cell-Gate Field-Effect Transistor. *Langmuir* **2021**, acs.langmuir.1c01044.

[118] Schöning, M.; Brinkmann, D.; Rolka, D.; Demuth, C.; Poghossian, A. CIP (cleaning-in-place) suitable “non-glass” pH sensor based on a Ta2O5-gate EIS structure. *Sensors and Actuators B: Chemical* **2005**, *111-112*, 423–429.

[119] Kao, C. H.; Chen, H.; Kuo, L. T.; Wang, J. C.; Chen, Y. T.; Chu, Y. C.; Chen, C. Y.; Lai, C. S.; Chang, S. W.; Chang, C. W. Multi-analyte biosensors on a CF4 plasma treated Nb 2O5-based membrane with an extended gate field effect transistor structure. *Sensors and Actuators, B: Chemical* **2014**, *194*, 419–426.

[120] Bergveld, P. The future of biosensors. *Sensors and Actuators A: Physical* **1996**, *56*, 65–73.

[121] Wu, Y.-C.; Wu, S.-J.; Lin, C.-H. Mass-produced polyethylene-terephthalate film coated with tantalum pentoxide for pH measurement under ISFET detection configuration. *Microsystem Technologies* **2017**, *23*, 293–298.

[122] Murakami, K.; Kitasako, Y.; F. Burrow, M.; Tagami, J. In vitro pH analysis of active and arrested dentinal caries in extracted human teeth using a micro pH sensor. *Dental Materials Journal* **2006**, *25*, 423–429.

[123] Fujii, M.; Kitasako, Y.; Sadr, A.; Tagami, J. Roughness and pH changes of enamel surface induced by soft drinks in vitro-applications of stylus profilometry, focus variation 3D scanning microscopy and micro pH sensor. *Dental Materials Journal* **2011**, *30*, 404–410.

[124] Yang, C.-M.; Chiang, T.-W.; Yeh, Y.-T.; Das, A.; Lin, Y.-T.; Chen, T.-C. Sensing and pH-imaging properties of niobium oxide prepared by rapid thermal annealing for electrolyte–insulator–semiconductor structure and light-addressable potentiometric sensor. *Sensors and Actuators B: Chemical* **2015**, *207*, 858–864.

[125] Özsoylu, D.; Kizildag, S.; Schöning, M. J.; Wagner, T. Effect of Plasma Treatment on the Sensor Properties of a Light-Addressable Potentiometric Sensor (LAPS). *physica status solidi (a)* **2019**, *216*, 1900259.

[126] Özsoylu, D.; Kizildag, S.; Schöning, M. J.; Wagner, T. Differential chemical imaging of extracellular acidification within microfluidic channels using a plasma-functionalized light-addressable potentiometric sensor (LAPS). *Physics in Medicine* **2020**, *10*, 100030.

[127] Yoshinobu, T.; Miyamoto, K.-i.; Werner, C. F.; Poghossian, A.; Wagner, T.; Schön-

ing, M. J. Light-Addressable Potentiometric Sensors for Quantitative Spatial Imaging of Chemical Species. *Annual Review of Analytical Chemistry* **2017**, *10*, 225–246.

[128] Yoshinobu, T.; Schöning, M. J. Light-addressable potentiometric sensors (LAPS) for cell monitoring and biosensing. *Current Opinion in Electrochemistry* **2021**, 100727.

[129] Grosso, D.; Boissière, C.; Faustini, M. *The Sol-Gel Handbook*; Wiley-VCH Verlag GmbH & Co. KGaA: Weinheim, Germany, 2015; pp 277–316.

[130] U.S. Department of Energy, Innovating clean energy technologies in advanced manufacturing - Roll to Roll Processing. *Quadrennial Technology Review* **2015**, 34.

[131] Cheng, I.-C.; Wagner, S. In *Flexible Electronics Materials and Applications*; Wong, William S., Salleo, A., Ed.; Springer: New York, 2009; Chapter 1, pp 1–28.

[132] Grau, G.; Cen, J.; Kang, H.; Kitsomboonloha, R.; Scheideler, W. J.; Subramanian, V. Gravure-printed electronics: recent progress in tooling development, understanding of printing physics, and realization of printed devices. *Flexible and Printed Electronics* **2016**, *1*, 023002.

[133] Calzada, M. L. In *The Sol-Gel Handbook*; Levy, D., Zayat, M., Eds.; Wiley-VCH Verlag GmbH & Co. KGaA: Weinheim, Germany, 2015; Chapter 27, pp 841–882.

[134] Matavž, A.; Malič, B. Inkjet printing of functional oxide nanostructures from solution-based inks. *Journal of Sol-Gel Science and Technology* **2018**, *87*, 1–21.

[135] Beale, C.; Hamacher, S.; Bensaid, O.; Yakushenko, A.; Mayer, D.; Wolfrum, B.; Offenhäusser, A. Characterization of Flash Lamp Cured, Sol-Gel Derived Tantalum Oxide Films. MRS Fall Meeting & Exhibit. Boston, 2019.

[136] Beale, C.; Hamacher, S.; Yakushenko, A.; Bensaid, O.; Willbold, S.; Beltramo, G.; Möller, S.; Hartmann, H.; Neumann, E.; Mussler, G.; Shkurmanov, A.; Mayer, D.;

Wolfrum, B.; Offenhäusser, A. Tantalum(v) 1,3-propanediolate β-diketonate solution as a precursor to sol–gel derived, metal oxide thin films. *RSC Advances* **2020**, *10*, 13737–13748.

[137] Beale, C.; Hamacher, S.; Yakushenko, A.; Bensaid, O.; Willbold, S.; Beltramo, G.; Möller, S.; Hartmann, H.; Neumann, E.; Mussler, G.; Shkurmanov, A.; Mayer, D.; Wolfrum, B.; Offenhäusser, A. Correction: Tantalum(v) 1,3-propanediolate β-diketonate solution as a precursor to sol–gel derived, metal oxide thin films. *RSC Advances* **2020**, *10*, 32102–32102.

[138] Beale, C.; Hamacher, S.; Mayer, D.; Offenhäusser, A. DE102019006976A1 Verfahren zur Herstellung einer Metallglykolat-ß-diketonatlösung oder einer Metallglykolat-ß-diketoesterlösung, Metallglykolat-ß-diketonatlösung oder Metallglykolat-ß-diketoesterlösung und deren Verwendung. 2021.

[139] Schubert, U. *The Sol-Gel Handbook*; Wiley-VCH Verlag GmbH & Co. KGaA: Weinheim, Germany, 2015; pp 1–28.

[140] Deshmukh, R.; Niederberger, M. *The Sol-Gel Handbook*; Wiley-VCH Verlag GmbH & Co. KGaA: Weinheim, Germany, 2015; p 34.

[141] Seisenbaeva, G. A.; Kessler, V. G. Precursor directed synthesis – “molecular” mechanisms in the Soft Chemistry approaches and their use for template-free synthesis of metal, metal oxide and metal chalcogenide nanoparticles and nanostructures. *Nanoscale* **2014**, *6*, 6229–6244.

[142] Ebelmen, M. On the artificial production of diaphanous quartz. *The London, Edinburgh, and Dublin Philosophical Magazine and Journal of Science* **1845**, *27*, 404–404.

[143] Rose, H. Ueber das Tantal und seine Verbindungen mit Chlor und mit Brom. *Annalen der Physik und Chemie* **1856**, *175*, 65–87.

[144] Lindner, K.; Feit, H. Über einige Additionsreaktionen, Molekularverbindungen und die Hydrolyse des Tantalpentachlorides. *Zeitschrift für anorganische und allgemeine Chemie* **1923**, *132*, 10–14.

[145] Funk, H.; Niederländer, K. Über die Einwirkung von Niob-und Tantalpentachlorid auf organische Verbindungen. *Berichte der deutschen chemischen Gesellschaft (A and B Series)* **1928**, *61*, 249–253.

[146] Funk, H.; Niederländer, K. Über die Einwirkung von Niob- und Tantalpentachlorid auf organische Verbindungen (II). *Berichte der deutschen chemischen Gesellschaft (A and B Series)* **1928**, *61*, 1385–1388.

[147] Funk, H.; Niederländer, K. Über die Einwirkung von Niob- und Tantalpentachlorid auf organische Verbindungen (III. Mitteil.). *Berichte der deutschen chemischen Gesellschaft (A and B Series)* **1929**, *62*, 1688–1691.

[148] Funk, H. Über die Einwirkung von Niob- und Tantalpentachlorid auf organische Verbindungen (IV. Mitteil.). *Berichte der deutschen chemischen Gesellschaft (A and B Series)* **1934**, *67*, 1801–1804.

[149] Geffcken, W.; Berger, E. DE000000736411 Verfahren zur Änderung des Reflexionsvermögens optischer Gläser. 1939.

[150] Whitley, A. New Metal Alkoxides. Ph.D. thesis, Birkbeck College, University of London, 1954.

[151] Bradley, D. C.; Wardlaw, W.; Whitley, A. Normal alkoxides of quinquevalent tantalum. *Journal of the Chemical Society (Resumed)* **1955**, 726–728.

[152] Bradley, D. C.; Chakravarti, B. N.; Wardlaw, W. 460. Normal alkoxides of quinquevalent niobium. *Journal of the Chemical Society (Resumed)* **1956**, 2381–2384.

[153] Turova, N.; Korolev, A.; Tchebukov, D.; Belokon, A.; Yanovsky, A.; Struchkov, Y. Tantalum(V) alkoxides : Electrochemical synthesis, mass-spectral investigation and oxoalkoxocomplexes. *Polyhedron* **1996**, *15*, 3869–3880.

[154] Ling, H. C.; Yan, M. F.; Rhodes, W. W. In *Science of Ceramic Chemical Processing*; Hench, L. L. U. o. F., Ulrich, D. R. A. F. O. o. S. R., Eds.; John Wiley & Sons, Inc.: New York, 1986; Chapter 31, pp 285–303.

[155] Silverman, L. A. Sol-gel derived tantalum oxide thin films. Ph.D. thesis, Massachusetts Institute of Technology, 1987.

[156] Bradley, D. C.; Wardlaw, W.; Whitley, A. 237. Structural chemistry of the alkoxides. Part V. Isomeric butoxides and pentyloxides of quinquevalent tantalum. *Journal of the Chemical Society (Resumed)* **1956**, 1139–1142.

[157] Bradley, D. C.; Chakravarti, B. N.; Wardlaw, W. 854. Structural chemistry of the alkoxides. Part VIII. Isomeric butoxides and pentyloxides of niobium. *Journal of the Chemical Society (Resumed)* **1956**, 4439–4442.

[158] Bradley, D. C. A structural theory for metal alkoxide polymers. *Nature* **1958**, *182*, 1211–1214.

[159] Bradley, D. C.; Charkravarti, B. N.; Chatterjee, A. K.; Wardlaw, W.; Whitley, A. 19. Niobium and tantalum mixed alkoxides. *Journal of the Chemical Society (Resumed)* **1958**, 99–101.

[160] Bradley, D. C.; Holloway, C. E. Nuclear magnetic resonance studies on niobium and tantalum penta-alkoxides. *Journal of the Chemical Society A: Inorganic, Physical, Theoretical* **1968**, 219.

[161] Bradley, D.; Chakravarti, B.; Chatterjee, A. Quinquevalent compounds of uranium—I

Alkoxides and complex chlorides. *Journal of Inorganic and Nuclear Chemistry* **1957**, *3*, 367–369.

[162] Bradley, D. C.; Chatterjee, A. K. Quinquevalent compounds of uranium-II Uranium penta-n-alkoxides. *Journal of Inorganic and Nuclear Chemistry* **1957**, *4*, 279–282.

[163] Bradley, D. C.; Kapoor, R. N.; Smith, B. C. 189. Quinquevalent compounds of uranium. Part III. Uranium penta-alkoxides. *Journal of the Chemical Society (Resumed)* **1963**, 1023–1027.

[164] Lee, J.; Gouma, P. I. *Sol-Gel Processing for Conventional and Alternative Energy*; 2012; pp 217–237.

[165] Bradley, D.; Mehrotra, R.; Rothwell, I.; Singh, A. *Alkoxo and Aryloxo Derivatives of Metals*; Elsevier, 2001; pp 3–181.

[166] Mehrotra, R. C.; Kapoor, P. N. Organic compounds of tantalum: I. Reactions of tantalum penta-ethoxide with β-ketoesters. *Journal of The Less-Common Metals* **1964**, *7*, 453–457.

[167] Mehrotra, R.; Kapoor, P. Organic compounds of niobium: II. Reactions of niobium penta-ethoxide with β-ketoesters. *Journal of the Less Common Metals* **1964**, *7*, 176–179.

[168] Kapoor, P.; Mehrotra, R. Organic compounds of niobium and tantalum IV. Reactions of niobium and tantalum pentaethoxides with β-diketones. *Journal of the Less Common Metals* **1965**, *8*, 339–346.

[169] Mehrotra, R.; Kapoor, R.; Prakash, S.; Kapoor, P. Organic compounds of niobium and tantalum. Reactions of niobium and tantalum pentaethoxides with ethyl benzoylacetate. *Australian Journal of Chemistry* **1966**, *19*, 2079–2081.

[170] Kapoor, R. N.; Prakash, S.; Kapoor, P. N. Organic compounds of niobium and tantalum. Reactions of niobium and tantalum pentaethoxides with dibenzoylmethane. *Bulletin of the Chemical Society of Japan* **1967**, *40*, 1384–1386.

[171] Mehrotra, R.; Kapoor, P. Organic compounds of niobium: V. Reaction of niobium pentaethoxide with glycols. *Journal of the Less Common Metals* **1965**, *8*, 419–427.

[172] Mehrotra, R. C.; Kapoor, P. N. Organic compounds of tantalum - Reactions of tantalum penta-ethoxide with glycols. *Journal of the Less-Common Metals* **1965**, *10*, 237–245.

[173] Mehrotra, R.; Rai, A.; Kapoor, P.; Bohra, R. Organic derivatives of niobium(V) and tantalum(V). *Inorganica Chimica Acta* **1976**, *16*, 237–267.

[174] Yoldas, B. E. Deposition and properties of optical oxide coatings from polymerized solutions. *Applied Optics* **1982**, *21*, 2960–2964.

[175] Yoldas, B. E. US4361598A Polymerized solutions for depositing optical oxide coatings. 1982.

[176] Silverman, L. A.; Teowee, G.; Uhlmann, D. R. Characterization of Sol-Gel Derived Tantalum Oxide Films. *MRS Proceedings* **1986**, *72*, 331.

[177] Griesmar, P.; Papin, G.; Sanchez, C.; Livage, J. Sol-gel route to niobium pentoxide. *Chemistry of Materials* **1991**, *3*, 335–339.

[178] Wu, E.; Chen, K. C.; Mackenzie, J. D. Ferroelectric ceramics – the sol-gel method versus conventional processing. Materials Research Society Symposia Proceedings - Volume 32. Albuquerque, 1984; pp 169–174.

[179] Bradley, D. C. Metal alkoxides as precursors for electronic and ceramic materials. *Chemical Reviews* **1989**, *89*, 1317–1322.

[180] Tanitsu, K.; Nakayama, M.; Sato, Y. US4960618 Process for formation of metal oxide film. 1990.

[181] Tanitsu, K.; Nakayama, M.; Hashimoto, A.; Nishimura, T. US5156884 Method for forming a film of oxidized metal. 1992.

[182] Ohishi, T.; Maekawa, S.; Katoh, A. Synthesis and properties of tantalum oxide films prepared by the sol-gel method using photo-irradiation. *Journal of Non-Crystalline Solids* **1992**, *147-148*, 493–498.

[183] Boyd, I. W.; Zhang, J.-Y. Photo-induced growth of dielectrics with excimer lamps. *Solid-State Electronics* **2001**, *45*, 1413–1431.

[184] Tohge, N.; Shinmou, K.; Minami, T. Effects of UV-irradiation on the formation of oxide thin films from chemically modified metal-alkoxides. *Journal of Sol-Gel Science and Technology* **1994**, *2*, 581–585.

[185] Suzuki, K.; Sakamoto, W.; Yogo, T.; Hirano, S.-i. UV processing of oriented KTa0.50Nb0.50O3 thin films. *Journal of the Ceramic Society of Japan* **1999**, *107*, 1032–1036.

[186] Park, T. H.; Yang, K. H.; Kang, D. K.; Lim, T. Y.; Auh, K. H.; Kim, B. H. Electrical properties of ferroelectric SBT thin films prepared using photosensitive sol-gel solution. *Journal of Materials Science* **2003**, *38*, 1295–1300.

[187] Lim, T. Y.; Yang, K. H.; Kim, B. H.; Auh, K. H. Fabrication and characterization of direct patterning ferroelectric Sr0.9Bi2.1Ta2O9thin films by photosensitive sol-gel solution. *Thin Solid Films* **2005**, *471*, 12–18.

[188] Thompson, J. O.; Nelson, C. L.; Punsalan, D. US7381633B2 Method of making a patterned metal oxide film. 2008.

[189] Park, H.-H.; Choi, D.-G.; Jeong, J.-H.; Kim, K.-D.; Choi, J.-H.; Lee, J.-H.; Park, S.-J.; Jeon, S.-H.; Kim, S.-R. US7994053B2 Patterning method of metal oxide thin film using nanoimprinting, and manufacturing method of light emitting diode. 2011.

[190] Noma, N.; Hamano, M. Preparation of new photosensitive Nb2O5gel films modified with benzoylacetone and properties of heat-treated films. *Journal of Sol-Gel Science and Technology* **2012**, *64*, 297–303.

[191] Segawa, H.; Inoue, S.; Watanabe, K.; Ohashi, R.; Nitani, H.; Nomura, M. A study of photoreactions in photosensitive TiO2 hybrid gel films induced by UV irradiation. *Journal of the Ceramic Society of Japan* **2015**, *123*, 793–799.

[192] Nakajima, T.; Shinoda, K.; Tsuchiya, T. UV-assisted nucleation and growth of oxide films from chemical solutions. *Chemical Society Reviews* **2014**, *43*, 2027–2041.

[193] Bretos, I.; Jiménez, R.; Ricote, J.; Calzada, M. L. Low-temperature crystallization of solution-derived metal oxide thin films assisted by chemical processes. *Chemical Society Reviews* **2018**, *47*, 291–308.

[194] Calzada, M. L.; Sirera, R.; Carmona, F.; Jiménez, B. Investigations of a diol-based sol-gel process for the preparation of lead titanate materials. *Journal of the American Ceramic Society* **1995**, *78*, 1802–1808.

[195] Calzada, M. L.; González, A.; Poyato, R.; Pardo, L. Photo-sensitive sol-gel solutions for the low-temperature UV-assisted processing of PbTiO 3 based ferroelectric thin films. *J. Mater. Chem.* **2003**, *13*, 1451–1457.

[196] Kemmitt, T.; Daglish, M. Decomposition of Coordinated Acetylacetonate in Lead Zirconate Titanate (PZT) Precursor Solutions. *Inorganic Chemistry* **1998**, *37*, 2063–2065.

[197] Kao, M. C.; Lee, M. S.; Wang, C. M.; Chen, H. Z.; Chen, Y. C. Properties of LiTaO3thin films derived by a diol-based sol-gel process. *Japanese Journal of Ap-*

plied Physics, Part 1: Regular Papers and Short Notes and Review Papers **2002**, *41*, 2982–2986.

[198] González García, A. Láminas delgadas y ultradelgadas de tantalato de estroncio y bismuto obtenidas a partir de derivados de glicolato de tántalo para su uso en memorias ferroeléctricas no volátiles. Ph.D. thesis, Autonomous University of Madrid, 2002.

[199] Calzada, M. L.; González, A.; García-López, J.; Jiménez, R. Crystallization, Heterostructure, Microstructure, and Properties of Ferroelectric Strontium Bismuth Tantalate Films Derived from Tantalum Glycolate Solutions. *Chemistry of Materials* **2003**, *15*, 4775–4783.

[200] Calzada, M. L.; González, A. Tantalum penta-glycolate sol as a precursor of strontium bismuth tantalate ferroelectric thin films. *Journal of the American Ceramic Society* **2005**, *88*, 2702–2708.

[201] Calzada, M. L.; Algueró, M.; Ricote, J.; Santos, A.; Pardo, L. Preliminary results on sol-gel processing of <100> oriented Pb(Mg1/3Nb2/3)O3-PbTiO3thin films using diol-based solutions. *Journal of Sol-Gel Science and Technology* **2007**, *42*, 331–336.

[202] Calzada, M. L.; Algueró, M.; Santos, A.; Stewart, M.; Cain, M. G.; Pardo, L. Piezoelectric, ferroelectric Pb(Mg1/3Nb2/3)O3- PbTiO3thin films with compositions around the morphotropic phase boundary prepared by a sol-gel process of reduced thermal budget. *Journal of Materials Research* **2009**, *24*, 526–533.

[203] Bretos, I.; Calzada, M. L. In *Multifunctional Polycrystalline Ferroelectric Materials - Processing and Properties*; Pardo, L., Ricote, J., Eds.; Springer: Dordrecht, 2011; Chapter 5, pp 152–155, 182–186.

[204] Scott, J. F. *Ferroelectric Memories*; Springer-Verlag: Berlin, 2000; p 166.

[205] Ambrožič, G.; Škapin, S. D.; Žigon, M.; Orel, Z. C. The synthesis of zinc oxide nanoparticles from zinc acetylacetonate hydrate and 1-butanol or isobutanol. *Journal of Colloid and Interface Science* **2010**, *346*, 317–323.

[206] Staniuk, M.; Zindel, D.; Van Beek, W.; Hirsch, O.; Kränzlin, N.; Niederberger, M.; Koziej, D. Matching the organic and inorganic counterparts during nucleation and growth of copper-based nanoparticles - in situ spectroscopic studies. *CrystEngComm* **2015**, *17*, 6962–6971.

[207] Sodhi, R. K.; Paul, S. An Overview of Metal Acetylacetonates: Developing Areas/Routes to New Materials and Applications in Organic Syntheses. *Catalysis Surveys from Asia* **2018**, *22*, 31–62.

[208] Lambert, J. B.; Mazzola, E. P.; Ridge, C. D. *Nuclear Magnetic Resonance Spectroscopy: An Introduction to Principles, Applications, and Experimental Methods*, 2nd ed.; John Wiley & Sons, Inc.: Hoboken, 2019; pp 85, 99.

[209] Takebayashi, Y.; Yoda, S.; Sugeta, T.; Otake, K.; Sako, T.; Nakahara, M. Acetone hydration in supercritical water: 13C-NMR spectroscopy and Monte Carlo simulation. *The Journal of Chemical Physics* **2004**, *120*, 6100–6110.

[210] Colomer, M. T.; Jurado, J. R. Structural, Microstructural, and Electrical Transport Properties of TiO2-RuO2 Ceramic Materials Obtained by Polymeric Sol-Gel Route. *Chemistry of Materials* **2000**, *12*, 923–930.

[211] Likhodii, S. S.; Burnham, W. M. Ketogenic diet: does acetone stop seizures? *Medical science monitor : international medical journal of experimental and clinical research* **2002**, *8*, HY19–24.

[212] Zhao, Y.; Ang, J. Q. L.; Ng, A. W. T.; Yeung, Y.-Y. Oxidative transformation of cyclic

ethers/amines to lactones/lactams using a DIB/TBHP protocol. *RSC Advances* **2013**, *3*, 19765.

[213] Ambrose, D.; Sprake, C. Thermodynamic properties of organic oxygen compounds XXV. Vapour pressures and normal boiling temperatures of aliphatic alcohols. *The Journal of Chemical Thermodynamics* **1970**, *2*, 631–645.

[214] NIST Chemistry WebBook, SRD 69, U. D. o. C. Ethanol. 2018; https://webbook.nist.gov/chemistry/.

[215] Stull, D. R. Vapor Pressure of Pure Substances. Organic and Inorganic Compounds. *Industrial & Engineering Chemistry* **1947**, *39*, 517–540.

[216] NIST Chemistry WebBook, SRD 69, U. D. o. C. 1,3-Propanediol. 2018; https://webbook.nist.gov/chemistry/.

[217] Pollard, K. D.; Puddephatt, R. J. Chemical Vapor Deposition of Tantalum Oxide from Tetraethoxo(β-diketonato)tantalum(V) Complexes. *Chemistry of Materials* **1999**, *11*, 1069–1074.

[218] Matavž, A.; Frunza, R. C.; Drnovšek, A.; Bobnar, V.; Malič, B. Inkjet printing of uniform dielectric oxide structures from sol-gel inks by adjusting the solvent composition. *Journal of Materials Chemistry C* **2016**, *4*, 5634–5641.

[219] Rebohle, L.; Prucnal, S.; Reichel, D. *Flash Lamp Annealing: From basics to applications*; Springer, Cham, 2019; Chapter 1, pp 1–14.

[220] Beale, C.; Altana, A.; Hamacher, S.; Yakushenko, A.; Mayer, D.; Wolfrum, B.; Offenhäusser, A. Inkjet printed Ta2O5 on a flexible substrate for capacitive pH sensing at high ionic strength. *Sensors and Actuators B: Chemical* **2022**, *369*, 132250.

[221] Rebohle, L.; Prucnal, S.; Reichel, D. *Flash Lamp Annealing: From basics to applications*; Springer, Cham, 2019; Vol. 288; Chapter 2, pp 15–70.

[222] Sharkov, E. A. *Passive Microwave Remote Sensing of the Earth*; 2003; Chapter 6, pp 203–221.

[223] Thévenin, F.; Provost, J.; Morel, P.; Berthomieu, G.; Bouchy, F.; Carrier, F. Asteroseismology and calibration of α Cen binary system. *Astronomy & Astrophysics* **2002**, *392*, L9–L12.

[224] Ségransan, D.; Kervella, P.; Forveille, T.; Queloz, D. First radius measurements of very low mass stars with the VLTI. *Astronomy & Astrophysics* **2003**, *397*, L5–L8.

[225] Brown, A. G. A. et al. Gaia Data Release 2. *Astronomy & Astrophysics* **2018**, *616*, A1.

[226] Wild, F. What is Pluto? 2017; https://www.nasa.gov/audience/forstudents/5-8/features/nasa-knows/what-is-pluto-58.html.

[227] Williams, D. R. Sun Fact Sheet. 2004; https://nssdc.gsfc.nasa.gov/planetary/factsheet/sunfact.html.

[228] Guillot, M. J.; McCool, S. C.; Schroder, K. A. Simulating the Thermal Response of Thin Films During Photonic Curing. Volume 7: Fluids and Heat Transfer, Parts A, B, C, and D. Houston, USA, 2012; pp 19–27.

[229] Luo, S. et al. Instantaneous photoinitiated synthesis and rapid pulsed photothermal treatment of three-dimensional nanostructured TiO2thin films through pulsed light irradiation. *Journal of Materials Research* **2017**, *32*, 1701–1709.

[230] Trantidou, T.; Payne, D. J.; Tsiligkiridis, V.; Chang, Y.-C.; Toumazou, C.; Prodromakis, T. The dual role of Parylene C in chemical sensing: Acting as an encapsulant and as a sensing membrane for pH monitoring applications. *Sensors and Actuators B: Chemical* **2013**, *186*, 1–8.

[231] PDS 2010 LABCOTER ™ 2 Parylene Deposition System Operator's Manual. 2010.

[232] Britton, H. T. S.; Robinson, R. A. CXCVIII.—Universal buffer solutions and the dissociation constant of veronal. *J. Chem. Soc.* **1931**, 1456–1462.

[233] Silicon X-ray photoelectron spectra, silicon electron configuration, and other elemental information. 2022; https://www.thermofisher.com/de/de/home/materials-science/learning-center/periodic-table/metalloid/silicon.html.

[234] Lagow, C. H.; Sladek, K. J.; Richardson, P. C. Anodic Insulated Tantalum Oxide Electrocardiograph Electrodes. *IEEE Transactions on Biomedical Engineering* **1971**, *BME-18*, 162–164.

[235] Ghoneim, M. T.; Sadraei, A.; de Souza, P.; Moore, G. C.; Bazant, M. Z.; Dagdeviren, C. A Protocol to Characterize pH Sensing Materials and Systems. *Small Methods* **2018**, *1800265*, 1800265.

[236] Yuan, X.; Wolf, N.; Hondrich, T. J. J.; Shokoohimehr, P.; Milos, F.; Glass, M.; Mayer, D.; Maybeck, V.; Prömpers, M.; Offenhäusser, A.; Wördenweber, R. Engineering Biocompatible Interfaces via Combinations of Oxide Films and Organic Self-Assembled Monolayers. *ACS Applied Materials & Interfaces* **2020**, *12*, 17121–17129.

[237] Yin, L. T.; Chou, J. C.; Chung, W. Y.; Sun, T. P.; Hsiung, S. K. Study of indium tin oxide thin film for separative extended gate ISFET. *Materials Chemistry and Physics* **2001**, *70*, 12–16.

[238] Simpson, R.; White, R. G.; Watts, J. F.; Baker, M. A. XPS investigation of monatomic and cluster argon ion sputtering of tantalum pentoxide. *Applied Surface Science* **2017**, *405*, 79–87.

[239] Verma, P. K.; Steinbacher, A.; Koch, F.; Nuernberger, P.; Brixner, T. Monitoring ultra-

fast intramolecular proton transfer processes in an unsymmetric β-diketone. *Physical Chemistry Chemical Physics* **2015**, *17*, 8459–8466.

[240] Joseph, C.; Bourson, P.; Fontana, M. D. Amorphous to crystalline transformation in Ta2O5 studied by Raman spectroscopy. *Journal of Raman Spectroscopy* **2012**, *43*, 1146–1150.

[241] Damart, T.; Coillet, E.; Tanguy, A.; Rodney, D. Numerical study of the structural and vibrational properties of amorphous Ta 2 O 5 and TiO 2 -doped Ta 2 O 5. *Journal of Applied Physics* **2016**, *119*, 175106.

[242] Amsel, G.; Nadai, J.; Ortega, C.; Rigo, S.; Siejka, J. Precision absolute thin film standard reference targets for nuclear reaction microanalysis of oxygen isotopes. *Nuclear Instruments and Methods* **1978**, *149*, 705–712.

[243] Amsel, G.; Nadai, J.; Ortega, C.; Siejka, J. Precision absolute thin film standard reference targets for nuclear reaction microanalysis of oxygen isotopes. *Nuclear Instruments and Methods* **1978**, *149*, 713–720.

[244] Amsel, G.; Davies, J. Precision standard reference targets for microanalysis by nuclear reactions. *Nuclear Instruments and Methods in Physics Research* **1983**, *218*, 177–182.

[245] Chen, L.; Hoffman, R. W. Angle-resolved x-ray photoelectron spectroscopy method for the thickness measurement of metal oxide/metal ultrathin films. *Journal of Vacuum Science & Technology A: Vacuum, Surfaces, and Films* **1993**, *11*, 2303–2307.

[246] Zhou, J.-H.; Sui, Z.-J.; Zhu, J.; Li, P.; Chen, D.; Dai, Y.-C.; Yuan, W.-K. Characterization of surface oxygen complexes on carbon nanofibers by TPD, XPS and FT-IR. *Carbon* **2007**, *45*, 785–796.

[247] Tetzner, K.; Schroder, K. A.; Bock, K. Photonic curing of sol–gel derived HfO2 di-

electrics for organic field-effect transistors. *Ceramics International* **2014**, *40*, 15753–15761.

[248] Tetzner, K.; Lin, Y. H.; Regoutz, A.; Seitkhan, A.; Payne, D. J.; Anthopoulos, T. D. Sub-second photonic processing of solution-deposited single layer and heterojunction metal oxide thin-film transistors using a high-power xenon flash lamp. *Journal of Materials Chemistry C* **2017**, *5*, 11724–11732.

[249] Alim, M. A. *Immittance Spectroscopy - Applications to Material Systems*, 1st ed.; Scrivener Publishing: Hoboken, 2018.

[250] Itagaki, M.; Suzuki, S.; Shitanda, I.; Watanabe, K. Electrochemical Impedance and Complex Capacitance to Interpret Electrochemical Capacitor. *Electrochemistry* **2007**, *75*, 649–655.

[251] Alim, M. A. *Immittance Spectroscopy - Applications to Material Systems*, 1st ed.; Scrivener Publishing: Hoboken, 2018; Chapter 4, pp 85–108.

[252] Kirby, B. J. *Micro- and Nanoscale Fluid Mechanics: Transport in Microfluidic Devices*; Cambridge University Press: Cambridge, UK, 2010; Chapter 9, pp 199–224.

[253] Kirby, B. J. *Micro- and Nanoscale Fluid Mechanics: Transport in Microfluidic Devices*; Cambridge University Press: Cambridge, UK, 2010; Chapter Appendix E, pp 440–449.

[254] Kirby, B. J. *Micro- and Nanoscale Fluid Mechanics: Transport in Microfluidic Devices*; Cambridge University Press: Cambridge, UK, 2010; Chapter Appendix B, pp 407–417.

[255] Kirby, B. J. *Micro- and Nanoscale Fluid Mechanics: Transport in Microfluidic Devices*; Cambridge University Press: Cambridge, UK, 2010; Chapter 16, pp 355–372.

[256] Bousse, L.; Bergveld, P. On the impedance of the silicon dioxide/electrolyte interface. *Journal of Electroanalytical Chemistry and Interfacial Electrochemistry* **1983**, *152*, 25–39.

[257] Bootsma, G.; De Rooij, N.; van Silfhout, A. The solid/liquid interface. *Sensors and Actuators* **1981**, *1*, 111–136.

[258] Smith, A. M.; Lee, A. A.; Perkin, S. The Electrostatic Screening Length in Concentrated Electrolytes Increases with Concentration. *The Journal of Physical Chemistry Letters* **2016**, *7*, 2157–2163.

[259] Kirby, B. J. *Micro- and Nanoscale Fluid Mechanics: Transport in Microfluidic Devices*; Cambridge University Press: Cambridge, UK, 2010; Chapter 10, pp 225–249.

[260] Kirby, B. J. *Micro- and Nanoscale Fluid Mechanics: Transport in Microfluidic Devices*; Cambridge University Press: Cambridge, UK, 2010; Chapter 11, pp 250–264.

[261] Huang, J. Diffusion impedance of electroactive materials, electrolytic solutions and porous electrodes: Warburg impedance and beyond. *Electrochimica Acta* **2018**, *281*, 170–188.

[262] Olthuis, W.; Streekstra, W.; Bergveld, P. Theoretical and experimental determination of cell constants of planar-interdigitated electrolyte conductivity sensors. *Sensors and Actuators B: Chemical* **1995**, *24*, 252–256.

[263] Bagshaw, E. A.; Wadham, J. L.; Tranter, M.; Beaton, A. D.; Hawkings, J. R.; Lamarche-Gagnon, G.; Mowlem, M. C. Measuring pH in low ionic strength glacial meltwaters using ion selective field effect transistor (ISFET) technology. *Limnology and Oceanography: Methods* **2021**, *19*, 222–233.

[264] Glueckauf, E. The influence of ionic hydration on activity coefficients in concentrated electrolyte solutions. *Transactions of the Faraday Society* **1955**, *51*, 1235.

[265] Schwabe, K. Azidität konzentrierter elektrolytlösungen. *Electrochimica Acta* **1967**, *12*, 67–93.

[266] Olthuis, W.; Volanschi, A.; Bomer, J.; Bergveld, P. A new probe for measuring electrolytic conductance. *Sensors and Actuators B: Chemical* **1993**, *13*, 230–233.

[267] Olthuis, W.; Smith, A.; van der Zalm, R.; Bergveld, P. New operational modes for the Ta2O5-based electrolyte conductance cell. *Sensors and Actuators B: Chemical* **1994**, *18*, 65–68.

[268] Olthuis, W.; Sprenkels, A.; Bomer, J.; Bergveld, P. Planar interdigitated electrolyte-conductivity sensors on an insulating substrate covered with Ta2O5. *Sensors and Actuators B: Chemical* **1997**, *43*, 211–216.

[269] Zhang, J. et al. "Water-in-salt" polymer electrolyte for Li-ion batteries. *Energy & Environmental Science* **2020**, *13*, 2878–2887.

[270] Pan, L.; Huang, H.; Liu, T.; Niederberger, M. Structurally disordered Ta2O5 aerogel for high-rate and highly stable Li-ion and Na-ion storage through surface redox pseudocapacitance. *Electrochimica Acta* **2019**, *321*, 134645.

[271] Monk, P.; Mortimer, R.; Rosseinsky, D. *Electrochromism and Electrochromic Devices*; Cambridge University Press: Cambridge, pp 125–252.

[272] Fu, Z.-W.; Qin, Q.-Z. Lithium Intercalation and Transport Behavior in a Ta2O5 Film Fabricated by Pulsed Laser Deposition. *Journal of The Electrochemical Society* **2000**, *147*, 4610.

[273] Fu, Z.-W.; Huang, F.; Chu, Y.-Q.; Zhang, Y.; Qin, Q.-Z. Characterization of Amorphous Ta2O5 Film as a Novel Anode Material. *Journal of The Electrochemical Society* **2003**, *150*, A776.

[274] Liu, J.; Banis, M. N.; Li, X.; Lushington, A.; Cai, M.; Li, R.; Sham, T.-K.; Sun, X. Atomic Layer Deposition of Lithium Tantalate Solid-State Electrolytes. *The Journal of Physical Chemistry C* **2013**, *117*, 20260–20267.

[275] Xia, S.; Ni, J.; Savilov, S. V.; Li, L. Oxygen-deficient Ta2O5 nanoporous films as self-supported electrodes for lithium microbatteries. *Nano Energy* **2018**, *45*, 407–412.

[276] Gschwend, G. C.; Girault, H. H. Discrete Helmholtz model: a single layer of correlated counter-ions. Metal oxides and silica interfaces, ion-exchange and biological membranes. *Chemical Science* **2020**, *11*, 10304–10312.

[277] Ramos, A.; Morgan, H.; Green, N. G.; Castellanos, A. AC Electric-Field-Induced Fluid Flow in Microelectrodes. *Journal of Colloid and Interface Science* **1999**, *217*, 420–422.

[278] González, A.; Ramos, A.; Green, N. G.; Castellanos, A.; Morgan, H. Fluid flow induced by nonuniform ac electric fields in electrolytes on microelectrodes. II. A linear double-layer analysis. *Physical Review E* **2000**, *61*, 4019–4028.

[279] Green, N. G.; Ramos, A.; González, A.; Morgan, H.; Castellanos, A. Fluid flow induced by nonuniform ac electric fields in electrolytes on microelectrodes. I. Experimental measurements. *Physical Review E* **2000**, *61*, 4011–4018.

[280] Green, N. G.; Ramos, A.; González, A.; Morgan, H.; Castellanos, A. Fluid flow induced by nonuniform ac electric fields in electrolytes on microelectrodes. III. Observation of streamlines and numerical simulation. *Physical Review E* **2002**, *66*, 026305.

[281] Folkertsma, L.; Gehrenkemper, L.; Eijkel, J.; Gerritsen, K.; Odijk, M. Reference-Electrode Free pH Sensing Using Impedance Spectroscopy. *Proceedings* **2018**, *2*, 742.

[282] van Kerkhof, J. C.; Eijkel, J. C.; Bergveld, P. ISFET responses on a stepwise change in electrolyte concentration at constant pH. *Sensors and Actuators: B. Chemical* **1994**, *18*, 56–59.

[283] Kielland, J. Individual Activity Coefficients of Ions in Aqueous Solutions. *Journal of the American Chemical Society* **1937**, *59*, 1675–1678.

[284] Nightingale, E. R. Phenomenological Theory of Ion Solvation. Effective Radii of Hydrated Ions. *The Journal of Physical Chemistry* **1959**, *63*, 1381–1387.

[285] Brown, M. A.; Goel, A.; Abbas, Z. Effect of Electrolyte Concentration on the Stern Layer Thickness at a Charged Interface. *Angewandte Chemie* **2016**, *128*, 3854–3858.

[286] Bousse, L.; Mostarshed, S.; Van Der Shoot, B.; de Rooij, N.; Gimmel, P.; Göpel, W. Zeta potential measurements of Ta2O5 and SiO2 thin films. *Journal of Colloid and Interface Science* **1991**, *147*, 22–32.

[287] Diot, J.; Joseph, J.; Martin, J.; Clechet, P. pH dependence of the Si/SiO2 interface state density for EOS systems. *Journal of Electroanalytical Chemistry and Interfacial Electrochemistry* **1985**, *193*, 75–88.

[288] Waegele, M. M.; Gunathunge, C. M.; Li, J.; Li, X. How cations affect the electric double layer and the rates and selectivity of electrocatalytic processes. *Journal of Chemical Physics* **2019**, *151*, 1DUMMT.

[289] Sverjensky, D. A. Prediction of surface charge on oxides in salt solutions: Revisions for 1:1 (M+L-) electrolytes. *Geochimica et Cosmochimica Acta* **2005**, *69*, 225–257.

[290] Sverjensky, D. A. Interpretation and prediction of triple-layer model capacitances and the structure of the oxide-electrolyte-water interface. *Geochimica et Cosmochimica Acta* **2001**, *65*, 3643–3655.

[291] Davis, J. A.; James, R. O.; Leckie, J. O. Surface ionization and complexation at the oxide/water interface. *Journal of Colloid and Interface Science* **1978**, *63*, 480–499.

[292] Caetano, D. L. Z.; Bossa, G. V.; de Oliveira, V. M.; Brown, M. A.; de Carvalho, S. J.; May, S. Role of ion hydration for the differential capacitance of an electric double layer. *Physical Chemistry Chemical Physics* **2016**, *18*, 27796–27807.

[293] Outhwaite, C. W.; Lamperski, S.; Bhuiyan, L. B. Influence of electrode polarization on the capacitance of an electric double layer at and around zero surface charge. *Molecular Physics* **2011**, *109*, 21–26.

[294] Hasted, J. B.; Ritson, D. M.; Collie, C. H. Dielectric Properties of Aqueous Ionic Solutions. Parts I and II. *The Journal of Chemical Physics* **1948**, *16*, 1–21.

[295] Ben-Yaakov, D.; Andelman, D.; Podgornik, R. Dielectric decrement as a source of ion-specific effects. *The Journal of Chemical Physics* **2011**, *134*, 074705.

[296] Hatlo, M. M.; van Roij, R.; Lue, L. The electric double layer at high surface potentials: The influence of excess ion polarizability. *EPL (Europhysics Letters)* **2012**, *97*, 28010.

[297] Qing, L.; Lei, J.; Zhao, T.; Qiu, G.; Ma, M.; Xu, Z.; Zhao, S. Effects of Kinetic Dielectric Decrement on Ion Diffusion and Capacitance in Electrochemical Systems. *Langmuir* **2020**, *36*, 4055–4064.

[298] Krekeler, C.; Hess, B.; Delle Site, L. Density functional study of ion hydration for the alkali metal ions (Li+,Na+,K+) and the halide ions (F-,Br-,Cl-). *The Journal of Chemical Physics* **2006**, *125*, 054305.

[299] Goldsack, D. E.; Franchetto, R. C. The viscosity of concentrated electrolyte solutions. II. Temperature dependence. *Canadian Journal of Chemistry* **1978**, *56*, 1442–1450.

[300] Collins, K. Charge density-dependent strength of hydration and biological structure. *Biophysical Journal* **1997**, *72*, 65–76.

[301] Collins, K. Ions from the Hofmeister series and osmolytes: effects on proteins in solution and in the crystallization process. *Methods* **2004**, *34*, 300–311.

[302] Mähler, J.; Persson, I. A study of the hydration of the alkali metal ions in aqueous solution. *Inorganic Chemistry* **2012**, *51*, 425–438.

[303] Marcus, Y. Ionic radii in aqueous solutions. *Chemical Reviews* **1988**, *88*, 1475–1498.

[304] Osofsky, M. S.; Krowne, C. M.; Charipar, K. M.; Bussmann, K.; Chervin, C. N.; Pala, I. R.; Rolison, D. R. Disordered RuO2 exhibits two dimensional, low-mobility transport and a metal-insulator transition. *Scientific Reports* **2016**, *6*, 21836.

[305] Lee, P. A.; Ramakrishnan, T. V. Disordered electronic systems. *Reviews of Modern Physics* **1985**, *57*, 287–337.

[306] Iles, G. S.; Casale, M. E. A. Ruthenium Oxide Glaze Resistors. *Platinum Metals Review* **1967**, *11*, 126–129.

[307] Casale, M. E. A.; Collier, O. N.; Iles, G. S. US3637530 Resistor Composition. 1972.

[308] Shorikov, Y. S.; Asanov, I.; Korablina, E.; Mazalov, L. N.; Parygina, G. K.; Treiger, B. A. X-ray and x-ray-electron investigations of the solid solutions Ru(1-x)MxO2 (M = V, Nb) with rutile structure. *Izvestiya Akademii Nauk SSSR, Neorganicheskie Materialy* **1986**, *22*, 974–978.

[309] Shorikov, Y. S.; Mazalov, L. N.; Kravtsova, E. A.; Parygina, G. K.; Rumyantseva, E. A. Electron structure and electroconductivity of rutile-like solid solutions Ru(1-x)MxO2 (M - V, Nb, W). *Izvestiya Akademii Nauk SSSR, Neorganicheskie Materialy* **1991**, *27*, 832–836.

[310] Chen, Y.-Y. US6480093B1 Composite film resistors and method of making the same. 2002.

[311] Shimoda, T.; Li, J. US9178022B2 Precursor composition and method for forming amorphous conductive oxide film. 2015.

[312] Manjakkal, L.; Cvejin, K.; Kulawik, J.; Zaraska, K.; Socha, R. P.; Szwagierczak, D. X-ray photoelectron spectroscopic and electrochemical impedance spectroscopic analysis of RuO2-Ta2O5thick film pH sensors. *Analytica Chimica Acta* **2016**, *931*, 47–56.

[313] Manjakkal, L.; Zaraska, K.; Cvejin, K.; Kulawik, J.; Szwagierczak, D. Potentiometric RuO2-Ta2O5pH sensors fabricated using thick film and LTCC technologies. *Talanta* **2016**, *147*, 233–240.

[314] Chervin, C. N.; Lubers, A. M.; Pettigrew, K. A.; Long, J. W.; Westgate, M. A.; Fontanella, J. J.; Rolison, D. R. Making the Most of a Scarce Platinum-Group Metal: Conductive Ruthenia Nanoskins on Insulating Silica Paper. *Nano Letters* **2009**, *9*, 2316–2321.

[315] Yan, X.; Liu, H.; Kong Yong Liew, Size control of polymer-stabilized ruthenium nanoparticles by polyol reduction. *Journal of Materials Chemistry* **2001**, *11*, 3387–3391.

[316] Murakami, Y.; Li, J.; Hirose, D.; Kohara, S.; Shimoda, T. Solution processing of highly conductive ruthenium and ruthenium oxide thin films from ruthenium–amine complexes. *Journal of Materials Chemistry C* **2015**, *3*, 4490–4499.

[317] Ernst, R. D.; Melendez, E.; Stahl, L.; Ziegler, M. L. cis- and trans-Diene coordination in ruthenium(II) acetylacetonate compounds. *Organometallics* **1991**, *10*, 3635–3642.

[318] Hasegawa, T.; Lau, T. C.; Taube, H.; Schaefer, W. P. Electronic effects of bis(acetylacetone) in ruthenium(II) and ruthenium(III) complexes. *Inorganic Chemistry* **1991**, *30*, 2921–2928.

[319] Ribeiro, J.; Tremiliosi-Filho, G.; Olivi, P.; de Andrade, A. R. XAS characterization of the RuO2–Ta2O5 system local (crystal) structure. *Materials Chemistry and Physics* **2011**, *125*, 449–460.

[320] Ribeiro, J.; Purgato, F.; Kokoh, K.; Léger, J.-M.; de Andrade, A. Application of Ti/RuO2–Ta2O5 electrodes in the electrooxidation of ethanol and derivants: Reactivity versus electrocatalytic efficiency. *Electrochimica Acta* **2008**, *53*, 7845–7851.

[321] Frunză, R. C.; Kmet, B.; Jankovec, M.; Topič, M.; Malič, B. Ta2O5-based high-K dielectric thin films from solution processed at low temperatures. *Materials Research Bulletin* **2014**, *50*, 323–328.

[322] Matavž, A.; Malič, B.; Bobnar, V. Inkjet printing of metal-oxide-based transparent thin-film capacitors. *Journal of Applied Physics* **2017**, *122*.

[323] Novacentrix, Printed Electronics Product Leadership. https://www.novacentrix.com/products/overview.

[324] Manjakkal, L.; Cvejin, K.; Bajac, B.; Kulawik, J.; Zaraska, K.; Szwagierczak, D. Microstructural, Impedance Spectroscopic and Potentiometric Analysis of Ta 2 O 5 Electrochemical Thick Film pH Sensors. *Electroanalysis* **2015**, *27*, 770–781.

[325] Mikolajick, T.; Kühnhold, R.; Ryssel, H. The pH-sensing properties of tantalum pentoxide films fabricated by metal organic low pressure chemical vapor deposition. *Sensors and Actuators B: Chemical* **1997**, *44*, 262–267.

[326] Kwon, D.-h.; Cho, B.-W.; Kim, C.-S.; Sohn, B.-K. A new approach to low drift Ta2O5 pH-ISFET by RF reactive sputtering and sol-gel method. The 8th International Conference on Solid-State Sensors and Actuators, and Eurosensors IX. 1995; pp 917–920.

[327] Kwon, D.-H.; Cho, B.-W.; Kim, C.-S.; Sohn, B.-K. Effects of heat treatment on Ta2O5 sensing membrane for low drift and high sensitivity pH-ISFET. *Sensors and Actuators B: Chemical* **1996**, *34*, 441–445.

APPENDIX

Appendix One

Proposed Synthesis (Acetylacetone) - Replacing Ta(V) Ethoxide with Ti(IV) Isopropoxide

As previously published,[136,137] anhydrous ethanol (42.00 mmol, 1935 mg [AcrosOrganics, 99.5%, ExtraDry, absolute]), acetylacetone (6.00 mmol, 601 mg, [Alfa-Aesar, 95%]), and titanium(IV) isopropoxide (6.01 mmol, 1708 mg [Sigma-Aldrich, 97%]) were mixed together via magnetic stirring in a dry Schlenk flask in an argon filled glovebox, and were subsequently removed from the glovebox and connected to a Schlenk line. The Schlenk flask containing the reagents (reaction flask) was immersed in silicone oil, with the oil temperature being held and maintained at 80°C to promote chelation of acetylacetone and match the preparation of the tantalum(V) ethoxide acetylacetonate precursor. The reaction was carried out in argon, and reflux was conducted for 8 hours with mixing to allow enough time for complexation of acetylacetone to titanium; the reaction time was minimized as much as possible in order to prevent decomposition of the complex.[196]

After 8 hours, the flask was cooled to 23°C over a 2 hour period. 1,3-Propanediol (36.38 mmol, 2768 mg [Sigma-Aldrich, for synthesis]) was then added via syringe through the Schlenk flask valve and mixed, where bubbles appeared for a short time but eventually disappeared. After 12 hours of mixing at a reduced temperature, the Schlenk flask was removed from the Schlenk line. The product was subsequently transferred from the Schlenk flask to a round bottom flask, and the round bottom flask was then connected to a rotary evaporator. The rotation speed was set to 95 rpm, the pressure was set to 30 mbar, and the water bath temperature was set to 40°C. Vigorous bubbling was present at the beginning, but the bubbling eventually dissipated. The flask remained attached for 8 hours, where afterward it was found that the mass loss (3030 mg) was close to the calculated ethanol and isopropanol loss (3380 mg).

After adding 1,3-propanediol at room temperature, the Ti(IV) acetylacetonate solution turns turbid over time as shown in Figure A.1, in contrast to the Ta(V) solutions. This may be due to the formation of a $Ti(IV)(OC_3H_6O)_2$ precipitate, with both terminal oxygens on the diol bound to the cation as reported by Kemmitt and Daglish.[196] In contrast to the even valency of +4 for Ti(IV), Ta(V) has an odd valency of +5 and suggests that the proposed synthesis may only work for Ta(V),[172,198–200] and possibly Nb(V),[171] glycolate β-diketonate solutions.

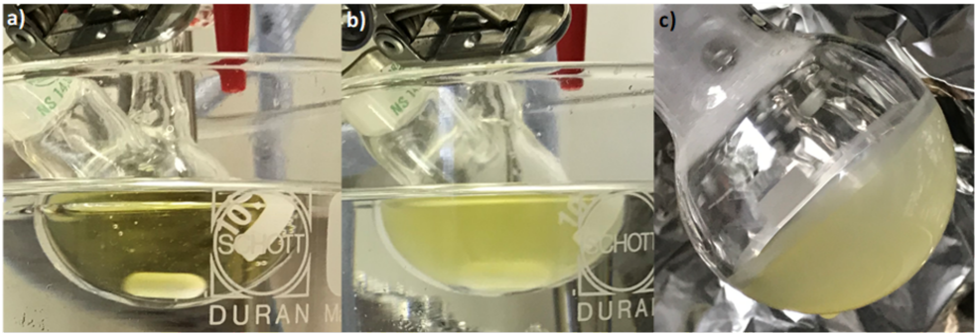

Figure A.1 After addition of 1,3-propanediol to the Ti(IV) acetylacetonate solution (a), 12 hours after 1,3-propanediol addition (b), and after removal of isopropanol and ethanol (c). In contrast to the Ta(V) solutions, the Ti(IV) solution turns turbid over time at room temperature (© The Royal Society of Chemistry 2020).

Appendix Two

Parylene C Deposition

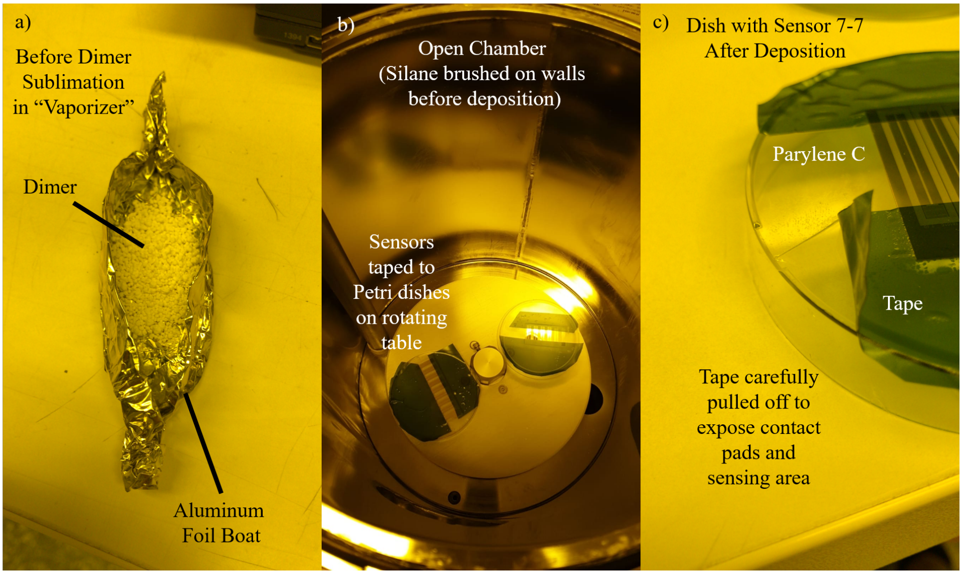

Figure B.1 Dimer in the boat before being placed in the "vaporizer" (as named in industry[231] where "vaporization" occurs, but technically incorrect as the dimer sublimates) (a), open chamber where sensors on Petri dishes are set on the rotating table at the bottom of the chamber, with a few brush strokes of silane on the wall before starting the deposition process (b), and careful peeling off of the clean room dicing tape (1008R-11.5, Ultron Systems, Inc.) to expose the sensor and contact pads while leaving the feed lines passivated (c).

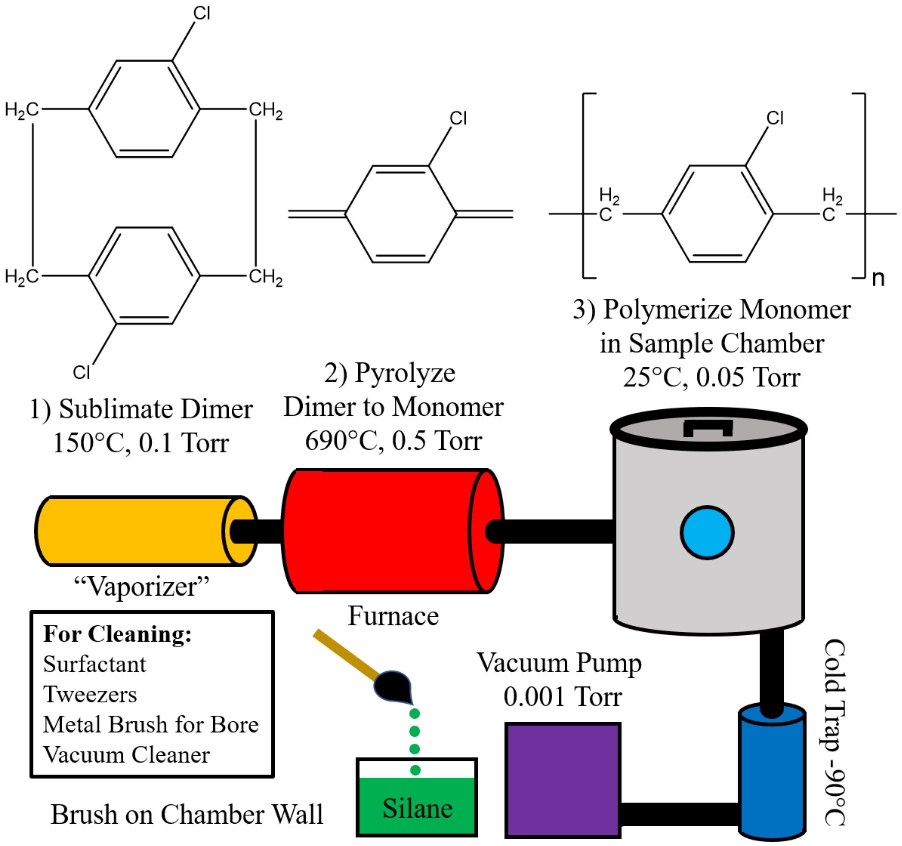

Figure B.2 Parylene deposition as described by the manufacturer[231] for the SCS Labcoter 2 - Parylene Deposition System 2010 (Specialty Coating Systems, Inc. USA) for depositing a parylene C passivation layer with the dichloro-p-cyclophane dimer (DPX-C, Specialty Coating Systems, Inc.), and γ-methyacryloxypropyl-trimethoxysilane as silane for adhesion (A-174 Silane, Specialty Coating Systems, Inc.). As the pressure decreases upon pumping down, the silane evaporates off the wall and deposits on the sample at ~40 Torr. A 2 v/v % Micro-90 surfactant solution (International Products Corporation, USA) in deionized water was used for cleaning the device.

Appendix Three

Images for Flash Lamp Experiment

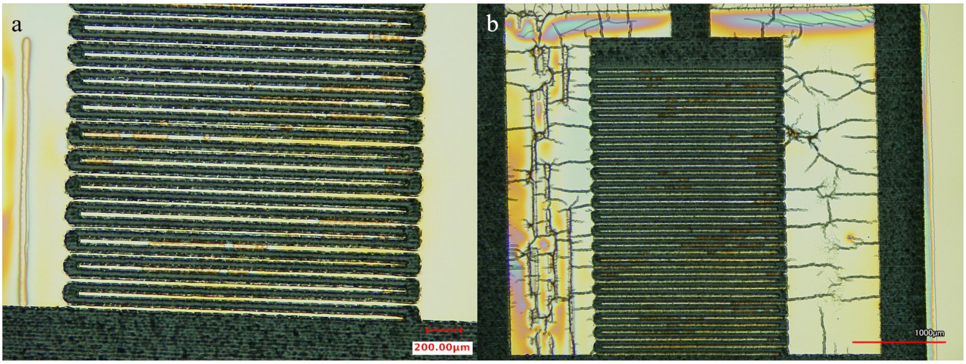

Figure C.1 (Same as Figure 4.2) Sample 1 Firing Parameters - 1x 770 mJ cm^{-2}, 350 V, 500 µs, 1 undivided pulse, no capacitance change (a - before flash lamp, b - after flash lamp).

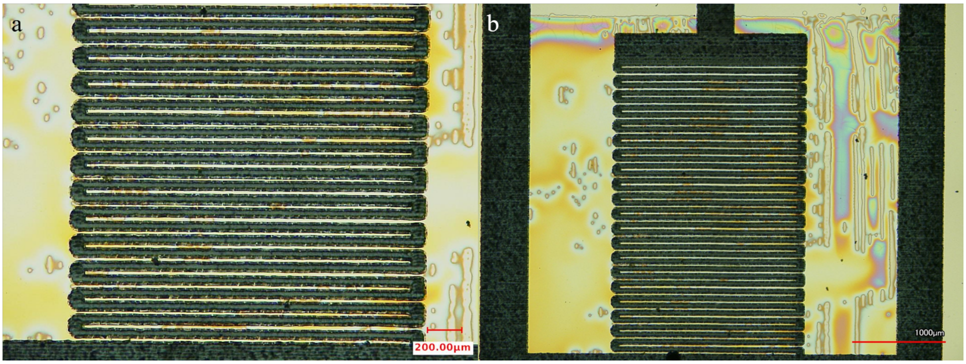

Figure C.2 Sample 2 Firing Parameters (increase voltage, decrease envelope, divide pulse) - 1x 558 mJ cm^{-2}, 450 V, 400 µs, 5 µpulses with 50% duty cycle, no capacitance change (a - before flash lamp, b - after flash lamp).

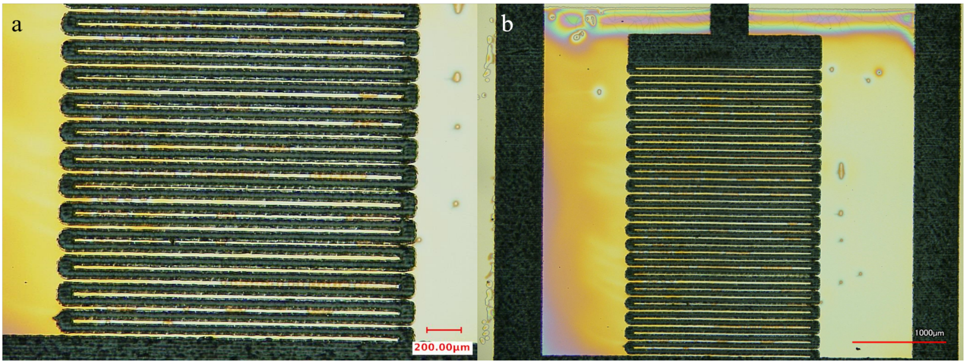

Figure C.3 Sample 3 Firing Parameters (increase shot count) - 20x at 2 Hz, 558 mJ cm^{-2}, 450 V, 400 µs, 5 µpulses with 50% duty cycle, no capacitance change (a - before flash lamp, b - after flash lamp).

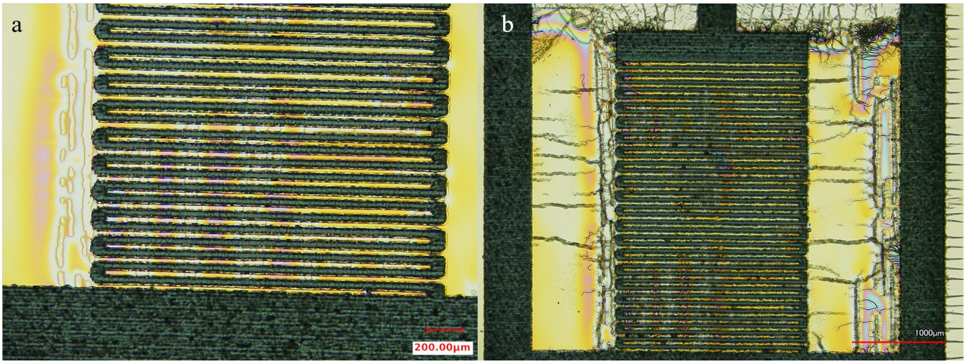

Figure C.4 Sample 4 Firing Parameters (increase shot envelope) - 20x at 2 Hz, 1130 mJ cm^{-2}, 450 V, 800 µs, 5 µpulses with 50% duty cycle, no capacitance change (a - before flash lamp, b - after flash lamp).

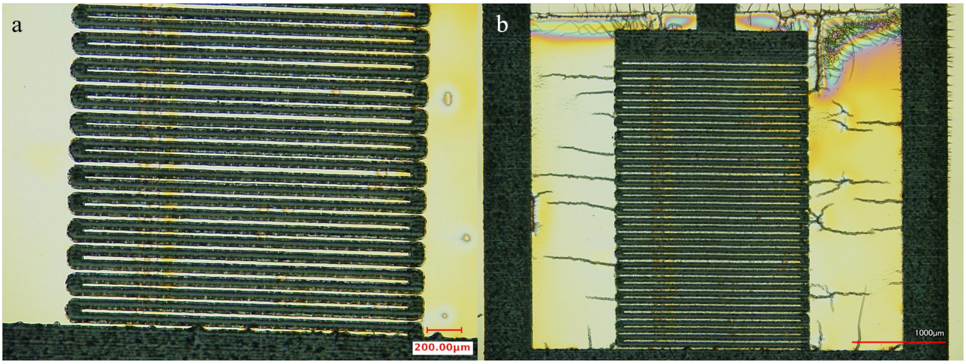

Figure C.5 Sample 5 Firing Parameters (decrease shot envelope) - 20x at 2 Hz, 862 mJ cm^{-2}, 450 V, 600 µs, 5 µpulses with 50% duty cycle, no capacitance change (a - before flash lamp, b - after flash lamp).

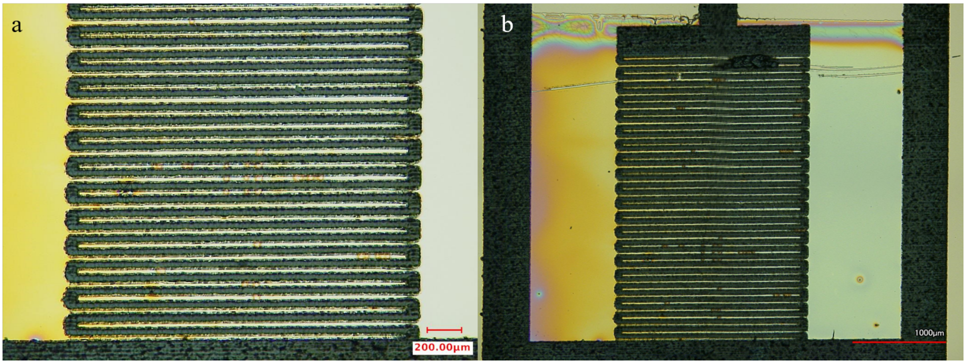

Figure C.6 Sample 6 Firing Parameters (decrease shot envelope) - 20x at 2 Hz, 692 mJ cm^{-2}, 450 V, 500 µs, 5 µpulses with 50% duty cycle, no capacitance change (a - before flash lamp, b - after flash lamp).

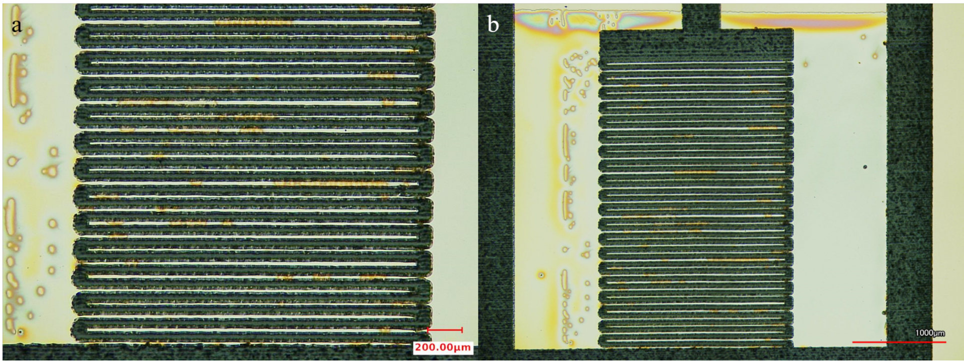

Figure C.7 Sample 7 Firing Parameters (reiteration) - 20x at 2 Hz, 692 mJ cm^{-2}, 450 V, 500 µs, 5 µpulses with 50% duty cycle, no capacitance change (a - before flash lamp, b - after flash lamp).

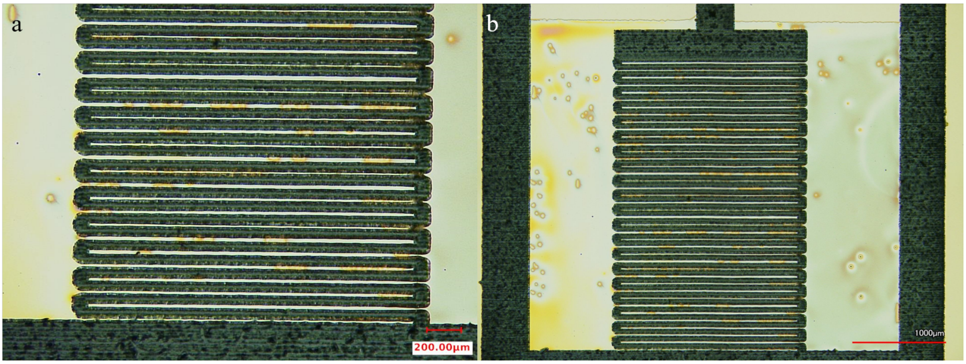

Figure C.8 Sample 8 Firing Parameters (increase shot count) - 120x at 2 Hz, 692 mJ cm^{-2}, 450 V, 500 µs, 5 µpulses with 50% duty cycle, no capacitance change (a - before flash lamp, b - after flash lamp).

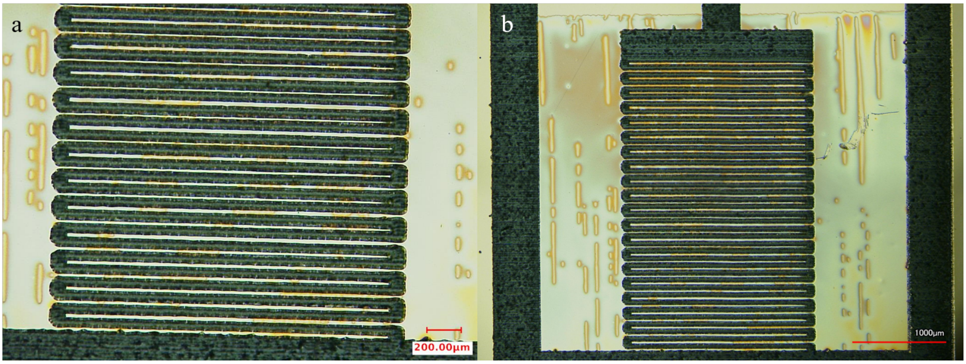

Figure C.9 Sample 9 Firing Parameters (add µpulses) - 120x at 2 Hz, 739 mJ cm^{-2}, 450 V, 500 µs, 7 µpulses with 50% duty cycle, no capacitance change (a - before flash lamp, b - after flash lamp).

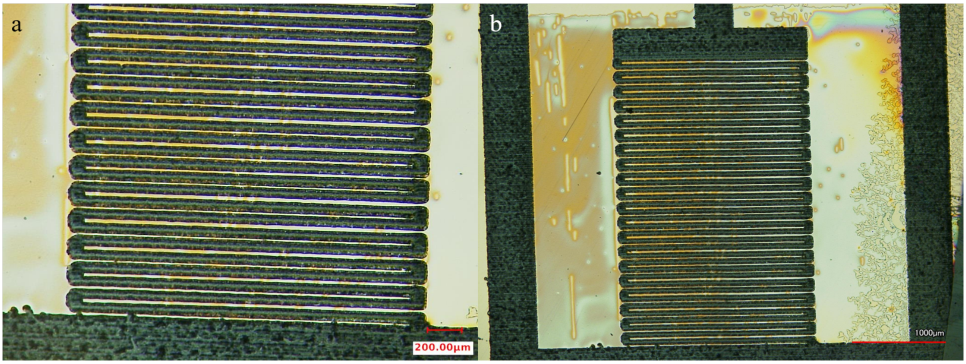

Figure C.10 Sample 10 Firing Parameters (increase shot count) - 1200x at 2 Hz, 739 mJ cm^{-2}, 450 V, 500 µs, 7 µpulses with 50% duty cycle, no capacitance change (a - before flash lamp, b - after flash lamp).

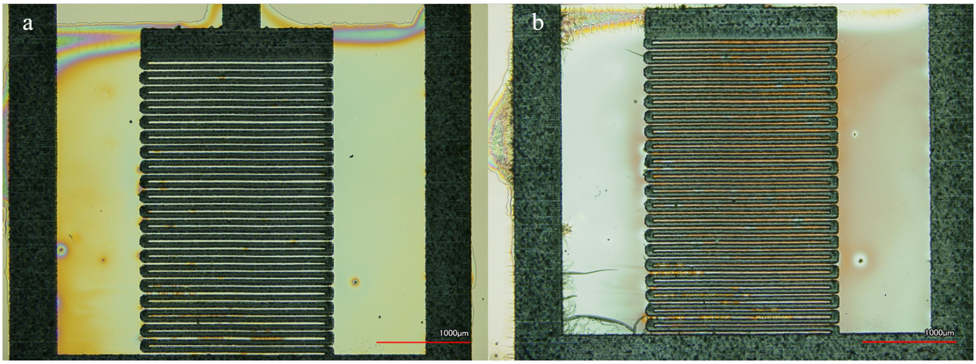

Figure C.11 Sample 11 Firing Parameters (increase shot count) - 2400x at 2 Hz, 739 mJ cm^{-2}, 450 V, 500 µs, 7 µpulses with 50% duty cycle, [3.4 pF before, 4.2 pF after, 1.2 pF parasitics] (a - before flash lamp, b - after flash lamp).

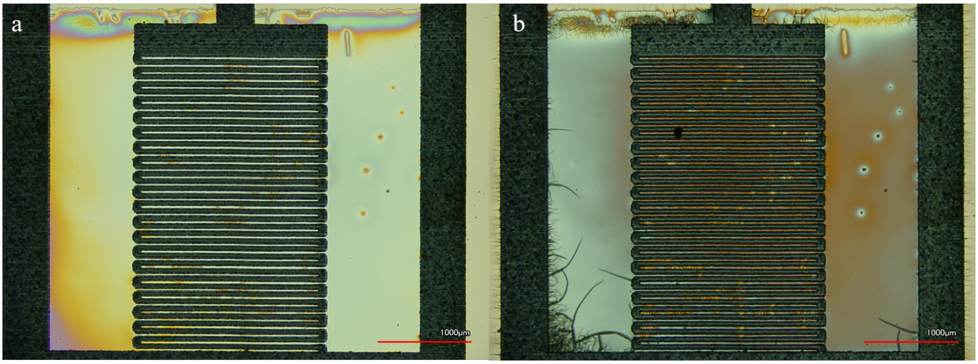

Figure C.12 Sample 12 Firing Parameters (reiteration) - 2400x at 2 Hz, 739 mJ cm^{-2}, 450 V, 500 µs, 7 µpulses with 50% duty cycle, [3.5 pF before, 4.3 pF after, 1.2 pF parasitics] (a - before flash lamp, b - after flash lamp).

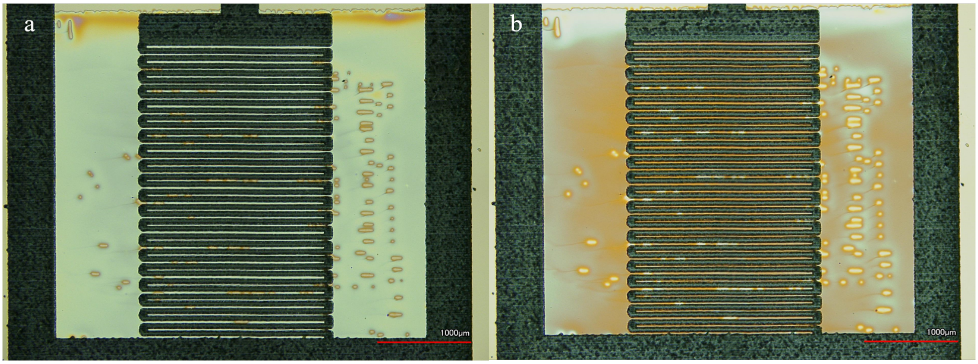

Figure C.13 Sample 13 Firing Parameters (decrease duty cycle) - 2400x at 2 Hz, 663 mJ cm^{-2}, 450 V, 500 µs, 7 µpulses with 40% duty cycle, [3.3 pF before, 5.0 pF after, 1.2 pF parasitics] (a - before flash lamp, b - after flash lamp).

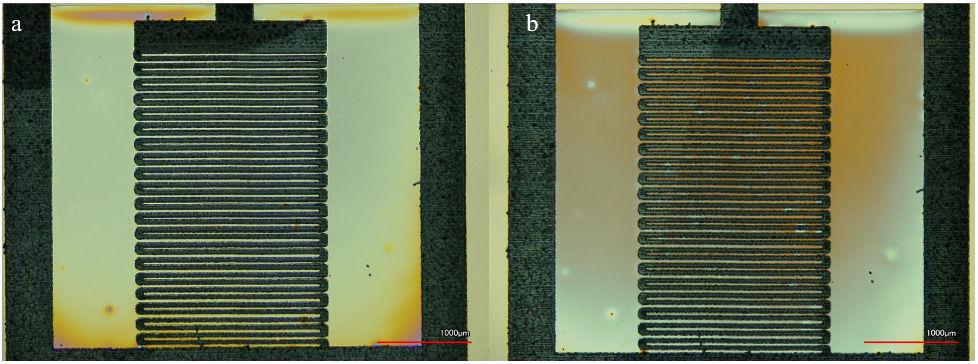

Figure C.14 (Same as Figure 4.3) Sample 14 Firing Parameters (reiteration) - 2400x at 2 Hz, 663 mJ cm^{-2}, 450 V, 500 µs, 7 µpulses with 40% duty cycle, [3.5 pF before, 5.0 pF after, 1.2 pF parasitics] (a - before flash lamp, b - after flash lamp).

Appendix Four

EGFET Drift and Sensitivity

A 4200A-SCS Parameter Analyzer (Keithley Instruments, USA) was used for measurements, with the device connecting to the transistor via clamping to probe heads and a breadboard; the probe heads were connected to the analyzer in a PM5 Probe Station (Cascade Microtech, USA). The transistor used was a commercial nMos CD4007UBE (Texas Instruments, USA), with pin 6 as the gate, pin 7 as the source, and pin 8 as the drain. Measurements were run in the dark.

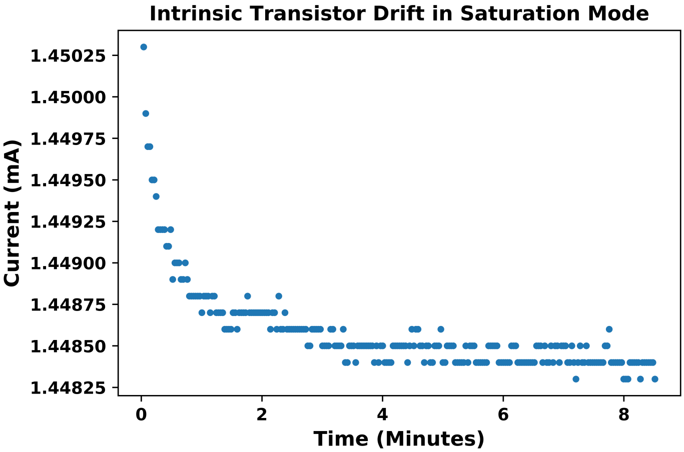

Figure D.1 I_{DS} over time in saturation mode with the gate connected directly to the analyzer, with biases of $V_{GS} = 3$ V and $V_{DS} = 5$ V. The intrinsic drift is less than 0.001 mA min^{-1}, which is much lower than when measuring with Ta_2O_5.

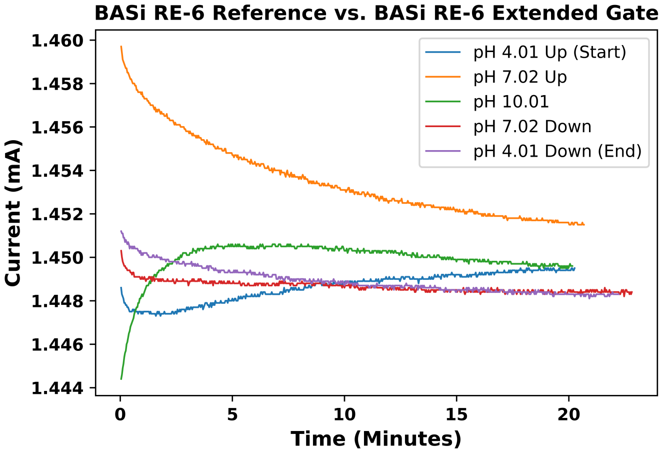

Figure D.2 I_{DS} over time in saturation mode with two BASi RE-6 reference electrodes (one as the extended-gate, and one as the reference in Britton-Robinson buffer solution), with biases of $V_{GS} = 3$ V and $V_{DS} = 5$ V. The measurement was started in pH $= 4$, then pH $= 7$, then pH $= 10$, then pH 7 again, then finally pH 4 again. The drift in all cases is less than 0.0004 mA min^{-1}, which is much lower than when measuring with Ta_2O_5.

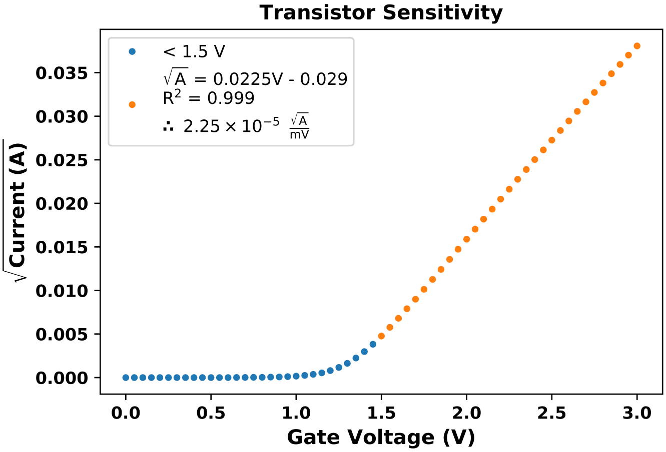

Figure D.3 Transistor V_{GS} sweeped from 0 V to 3 V, with a V_{DS} bias of 5 V, and plotted versus $\sqrt{I_{DS}}$, in order to determine the correct conversion for saturation mode where $I_{DS} \propto (V_{GS} - V_T)^2$. The linear portion from 1.5 V to 3.0 V is used for the calculation.

Appendix Five

Sensor 7-7 Supporting Immittance Spectra

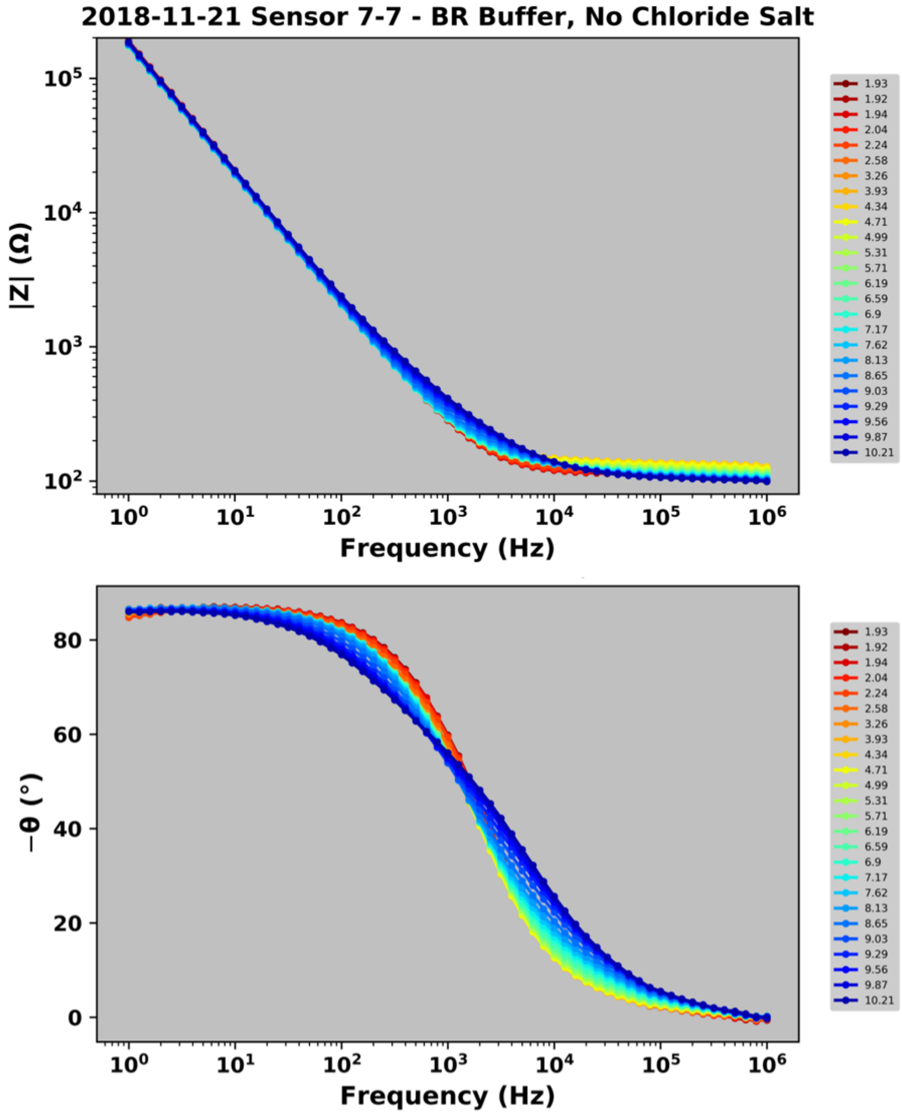

Figure E.1 Bode plot for the "no added chloride salt" buffer, with each pH point color coded from red (acidic) to more basic (blue) (© 2022 Elsevier B.V. All rights reserved.).[220]

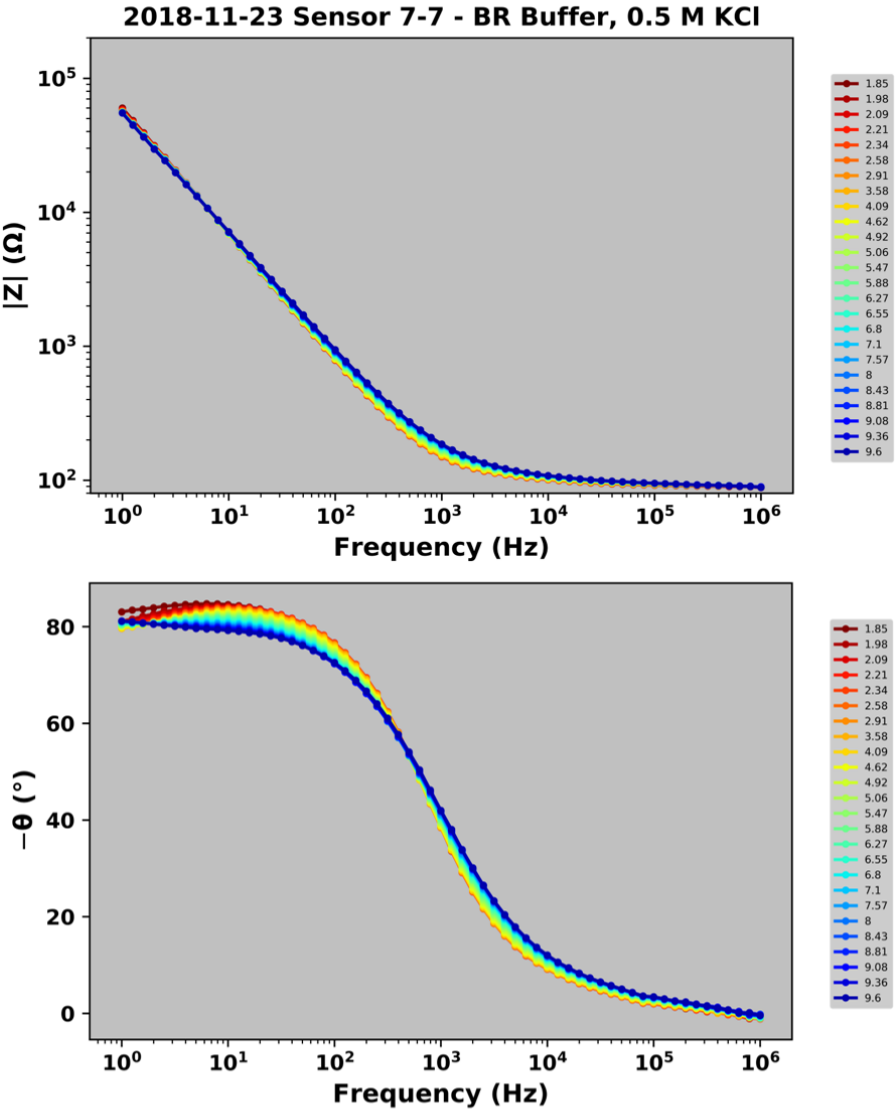

Figure E.2 Bode plot for the 0.5 M KCl buffer, with each pH point color coded from red (acidic) to more basic (blue) (© 2022 Elsevier B.V. All rights reserved.).[220]

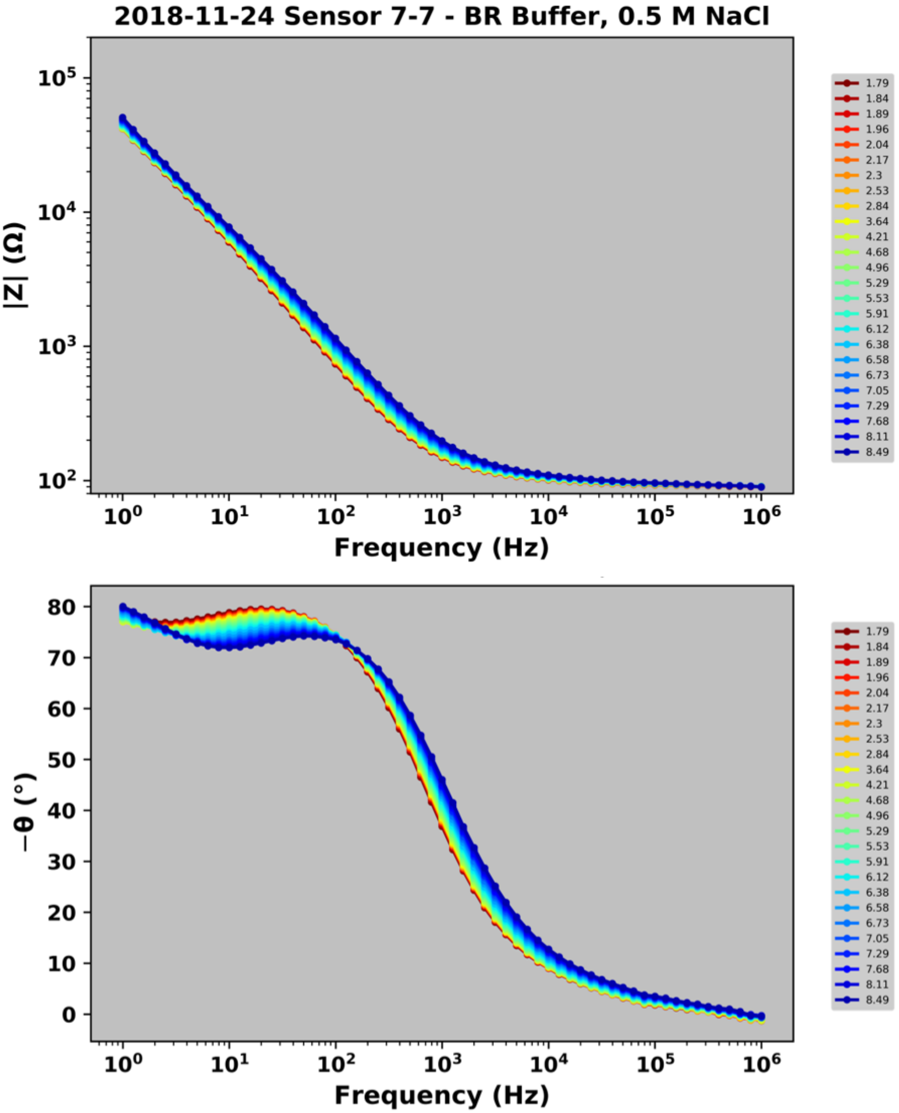

Figure E.3 Bode plot for the 0.5 M NaCl buffer, with each pH point color coded from red (acidic) to more basic (blue) (© 2022 Elsevier B.V. All rights reserved.).[220]

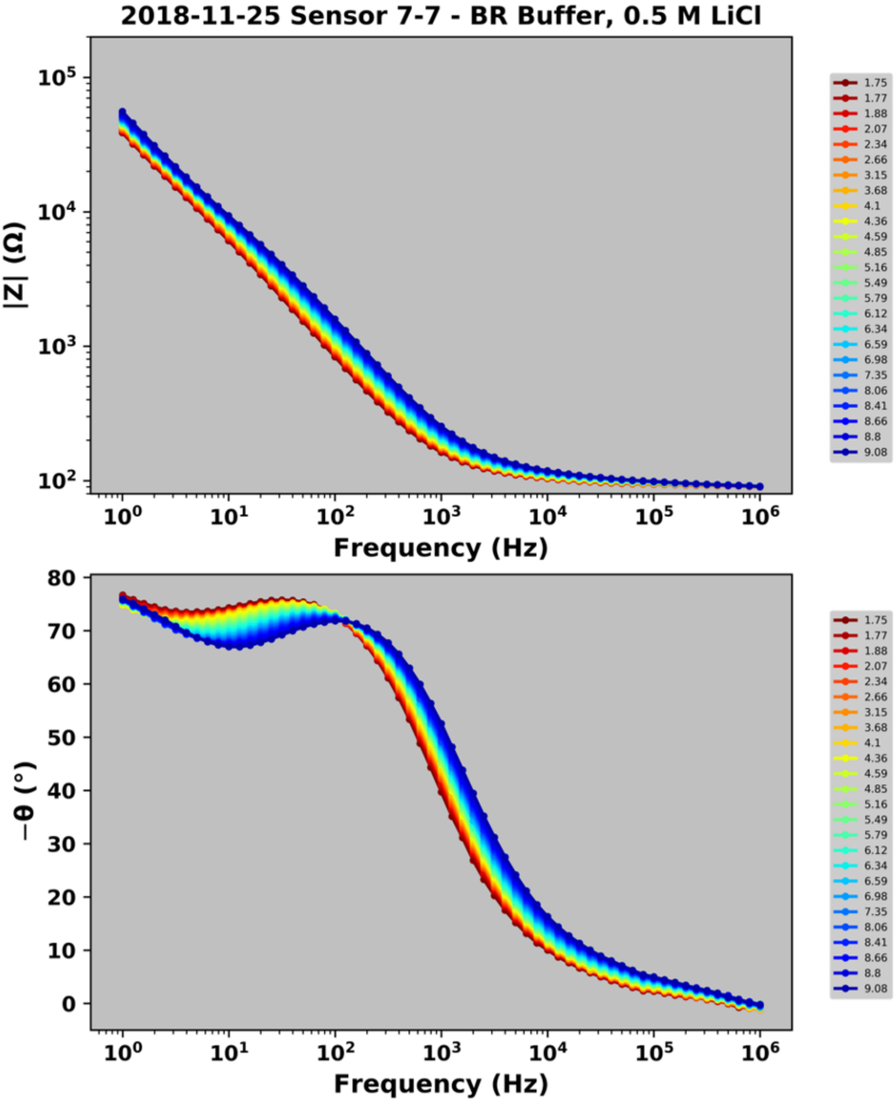

Figure E.4 Bode plot for the 0.5 M LiCl buffer, with each pH point color coded from red (acidic) to more basic (blue) (© 2022 Elsevier B.V. All rights reserved.).[220]

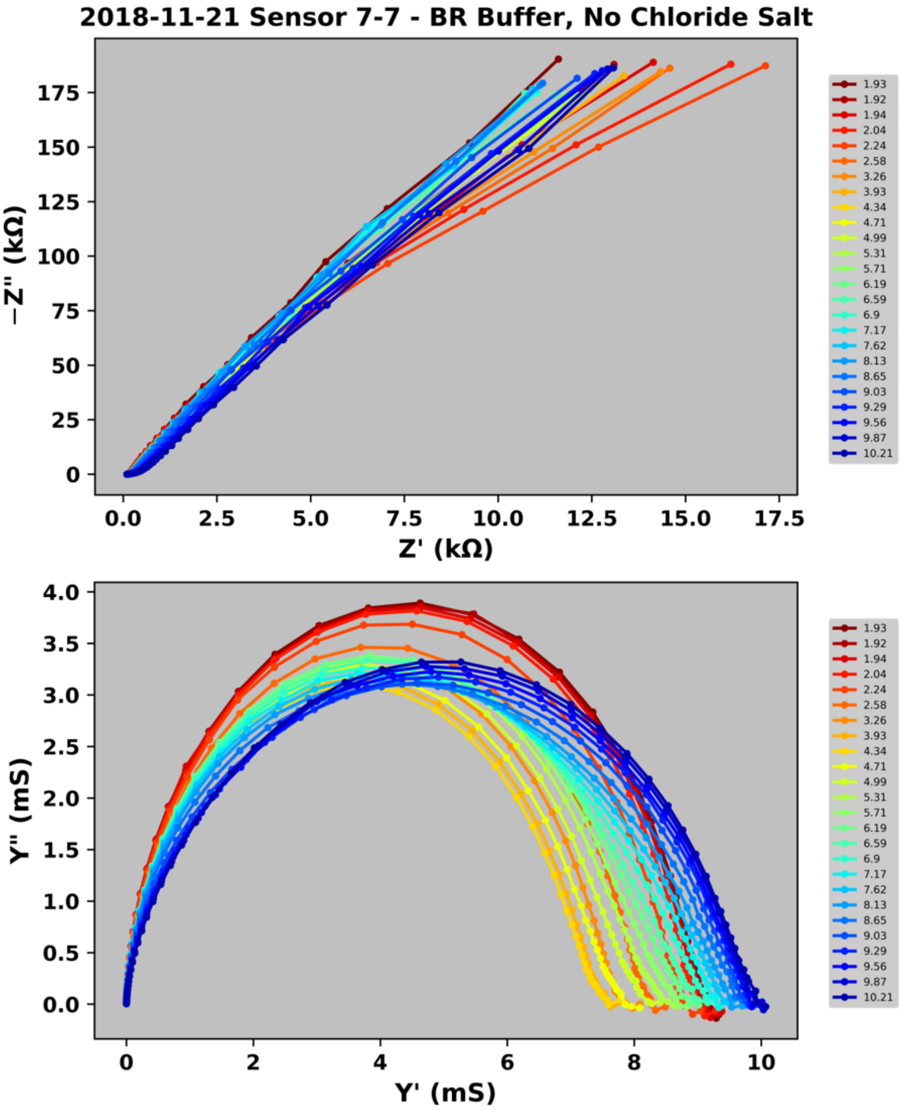

Figure E.5 Nyquist and admittance plots for the "no added chloride salt" buffer, with each pH point color coded from red (acidic) to more basic (blue) (© 2022 Elsevier B.V. All rights reserved.).[220]

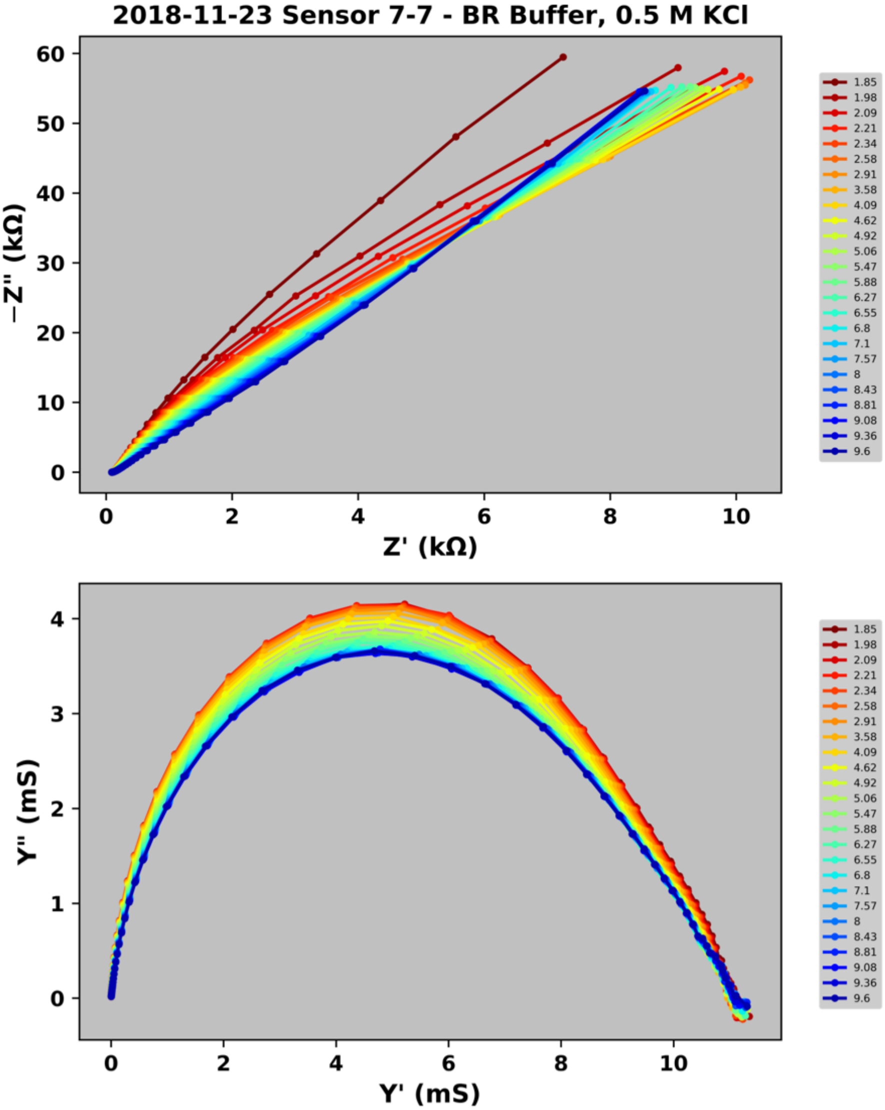

Figure E.6 Nyquist and admittance plots for the 0.5 M KCl buffer, with each pH point color coded from red (acidic) to more basic (blue) (© 2022 Elsevier B.V. All rights reserved.).[220]

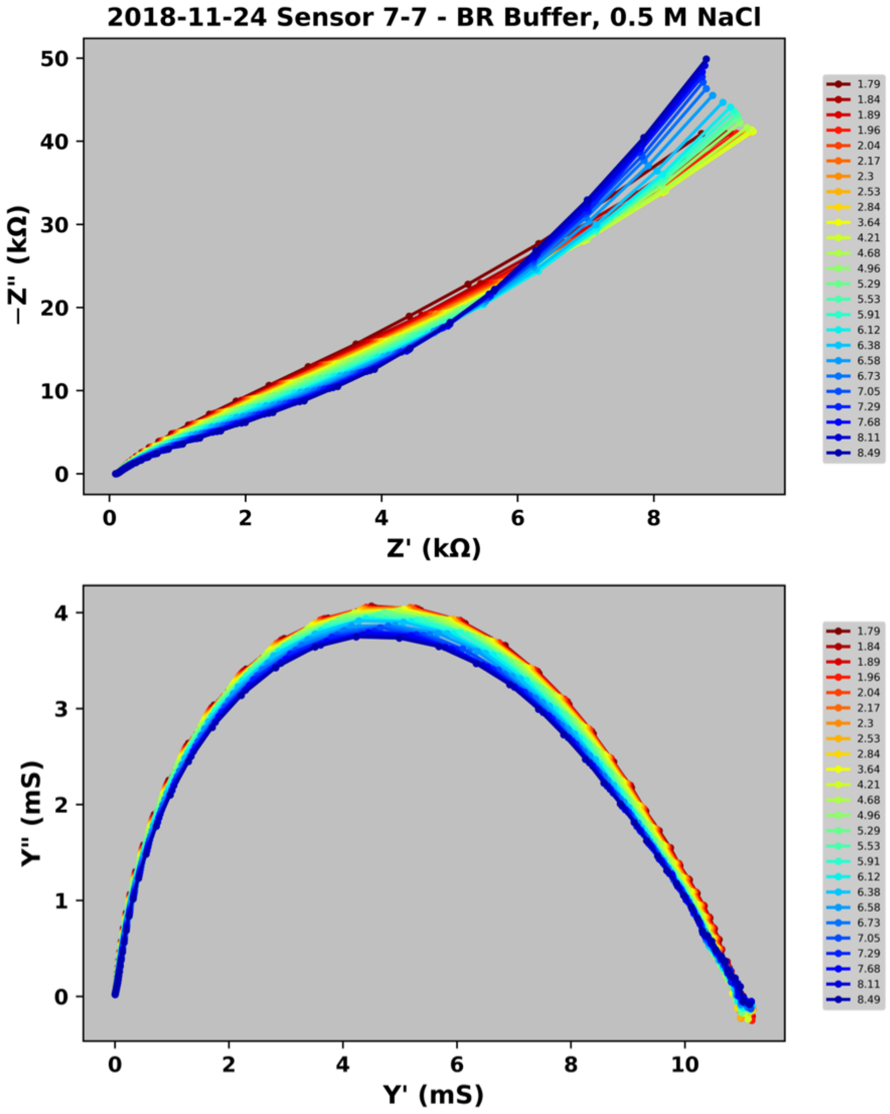

Figure E.7 Nyquist and admittance plots for the 0.5 M NaCl buffer, with each pH point color coded from red (acidic) to more basic (blue) (© 2022 Elsevier B.V. All rights reserved.).[220]

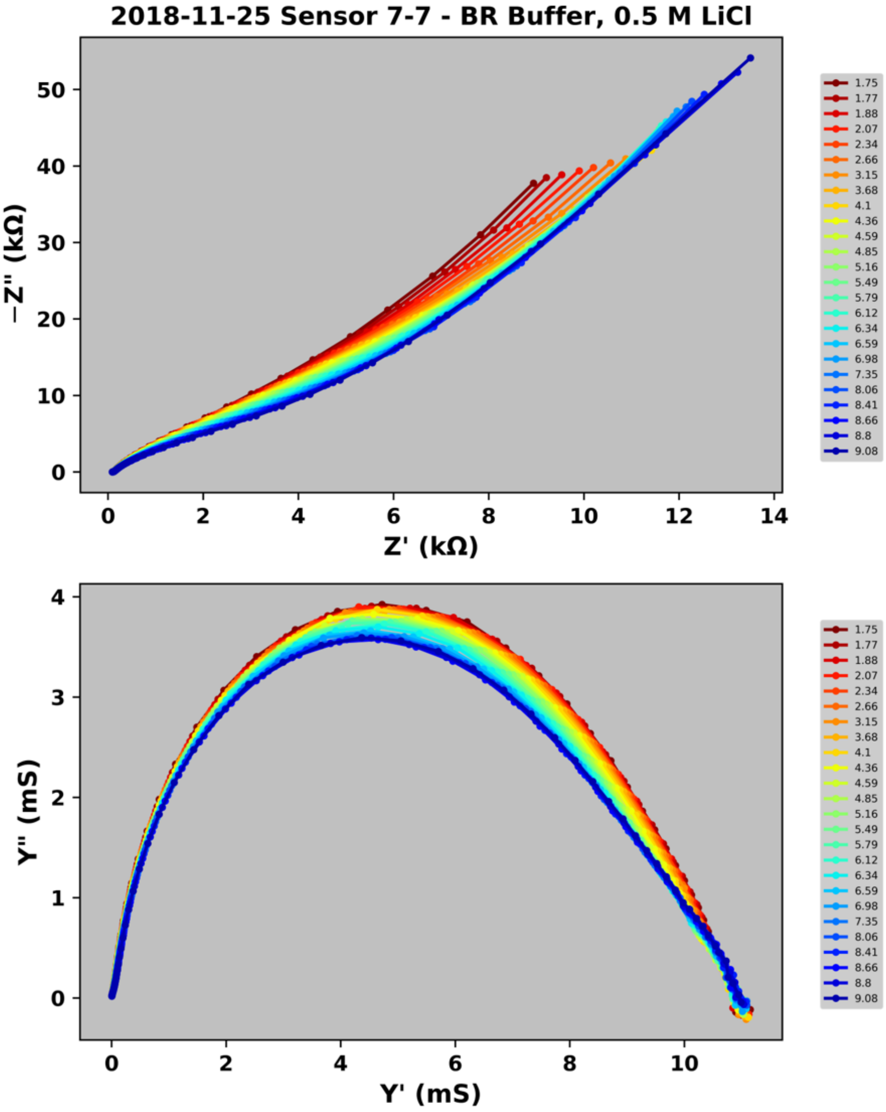

Figure E.8 Nyquist and admittance plots for the 0.5 M LiCl buffer, with each pH point color coded from red (acidic) to more basic (blue) (© 2022 Elsevier B.V. All rights reserved.).[220]

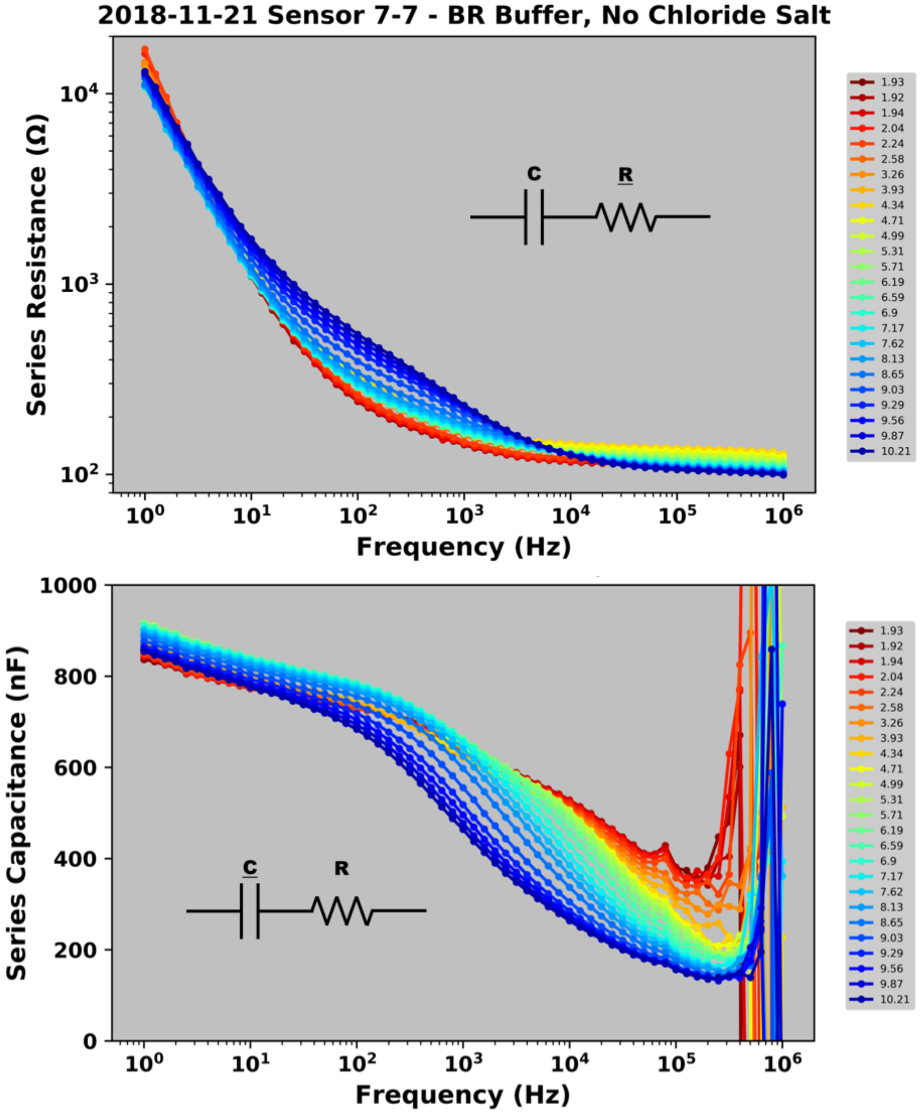

Figure E.9 Series resistance and series capacitance plots for the "no added chloride salt" buffer, with each pH point color coded from red (acidic) to more basic (blue) (© 2022 Elsevier B.V. All rights reserved.).[220]

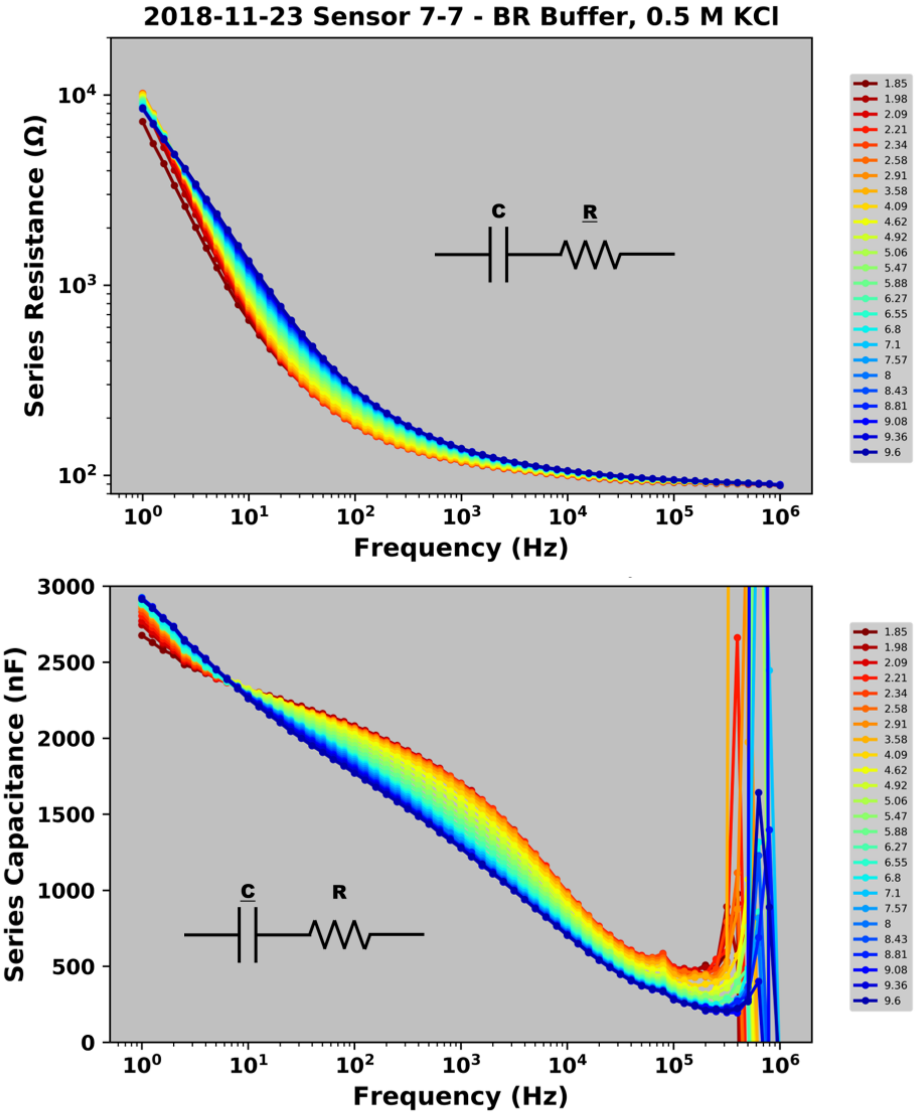

Figure E.10 Series resistance and series capacitance plots for the 0.5 M KCl buffer, with each pH point color coded from red (acidic) to more basic (blue) (© 2022 Elsevier B.V. All rights reserved.).[220]

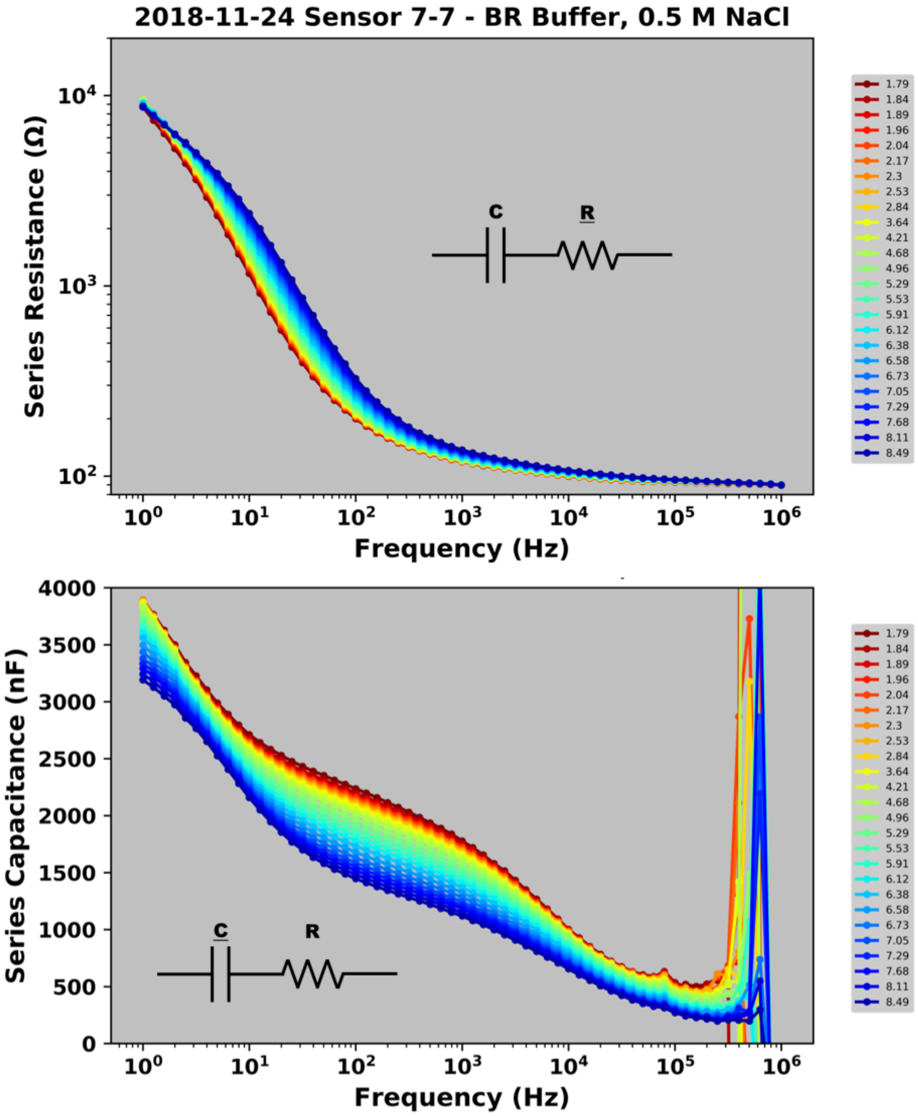

Figure E.11 Series resistance and series capacitance plots for the 0.5 M NaCl buffer, with each pH point color coded from red (acidic) to more basic (blue) (© 2022 Elsevier B.V. All rights reserved.).[220]

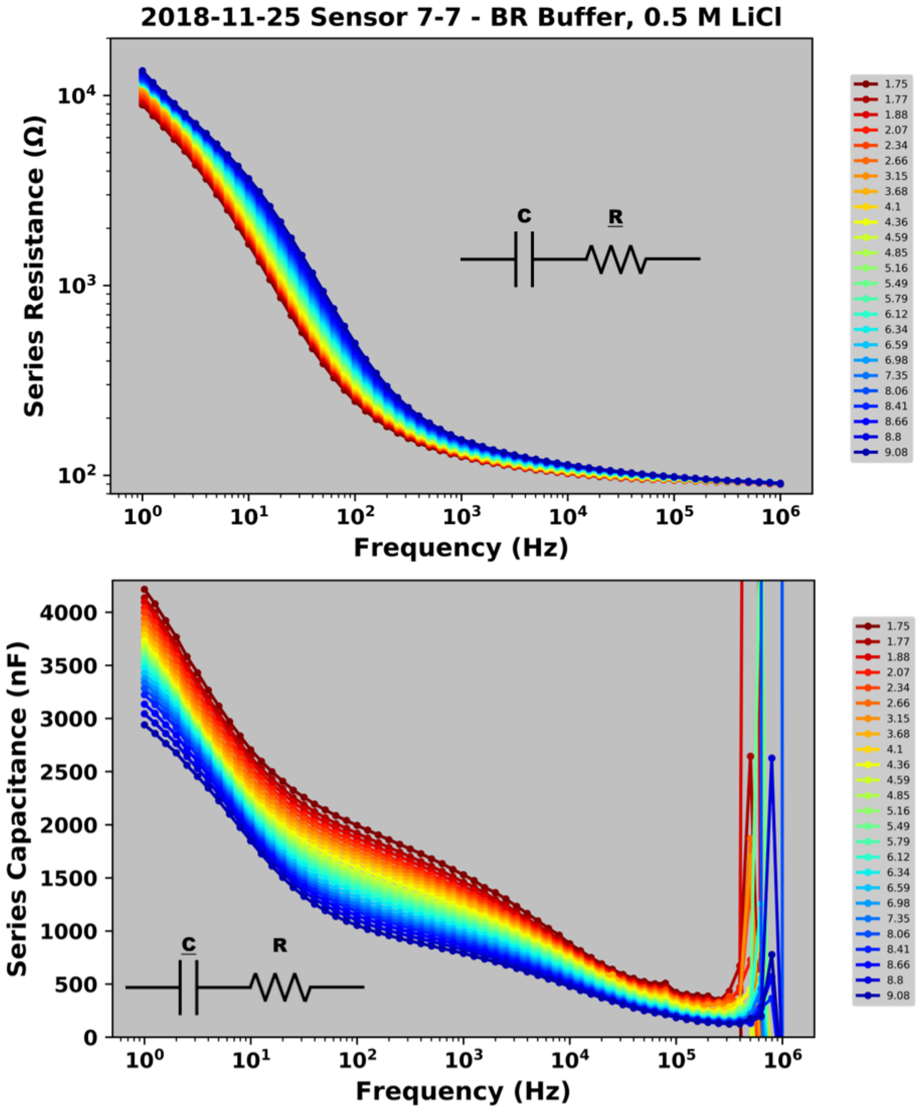

Figure E.12 Series resistance and series capacitance plots for the 0.5 M LiCl buffer, with each pH point color coded from red (acidic) to more basic (blue) (© 2022 Elsevier B.V. All rights reserved.).[220]

Appendix Six

“Low Sodium Kimchi” pH and Immittance Spectra

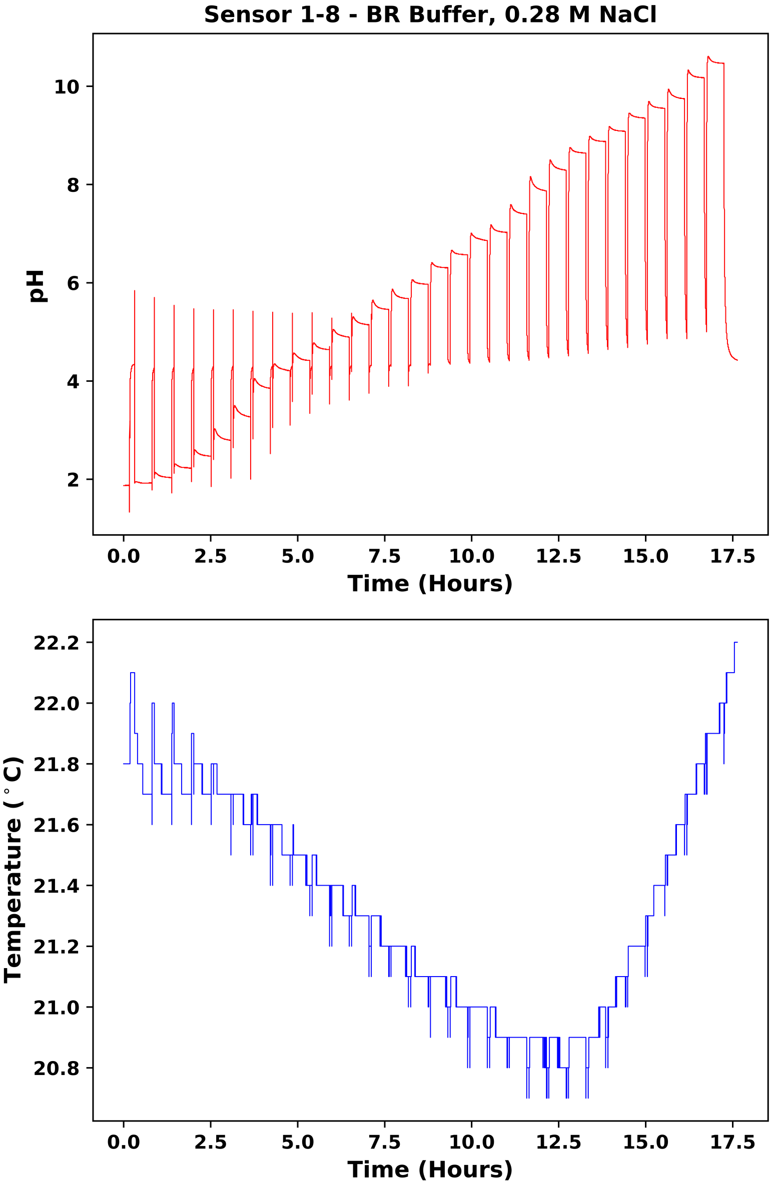

Figure F.1 pH and temperature for sensor 1-8 in 0.28 M NaCl buffer, with "spikes and dips" between the 30 minute pH measurement intervals being when the pH electrode was removed from the measurement solution.

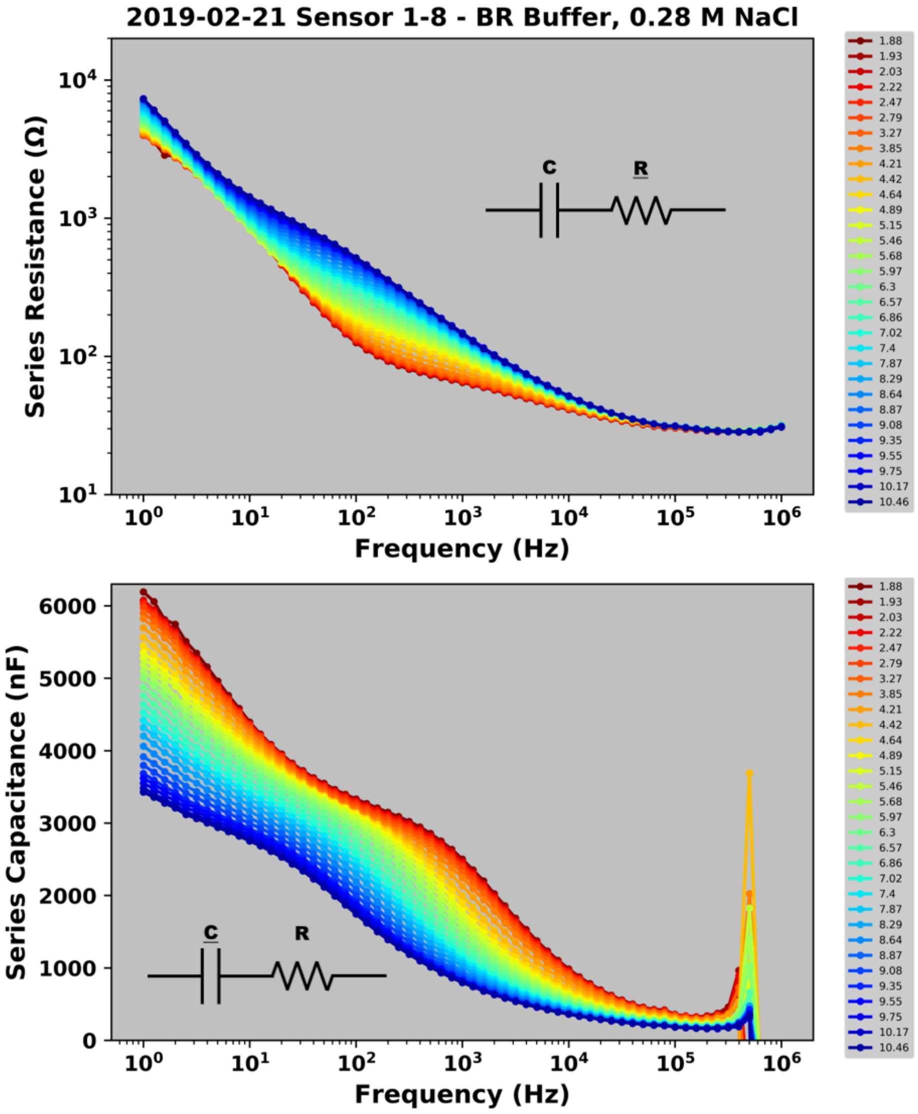

Figure F.2 Series resistance and series capacitance plots for sensor 1-8 in the 0.28 M NaCl buffer, with each pH point color coded from red (acidic) to more basic (blue).

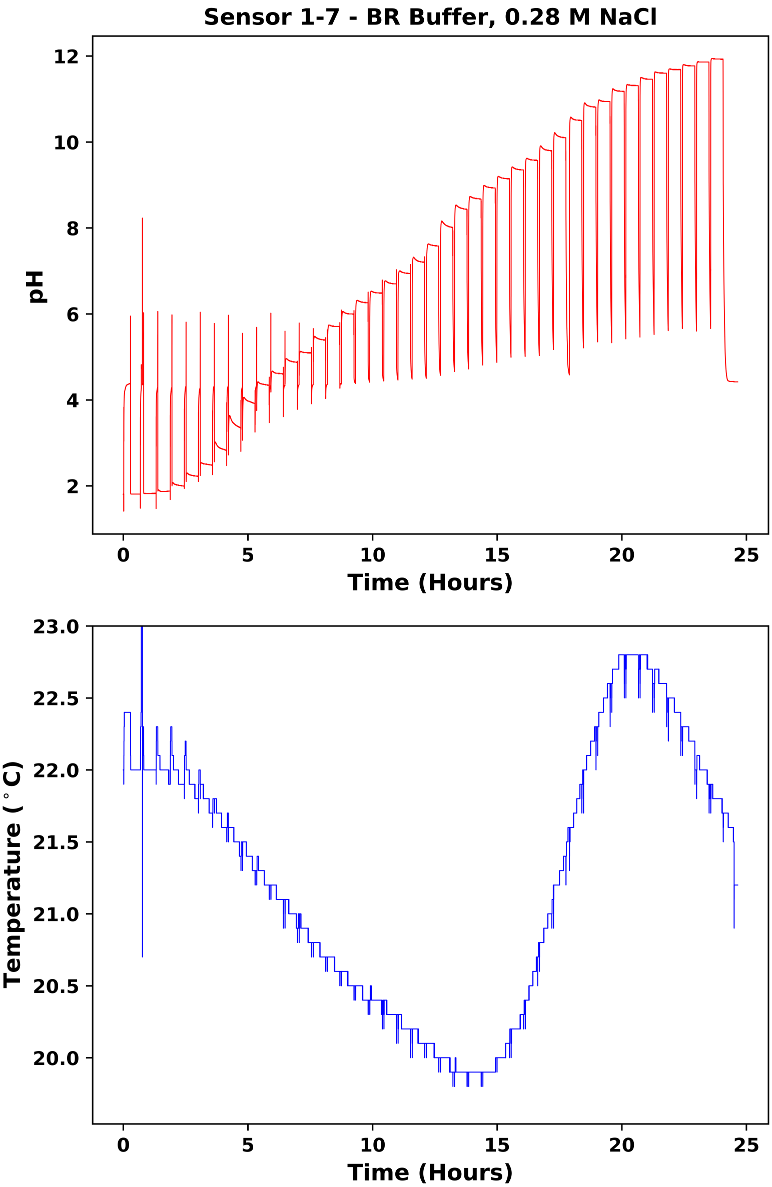

Figure F.3 pH and temperature for sensor 1-7 in 0.28 M NaCl buffer, with "spikes and dips" between the 30 minute pH measurement intervals being when the pH electrode was removed from the measurement solution.

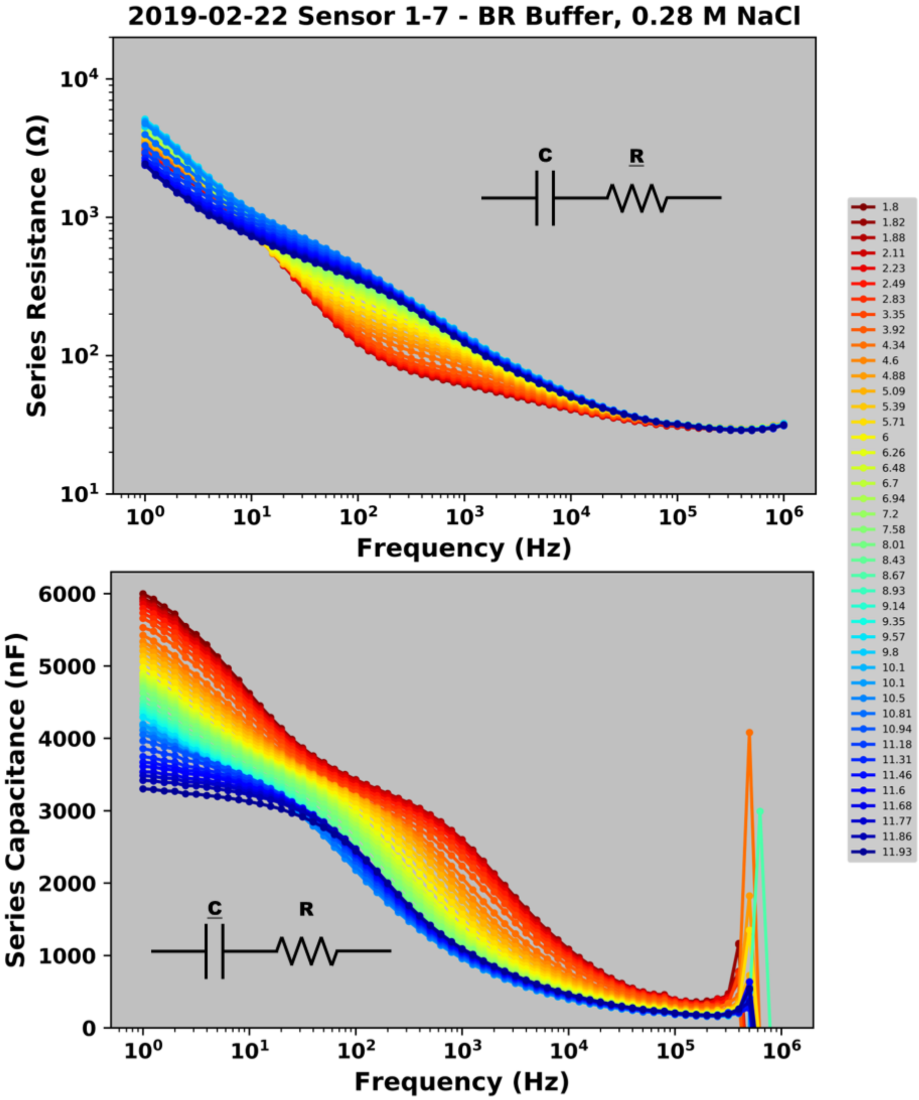

Figure F.4 Series resistance and series capacitance plots for sensor 1-7 in the 0.28 M NaCl buffer, with each pH point color coded from red (acidic) to more basic (blue).

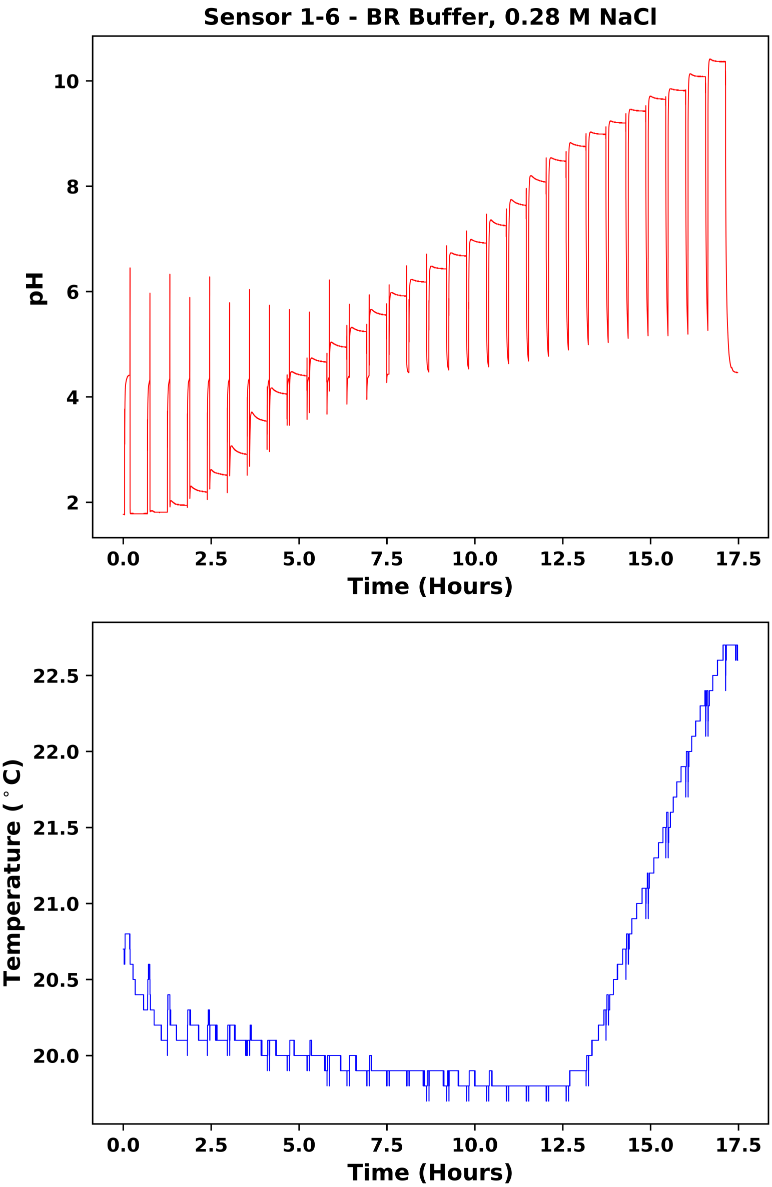

Figure F.5 pH and temperature for sensor 1-6 in 0.28 M NaCl buffer, with "spikes and dips" between the 30 minute pH measurement intervals being when the pH electrode was removed from the measurement solution.

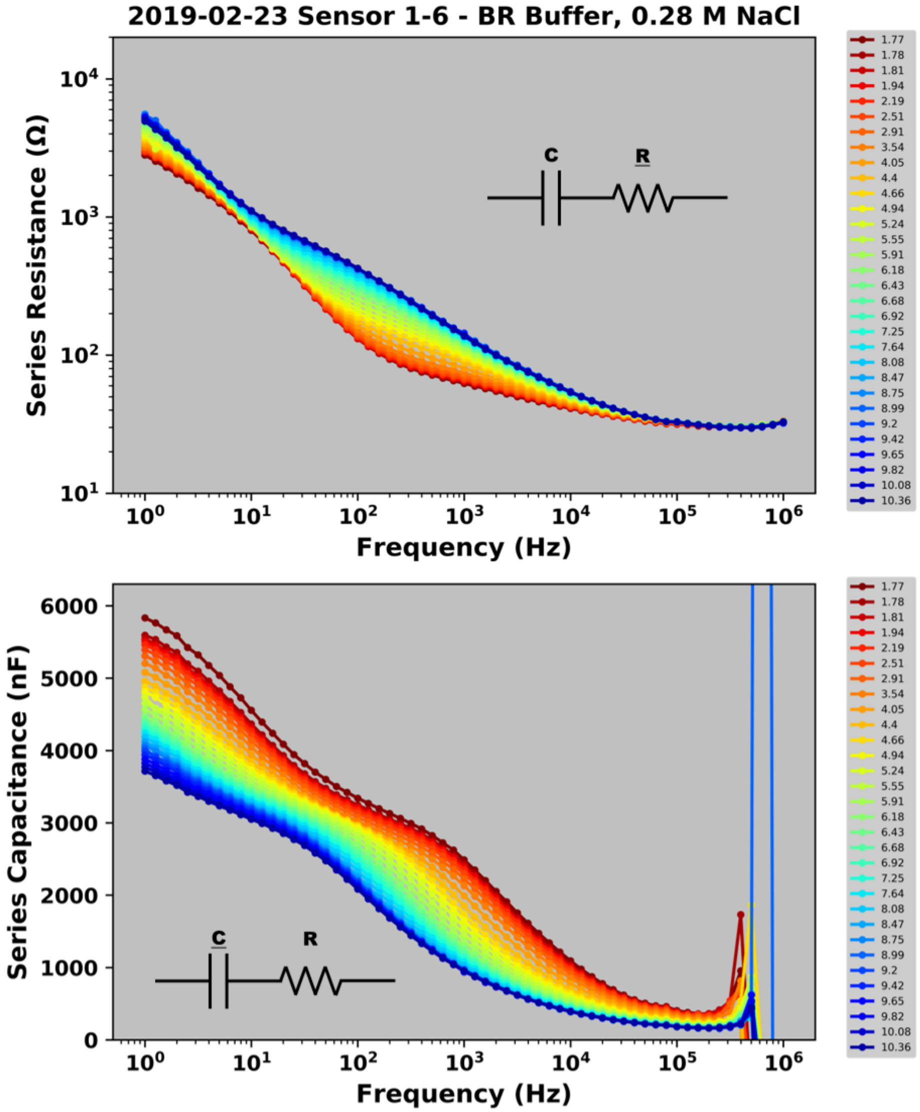

Figure F.6 Series resistance and series capacitance plots for sensor 1-6 in the 0.28 M NaCl buffer, with each pH point color coded from red (acidic) to more basic (blue).

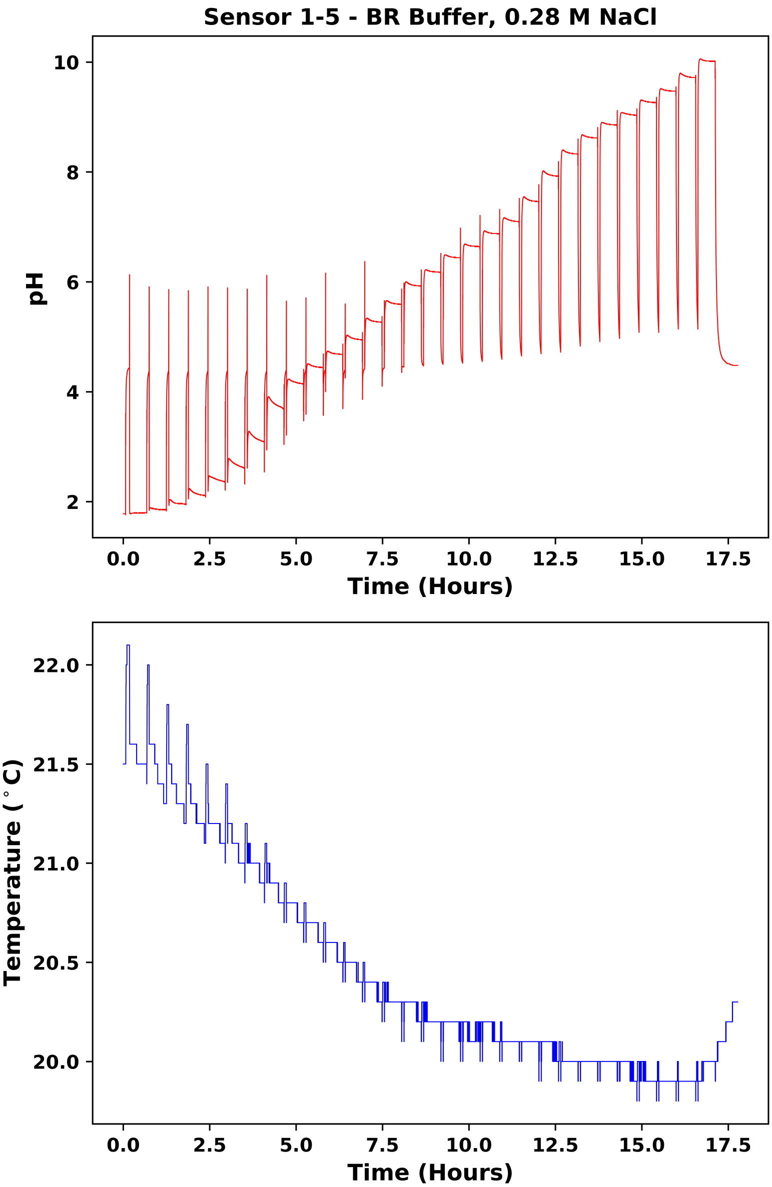

Figure F.7 pH and temperature for sensor 1-5 in 0.28 M NaCl buffer, with “spikes and dips” between the 30 minute pH measurement intervals being when the pH electrode was removed from the measurement solution.

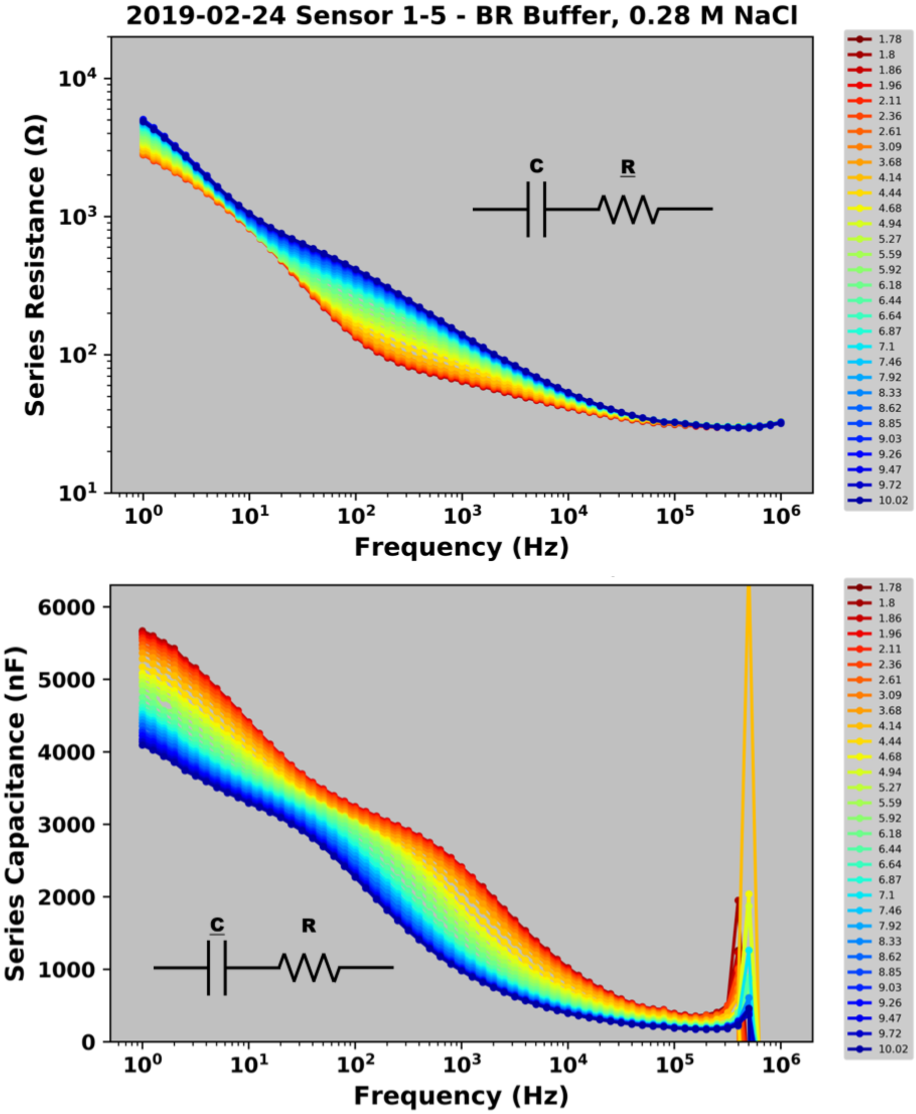

Figure F.8 Series resistance and series capacitance plots for sensor 1-5 in the 0.28 M NaCl buffer, with each pH point color coded from red (acidic) to more basic (blue).

Appendix Seven

Estimated NaOH Molarity Increase for Automated Setup

From Figures 5.8 and 5.14 for the "no added chloride salt" solution, the amount of 30 second additions to 200 mL of buffer for reaching pH 6.9 is 15 (the first pH point is without any added 1 M NaOH). Additionally, from Figure G.1 the amount of 0.2 M NaOH required to get to pH 7 in 100 mL of buffer was 52.5 mL in 1931.[232] The moles of NaOH added in the latter case is then:

$$\frac{0.2\,\text{mol NaOH}}{1\,\text{L}} \cdot \frac{1\,\text{L}}{1000\,\text{mL}} \cdot 52.5\,\text{mL of } 0.2\,\text{M NaOH} = 0.0105\,\text{mol NaOH} \tag{G.1}$$

If instead a 1 M NaOH solution is used in 200 mL of buffer solution, as was performed for the experiments discussed here, the volume required to get to pH 7 can be determined:

$$\frac{200\,\text{mL Buffer}}{100\,\text{mL Buffer}} \cdot 0.0105\,\text{mol NaOH} \cdot \frac{1\,\text{L}}{1\,\text{mol NaOH}} \cdot \frac{1000\,\text{mL}}{1\,\text{L}} = 21\,\text{mL of } 1\,\text{M NaOH} \tag{G.2}$$

Then if it takes 15 additions of 1 M NaOH to get to pH 6.9 in 200 mL of buffer solution, and the pH value is rounded up to pH 7, then the volume of added 1 M NaOH per addition can be estimated:

$$\frac{21\,\text{mL of } 1\,\text{M NaOH}}{15\,\text{Additions}} = \frac{1.4\,\text{mL of } 1\,\text{M NaOH}}{\text{Addition}} \tag{G.3}$$

The moles per addition would then be:

$$\frac{1.4\,\text{mL of } 1\,\text{M NaOH}}{\text{Addition}} \cdot \frac{1\,\text{mol NaOH}}{1\,\text{L}} \cdot \frac{1\,\text{L}}{1000\,\text{mL}} = \frac{0.0014\,\text{mol NaOH}}{\text{Addition}} \tag{G.4}$$

Assuming linear behavior from Figure G.1,[232] the calculated values for up to 42 base additions (the number of additions in Figures F.3 and F.4) are then tabulated below in Table G.1.

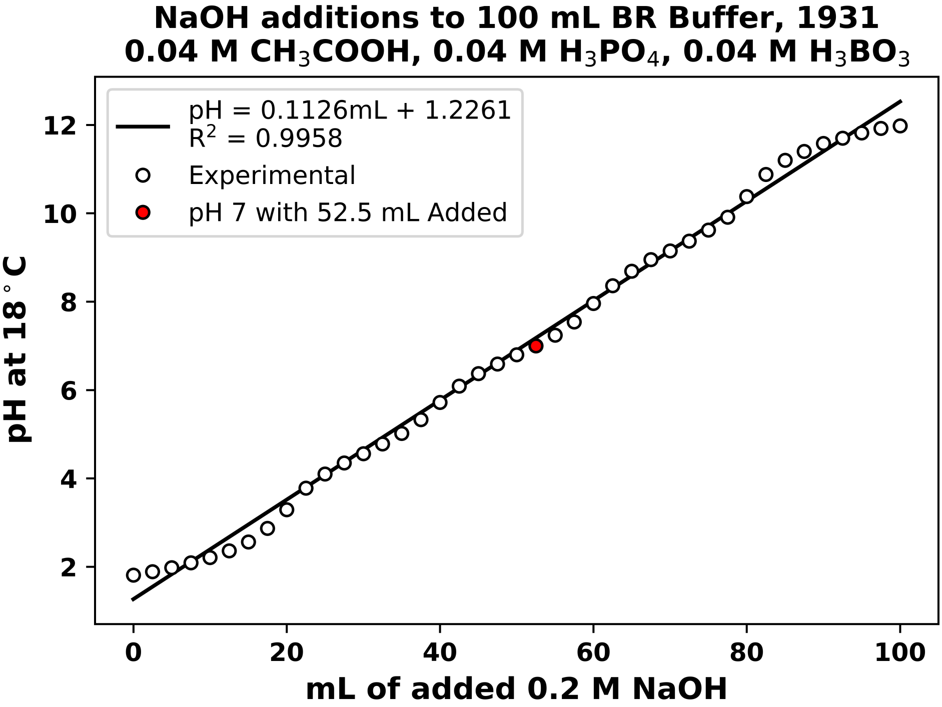

Figure G.1 Original data plotted for 0.2 M NaOH additions to 0.04 M phosphoric acid, 0.04 M acetic acid, and 0.04 M boric acid.[232]

Table G.1 Estimated increase in NaOH molarity with each 30 second addition, where from the “no added chloride salt” solution measurements some pH and addition pairs will be listed: 0 additions - pH 1.93; 5 additions - pH 2.58; 10 additions - pH 4.99; 15 additions - pH 6.9; 20 additions - pH 9.03; 24 additions - pH 10.21. This table is continued on the next page.

Additions	Added Volume (mL)	Total Volume (mL)	Added Moles	NaOH Molarity
0	0.0	200.0	0.0000	0.0000
1	1.4	201.4	0.0014	0.0070
2	2.8	202.8	0.0028	0.0138
3	4.2	204.2	0.0042	0.0206
4	5.6	205.6	0.0056	0.0272
5	7.0	207.0	0.0070	0.0338
6	8.4	208.4	0.0084	0.0403
7	9.8	209.8	0.0098	0.0467
8	11.2	211.2	0.0112	0.0530
9	12.6	212.6	0.0126	0.0593
10	14.0	214.0	0.0140	0.0654
11	15.4	215.4	0.0154	0.0715
12	16.8	216.8	0.0168	0.0775
13	18.2	218.2	0.0182	0.0834
14	19.6	219.6	0.0196	0.0893
15	21.0	221.0	0.0210	0.0950
16	22.4	222.4	0.0224	0.1007
17	23.8	223.8	0.0238	0.1063
18	25.2	225.2	0.0252	0.1119
19	26.6	226.6	0.0266	0.1174
20	28.0	228.0	0.0280	0.1228

Additions	Added Volume (mL)	Total Volume (mL)	Added Moles	NaOH Molarity
21	29.4	229.4	0.0294	0.1282
22	30.8	230.8	0.0308	0.1334
23	32.2	232.2	0.0322	0.1387
24	33.6	233.6	0.0336	0.1438
25	35.0	235.0	0.0350	0.1489
26	36.4	236.4	0.0364	0.1540
27	37.8	237.8	0.0378	0.1590
28	39.2	239.2	0.0392	0.1639
29	40.6	240.6	0.0406	0.1687
30	42.0	242.0	0.0420	0.1736
31	43.4	243.4	0.0434	0.1783
32	44.8	244.8	0.0448	0.1830
33	46.2	246.2	0.0462	0.1877
34	47.6	247.6	0.0476	0.1922
35	49.0	249.0	0.0490	0.1968
36	50.4	250.4	0.0504	0.2013
37	51.8	251.8	0.0518	0.2057
38	53.2	253.2	0.0532	0.2101
39	54.6	254.6	0.0546	0.2145
40	56.0	256.0	0.0560	0.2188
41	57.4	257.4	0.0574	0.2230
42	58.8	258.8	0.0588	0.2272

Appendix Eight

Computer Code for Automated Setup

H.1 Control and Measurement Code (Python 3)

```
# -*- coding: utf-8 -*-
"""
Created on Fri Aug  4 10:24:43 2017

Automized measurement for printed pH- sensors v1.0

TURN COMPUTER SLEEP OFF!!!

@author: c.beale

ALA_VM8 Maniforld Valve Serial Ports:
4 = valve 1
5 = valve 2
6 = valve 3
7 = valve 4
8 = valve 5
9 = valve 6
10 = valve 7
11 = valve 8
"""

from pyfirmata import Arduino, util
from time import sleep
import serial
import subprocess
import datetime
import numpy as np
```

```
#record_pH = Popen-serial-v1.py (pH meter)
#Live_Plot = Popen-LivePlot_pH.py
#pH_meter = os.system("python D:\Chris\test\serial-v1.py")
#pH_meter = subprocess.Popen(["python",
'C:\\Data\\Chris\\Dispenser\\pH_Text_serial-v2.py'])
#live_plot = subprocess.Popen(["python",
"D:\\Chris\\test\\LivePlot_pH.py"])

#Define Global Parameters, which vary for each measurement, time in seconds

MixTime = 1800      #30 minute mix time after base addition
NumIni = 1          #Number of measurements before adding solution
NumAcidMeas = 0     #Number of acid additions/measurements
NumBaseMeas = 30     #Number of base additions/measurements
NumCycle = 1        #Number of acid/base cycles
DropTimeBase = 30    #Base valve open time (seconds)
DropTimeAcid = 10    #Acid valve open time (seconds)
EqTimeAcid = 60      #Acid equilibration time (seconds)
EqTimeBase = 60      #Base equilibration time (seconds)
NumMUXChannel = 5   #Number of MUX Channel used in this measurement
TimeEISMeasure = 240 #time needed per EIS Measurement

TimeEIS = 1*TimeEISMeasure + 60
#NumMUXChannel*TimeEISMeasure #Time (seconds) to measure Z spectrum

command1 = "C:\\Program"
command2 = "Files\\PalmSens"
command3 = "BV\\PSTrace"
command4 = "5.5\\PSTrace"
command5 = "5.5.exe"
command6 = "D:\\Chris\\Dispenser\\Impedance.psscript"
command7 = "-d1"

board = Arduino('COM6') #ALA_VM8 Maniforld Valve
valve_7 = 10 #Base valve
valve_8 = 11 #Acid valve (never used in a measurement)

port_arm = 'COM7' #Braccio Robot Arm
ser_arm = serial.Serial()
ser_arm.baudrate = 9600
ser_arm.port = port_arm
ser_arm.open()
```

```
print('Executing...')
#Measure impedance before adding base to the Britton-Robinson buffer
read_Z = subprocess.Popen([command1, command2, command3,
command4, command5, command6, command7]) #Open/run PalmSens PSTrace
sleep(TimeEIS) #Wait while it's measuringing impedance
read_Z.kill() #Close/kill PalmSens PSTrace

sleep(60)#Wait 60 seconds
#Cycle Loop
time = [] #Initialize time stamp list
for i in range (NumCycle): #I only ever used 1 cycle
    #Add Base
    for j in range(NumBaseMeas): #For each time I increased the pH
        Step = str(j + 1)
        print("pH Increase Step: " + Step)

        board.digital[valve_7].write(1) #Open NaOH valve
        sleep(DropTimeBase) #Wait while the NaOH drops into solution
        board.digital[valve_7].write(0) #Close NaOH valve

        sleep(1) #Wait 1 second

        chrono = str(datetime.datetime.now()) #Timestamp for after adding NaOH
        time += [chrono,] #Add timestamp to the list

        ser_arm.write(bytes([1])) #Move the pH electrode from KCl to BR-soln

        sleep(MixTime) #Leave the pH electrode in the BR-soln for this long

        chrono = str(datetime.datetime.now()) #Timestamp for mix end
        time += [chrono,] #Add timestamp to the list
        time += [' ',] #Add a new line
        ar_time = np.array([time]) #Convert the list to a numpy array
        ar = np.transpose(np.vstack((ar_time))) #Transpose the time array
        np.savetxt('pH_Measure_Log.txt', ar,fmt='%s',
        delimiter = ',', newline = '\r\n') #Save the timestamps to txt

        ser_arm.write(bytes([0])) #Move the pH electrode from BR-Soln to KCl

        sleep(30) #Wait 30 seconds

        read_Z = subprocess.Popen([command1, command2, command3,
        command4, command5, command6, command7]) #Open/run PSTrace
        sleep(TimeEIS) #Wait while it's measuringing impedance
```

```
        read_Z.kill() #Close/kill PalmSens PSTrace

    for k in range(NumAcidMeas): #Never used, but could be built upon
        Step = str(k + 1)
        print("pH Decrease Step: " + Step)

        board.digital[valve_8].write(1)
        sleep(DropTimeAcid)
        board.digital[valve_8].write(0)

        sleep(1)

        ser_arm.write(bytes([1]))

        sleep(EqTimeAcid)

        ser_arm.write(bytes([0]))

        sleep(EqTimeAcid)

        read_Z = subprocess.Popen([command1, command2, command3,
        command4, command5, command6, command7])
        sleep(TimeEIS)
        read_Z.kill()

sleep(10) #Wait 10 seconds

board.exit()
ser_arm.close()
print('...process executed.')
#pH_meter.kill()
#live_plot.kill()
```

H.2 Arduino Braccio Arm (C++)

```
/*
  pH-Electrode_v4

  First version allowing for serial commands from python. Servos have been
  realigned manually in order for the pH electrode to start as close as
  possible to the safety position.
```

```
  Created on 03 Sep 2018
  by Christopher Beale

  Forschungszentrum Juelich
*/

#include <Braccio.h>
#include <Servo.h>
#include <SoftwareSerial.h>


Servo base;
Servo shoulder;
Servo elbow;
Servo wrist_rot;
Servo wrist_ver;
Servo gripper;


void setup() {
  //Initialization functions and set up the initial position for Braccio
  //All the servo motors will be positioned in the "safety" position
  //(manually realligned):
  Serial.begin(9600);
  Braccio.begin();
  pinMode(13, OUTPUT);
}

//Command Variables
int Position_ = 0;
int Request_ = 0;
bool Initializing_ = true;

//Electrode Positions
int Remove = 0; //Removed postion
int Clean = 45;
int Measure = 90; //Measurement position

//Servo Variables
int fixed_M2 = 45; //Elbow fixed
int initial_M3 = 180;
int initial_M4 = 0;
int flat_M5 = 156; //Hand stays parallel to Earth
int no_M6 = 60; //Gripper motor has been removed
```

```
//Degree Counters
int degree = 0; //Slow movement counter in degrees
int upM3 = 0; //M3 up-counter
int upM4 = 0; //M4 up-counter
int downM3 = 0; //M3 down-counter
int downM4 = 0; //M4 down-counter
int msDelay = 100; //Time at each degree in ms

// LED blinker (Debugging Purposes)
unsigned long timer=0;
bool ledState=false;

void loop() {
  // LED blinker
  if(millis() - timer > 500)
    {
    ledState=!ledState;
    digitalWrite(13, ledState);
    timer=millis();
    }
  /*
  Step Delay: a milliseconds delay between the movement of each servo.
  Allowed values from 10 to 30 msec.
  M1=base degrees. Allowed values from 0 to 180 degrees
  M2=shoulder degrees. Allowed values from 15 to 165 degrees
  M3=elbow degrees. Allowed values from 0 to 180 degrees
  M4=wrist vertical degrees. Allowed values from 0 to 180 degrees
  M5=wrist rotation degrees. Allowed values from 0 to 180 degrees
  M6=gripper degrees. Allowed values from 10 to 73 degrees.
   10: the toungue is open, 73: the gripper is closed.
  */

  //Start at Position_ = 0
  if (Initializing_){
    Braccio.ServoMovement(30, Remove, fixed_M2, initial_M3,
                          initial_M4, flat_M5,  no_M6);
    Initializing_ = false;
  }else{
    //Take Request
    if (Serial.available()>0){
      Request_ = Serial.read();
    }
    //Move to position
```

```
if (Request_ != 1 && Position_ == 0){
  Braccio.ServoMovement(30, Remove, fixed_M2, initial_M3,
                        initial_M4, flat_M5,  no_M6);
}else if (Request_ != 0 && Position_ == 1){
  Braccio.ServoMovement(30, Measure, fixed_M2, initial_M3,
                        initial_M4, flat_M5,  no_M6);
}else if (Request_ == 1 && Position_ == 0){
  //Remove Position Up
  for(degree = 1; degree <= 20; degree++){
    upM3 = 180 - degree;
    upM4 = 0 + degree;
    Braccio.ServoMovement(10, Remove, fixed_M2, upM3,
                          upM4,  flat_M5,   no_M6);
    delay(msDelay); //(1 degree ms step time)
  }
  //Move to Clean Position
  Braccio.ServoMovement(30, Clean,  fixed_M2, upM3,
                        upM4,  flat_M5,  no_M6);
  //Clean position down
  for(degree = 1; degree <= 20; degree++){
    downM3 = 160 + degree;
    downM4 = 20 - degree;
    Braccio.ServoMovement(10, Clean, fixed_M2, downM3,
                          downM4,  flat_M5,   no_M6);
    delay(msDelay); //(1 degree ms step time)
  }
  delay(5000);
  //Clean Position up
  for(degree = 1; degree <= 20; degree++){
    upM3 = 180 - degree;
    upM4 = 0 + degree;
    Braccio.ServoMovement(10, Clean, fixed_M2, upM3,
                          upM4,  flat_M5,   no_M6);
    delay(msDelay); //(1 degree ms step time)
  }
  //Move to Measure Position
  Braccio.ServoMovement(30, Measure,  fixed_M2, upM3,
                        upM4,  flat_M5,  no_M6);
  //Measure Position Down
  for(degree = 1; degree <= 20; degree++){
    downM3 = 160 + degree;
    downM4 = 20 - degree;
    Braccio.ServoMovement(10, Measure, fixed_M2, downM3,
                          downM4,  flat_M5,   no_M6);
```

```
    delay(msDelay); //(1 degree ms step time)
  }
  Position_ = 1;
}else if (Request_ == 0 && Position_ == 1){
  //Measurement position up
  for(degree = 1; degree <= 20; degree++){
    upM3 = 180 - degree;
    upM4 = 0 + degree;
    Braccio.ServoMovement(10, Measure, fixed_M2, upM3,
                          upM4,  flat_M5,   no_M6);
    delay(msDelay); //(1 degree ms step time)
  }
  //Move to Clean Position
  Braccio.ServoMovement(30, Clean,  fixed_M2, upM3,
                      upM4,  flat_M5,  no_M6);
  //Clean position down
  for(degree = 1; degree <= 20; degree++){
    downM3 = 160 + degree;
    downM4 = 20 - degree;
    Braccio.ServoMovement(10, Clean, fixed_M2, downM3,
                          downM4,  flat_M5,   no_M6);
    delay(msDelay); //(1 degree ms step time)
  }
  delay(5000);
  //Clean Position up
  for(degree = 1; degree <= 20; degree++){
    upM3 = 180 - degree;
    upM4 = 0 + degree;
    Braccio.ServoMovement(10, Clean, fixed_M2, upM3,
                          upM4,  flat_M5,   no_M6);
    delay(msDelay); //(1 degree ms step time)
  }
  //Move electrode to removed position
  Braccio.ServoMovement(30, Remove,  fixed_M2, upM3,
                      upM4,  flat_M5,  no_M6);
  //pH Down
  for(degree = 1; degree <= 20; degree++){
    downM3 = 160 + degree;
    downM4 = 20 - degree;
    Braccio.ServoMovement(10, Remove, fixed_M2, downM3,
                          downM4,  flat_M5,   no_M6);
    delay(msDelay); //(1 degree ms step time)
  }
  Position_ = 0;
```

```
    }
  }
}
```

Band / Volume 73
Development, characterization, and application of compliantintracortical implants
K. Srikantharajah (2021), xiv, 155, xv-xvii pp
ISBN: 978-3-95806-587-1

Band / Volume 74
Modelling, implementation and characterization of a Bias-DAC in CMOS as a building block for scalable cryogenic control electronics for future quantum computers
P. N. Vliex (2021), xiv, 107, xv-xxviii pp
ISBN: 978-3-95806-588-8

Band / Volume 75
Development of Electrochemical Aptasensors for the Highly Sensitive, Selective, and Discriminatory Detection of Malaria Biomarkers
G. Figueroa Miranda (2021), XI, 135 pp
ISBN: 978-3-95806-589-5

Band / Volume 76
Nanostraw- Nanocavity MEAs as a new tool for long-term and high sensitive recording of neuronal signals
P. Shokoohimehr (2021), xi, 136 pp
ISBN: 978-3-95806-593-2

Band / Volume 77
Surface plasmon-enhanced molecular switching for optoelectronic applications
B. Lenyk (2021), x, 129 pp
ISBN: 978-3-95806-595-6

Band / Volume 78
Engineering neuronal networks in vitro: From single cells to population connectivity
I. Tihaa (2021), viii, 242 pp
ISBN: 978-3-95806-597-0

Band / Volume 79
Spectromicroscopic investigation of local redox processes in resistive switching transition metal oxides
T. Heisig (2022), vi, 186 pp
ISBN: 978-3-95806-609-0

Band / Volume 80
Integrated Control Electronics for Qubits at Ultra Low Temperature
D. Nielinger (2022), xviii, 94, xix-xxvi
ISBN: 978-3-95806-631-1

Band / Volume 81
Higher-order correlation analysis in massively parallel recordings in behaving monkey
A. Stella (2022), xiv, 184 pp
ISBN: 978-3-95806-640-3

Band / Volume 82
Denoising with Quantum Machine Learning
J. Pazem (2022), 106 pp
ISBN: 978-3-95806-641-0

Band / Volume 83
Hybrid hydrogels promote physiological functionality of long-term cultured primary neuronal cells in vitro
C. Meeßen (2022), x, 120 pp
ISBN: 978-3-95806-643-4

Band / Volume 84
Surface states and Fermi-level pinning on non-polar binary and ternary (Al,Ga)N surfaces
L. Freter (2022), 137 pp
ISBN: 978-3-95806-644-1

Band / Volume 85
Dynamical and statistical structure of spatially organized neuronal networks
M. Layer (2022), xiii, 167 pp
ISBN: 978-3-95806-651-9

Band / Volume 86
Persistent firing and oscillations in the septo-hippocampal system and their relation to locomotion
K. Korvasová (2022), 111 pp
ISBN: 978-3-95806-654-0

Band / Volume 87
Sol-Gel-Synthese, Tintenstrahldruck und Blitzlampentemperung von Tantaloxid-Dünnschichten zur pH-Messung
C. D. Beale (2022), xlix, 339 pp
ISBN: 978-3-95806-656-4

Weitere ***Schriften des Verlags im Forschungszentrum Jülich*** unter
http://wwwzb1.fz-juelich.de/verlagextern1/index.asp

Information
Band / Volume 87
ISBN 978-3-95806-656-4

Mitglied der Helmholtz-Gemeinschaft

JÜLICH
Forschungszentrum